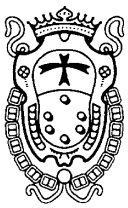

Scuola Normale Superiore di Pisa
Classe di Scienze

Tesi di Perfezionamento in Fisica

Ultra-Low Frequency Inverted Pendulum for the VIRGO Test Mass Suspension

Author:
Giovanni Losurdo

Supervisor:
Prof. Francesco Fidecaro

October 1998

A Tito

Contents

Introduction

The discovery of PSR1913+16 binary pulsar and the observation of its orbital period decay provided the undirect evidence that gravitational waves do exist. Several interferometric gravitational waves detectors will be operating in the world in a few years. The goals of interferometric detectors, of unprecedented sensitivity over a wide band, are ambitious: the first detection and the beginning of a new astronomy. The Italian-French VIRGO antenna is one of these detectors and it is now being built on the Cascina site, near Pisa.

VIRGO aims to have a detection range of frequency extending from a few Hz to several kHz. The sensitivity of ground based antennas in this range is limited by seismic noise. Since ten years ago, Pisa VIRGO Group is working on the project of the mirror suspensions, called *superattenuators*, aimed to isolate the mirror from ground vibrations and to extend the low frequency sensitivity threshold down to few Hz. This work is part of this research field.

Aims of the work In this thesis we propose a newly conceived Inverted Pendulum top stage for the VIRGO superattenuator, capable of:

1. performing a pre-isolation action.
2. acting as a soft positioning device for the suspended mirror;
3. providing a suitable platform for active damping of the SA resonances.

These carachteristics not only allow to improve the overall isolation performance of the superattenuator, but, above all, allow to simplify the interferometer locking strategy. Other groups involved in gravitational waves detection research are developing pre-isolators for their suspension systems. The one proposed here has been validated and approved suitable for VIRGO.

Plan of the thesis This thesis is divided into 8 chapters:

- chapters 1,2,3 are an introduction to GW physics: theory, evidences of existence, principle of interferometric detection, expected sources are reviewed. The operation of an interferometric detectors, the limitations to its sensitivity and the design of VIRGO interferometer are described;

- in chapter 4 the VIRGO superattenuator design and its performance are described;
- chapter 5 should be read as a proposal: it explains why an Inverted Pendulum is suitable as a top stage for the VIRGO superattenuator. The physics of the Inverted Pendulum is outlined, the calculations are reviewed and the design of the top stage is described.
- chapter 6,7,8 describe the experimental work done: the experimental setup used for the tests, the tests of the Inverted Pendulum as a passive pre-isolator, the tests of the Inverted Pendulum as a platform for active controls of the mirror.

Chapter 1

Gravitational Waves

1.1 The binary pulsar PSR1913+16

The theory of general relativity was published in 1916 [1]. Although up to now gravitational waves remain undetected, an important astrophysical discovery has given the scientific community the indirect evidence that they do exist: the binary pulsar PSR1913+16. In 1974 Russel Hulse and Joseph Taylor observed for the first time the radio pulses of a neutron star bound to a dark companion in a binary system. After more than 20 years of observations data are useful to test general relativity to an high level of accuracy [14, 15] and also to compare general relativity with other theories of gravity.

Pulsar 1913+16 is an accurate clock moving at high velocity ($v/c \sim 10^{-3}$) in the strong gravitational field of a dark companion, with orbital period of $7^h\ 45^m$. The data from the observation consist of pulse arrival times. Doppler shift of the pulse period is related to the pulsar orbit and to relativistic effects such as gravitational redshift. The data analysis allows to determine, to high level of accuracy, the parameters that give a complete description of the dynamics of the binary system. General relativity predicts such a system to lose energy and angular momentum via emission of gravitational waves. This loss turns into a decrease of the orbital period of the pulsar. Hulse and Taylor have measured the orbital period rate of decay, which is in good agreement with general relativity predictions: their measurement is considered as the first evidence of the existence of gravitational waves (GW).

1.1.1 Keplerian and post-keplerian parameters

In this section we review the results of the measurements performed by Hulse and Taylor, in order to put in evidence the very good accuracy allowed by this astrophysical laboratory.

The parameters, determined by fitting experimental data with the theoretical model, are divided in two groups:

- *keplerian parameters* (which determine the newtonian orbit):
  1. P: the orbital period;
  2. e: the orbit eccentricity;
  3. $x = a \sin i/c$, where a is the semimajor axis of the orbit, i is the angle between the orbital angular momentum and the line of sight from Earth to pulsar, c is the velocity of light;
  4. ω: the longitude of periastron;
  5. T_0: the time of periastron passage;
- *post-keplerian (PK) parameters* (associated to relativistic effects):
  1. $\dot{\omega}$: the advance of periastron;
  2. γ: the time dilation and gravitational redshift parameter;
  3. $\dot{P}$: the orbital period rate of decay.

The values of these parameters obtained from the data of ten years high quality timing observation are listed in the table [13].

parameter	**value**
P (s)	27906.9807807(9)
e	0.6171309(6)
x (s)	2.341759(3)
ω (°)	226.57531(9)
T_0 (MJD)	46443.99588321(5)
$\dot{\omega}$ (°yr^{-1})	4.226628(18)
γ (ms)	4.294(3)
$\dot{P}$	-2.425(10)$\times 10^{-12}$

The PK parameters are functions of the two star masses: from the equations

$$\dot{\omega}^{\rm th}(m_p, m_c) = \dot{\omega}^{\rm obs} \quad (1.1)$$

$$\gamma^{\rm th}(m_p, m_c) = \gamma^{\rm obs} \quad (1.2)$$

the masses of the two stars have been accurately derived [12]:

$$m_p = 1.442 \pm 0.003\ M_\odot \qquad ; \qquad m_c = 1.386 \pm 0.003\ M_\odot$$

where m_p is the mass of the pulsar and m_c that of the dark companion[1].

[1] This result has been published in 1989. It is interesting to compare it with the former result published in 1982:

$$m_p = 1.42 \pm 0.06\ M_\odot \qquad ; \qquad m_c = 1.41 \pm 0.06\ M_\odot$$

Seven years of further observation reduced the uncertainty $\delta m/m$ from about 4% to about 0.2%.

1.1.2 Orbit decay

According to general relativity the binary system emits GW with luminosity (see [19] and references therein):

$$\mathcal{L} = \frac{32}{5}\frac{G^4}{c^5}\frac{(m_p m_c)^2(m_p+m_c)}{a^5}f(e), \tag{1.3}$$

where $f(e)$ is a function[2] of the orbit ellipticity e and a is the semimajor axis of the orbit[3]. The system loses energy and angular momentum via GW emission: PSR1913+16 is spiralling towards its companion and the two stars will coalesce in $3.5 \cdot 10^8$ years. The general relativity prediction of the period decrease is straightforward using the values of the star masses calculated above:

$$\begin{aligned} \dot{P}^{\rm th} &= -\frac{192\pi}{5}\left[\frac{2\pi G}{c^3 P}\right]^{5/3}\frac{m_p m_c}{(m_p+m_c)^{1/3}}f(e) \\ &= (-2.40216 \pm 0.00021)\times 10^{-12} \end{aligned} \tag{1.4}$$

The result of the observation is:

$$\dot{P}^{\rm obs} = -2.425(10)\times 10^{-12} \tag{1.5}$$

To correctly compare theory and experiment the perturbing effect of the Galaxy gravitational field has to be subtracted[4] [16]. The result is:

$$\boxed{\frac{\dot{P}^{\rm obs} - \dot{P}^{\rm gal}}{\dot{P}^{\rm th}} = 1.0032 \pm 0.0035} \tag{1.6}$$

The agreement between the general relativity prediction and the observation is at $3 \cdot 10^{-3}$ level: this result is a success of general relativity and is considered as the indirect proof of GW existence. Moreover, as pointed out by Damour [18], this is also a proof of the propagation properties of the gravitational field in the strong field regime.

[2]The function $f(e)$ is written [11]:

$$f(e) = (1-e^2)^{-7/2}\left(1+\frac{73}{24}e^2+\frac{37}{96}e^4\right)$$

In case of circular orbit ($e=0$), $f(e)=1$ and the GW luminosity is minimum.

[3]For the sake of simplicity: in the case of circular orbit and $m_p = m_c = m$ (1.3) is written:

$$\mathcal{L} = \frac{64}{5}\frac{G^4}{c^5}\frac{m^5}{R^5}$$

where R is the orbit radius.

[4]The observed period $P^{\rm obs}$ depends on the relative velocity of the pulsar and the solar system. Then, $\dot{P}^{\rm obs}$ depends on their relative acceleration. The pulsar and the Sun accelerate towards the galactic centre in such a way that a non null relative acceleration is present, which turns into an error on the measured $\dot{P}^{\rm obs}$.

1.1.3 Other theories of gravity

The observation of the PSR1913+16 and of other similar systems (such as PSR1534+12 [32]) has provided a natural laboratory to test gravity theories in a strong-field regime. Damour and Esposito-Farèse [17, 18] have studied a class of two parameters tensor-scalar theories of gravity, compatible with the equivalence principle, at the light of the results coming from binary pulsars experiments, and have calculated the constraints imposed to the parameters by the observations. This class of theory predicts the existence of scalar GW beside the usual tensor waves. The detection of GW from coalescing binaries and the observations of binary pulsars could prove quantitatively the radiative aspects of relativistic gravity and help to discriminate between general relativity and other theories.

1.2 Gravitational Waves

In the weak field approximation Einstein equations can be linearized and then admit wave solutions describing ripples in the space-time metric propagating at the speed of light: *gravitational waves*. In the following we describe shortly the theory of GW, referring the reader to [2, 3] for details.

The flat space of Special Relativity is described by the Minkowski metric:

$$\mathrm{d}s^2 = \eta_{\mu\nu}\mathrm{d}x^\mu \mathrm{d}x^\nu = -c^2\mathrm{d}t^2 + \sum_{i=1}^{3} \mathrm{d}x_i^2 \tag{1.7}$$

The metric of regions of space-time where the gravitational field of astrophysical objects is weak can be written in the form:

$$g_{\mu\nu} = \eta_{\mu\nu} + h_{\mu\nu} \tag{1.8}$$

with $|h_{\mu\nu}| \ll 1$. The tensor $\mathbf{h}$ is a small perturbation to the flat space geometry. To first order with respect to $h_{\mu\nu}$ the field equations are linear. The freedom in the choice of the coordinate system can be used to impose $\mathbf{h}$ to be transverse and traceless (TT gauge). In this gauge the coordinates are marked by the world lines of freely falling test masses (that is, the coordinates of freely falling test masses are constant). With such a choice, Einstein equations in the weak field approximation, are written:

$$\left(\nabla^2 - \frac{1}{c^2}\frac{\partial^2}{\partial t^2}\right) h_{\mu\nu} = 0 \tag{1.9}$$

and describe the propagation of waves at speed c.

Let $\hat{z}$ be the propagation direction: in the chosen gauge $\mathbf{h}$ is written in the form

$$\mathbf{h} = \begin{pmatrix} 0 & 0 & 0 & 0 \\ 0 & a & b & 0 \\ 0 & b & -a & 0 \\ 0 & 0 & 0 & 0 \end{pmatrix}$$

The tensor **h** can be written as the sum of two components:

$$\mathbf{h} = a\hat{h}^{+} + b\hat{h}^{\times} \tag{1.10}$$

where the basis tensors "h plus" and "h cross" represents the two possible polarizations states and are written:

$$\hat{h}^{+} = \begin{pmatrix} 0 & 0 & 0 & 0 \\ 0 & 1 & 0 & 0 \\ 0 & 0 & -1 & 0 \\ 0 & 0 & 0 & 0 \end{pmatrix} \; ; \; \hat{h}^{\times} = \begin{pmatrix} 0 & 0 & 0 & 0 \\ 0 & 0 & 1 & 0 \\ 0 & 1 & 0 & 0 \\ 0 & 0 & 0 & 0 \end{pmatrix}$$

The emission of GW is associated to mass acceleration, as the emission of electromagnetic radiation is associated to charged particles acceleration. But, while an oscillating electric dipole emits radiation, this is not true in the gravitational case, due to momentum and angular momentum conservation laws. The emission of GW is associated to the variations of the quadrupole moment tensor of a mass distribution, defined as:

$$Q_{ij} = \int_V \rho(\vec{x}) \left(x_i x_j - \frac{1}{3}\delta_{ij}|\vec{x}|^2 \right) \mathrm{d}V \tag{1.11}$$

The power emitted in form of GW (GW luminosity) is:

$$\mathcal{L} = \frac{1}{5}\frac{G}{c^5} <\dddot{Q}_{ij}\dddot{Q}_{ij}> \tag{1.12}$$

where $<>$ indicates the time average over the wave period or the duration of the wave burst. From (1.12) comes out that there cannot be GW emission from a spherically symmetric mass distribution. Moreover, (1.12) can be used to estimate the GW luminosity of an astrophysical source of mass M and characteristic radius R. Let T be the characteristic time for the evolution of the source and let ϵ be a factor measuring the asymmetry in the mass distribution; thus the quadrupole moment is roughly $Q \sim \epsilon M R^2$. The GW luminosity is then:

$$\mathcal{L} \sim \epsilon^2 \frac{G}{c^5} \frac{M^2 R^4}{T^6} \tag{1.13}$$

The source mass can be expressed in terms of the Schwarzschild radius: $R_S = 2GM/c^2$. Introducing a characteristic speed $v = R/T$ the (1.13) reduces to

$$\mathcal{L} \sim \epsilon^2 \frac{c^5}{G} \left(\frac{R_S}{R} \right)^2 \left(\frac{v}{c} \right)^6 \tag{1.14}$$

The last equation shows that an efficient source of GW should be compact ($R \sim R_S$), relativistic ($v \sim c$), highly anisotropic ($\epsilon \sim 1$).

The amplitude at distance r of the GW emitted by this mass distribution is (in TT gauge):

$$h_{ij} = \frac{2}{r}\frac{G}{c^4}\frac{\mathrm{d}^2}{\mathrm{d}t^2}Q_{ij}(t - r/c) \tag{1.15}$$

where r is the distance of the observer from the source. For a rough estimate of h one can use the same approximation of (1.13), thus getting the expression [19]

$$\boxed{h \sim \frac{G}{c^4} \cdot \frac{E^{\mathrm{ns}}}{r}} \tag{1.16}$$

where $E^{\mathrm{ns}} = \epsilon M R^2/T^2$.

1.3 Radiation-matter interaction

Let us consider a "+" polarized plane gravitational wave of frequency f_{gw} propagating along the $\hat{z}$ direction and impinging over a circle of test masses laying in the $x\hat{O}y$ plane. Let the centre O of the circle coincide with the origin of the reference frame. The metric element is then written:

$$\mathrm{d}s^2 = -c^2\mathrm{d}t^2 + [1 + h(2\pi f_{\mathrm{gw}}t - \vec{\mathbf{k}}\cdot\vec{\mathbf{x}})]\mathrm{d}x^2 + [1 - h(2\pi f_{\mathrm{gw}}t - \vec{\mathbf{k}}\cdot\vec{\mathbf{x}})]\mathrm{d}y^2 + \mathrm{d}z^2 \tag{1.17}$$

Suppose that two of the test masses (the ones on the $\hat{x}$ and $\hat{y}$ axes) are the end mirrors of a Michelson interferometer (whose beam splitter is placed in the origin of the reference frame at distance L from each of the mirrors). For a photon propagating in the interferometer $\mathrm{d}s^2 = 0$. Then it is possible to calculate from (1.17) the time the light takes to complete a round trip in each arm of the interferometer. The light travel time in the $\hat{x}$ arm form the beam splitter to the mirror (at distance L) is:

$$\tau_x^{(1)} = \int_0^{t_1} \mathrm{d}t = \frac{1}{c}\int_0^L \sqrt{(1+h)}\mathrm{d}x \simeq \frac{1}{c}\int_0^L \left(1 + \frac{1}{2}h\right)\mathrm{d}x \tag{1.18}$$

In the same way, the return trip takes a time

$$\tau_x^{(2)} \simeq \frac{1}{c}\int_L^0 \left(1 + \frac{1}{2}h\right)\mathrm{d}x \tag{1.19}$$

The two integrals can be easily calculated by replacing $h(t) = h_0 \exp[i2\pi f_{\mathrm{gw}}t]$ and remembering that $t = x/c$ in (1.18) and $t = (2L - x)/c$ in (1.19).

The result for the round trip travel time is:

$$\tau_x \;=\; \tau_x^{(1)} + \tau_x^{(2)} \tag{1.20}$$

$$
\begin{aligned}
&= \frac{2L}{c} + \frac{1}{2c}\int_0^L h\mathrm{d}x - \frac{1}{2c}\int_0^L h\mathrm{d}x \\
&= \tau_0 + \frac{h_0}{4\pi i f_{\mathrm{gw}}}\left[e^{i2\pi f_{\mathrm{gw}}\tau_0} - 1\right]
\end{aligned}
$$

where $\tau_0 = 2L/c$ is the *classical* return trip time.

In the $\hat{y}$ arm the light picks the effect of $h_{22} = -h_{11}$ and one gets:

$$\tau_y = \tau_0 - \frac{h_0}{4\pi i f_{\mathrm{gw}}}\left[e^{i2\pi f_{\mathrm{gw}}\tau_0} - 1\right] \tag{1.21}$$

From the point of view of an observer in the laboratory, the phase variation of the interferometer output can be interpreted as a variation of the arms length (see fig. 1.1):

$$L_x = c\frac{\tau_x}{2} = L\left(1 + \frac{h}{2}\right) \tag{1.22}$$

$$L_y = c\frac{\tau_x}{2} = L\left(1 - \frac{h}{2}\right) \tag{1.23}$$

When the two waveforms arrive at the beam splitter they are "out of sync" and the time difference is

$$\Delta\tau(t) = h(t)\tau_0 e^{i\pi f_{\mathrm{gw}}\tau_0}\frac{\sin(\pi f_{\mathrm{gw}}\tau_0)}{\pi f_{\mathrm{gw}}\tau_0} \tag{1.24}$$

Thus, at the interferometer output a photodiode would measure a phase variation:

$$\delta\phi(t) = \frac{4\pi L}{\lambda}h(t)e^{i\pi f_{\mathrm{gw}}\tau_0}\mathrm{sinc}(\pi f_{\mathrm{gw}}\tau_0) \tag{1.25}$$

where λ is the laser wavelength and $\mathrm{sinc}x = \sin x/x$.

From (1.26) it is clear that an interferometer can be used as a GW detector. The interferometer response to impinging GW is plotted in fig. 1.2 as a function of f_{gw}: the interferometric transducer acts as a low pass filter starts attenuating at frequencies $f \sim c/2L$, that is when the period of the wave is comparable to the return trip time τ_0. Anyway, for low frequency wave $f_{\mathrm{gw}}\tau_0 \ll 1$ the interferometer response is flat:

$$\boxed{\frac{\delta\phi(t)}{h(t)} = \frac{4\pi L}{\lambda}} \tag{1.26}$$

Eq. (1.26) shows straightforwardly that the longer the interferometer arms the more sensitive the detector. In the low frequency approximation from (1.22) and (1.23) one can

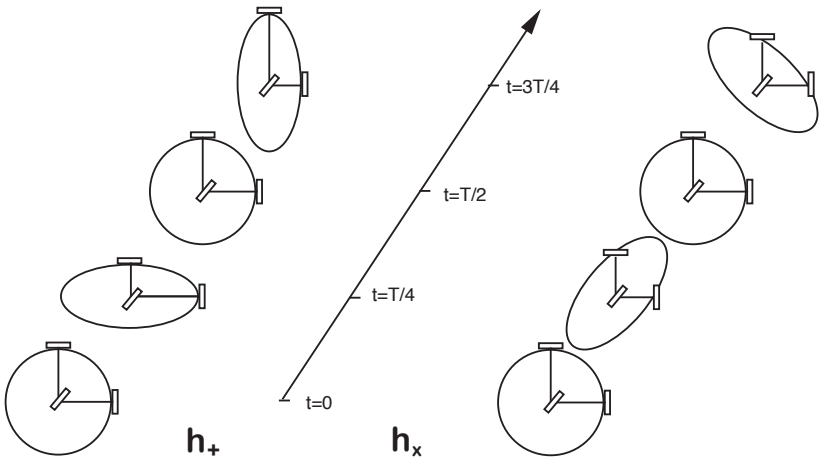

Figure 1.1: Effect of a monochromatic GW of frequency $f = 2\pi/T$ over a circle of test masses: a) when the wave is "+" polarized; b) when the wave is "×" polarized. The figure shows especially the effect of the wave on a Michelson interferometer.

derive the "arm length variation" measured in the laboratory frame:

$$\delta x(t) = \frac{L}{2}h(t) \qquad \delta y(t) = -\frac{L}{2}h(t) \tag{1.27}$$

1.4 Astrophysical Sources of GW

A large amount of theoretical work has been done to predict waveforms and intensities of the gravitational radiation emitted in astrophysical events. The task is difficult because of the subtleties of the theory, the complexity of the systems under study and, above all, because of the fact that little is known about the dynamical behaviour of compact objects as supernova cores. A fair amount of uncertainty affects the calculated GW amplitudes as well as the event rates. In the following sections we review the main results about expected GW sources emitting in the operating frequency range of ground based antennas (from few Hz to few kHz) (see [20, 22] and references therein): coalescing binary compact stars, gravitational collapses, spinning neutron stars, stochastic background. In chapter 3 the expected intensities of GW are compared with the target sensitivity of the forthcoming interferometric antennas.

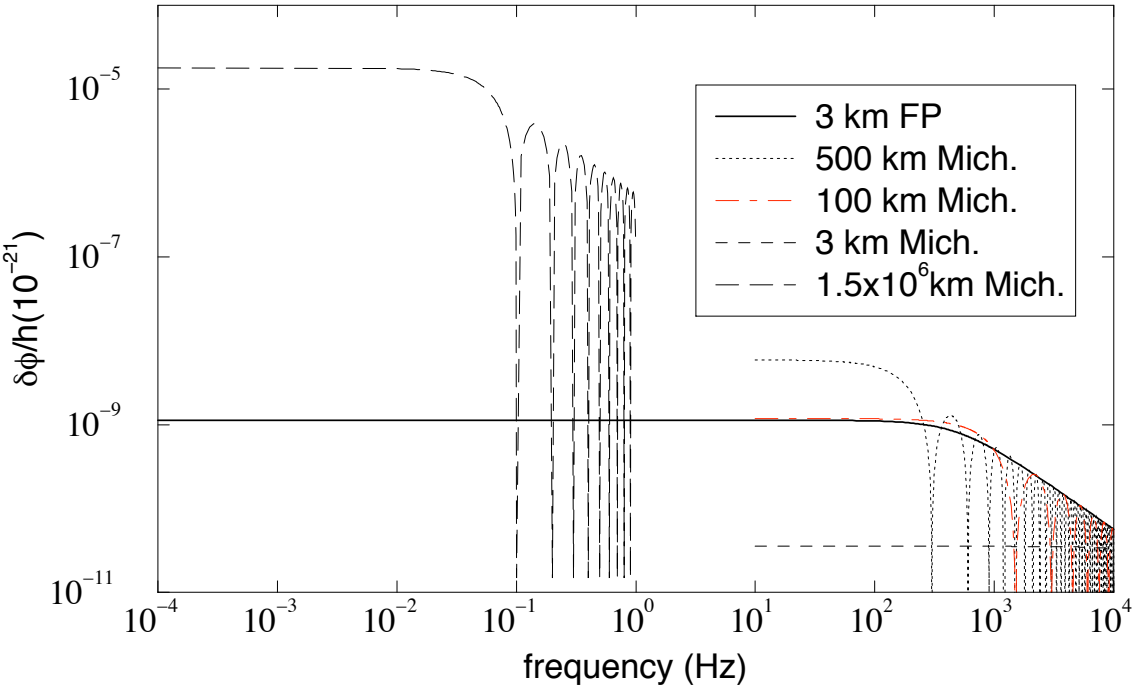

Figure 1.2: The phase response of an interferometer to GW for different lenghts of the arms (the GW amplitude h is expressed in units of 10^{-21}): the sensitivity of a Michelson interferometer increases with its length, at the cost of reducing the bandwidth. The performance of a 3 km Fabry-Perot (FP) interferometer like VIRGO (see next chapter) is comparable to the 100 km Michelson. The response of a $1.5 \cdot 10^6$ km long Michelson (as the forthcoming space interferometer LISA) is also shown.

1.5 Coalescing binaries

Among all the expected sources of gravitational radiation, coalescing compact binary systems composed of neutron stars (NS) or black holes (BH) are the ones the physicists look at with more confidence, and this is true for two main reasons: the system dynamics is simple, the expected amplitude of the emitted radiation is within the sensitivity of the forthcoming interferometric detectors, known binary systems such as PSR1913+16 and PSR1534+12 seems to confirm the theoretical models.

1.5.1 The newtonian/quadrupolar approach

As explained in section 1.1.2, a binary system as the one containing PSR1913+16 loses energy via GW emission and its orbital period decays. A first order calculation of the GW

emission of such a system can be performed in the so called *newtonian/quadrupolar* approximation: the stars are treated like point masses (the tidal deformations are negligible) and the radiation is generated only by the quadrupole moment oscillation. The resulting waveform is a *chirp* (see fig. 1.3), an oscillation increasing in amplitude and sweeping upwards in frequency. The observation of such a signal would allow to determine some important characteristics of the source:

- the measurement of the relative amplitude of the two polarization states permits to determine the inclination ι of the orbit to the line of sight according to the formula:

$$\frac{h_\times}{h_+} = \frac{2\cos\iota}{1+\cos^2\iota} \tag{1.28}$$

- the measurement of the frequency sweep permits to determine the *chirp mass* $\mathcal{M}$:

$$\mathcal{M} = \frac{(m_1 m_2)^{3/5}}{(m_1+m_2)^{1/5}} = M(\frac{\mu}{M})^{3/5} \tag{1.29}$$

  where m_1, m_2 are the star masses, μ, M are the reduced and the total mass of the system respectively.

- the waveform "shape" (the waves harmonic content) permits to determine the orbit ellipticity.

In case of circular orbit the frequency sweeping is described by the equation:

$$f(t) = \left(f_0^{-8/3} - \pi^{8/3}\frac{256}{5}\frac{G^{5/3}}{c^5}\mathcal{M}^{5/3}t \right)^{-3/8} \tag{1.30}$$

where $f_0 = f(t=0)$. The coalescence time is:

$$\tau_c = \frac{5}{256}\frac{c^5}{G^{5/3}}\mathcal{M}^{-5/3}(\pi f_0)^{-8/3} = 3.0\left[\frac{f_0}{100\text{Hz}}\right]\left[\frac{\mathcal{M}}{M_\odot}\right]^{-5/3} \tag{1.31}$$

The amplitudes in the two polarization states are written [4]:

$$h_+(r,\theta,t) = 6.0\cdot 10^{-21}(1+\cos^2\theta)\left[\frac{\mathcal{M}}{M_\odot}\right]^{5/3}\left[\frac{\text{Mpc}}{R}\right]\left[\frac{f(t)}{1\text{kHz}}\right]^{2/3}\cos(2\pi f t) \tag{1.32}$$

$$h_\times(r,\theta,t) = \pm 1.2\cdot 10^{-20}\cos\theta\left[\frac{\mathcal{M}}{M_\odot}\right]^{5/3}\left[\frac{\text{Mpc}}{R}\right]\left[\frac{f(t)}{1\text{kHz}}\right]^{2/3}\sin(2\pi f t) \tag{1.33}$$

The estimated rate of NS/NS coalescences is quite uncertain: 3 events/year out of a distance of 60-400 Mpc (see [23, 21] and references therein) and similar numbers are predicted for NS/BH and BH/BH events.

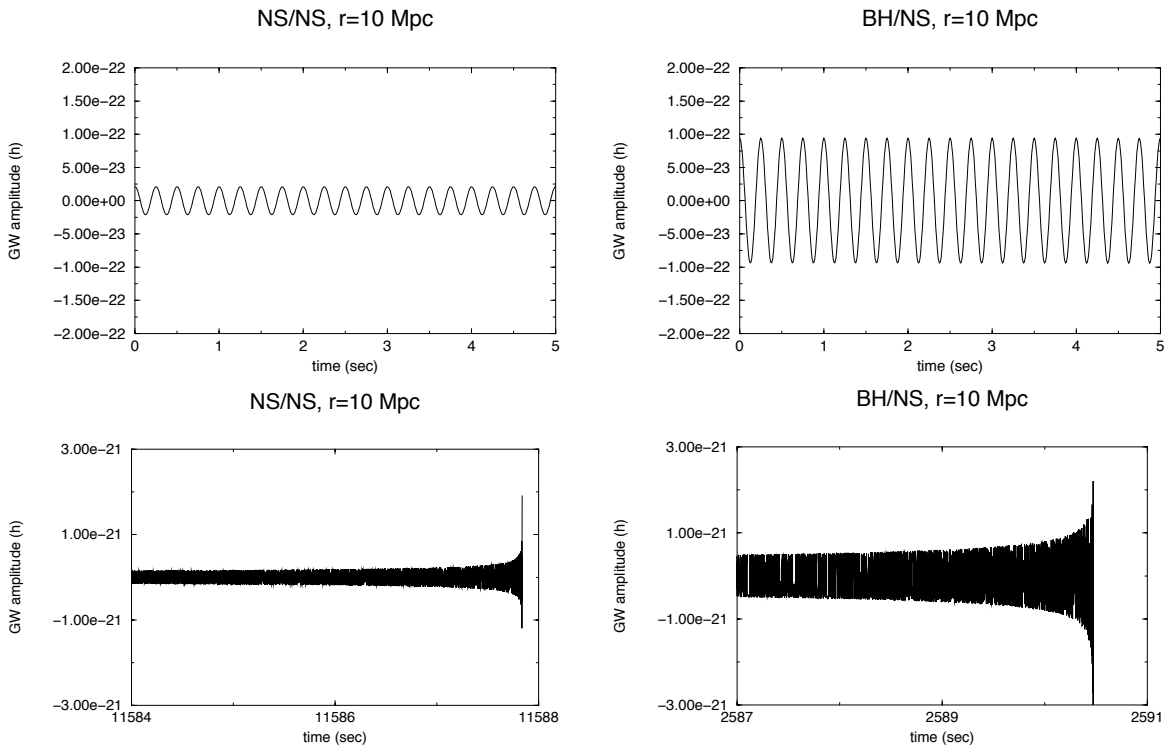

Figure 1.3: The h_+ GW emission of a coalescing binary system is calculated for a NS/NS binary (with $m_1 = m_2 = 1.4\ M_\odot$) and for a NS/BH binary ($m_1 = 1.4\ M_\odot, m_2 = 10\ M_\odot$) in the *inspiral* and *merger* regime. The calculation has been performed for a distance $r = 10$ Mpc and for optimal orientation of the source in the sky. The origin of the time axis corresponds to the instant when the frequency is $f_0 = 4$ Hz.

1.5.2 Post-newtonian corrections

The extraction of the GW signal from the noisy output data flow of an interferometric detector will be performed using the "matched filter" method: theoretical templates will be cross-correlated with the antenna output. Candidate events will result into a correlation larger than a threshold statistically defined. If signal and template gradually get out of phase the correlation may be reduced significantly. Therefore, the accuracy of the model used to produce the template is very important for the detection. Relativistic corrections to the newtonian template of fig. 1.3 modify above all the phase and have to be taken into account to increase the signal-to-noise ratio. It has been estimated [25] that, in order not to lose physical information which could be extracted from the data, the calculation must be extended to the "11/2 post-newtonian order", that is to $O\left[(v/c)^{11/2}\right]$. A French/Indian/American collaboration ([24] and references therein) is doing the effort and, up to now, the 9/2 post-newtonian correction has been calculated [26].

1.5.3 Coalescing binaries as a physics laboratory

The observation of GW from coalescing binaries would permit to obtain knowledge not only in astrophysics and general relativity but also in nuclear physics and cosmology. In this section some of the information which could be extracted from the measured waveforms are reviewed:

- accurate measurements of the inspiral waveform could discriminate between general relativity and other theories of gravity [17];
- NS/NS coalescence is a candidate to explain the origin of the $\gamma-$ray bursts [27]. The recent detection of the optical counterparts of some bursts performed by the Italian/Dutch satellite Beppo Sax allowed to demonstrate their cosmological origin [29]. The measured rate of γ bursts is consistent with the expected NS/NS mergers out of cosmological distances. On the other hand, light curves and spectra are compatible with a γ expanding "fireball", and this is difficult to explain with the merger models (other mechanisms have been suggested, such as the *Hypernova*, to explain the huge amount of energy associated to some of the detected bursts [30, 31]). Nevertheless, if the γ-ray bursts are originated in a merger event, the simultaneous detection of GW and γ burst may allow to test whether the gravitational radiation propagates at the speed of light to an accuracy of about 10^{-19} [21];
- the NS/NS binary systems are *standard candles*: the mass of a NS is known to be approximately equal to 1.4 $M_\odot$. The source distance can be determined from (1.33). The observation of the chirp provides a measurement of the *redshifted chirp mass* $(1+z)\mathcal{M}$. Combining this measurement with the assumption on the NS masses one can find out the redshift z even without any optical observation. Thus, the observation of a significant number of events could contribute to measure the Hubble parameter

and even provide access to the deceleration parameter and the cosmological constant [33];

- the final phase of a compact binaries merger would produce a waveform sensitive to the nuclear equation of state.

1.6 Supernovae

Some years ago supernovae (SN) were believed to be the GW sources most likely to be detected. Today it is clear that the theoretical models of GW emission in a stellar collapse are affected by serious uncertainties due to the approximation used into the numerical codes and to the wide range of possible initial conditions. The intensity of the emitted radiation depends mostly on the amount of the stellar mass converted into GW and on the non-spherical symmetry of the collapse dynamics.

Following Thorne [21] we review the processes which can trigger a GW emission during the collapse and the estimated intensities:

- *boiling of the newborn neutron star:* in a spherically collapse GW can be emitted when a convectively unstable neutron star is produced. High temperature nuclear matter from the centre of the forming NS is dredged up, cooled by neutrino emission, swept back downward and reheated. This phenomenon should generate $n \sim 10$ cycles of GW with a frequency $f \sim 100$ Hz. The expected amplitude is

$$h \sim 10^{-24} \cdot \frac{10\text{Mpc}}{r} \tag{1.34}$$

- *axisymmetric collapse:* in case of non-spherical but axisymmetric collapse a weak GW emission is expected as well:

$$h \sim 3 \cdot 10^{-24} \cdot \frac{10\text{Mpc}}{r} \tag{1.35}$$

  and the burst has spectral components in the range 200-1000 Hz;

- *non-axisymmetric collapse:* it is the event which produces the strongest GW burst, with amplitude

$$h \sim 10^{-21} \cdot \frac{10\text{Mpc}}{r} \tag{1.36}$$

Several supernovae per years are expected out of a distance 10 Mpc (VIRGO cluster). The fraction of non axisymmetric collapses is unknown.

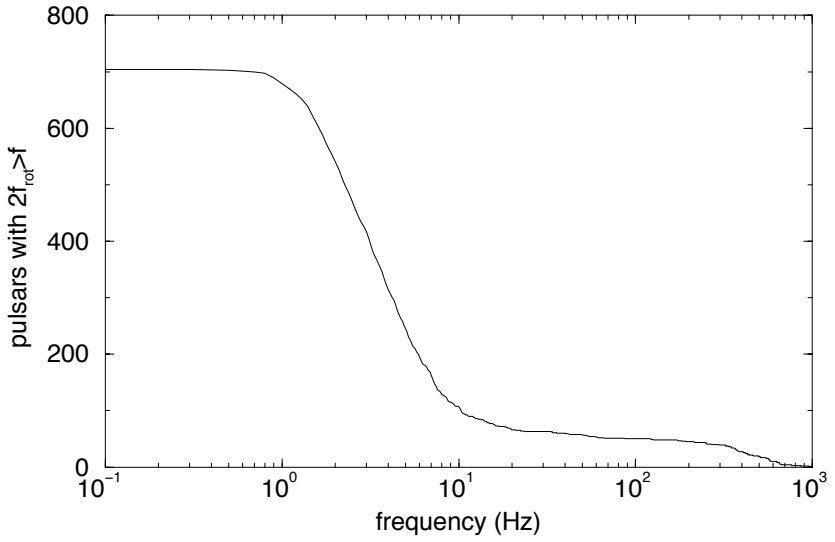

Figure 1.4: The integrated distribution of 703 of galactic pulsars with respect to the GW emission frequency $2f_{\rm rot}$.

1.7 Spinning neutron stars

Non axisymmetric rotating neutron stars emit periodic GW [28]. The emission is characterized by 3 parameters: the *poloidal ellipticity* ϵ_p, the *equatorial ellipticity* ϵ_e and the *wobble angle* θ_w between the principal axis of inertia and the axis of rotation. Let $f_{\rm rot}$ be the star spinning frequency and $f_{\rm prec}$ the precession frequency. Then, the radiation is emitted at frequencies:

$$\begin{cases} f_1 = 2f_{\rm rot} \\ f_2 = f_{\rm rot} + f_{\rm prec} \end{cases} \tag{1.37}$$

For typical masses and reasonable moments of inertia the amplitude is:

$$h \sim 6 \cdot 10^{-25} \left[\frac{f_{\rm rot}}{500{\rm Hz}}\right] \left[\frac{1{\rm kpc}}{r}\right] \left[\frac{\epsilon_e \text{ or } \epsilon_p\theta_w}{10^{-6}}\right] \tag{1.38}$$

An upper limit of $\epsilon_e, \epsilon_p \sim 10^{-4}$ has been suggested for the ellipticities ([21, 23] and references therein). The GW emitted by this kind of source are weak, but the SNR ratio can be increased by integrating the signal for a long time (months). In fig. 1.4 the integrated frequency distribution of 706 known galactic pulsars is shown: most of them would emit GW below 10 Hz. The problem of the pulsar GW detection will be analyzed in chapter 3.

1.8 Stochastic background

Current cosmological models predict the existence of a relic stochastic background of gravitational radiation produced during the early expansion of the universe. The spectrum of this background has the imprinting of the early cosmology and its detection could have an enormous impact on cosmology and high-energy physics. As a matter of fact, the relic gravitons carry information about the state of the universe at time scales $t \sim 10^{-20} - 10^{-26}$ sec or equivalently at temperature scales $T \sim 10^7 - 10^{10}$ GeV [37].

The stochastic gravitational radiation consists of many individual components randomly superimposed and is characterised by the dimensionless quantity:

$$\Omega_{\rm gw}(f) = \frac{1}{\rho_c}\frac{{\rm d}\rho_{\rm gw}(f)}{{\rm d}\log f} \tag{1.39}$$

where $\rho_{\rm gw}(f)$ is the energy density of the GW stochastic background and ρ_c is the critical energy density for closing the universe:

$$\rho_c = \frac{3H_0^2}{8\pi G} \tag{1.40}$$

Most inflationary models predict a flat[5] $\Omega_{\rm gw}(f)$ spectrum (known as Harrison-Zel'dovich spectrum). The strictest limit on $\Omega_{\rm gw}(f)$ comes from COBE observations of CMBR anisotropy ([36] and references therein):

$$\Omega_{\rm gw}^{\rm COBE}(f)h_{100}^2 < 7 \cdot 10^{-11}\left(\frac{H_0}{f}\right)^2 \quad \text{for } H_0 < f < 30\ H_0 \tag{1.41}$$

where h_{100} is defined by writing the Hubble parameter as:

$$H_0 = h_{100} \cdot 100\,\frac{\rm km}{\rm sec \cdot Mpc} \tag{1.42}$$

The COBE limit concerns a frequency range inaccessible to ground based antennas as well as to space interferometers. If the spectrum were flat and the limit (1.41) were valid in the 10-1000 Hz range, the detection with the interferometric antennas of the VIRGO/LIGO type would be hopeless. Nevertheless, recent string cosmology models [50, 51, 52] predict a more complex spectrum behaving as $\Omega_{\rm gw}(f) \propto f^3 \log^2 f$ at low frequency and $\Omega_{\rm gw}(f) \sim const.$ above a threshold frequency, depending on the details of the physics of the wave generation. These model satisfy the restrictions of the COBE observations and at the same time predicts GW in the VIRGO/LIGO frequency range with intensity that might be detectable.

[5] Actually, different models of inflationary expansion may lead to relic GW spectra with slightly different slopes [35].

Chapter 2

Interferometric detection of GW

2.1 Interferometric transducers for GW detection

A gravitational wave impinging on the free falling mirrors of a Michelson interferometer produces a variation of the arms length and, consequently, a displacement of the fringes (see eq. (1.26)): a free falling interferometer can be used as a gravitational wave detector. A suspended ground based interferometer can be considered free falling (in the plane defined by its arms) in a limited range of frequencies if the mirrors are properly isolated from ground vibrations. To dimension correctly the interferometer one should above all take into account two numbers:

- the *intensity* of GW: to find out the target sensitivity one has to consider not only the GW amplitude but also the possible rate of events. The closest large accumulation of stars is the Virgo Cluster, which contains about 2000 galaxies and many GW events should happen there. Then, a reasonable start is to calculate the expected amplitudes at a distance of 15 Mpc (the distance of the Virgo Cluster from Earth). From equations (1.33) and (1.36) one finds that a NS/NS inspiral or a maximum efficiency supernova collapse in the Virgo Cluster may generate a strain amplitude on Earth of $h \sim 10^{-21} - 10^{-22}$. It is then reasonable to aim to build a detector at least an order of magnitude more sensitive ($h \sim 10^{-22} - 10^{-23}$);

- the *sensitivity* of interferometric techniques: actual technology of lasers and mirrors may allow to achieve measurement accuracies of $\delta L \sim 10^{-18}$ m (at the Caltech prototype interferometer $\delta L = 8 \cdot 10^{-16}$ has been recently achieved [38].

From the numbers above it turns out that very long interferometers are necessary: $L \sim \delta L/h \sim 10 - 100$ km. Actually, one can stretch the equivalent length of the interferometer to about 100 km by *folding* the light path. This can be done using optical cavities like Fabry-Perot or Herriot delay lines some kilometers long (see next section).

At the moment five interferometric detectors are being built in the world: two in the USA (LIGO)[1] [6], one in Italy (VIRGO) [7], one in Germany (GEO600) [8] and one in Japan (TAMA) [9]. A sixth interferometer (ACIGA) [10] is expected to be built in Australia in the forthcoming years. LIGO and VIRGO antennas are similar in the main design features: they are kilometric interferometers (4 km arms in LIGO, 3 km arms in VIRGO), both make use of Fabry-Perot cavities inside the arms and of power recycling techniques. The main difference concerns the antenna bandwidth: VIRGO antenna aims to detect GW in the band from few Hz to few kHz, while LIGO will be initially low frequency limited at about 80 Hz.

2.2 Increasing the sensitivity: Fabry-Perot cavities

We pointed out in chapter 1 (see eq.(1.26)) that the detector sensitivity is proportional to the interferometer arms length. An unrealistic arm length (at least for budget reason!) is required for a Michelson detector. The problem is solved by increasing the optical length using optical cavities. VIRGO and LIGO make use of Fabry-Perot (FP) cavities. A Fabry-Perot interferometer is sketched in fig. 2.1: each FP is made of two mirrors (input and end mirrors); the end mirror has reflectivity close to unity within a few p.p.m..

Within the frequency stability of the laser is stable, a FP cavity is a displacement-to-phase transducer: the light that enters the cavity is *reflected* with a phase shift depending on the cavity length. If the length does not change during the time of light storage into the cavity, the phase shift is null. If the length changes of an amount δL the interferometer phase shift is:

$$\delta\phi = \frac{4\mathcal{F}}{\pi}\left(2\pi\frac{\delta L}{\lambda}\right) \tag{2.1}$$

where $\mathcal{F}$ is the FP *finesse*, a parameter measuring the "sharpness" of the cavity resonance. Under reasonable hypotheses on the mirrors losses and reflectivities, and under the "low frequency" condition $f_{GW}(2L/c) \ll 1$, the Fabry-Perot interferometer response to GW strain (fig. 1.2) is given by

$$\left|\frac{\delta\phi}{h}\right| \simeq \tau_s \frac{8\pi c}{\lambda}\frac{1}{\sqrt{1+(4\pi f_{GW}\tau_s)^2}} \tag{2.2}$$

where we have defined the *storage time*:

$$\tau_s = \frac{2L}{c}\frac{\mathcal{F}}{2\pi} \tag{2.3}$$

Eq. (2.2) shows that the FP interferometer response has a pole at frequency $f_p = 1/4\pi\tau_s$. At frequencies $f \gg f_p$ the phase sensitivity decreases. When compared with

[1] Actually, the Hanford LIGO facility contains two interferometers in the same vacuum pipe, one full length (4 km), the second one half the length of the first.

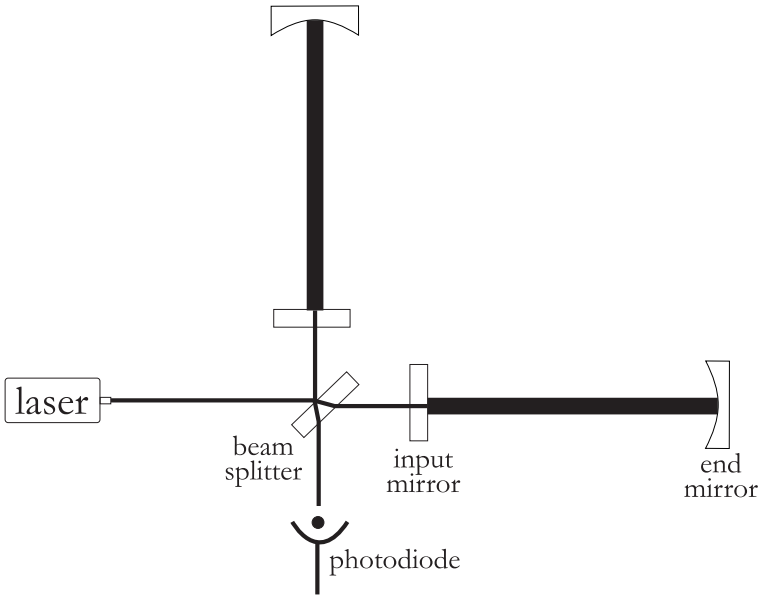

Figure 2.1: Scheme of a Fabry-Perot interferometer.

eq. (1.26) for the Michelson interferometer one finds that, in the "flat response" range ($f \ll f_p$):

$$\frac{\text{FP phase sensitivity}}{\text{Michelson phase sensitivity}} = \left[\frac{2L}{c}\frac{\mathcal{F}}{2\pi}\frac{8\pi c}{\lambda}\right]\left[\frac{4\pi L}{\lambda}\right]^{-1} = \frac{2\mathcal{F}}{\pi} \tag{2.4}$$

The sensitivity enhancement in a FP interferometer with respect to a Michelson of the same length can be described from a different point of view: when Fabry-Perot cavities of finesse $\mathcal{F}$ are inserted in the arms, the *effective* length of the interferometer is the optical length

$$L_{\text{opt}} = L \cdot \frac{2\mathcal{F}}{\pi} \tag{2.5}$$

For VIRGO antenna ($L = 3$ km and $\mathcal{F} = 50$) one gets an optical length $L_{\text{opt}} \approx 95$ km.

2.3 Noise

Noise of different nature affects the sensitivity of a ground based interferometer. They can logically be divided in two main categories:

- *mirror position disturbances*: these are perturbations of the mirror position associated to ground vibrations (residual seismic noise and fluctuations of the local gravity field), to the internal noise of the suspension system and mirror (thermal noise, creep,

up-conversion of non-linear effects) and to possible re-injection of noise by means of the actuators used for the active control of the suspension;

- *read-out noise*: the output signal of an interferometer fluctuates even if the mirrors were ideally isolated from the outer world, due to the intrinsic noises affecting the read-out system: laser shot noise, radiation pressure fluctuations, laser frequency and power fluctuations.

Due to the contributions of all the noises, the photodiode at the output of the interferometer will continuously record a phase shift $\delta\phi(t)$ indistinguishable from the one that a GW signal $h_n(t)$ would produce. The noise $h_n(t)$ is characterised by the "two-sided" *power spectral density* (or *spectrum*)

$$S_n(f) = \lim_{T\to\infty} \left| \frac{1}{\sqrt{T}} \int_{T/2}^{T/2} h_n(t) e^{i2\pi ft} \mathrm{d}t \right|^2 \tag{2.6}$$

In the GW community the "single-sided" (defined only for positive frequencies) *linear spectral density* is used rather than the (2.6):

$$\tilde{h}_n(f) \stackrel{\text{def}}{=} \sqrt{2S_n(f)} \tag{2.7}$$

2.4 "Free falling mirrors" in ground based interferometers

In section 1.3 we have described how a free falling Michelson interferometer responds to impinging GW. A ground based detector may be considered free falling (with respect to the horizontal plane) in a proper range of frequencies, if the mirrors are "suspended". The method to isolate a test mass m is to connect it to the noisy ground through a "spring"[2]. Neglecting the dissipative term, the equation of motion is

$$m\ddot{x} + k(x - x_0) = F_{ext} \tag{2.8}$$

where k is the spring stiffness ($k = mg/l$ in the pendulum case), x and x_0 are the mass and the suspension point position respectively and F_{ext} is the external force applied to the mass. In the frequency space the (2.8) is written:

$$x(\omega) = \frac{\omega_0^2 x_0(\omega) + F_{ext}(\omega)/m}{\omega_0^2 - \omega^2} \tag{2.9}$$

where $\omega_0 = 2\pi f_0$ and $f_0 = \sqrt{k/m}$ is the oscillator resonant frequency. Two comments can be done on the (2.9):

[2]The best way to do this is to suspend the test mass as a pendulum. In this case the restoring force is mostly gravitational and the dissipation is minimised.

- in absence of external forces the suspension point-payload transfer function is immediately written:

$$\frac{x(\omega)}{x_0(\omega)} = \frac{\omega_0^2}{\omega_0^2 - \omega^2} \tag{2.10}$$

Eq.(2.10) says that:

1. below the resonant frequency ($f \ll f_0$), the spring is *rigid*: the vibrations are entirely transmitted to the test mass and $x(\omega) = x_0(\omega)$;
2. above the resonant frequency ($f \gg f_0$), the spring is a soft connection to the noisy world and the vibrations are attenuated like:

$$\frac{x(\omega)}{x_0(\omega)} \simeq \frac{\omega_0^2}{\omega^2} \tag{2.11}$$

The equation above describes the ideal behaviour of an oscillator with massless links.

- For frequencies $\omega \gg \omega_0$ the effect of applying a force to the payload is described by the equation:

$$m\omega^2 x(\omega) + F_{ext}(\omega) \approx 0 \tag{2.12}$$

that is, the mass responds to the force as if it were free: above a certain frequency GW do not make distinction between a ground-based *suspended* interferometer and a *free falling* one.

For a complete description, one has to include the dissipative term into the equation of the system (see section 2.6). The amount of dissipation determines the quality factor Q. At the resonant frequency the motion of the test mass is "amplified" by a factor Q with respect to the average excitation value:

$$x(f_0) = Q x_0(f_0) \tag{2.13}$$

If N oscillators are cascaded, N eigenmodes are present. The transfer function, neglecting again the dissipation, is written:

$$\frac{x(\omega)}{x_0(\omega)} = \prod_{i=1}^{N} \frac{\omega_i^2}{\omega_i^2 - \omega^2} \tag{2.14}$$

where $\omega_i/2\pi$ are the N resonant frequencies. Above the resonant frequencies ($f \gg \omega_i/2\pi \ \forall i$) the attenuation is:

$$\frac{x(\omega)}{x_0(\omega)} \simeq \frac{\prod_i \omega_i^2}{\omega^{2N}} \tag{2.15}$$

From this simple model one learns that:

- an arbitrarily steep vibration low pass filter can be built cascading a large number of oscillators;
- the filter cut-off frequency depends on the resonant frequencies of the system: the lower the frequencies, the wider the range where vibrations are attenuated.

2.5 Ground vibrations

Ground vibrations induced by seismic activity, wind, ocean activity, human activity, couple to the mirrors in two ways: via the mechanical connection between the mirror and the ground and via the gravitational field associated to the local mass distribution fluctuations.

2.5.1 Seism

Seismic noise is produced by vibrations of the soil. To get rid of it and to make ground based GW detection possible, mirrors have to be isolated by suspending them from suitable filters (usually more or less complicated multi-stage pendula). Nevertheless, it is the main limitation to the sensitivity of ground based antennas in the low frequency range. There is no universal law describing the seismic noise. Its intensity can change of orders of magnitude from place to place and, in the same place, from day to day, depending on wind, ocean and human activity, and so on (see also [39]). A general $1/f^2$ behaviour at frequencies above 1 Hz has been found everywhere due to the transmission properties of soil and rocks. The seismic noise displacement spectrum is roughly isotropic and, in our laboratory, can be described by the empirical equation:

$$x_s(f) \sim \xi \cdot \frac{10^{-6}}{f^2} \left[\frac{f^2 + f_0^2}{f^2 + f_1^2} \right] \ \mathrm{m}/\sqrt{\mathrm{Hz}} \tag{2.16}$$

where

$$\begin{cases} \xi \sim 0.1 - 1 \ \ \mathrm{m} \cdot \mathrm{Hz}^{3/2} \\ f_0 \sim 0.1 \ \ \mathrm{Hz} \\ f_1 \sim 0.5 \ \ \mathrm{Hz} \end{cases} \tag{2.17}$$

The seismic noise displacement spectrum measured in a horizontal direction on a day with low human activity is shown in fig. 2.16.

At low frequency, together with the local seism spectral density one has to consider the differential seism between the input and end mirrors of the interferometer cavities. One expects that, below a threshold frequency, the seismic motions of two points 3 km apart have to be correlated. The threshold frequency f_{th} can be estimated by means of a simple model, where a seismic wave of frequency f propagates with velocity v_s along the interferometer arm of length L. The displacements of the mirrors induced by the seismic

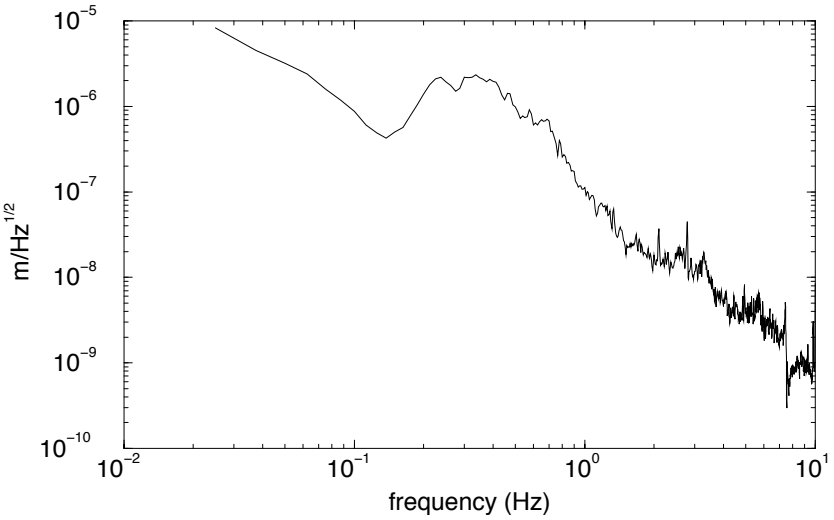

Figure 2.2: Horizontal seism displacement spectrum measured at Pisa INFN laboratories on a Sunday (low human activity, $\xi \sim 0.1$ while in weekdays $\xi \sim 0.3 - 0.5$). A rough $1/f^2$ slope is measured above 1 Hz. The broad peak at 0.14 Hz is found all over the world and is due to the oceans activity.

wave are correlated if $\lambda_s \gg L$ where $\lambda_s = v_s/f$, is the seismic wavelength. Then the correlation holds for

$$f \ll f_{\rm th} = \frac{v_s}{L} \tag{2.18}$$

If $L = 3$ km and $v_s \sim 0.5$ km/s (a reasonable value for sandy soil), one gets $f_{\rm th} \sim 0.15$ Hz.

2.5.2 Gravity gradient noise

Seismic noise is not a fundamental physical limit: in principle the low frequency threshold might be pushed towards zero by suspending the mirrors to longer and longer pendula. A limit exists to the efficiency of vibration isolation: due to the seismic waves, the mass density distribution around the mirrors fluctuates. Then, the local gravitational field fluctuates as well. These fluctuations directly couple to the mirrors, "short circuit" the vibration isolation system and produce a noise [73]:

$$\tilde{h}_{\rm ggn} = \frac{2}{3\sqrt{\pi}} \cdot \frac{G\rho}{L} \frac{x_s(f)}{f^2} \tag{2.19}$$

where L is the interferometer length, G is the gravitational constant, ρ is the average local soil density, $x_s(f)$ is the local seismic spectrum. The gravity gradient (or *newtonian*) noise limit sets the low frequency sensitivity achievable by a ground based interferometer.

2.6 Thermal noise

Thermal noise is associated with the internal dissipation phenomena. The fluctuation-dissipation theorem [42] relates the dissipation phenomena to the brownian motion of the system itself.

Consider a mechanical oscillator made of a mass m and a spring of stiffness k. In the hypotesis of dissipation due to the material structure, the system losses can be modelled in the frequency domain by adding an imaginary component to the elastic force [87, 89]. The equation of motion is then written:

$$-m\omega^2 x(\omega) + k\left[1 + i\phi(\omega)\right] x(\omega) = F_{\text{ext}} \tag{2.20}$$

The function $\phi(\omega)$ represents the phase lag between the mass displacement $x(\omega)$ and sinusoidal driving force. Experimentally, $\phi(\omega)$ is found to be roughly constant and, for low loss materials, $\phi \ll 1$.

Using the fluctuation-dissipation theory the thermal noise spectrum of the oscillator is calculated as:

$$x_{\text{th}}^2 = \frac{4k_B T\phi \cdot \omega_0^2}{m\omega\left[(\omega_0^2 - \omega^2)^2 + \omega_0^4\phi^2\right]} \tag{2.21}$$

where k_B is the Boltzmann constant, T is the temperature and $\omega_0/2\pi = \sqrt{k/m}$ is the oscillator resonant frequency. It can be shown that, for a low loss oscillator $Q = \phi^{-1}(\omega_0)$. The frequency dependence of the noise spectrum is:

$$x_{\text{th}}(\omega) = \sqrt{\frac{4k_B T}{m}} \cdot \begin{cases} \dfrac{\sqrt{\phi}}{\omega^{1/2}\omega_0} & \text{for } \omega \ll \omega_0 \\ \dfrac{1}{\sqrt{\phi\omega_0^3}} & \text{for } \omega = \omega_0 \\ \dfrac{\sqrt{\phi}\omega_0}{\omega^{5/2}} & \text{for } \omega \gg \omega_0 \end{cases} \tag{2.22}$$

It is noticeable that the off resonance part of the spectrum is proportional to $\sqrt{\phi}$: the thermal noise is reduced when using high Q materials (see fig. 2.3).

For a complex mechanical system such as a mirror suspension or the mirror lattice itself, the thermal noise has to be calculated keeping into account all of the modes. Each mode is characterised by the resonant frequency $\omega_n/2\pi$, its quality factor $Q_n = 1/\phi_n$ and its effective mass μ_n, defined as

$$\mu_n = \frac{E_n}{\omega_n^2 x_n^2} \tag{2.23}$$

where E_n is the mode energy and x_n the oscillation amplitude. The (2.21) for a multi-mode system is written:

$$x_{\text{th}}^2(\omega) = \frac{4k_B T}{\omega} \sum_n \frac{\phi_n \omega_n^2}{\mu_n\left[(\omega_n^2 - \omega^2)^2 + \omega_n^4\phi_n^2\right]} \tag{2.24}$$

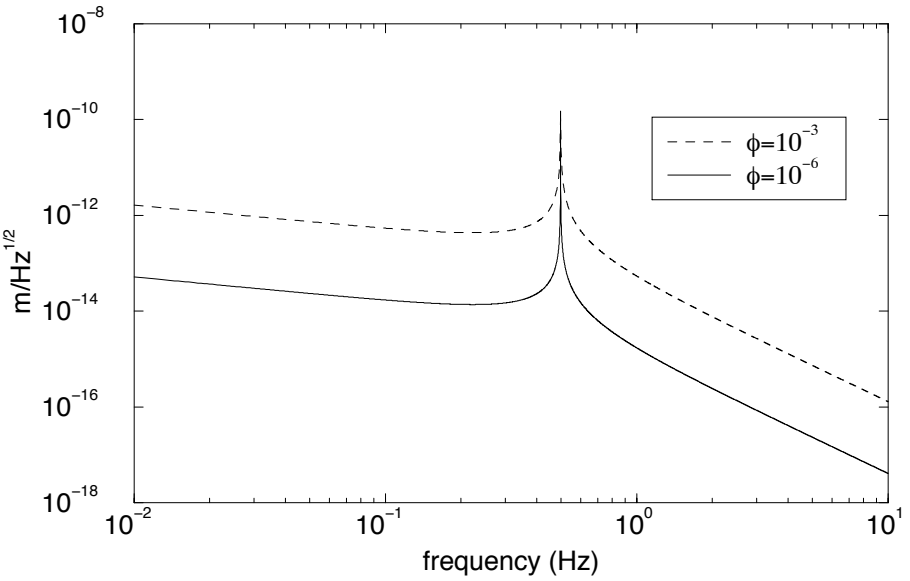

Figure 2.3: Calculated thermal noise spectral density for a pendulum ($l = 1$ m, $m = 1$ kg, $\omega_0 = \sqrt{g/l}$) for different values of the dissipation factor ϕ.

The frequency dependence well above or well below the resonances is the same as in (2.22).

Three thermal noise effects are relevant to the interferometer sensitivity:

- *pendulum mode*: the wires supporting the mirror bend in the mirror pendular motion. A dissipative action arises, whose intensity depends on the wire material;
- *mirror modes*: each mirror is a quartz cylinder with many mechanical drum modes. Thermal excitations of the mirror normal modes change the position or the the shape of its surface;
- *wires modes*: the normal modes of the suspension wires are also excited and the *violin modes* appear as a nearly harmonic sequence at high frequencies. The recoil of the wires manifests in mirror center of mass fluctuations.

2.7 Creep

The stressed mechanical parts of the mirrors suspensions may be affected by *creep*. A creep event is a sudden release of the stress accumulated in the lattice, which can simulate a GW burst event. Though the creep is a noise of *thermal* origin, it comes from a non linear phenomenon and has a non-gaussian spectrum. The creep may affect the detector in two different ways:

- **mechanical shot noise**: single creep events in the last part of the mirror suspensions (and especially in the wires supporting the mirror) are fake signals and their rate has to be reduced as much as possible;

- **integrated creep effect**: creep causes a weakening of the most stressed parts of the mirror suspension, turning into an measurable lowering of the vertical mirror position.

An in depth investigation has been performed by VIRGO Pisa and Perugia groups to identify the best steels and thermal treatment in order to reduce as far as possible the rate of the creep events [70, 71, 72].

2.8 Optical readout noise

The interferometric detectors aim to measure length variations of 10^{-18} m, that is about 1/1000 of a proton diameter. This number is meaningless when thinking of a single atom, whereas it makes sense when thinking of a crystal made of a huge number of atoms whose positions are averaged in space and time by the laser beam wavefront. Nevertheless, a quantum limit to the achievable precision exists, as predicted by the Heisenberg uncertainty principle.

2.8.1 Shot noise

A fundamental noise associated to the quantum nature of light limits the accuracy achievable by interferometric measurements. In this section the shot noise is calculated for a simple Michelson interferometer. The effects of the light phase modulation and of the power recycling will be examined in the next sections.

In case of perfect contrast ($C = 1$)[3] the interferometer output power is written:

$$P_{out} = \frac{P_{in}}{2}(1 + \cos\phi) \tag{2.25}$$

where P_{in} is the laser power, ϕ is the interferometric phase, and the average current in the photodiode is:

$$\bar{I} = \frac{e\eta P_{in}}{2\pi\hbar\nu} \tag{2.26}$$

[3]The contrast is defined as:

$$C = \frac{P_{\max} - P_{\min}}{P_{\max} + P_{\min}}$$

where $P_{\max}$ and $P_{\min}$ are the maximum and the minimum power impinging on the output photodiode as the interferometer phase changes of 2π.

where η is the quantum efficiency of the photodiode. The spectral density of the current shot noise fluctuations is:

$$\tilde{\delta I}_{\rm sn} = \sqrt{2e\bar{I}} = e\sqrt{\frac{2\eta P_{in}}{2\pi\hbar\nu}}\sqrt{1+\cos\phi} \tag{2.27}$$

Let $\delta\Phi$ be the phase variation induced by impinging GW. The corresponding power variation is :

$$\delta P_{\rm sig} = \frac{P_{in}}{2}\sin\phi\delta\Phi \tag{2.28}$$

From (2.26) one obtains the spectral current variation induced by the signal:

$$\tilde{\delta I}_{\rm sig} = \frac{e\eta}{2\pi\hbar\nu}\frac{P_{in}}{2}\sin\phi\tilde{\delta\Phi} \tag{2.29}$$

The signal-to-noise ratio (SNR) is larger than unity $\tilde{\delta I}_{\rm sig} > \tilde{\delta I}_{\rm sn}$ when

$$\tilde{\delta\Phi} \geq 2\sqrt{\frac{2\pi\hbar\nu}{\eta P_{in}}}\frac{\sqrt{1+\cos\phi}}{\sin\phi} \tag{2.30}$$

When the interferometer is operated on the dark fringe ($\phi \simeq \pi$) one gets:

$$\lim_{x\to\pi}\tilde{\delta\Phi} \geq \sqrt{\frac{4\pi\hbar\nu}{\eta P_{in}}} \tag{2.31}$$

corresponding to an equivalent noise:

$$\tilde{h}_{\rm shot} = \frac{1}{L}\sqrt{\frac{\hbar c\lambda}{2\pi\eta P_{in}}}, \tag{2.32}$$

The phase shot noise spectrum (2.31) is flat. Having FP cavities in the arms changes the effect of phase noises such as laser shot noise. For frequencies $f \gg f_p$ (defined in section 2.2) the same phase variation engenders different equivalent length variation, according to (2.2). The shot noise linear spectral density is then written:

$$h^{\rm FP}_{\rm shot}(f) \simeq \frac{\pi}{2\mathcal{F}L}\sqrt{\frac{\hbar c^2}{2\pi\nu P_{in}}}\sqrt{1+(4\pi f_{GW}\tau_s)^2} \tag{2.33}$$

The noise spectrum grows $h^{\rm FP}_{\rm shot}(f) \propto f$ for $f \gg f_p$.

The shot noise level can be reduced by increasing the laser power or the power stored into the interferometer, but the achievable accuracy of the measurement is limited by quantum mechanics.

2.8.2 Radiation pressure noise

The power fluctuation associated to the quantum nature of light generates a *radiation pressure noise*: fluctuations in radiation pressure make each mirror move with a spectrum:

$$\tilde{h}_{\rm rp}(f) = \frac{1}{mL}\sqrt{\frac{\hbar P_{in}}{2\pi^3 c\lambda}} \cdot \frac{1}{f^2} \tag{2.34}$$

While the shot noise is a phase noise, the radiation pressure fluctuations cause a real movement of the mirror. For a given value of P_{in} there exists a critical frequency below which the radiation pressure noise (which behaves as $1/f^2$) dominates over the shot noise. For actual available laser power, such frequency is outside the operation frequency range and the detectors sensitivities are shot noise limited.

2.8.3 "Heisenberg principle" for the interferometer: quantum limit

The simultaneous presence of shot noise and radiation pressure noise is an intrinsic limit to the achievable precision. An interferometer may be considered as an *Heisenberg microscope*: to increase the accuracy in measuring the mirror position one has to reduce the shot noise, that is to increase the laser power; this comes at the cost of worsening the radiation pressure noise and the "microscope" sensitivity at low frequency. The total optical readout noise is

$$\tilde{h}_{\rm OR}(f) = \sqrt{\tilde{h}^2_{\rm shot} + \tilde{h}^2_{\rm rp}} \tag{2.35}$$

At any given frequency f there is an "optimal" choice of the power $P_{\rm opt}$ which minimise the total noise (2.35):

$$P_{\rm opt} = \pi m c \lambda f^2 \tag{2.36}$$

By substituting (2.36) into (2.35) one obtains the *quantum limit* to the detector sensitivity:

$$\tilde{h}_{\rm QL}(f) = \frac{1}{\pi f L}\sqrt{\frac{\hbar}{m}} \tag{2.37}$$

$\tilde{h}_{\rm QL}$ is not a noise spectral density, but it's the locus of the minima of $\tilde{h}_{\rm or}(f)$ at any given frequency.

For a Fabry-Perot interferometer things are different, because folding makes the phase noises decrease while enhancing the displacement noises. The optical readout noise becomes:

$$\tilde{h}^{\rm FP}_{\rm OR}(f) = \sqrt{\left(\frac{\pi}{2\mathcal{F}}\right)^2 \tilde{h}^2_{\rm shot} + \left(\frac{2\mathcal{F}}{\pi}\right)^2 \tilde{h}^2_{\rm rp}} \tag{2.38}$$

Then

$$P^{\rm FP}_{\rm opt} = \left(\frac{\pi}{2\mathcal{F}}\right)^2 P_{\rm opt} \tag{2.39}$$

yielding expression (2.37) for the quantum limit, as expected.

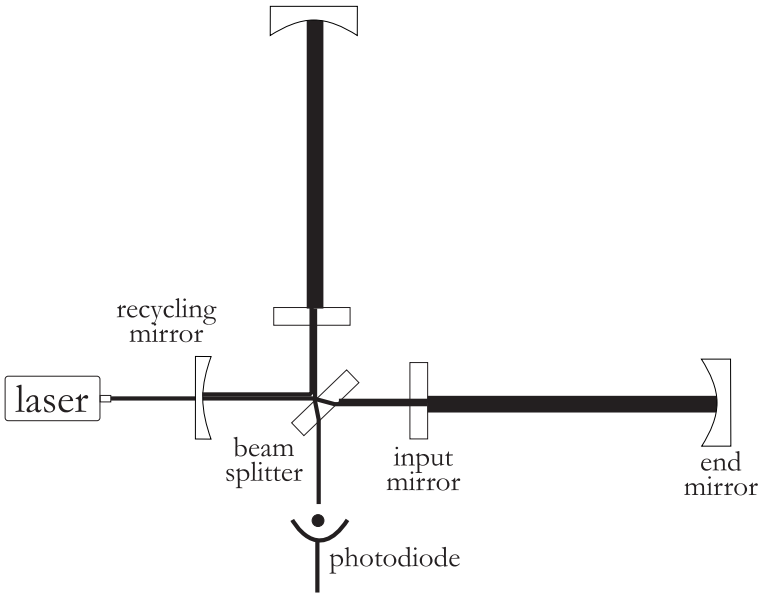

Figure 2.4: Scheme of a Fabry-Perot interferometer with power recycling.

2.9 Lowering the shot noise limit: power recycling

If the interferometer is locked on the dark fringe most of the power is reflected back towards the laser and is lost. A fraction of this waste power can be recycled: to do so, an additional mirror is inserted between the beam splitter and the laser and, properly phase and reflectivity matched, reflects the light towards the beam splitter (fig. 2.4). The rest of the interferometer can be described as a composite mirror, which, together with the recycling mirror, forms a *recycling cavity* to be kept in resonance. With this *power recycling technique* the power stored into the arms can be increased by a large factor, mainly limited by the beam losses (a recycling factor $\mathcal{R} \sim 50$ is foreseen for VIRGO) thus reducing the shot noise level. The recycling mirror and the two input mirror of the FP cavities constitute one more cavity to keep resonant.

2.10 Laser instabilities

2.10.1 Laser frequency fluctuations

In principle, an interferometer for GW detection can be made of two unequal arms. In practice, the two arms have to be nearly equal because of laser frequency fluctuations. Let $\nu(f)$ be the linear spectral density of the laser frequency fluctuations (in units of $\mathrm{Hz}/\sqrt{\mathrm{Hz}}$).

One can show that the equivalent strain noise is:

$$h_{\rm ff} = \frac{\tilde{\nu}(f)}{\nu}\frac{\Delta L_{\rm opt}}{L_{\rm opt}} \tag{2.40}$$

where $L_{\rm opt}$ is the difference in cavities optical length. In VIRGO an asymmetry parameter $\beta = \Delta L_{\rm opt}/L_{\rm opt} \sim 1\%$ is expected, due to the unavoidable differences in the mirrors characteristics and thus, in the finesse of the two cavities. Due to this unavoidable asymmetry a frequency stability $\tilde{\nu}(f) \sim 10^{-5}$ Hz/$\sqrt{\rm Hz}$ at 100 Hz is required, while the available uncontrolled laser presents $\tilde{\nu}(f) \sim 10^{2}$ Hz/$\sqrt{\rm Hz}$. This corresponds to reducing the laser frequency fluctuations by a factor of 10^7.

2.10.2 Laser power fluctuations

Besides the frequency fluctuations, lasers are affected by amplitude fluctuations also. These amplitude fluctuations are present on top of the fundamental shot noise and are true variations in the emitted power. Let us write again eq. (2.25) in the form:

$$P_{out} = \frac{P_{in}}{2}\left[1 + \cos(\phi_0 + \delta\Phi)\right] \tag{2.41}$$

where ϕ_0 is the chosen operation point and $\delta\Phi$ is the phase shift induced by a "signal". The phase sensitivity $|\partial P_{out}/\partial\delta\Phi|$ is maximum at $\phi_0 = \pi/2$ (whereas the SNR is not). With this choice, and keeping into account the input power fluctuations, the output power is written:

$$P_{out} = \frac{P_{in} + \delta P_{in}}{2}\left(1 - \sin\delta\Phi\right) \approx \frac{P_{in}}{2}\left(1 + \frac{\delta P_{in}}{\delta P_{in}} + \delta\Phi\right) \tag{2.42}$$

In eq. (2.42) both the signal $\delta\Phi$ and the power fluctuations appear at the first order.

In order not to mask the effect of a true signal it should be $\delta P_{in}/P_{in} \ll \delta\Phi \sim 10^{-11}$. This condition puts a constraint on the power stability level, which would extremely difficult to achieve.

2.10.3 Bypassing power fluctuations: "dark fringe" operation

To get rid of the power fluctuation noise it is better to operate the interferometer on the *dark fringe*, that is at $\phi_0 \simeq \pi$. In this case:

$$P_{out} = \frac{1}{2}(P_{in} + \delta P_{in})\delta\Phi^2 \approx \frac{1}{4}P_{in}\delta\Phi^2 \tag{2.43}$$

if the laser is stabilised to a good level ($\delta P_{in} \ll P_{in}$). The drawback of this choice is that the power dependence on the real signal phase shift is of the second order and the sensitivity is much worse. To increase the sensitivity maintaining the dark fringe choice the Pound-Drever signal extraction technique is used.

2.11 Heterodyne detection

A common *lock-in* technique to get rid of $1/f$ noise in interferometric detectors is to phase modulate the laser light in order to produce sidebands. Phase modulation can be done by introducing Pockels cells in the two arms of Michelson interferometer. If the two cells are driven in anti-phase with a sinusoidal voltage at frequency $\Omega/2\pi$, the output power is:

$$P_{out} = \frac{P_{in}}{2}\left[1 + \cos(\phi + 2m\sin\Omega t)\right] \tag{2.44}$$

The parameter m is the *modulation index* and measures the energy of the sidebands ($m \ll 1$). Equation (2.44) can be simplified if the interferometer is operated around the dark fringe ($\phi \simeq \pi + \delta\Phi$) and the modulation index is small ($m \ll 1$). Neglecting the higher order harmonics:

$$P_{out} \simeq \frac{P_{in}}{2}\left[1 - J_0(2m) + 2\delta\Phi J_1(2m)\sin\Omega t\right] \tag{2.45}$$

where J_0, J_1 are the Bessel function of order 0,1 respectively. Eq. (2.45) shows that modulating the light turns into a first order dependence of the output power with the signal while keeping the interferometer on the dark fringe.

2.11.1 Shot noise in a modulated interferometer

We repeat the calculation of the shot noise (see section 2.8.1) keeping into account the effect of the modulation. From (2.45),(2.26) comes that the signal and shot noise currents are written[4]:

$$\tilde{\delta I}_{\rm sig} = e\frac{\eta P_{in}}{2\pi\hbar\nu}J_1(2m)\delta\Phi \tag{2.46}$$

$$\tilde{\delta I}_{\rm sn} = \sqrt{2}e\sqrt{\frac{\eta P_{in}}{2\pi\hbar\nu}\left[1 - J_0(2m)\right]} \tag{2.47}$$

A phase variation is detectable if:

$$\delta\Phi \geq \sqrt{\frac{4\pi\hbar\nu}{\eta P_{in}}}\frac{\sqrt{1 - J_0(2m)}}{J_1(2m)} \tag{2.48}$$

In the limit $m \to 0$ the previous equation reduces to (2.31): the shot noise limit is the same in case of heterodyne or continuous detection.Heterodyne detection allows to perform the measurement at frequencies where the laser fluctuations are smaller and the $1/f$ noise of the electronic devices is less important.

[4]The factor $\sqrt{2}$ in the second equation comes from the demodulation process: the shot noise at the frequencies $\Omega - f$ and $\Omega + f$ adds incoherently at frequency f.

2.12 Other sources of noise

In this section we list some sources of noise which were considered in the interferometer design.

2.12.1 Acoustic noise

Up to now we have not mentioned that the interferometer has to be contained into an ultra high vacuum pipe, to isolate the mirrors from acoustic noise and from thermal noise associated to viscous damping, and to prevent the laser beam from scattering and phase shifts induced by fluctuation of the refractive index. The vacuum level to be achieved is established when analysing a different noise originated from the gas pressure fluctuations.

2.12.2 Refraction index fluctuations

Fluctuations of gas pressure generates fluctuations of the refractive index and, consequently, a phase noise. The intensity of the noise is proportional to the gas polarizability. The main residual gas is expected to be hydrogen. In order to keep this phase noise an order of magnitude below the shot noise level, the required H_2 partial pressure is 10^{-9} mbar.

2.12.3 Scattered light

Photons scattered by mirror imperfections and bouncing on the pipe walls get a different phase due the modulating effect of the pipe vibrations. If such photons recombine with the laser beam a phase noise arises. To get rid of this problem a set of mechanical filters (*baffles*), made of absorbing steel and shaped as truncated cones, is placed along the pipe. The baffles, absorbing the spurious photons, avoid their recombination with the beam [45].

2.12.4 Light in higher modes

The electric field of the laser beam may be decomposed into a sum of different modes. Each mode acquires a different phase shift while propagating in the cavities. Only one mode has to be selected for a correct operation. An optical filter has to be built, capable of selecting the TEM_{00} only. An optical cavity, called *mode cleaner*, is placed between the laser and the interferometer for this purpose.

2.13 Locking

The operation of an interferometric antenna for GW detection requires:

- the FP cavities to be resonant;
- the interferometer output to be held on the dark fringe;
- the recycling cavity to be resonant.

Fulfilling all these conditions requires the control of the length of the cavities (and then the relative positions of the optical components) to an high level of accuracy (less than 10^{-12} m). The set of operations necessary to achieve the goal is called *locking*. The locking is realised by extracting from the interferometer itself several *error signals* which monitor the interesting length, and by designing proper feedback filters to control the mirrors positions by means of actuators capable to change the mirror position without injecting noise in the interferometer frequency detection range.

Chapter 3

VIRGO Interferometric GW Detector

3.1 VIRGO antenna

In the previous chapter we have described the working of an interferometric GW detector. The aim of this chapter is to outline the design of the VIRGO antenna, now under construction at the site of Cascina, near Pisa (fig. 3.1), and to compare its target sensitivity with the expected intensity of the GW sources described in chapter 1.

3.1.1 Optics

The scheme of the VIRGO interferometer is shown in fig. 3.2. We define l_1, l_2 the lengths of the Michelson interferometer arms (distances from the beam splitter to the input mirrors of the FP cavities), L_1, L_2 the lengths of the FP cavities and l_r the distance between the beam splitter and the recycling mirror.

- **Laser:** it is a Nd:Yag emitting at $\lambda = 1064$ nm. Its output power in the TEM_{00} mode is about 20 W. The stability requirements are:

  1. *power:*
  $$\frac{\tilde{\delta P}}{P} < \begin{cases} 3 \cdot 10^{-5}/\sqrt{\text{Hz}} & \text{for } f = 10 \text{ Hz} \\ 3 \cdot 10^{-7}/\sqrt{\text{Hz}} & \text{for } 100 < f < 1000 \text{ Hz} \end{cases} \tag{3.1}$$

  2. *frequency:*
  $$\frac{\tilde{\delta\nu}}{\nu} \approx \begin{cases} 10^{-4}/\sqrt{\text{Hz}} & \text{for } f = 10 \text{ Hz} \\ 10^{-6}/\sqrt{\text{Hz}} & \text{for } 100 < f < 1000 \text{ Hz} \end{cases} \tag{3.2}$$

  This level of frequency stability requires a gain of about 10^7 in the control loop.

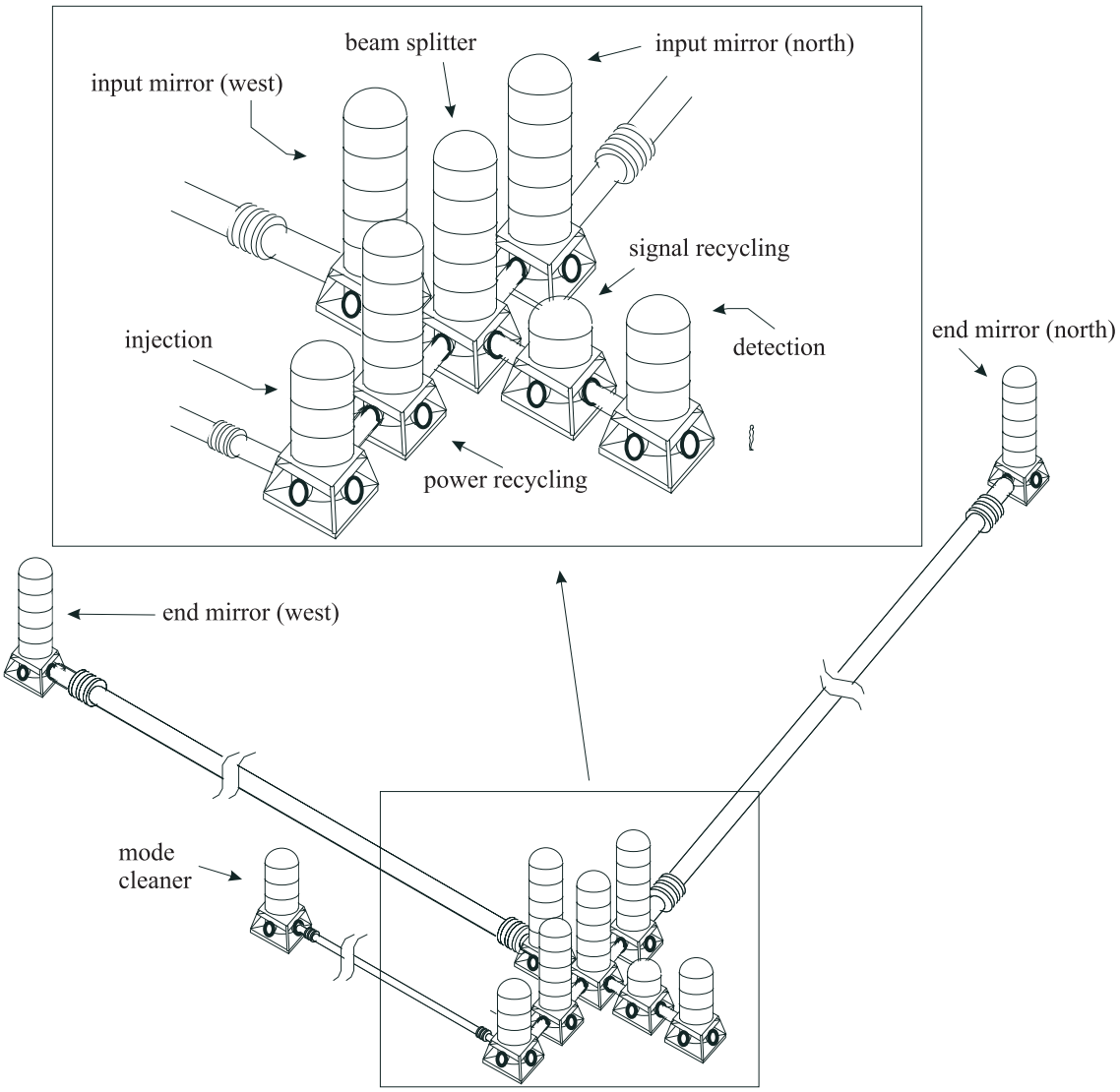

Figure 3.1: The vacuum setup of the VIRGO interferometer.

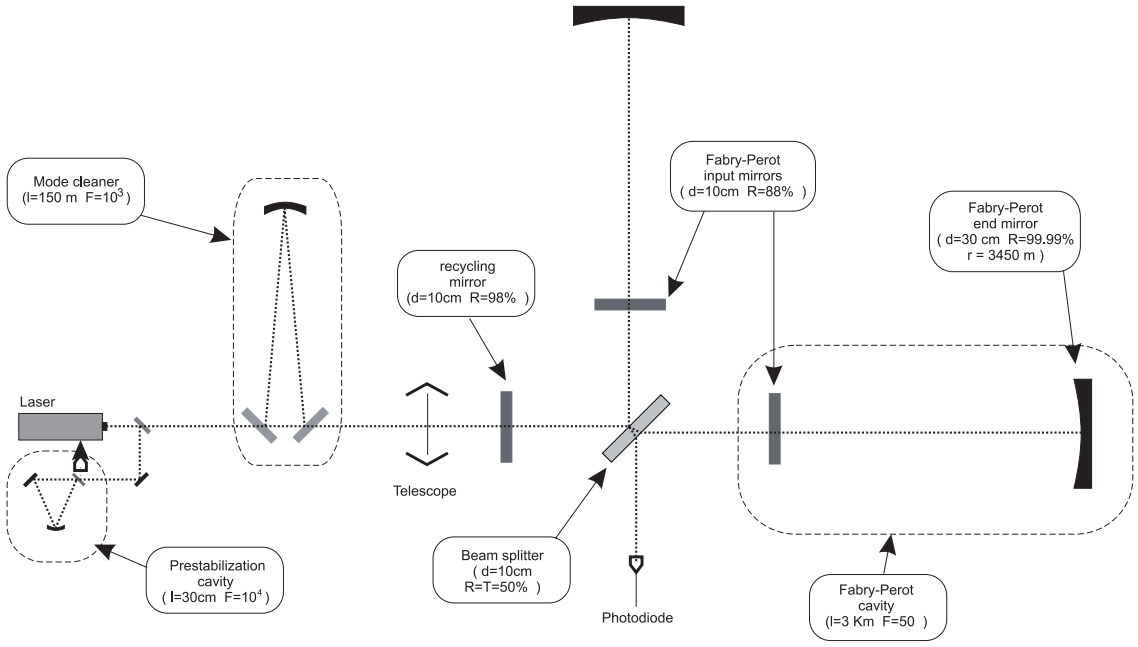

Figure 3.2: Schematic design of the VIRGO interferometer, with the 3 km long Fabry-Perot cavities and the recycling cavity.

The laser (including the stabilisation optronics and the phase modulator) is not under vacuum and is placed on an optical table in a clean room.

- **Input bench:** it is under vacuum and suspended from a *short superattenuator* (see section 4.6). It is equipped with a rigid triangular reference cavity for the frequency pre-stabilization, the input and output mirrors of the mode cleaner and the main beam expansion and alignment optronics.

- **Mode cleaner:** it is a triangular cavity 144 m long. Two mirrors (input and output ones) are mounted on the input bench. The third mirror is suspended from a short tower, connected to the input bench tower by a dedicated pipe.

- **Power recycling:** the recycling cavity is made by the recycling mirror and the interferometer itself. The cavity length is defined as $l_r = l_0 + (l_1 + l_2)/2$. The foreseen recycling factor is about 50: a power of about 1 kW is expected on the beam splitter.

- **Fabry-Perot cavities:** the FP will be 3 km long and will have a finesse $\mathcal{F} = 50$. The interferometer output is to be kept on the dark fringe for the carrier, while the sidebands are to be transmitted to carry the signal.

- **Detection system:** it is composed of a *detection bench*, suspended from a short tower and an optical table (outside the vacuum vessel). The bench supports the output mode cleaner (a small monolithic triangular cavity, designed to increase the contrast by filtering the spurious modes) and the optics for splitting and collimating the beam on the photodiodes. The table supports the photodiodes (InGaAs, quantum efficiency $\eta = 0.85$) for the locking and the signal detection.

3.1.2 Suspensions

The sensitivity of a ground based antenna is low frequency limited by natural seismic vibration of the ground. Suspending the optical components is a simple way to filter the ground vibrations: at frequencies above the resonant frequency of the pendulum formed by the suspended mass, the mirror can be considered *free falling*. VIRGO has developed a suspension system, called *superattenuator* (SA), capable to inhibit the seismic noise transmission to the mirror above 4-5 Hz. The SA is essentially a multi-stage pendulum about 10 m tall, where each suspended mass is a special device acting as a vibration low pass filter in all 6 degrees of freedom (d.o.f.). The SA is described in details in chapter 4.

Shorter suspensions are used for those parts of the optical scheme that do act on the same way with respect to the two arms: the input bench, the mode cleaner, the detection bench.

3.1.3 Vacuum system

The VIRGO vacuum volume is composed of two parts: the pipes (containing the optics) and the towers (10 m high, containing the superattenuators). The pipe is 1.2 m in diameter and composed of 15 m long modules connected by bellows and resting over special supports allowing the pipe "breath" induced by the baking or by the daily thermal variations. In the pipes partial pressures of 10^{-9} mbar for hydrogen, 10^{-14} mbar for hydrocarbons and 10^{-10}mbar for other gases are required. The limits on the hydrogen and other gases pressure come from the requirement for the noise due to fluctuations in the refractive index to be a factor 10 below the dominating noises. The limit on the hydrocarbons is more strict because these molecules can stick on the mirror surface and degrade its quality. The vacuum level is achieved in three steps: a rough pumping (from atmospheric pressure to 10^{-2} mbar, performed with dry pumps), an intermediate pumping (to 10^{-6} mbar, performed with turbo-molecular pumps) the ultra-high-vacuum pumping (down to the required pressure, performed with purely passive titanium sublimation pumps).

The ultra-high-vacuum required in the pipe cannot be achieved in the towers, because of the outgassing properties of the cables and, in general, the large number of devices the superattenuators are provided with. To solve the problem, the towers are divided in two parts by a separating roof and communicating only through a narrow conductance hole

necessary for the passage of the wire holding the last stage of the suspension (see chapter 4). Most of the cables are in the upper part, where a pressure of 10^{-6} mbar is foreseen.

3.2 Interferometer locking

Locking the interferometer means to actively control the test masses at the operation points necessary to keep the interferometer output on the dark fringe, the FP and the recycling cavities in resonance with the laser. These four conditions are fulfilled by controlling four independent lengths: $L_1, L_2, l_r, \Delta l$. The error signals are provided by a set of photodiodes monitoring the light power and phase along different points of the interferometer [53].

The requirements on the locking are of two types:

1. **maximum mirror rms displacement:** to fulfil the resonance conditions the previous lengths should be controlled with a precision of about $10^{-4}\lambda \approx 10^{-10}$ m. Actually, the rms motion of each mirror should not be larger than 10^{-12} m: this stricter limitation is due to the dynamic range of the read-out electronics (photodiodes and RF mixer);

2. **maximum mirror spectral noise:** the maximum tolerable spectral noise of the mirrors has been calculated [65]. The strictest requirements concerns the cavity mirrors: to have an equivalent strain noise 3 times smaller than VIRGO nominal sensitivity the maximum tolerable spectral motion for the FP mirrors is:

$$\delta x = \begin{cases} 10^{-18} & \mathrm{m}/\sqrt{\mathrm{Hz}} \quad \text{at 10 Hz} \\ 3 \cdot 10^{-20} & \mathrm{m}/\sqrt{\mathrm{Hz}} \quad \text{at 100 Hz} \end{cases} \tag{3.3}$$

The suspended mirrors may have a large (tens of μm) seismically excited residual motion in the range 0-2 Hz, where the superattenuator does not attenuate. This spurious motion must be compensated by means of proper actuators: the locking loop must have high gain in this range, and must not introduce noise in the detection range.

Such requirements impose to design a control system with a huge dynamic range (the rms motion of the mirrors must be reduced by a factor $\sim 10^8$ within a large bandwidth. The VIRGO solution consists in "cascading" 3 control stages (3 actuation points placed along the suspension) acting in different dynamic and frequency ranges. VIRGO suspension is suitable to the purpose: a pre-isolator stage has been introduced in the suspension design with the purpose of reducing the seismic excitation of the superattenuator modes and provide a suitable platform for active controls. The pre-isolator stage is the main subject of this work and will be described in the following. The control strategy will be described in section 8.2.

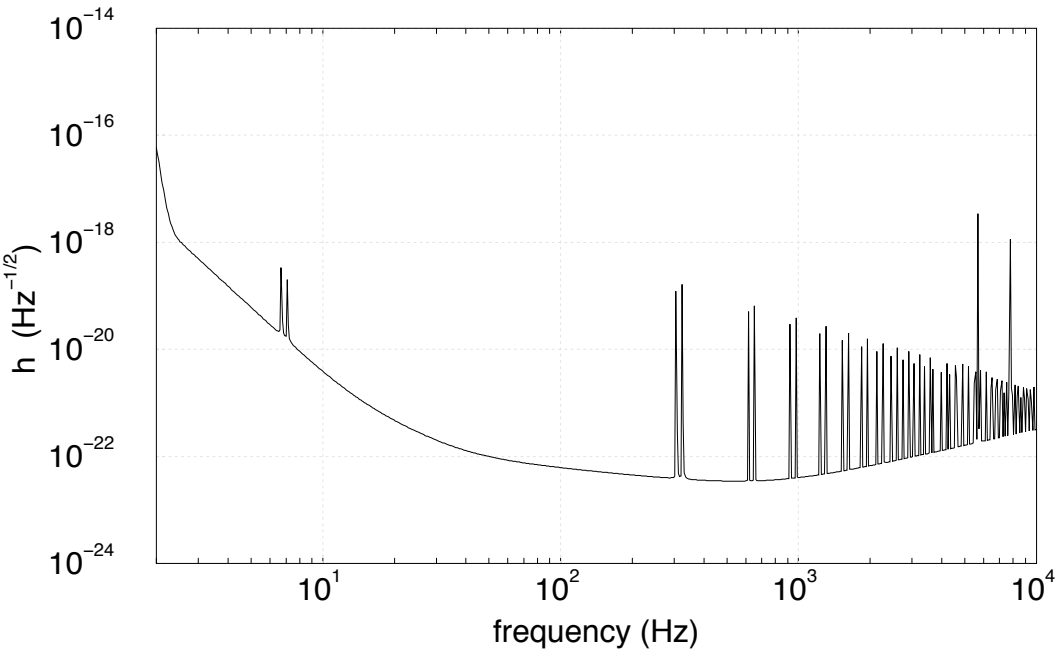

Figure 3.3: Spectral sensitivity of VIRGO antenna.

3.3 VIRGO sensitivity

Presently, the determination of the VIRGO sensitivity is based on the prediction on the intensity of the various noise sources. The expected noise can be converted into an equivalent strain spectral density $\tilde{h}_n(f)$, defined in section 2.3: this function is usually called VIRGO sensitivity. The sensitivity of an interferometric antenna depends not only on the absolute noise level, but is a matter of SNR. The SNR depends on many parameters, such as the observation time, the degree of theoretical knowledge of the GW emission mechanism of a certain source, on the data analysis strategy. For instance, a supernova event emitting GW with maximum amplitude h_0 may be detected or not depending on the spectral properties of the signal: if the bandwidth of the signal is large the SNR is degraded. Thence, it is not enough to know the amplitude of the wave and the noise of the detector to decide whether the source is detectable. In this section we give an overview of the SNR problem, comparing the VIRGO sensitivity with the various GW sources.

3.3.1 Sensitivity curve

VIRGO predicted sensitivity curve is shown in (fig. 3.3, 3.4). Four sources of noise are dominant in different ranges of frequency:

- **seismic noise:** the *seismic noise wall* is expected at 3-4 Hz, thanks to the attenuation performance of the suspensions;
- **newtonian noise:** a new calculation of the noise induced by local gravity field fluctuations [73] shows that this noise is dominant between 2 and 10 Hz. The double peak at about 7 Hz is thermal noise associated to the main mode of the marionetta-mirror system;
- **pendulum thermal noise:** dominates approximately between 10 and 30 Hz;
- **mirror thermal noise:** dominates between 30 and 500 Hz;
- **shot noise:** dominates above 500 Hz. The large peaks are due to the wires violin modes. The peaks are in pairs because the input and the end mirrors have different masses.

3.4 Signals from coalescing binaries

The coalescence of two compact stars (NS/NS, NS/BH, BH/BH) is the most promising GW event to be detected by the first generation interferometric antennas. The extraction of the signal from the interferometer noisy output will be performed by cross-correlating it with the signal expected from the theory (*template*). To achieve the goal of the detection it is very important to have accurate theoretical templates and a large effort is being made in this direction.

The SNR expected in VIRGO for a coalescence event has been calculated in the newtonian approximation [44], integrating over the range 10-500 Hz:

$$\mathrm{SNR} = 2.51 \left(\frac{R}{100\mathrm{Mpc}}\right)^{-1} \left(\frac{\mathcal{M}}{M_\odot}\right)^{5/6} \tag{3.4}$$

A threshold SNR > 8 is necessary to improve the rejection to 1 false alarm/year. From (3.4) one finds out that a NS/NS event ($m_1 \sim m_2 \sim 1.4 M_\odot$) is detectable at distance $R < 30$ Mpc. Different estimates on the rate on NS/NS events exist. Bonazzola and Marck [20] assume 1 merger per year within 200 Mpc. Therefore VIRGO would observe about 1 NS/NS event every 50 years. Higher SNR is then expected for NS/BH or BH/BH coalescences, depending on the mass of the involved black holes. More optimistic estimates on the rates allow to be more confident on the detection of coalescing stars, and particularly about the events involving a BH. Nevertheless it is evident that the big effort to be done in order to enhance the detector sensitivity is to substantially reduce the thermal noise level. From (1.31) it is possible to calculate the time $\tau(\nu_0)$ elapsed between the moment when the frequency of the GW emitted by a coalescing system is ν_0 and the merger. The result for two different values of ν_0 is: $\tau(4\mathrm{Hz}) = 11588$ sec and $\tau(70\mathrm{Hz}) = 5.6$ sec. ν_0 can

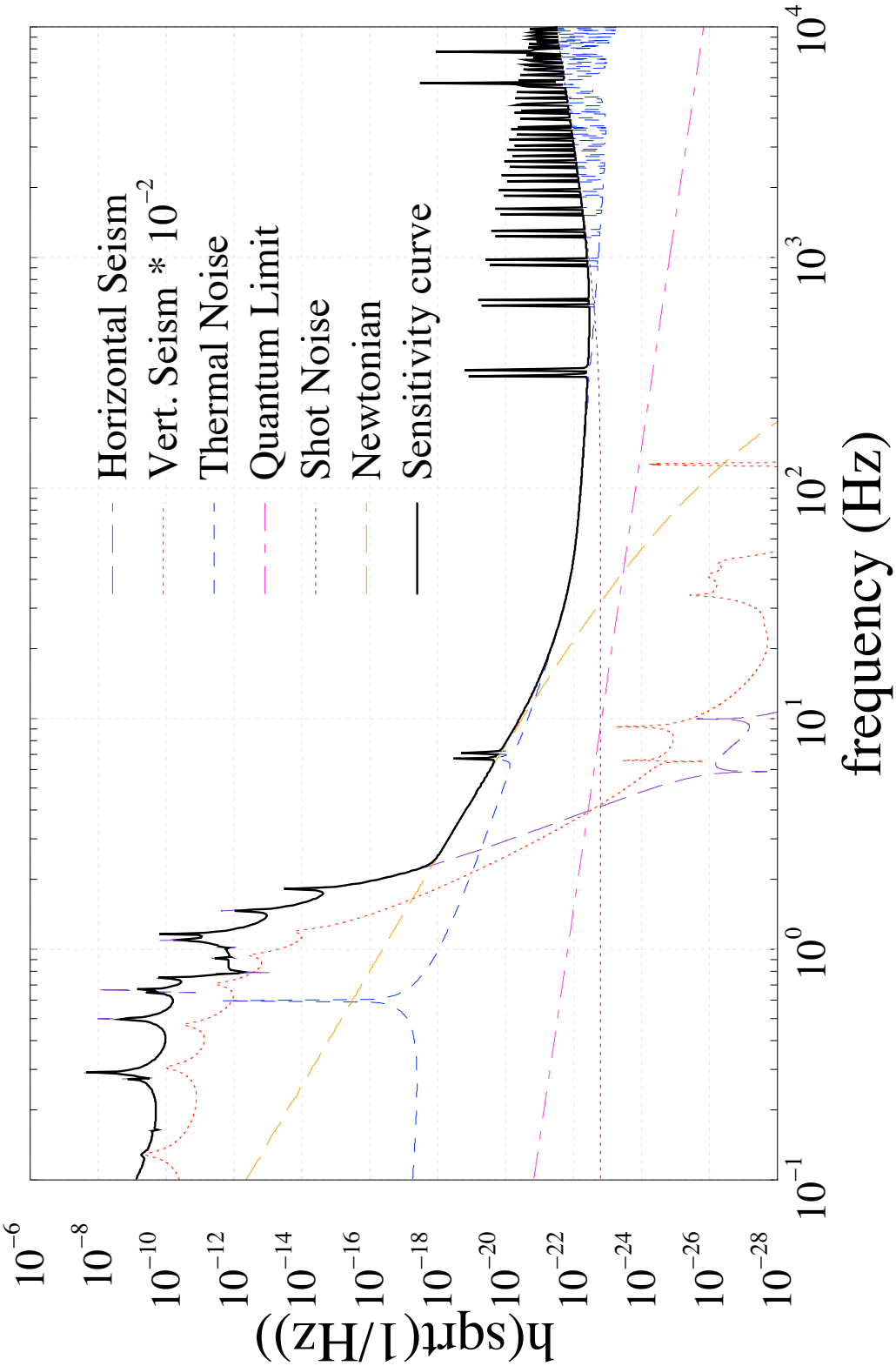

Figure 3.4: Spectral sensitivity of VIRGO: the contribution of all the noise sources is shown.

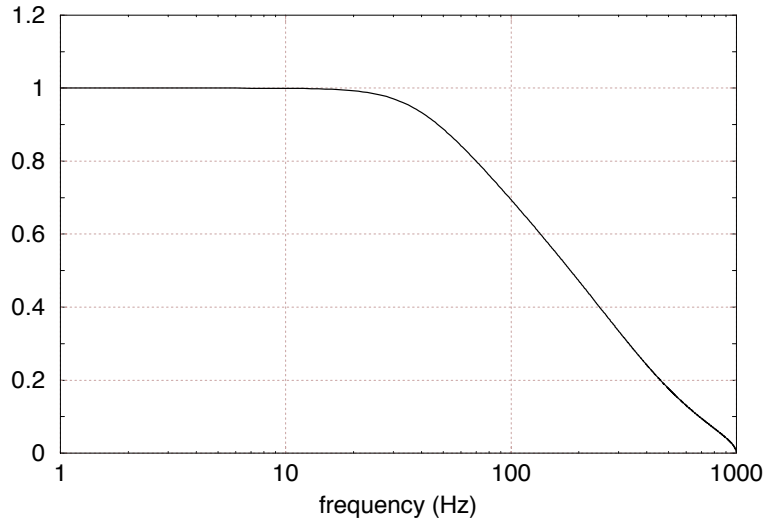

Figure 3.5: SNR integrated over the range $\nu_0 - 1$ kHz as a function of ν_0 (calculated from the expected VIRGO noise curve).

be considered as the low frequency threshold of a GW detector. In fig. 3.5 the integrated SNR is shown as a function of the "starting frequency": VIRGO can nominally "start" the integration at $\nu_{\rm min} = 4$ Hz and all the SNR is exploited. By comparison, about 20% of the SNR is lost when starting the integration at 70 Hz.

3.5 Burst from stellar collapses

During the last years it has become more evident that the detection of stellar collapses will not be an easy goal for the first interferometers:

- Large uncertainties affect the collapse hydrodynamics simulation codes and the produced templates. At the moment it seems reasonable that LIGO/VIRGO could aim to detect only events with SNR $\gg 1$;
- most of the predicted collapse processes produce GW detectable at galactic distances only. Non-axisymmetric collapses can be detected as far as Virgo Cluster;
- even in case of SNR > 1 a multiple coincidence detection is necessary in order to discriminate between real events and non-gaussian noise. The creation of a network of interferometers (and of other detectors such as bar antennas, neutrino observatories, optical telescopes, γ detectors) working in coincidence would allow not only

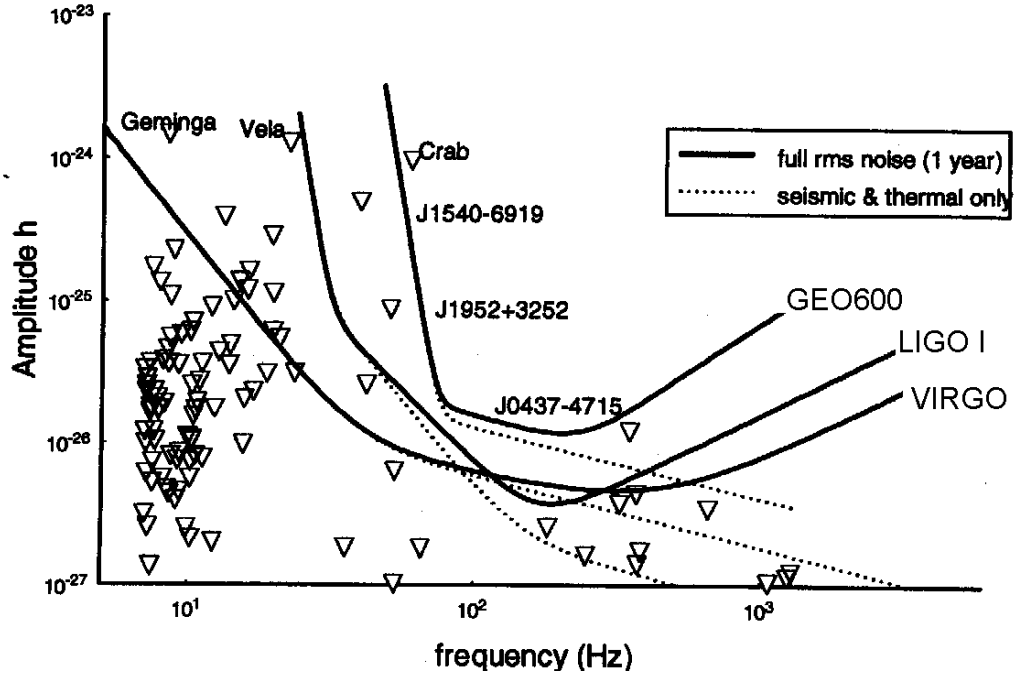

Figure 3.6: Upper limit of the GW amplitude emitted by several galactiv pulsars compared with the rms sensitivity of VIRGO, LIGO, GEO600, assuming one year of signal integration.

the unambiguous detection of a burst event but also, measuring the delay times, the determination of the source direction in the sky.

3.6 Periodic signals

Up to 1995 706 galactic pulsars were known. Most of them are located in the central region of our galaxy and their distances from Earth range from 5 to 20 kpc. Most of them would emit GW at frequencies below 10 Hz, as shown in fig. 1.4: this is one of the reasons for the large experimental effort to extend the VIRGO sensitivity down to low frequency. While the spinning frequencies are known with accuracy $10^{-4} - 10^{-11}$ the estimate of the GW intensity is affected by a large incertitude. Upper bounds can be put on the values of the ellipticity ϵ (see section 1.7) if one assumes that the observed slowing down of the period is entirely due to GW emission. Although this is not a realistic assumption, since energy losses via electromagnetic radiation or magnetospheric acceleration of charged particles are certainly important, such an upper bound permits a comparison with the actual detector

sensitivities. The signal-to-noise ratio for a periodic signal is

$$\mathrm{SNR} = \frac{h_0}{\tilde{h}(f)}\sqrt{T} \tag{3.5}$$

where h_0 is the GW amplitude, $\tilde{h}(f)$ is the detector sensitivity at the signal frequency and T is the integration time of the signal [1](fig. 3.6).

A global search for neutron stars radiation must be tried. The big problem is that the Doppler effect due to the Earth motion has to be subtracted independently for every direction of the sky. This requires calculation times which are presently orders of magnitudes larger than the human life. If a known pulsar is targeted, the sensitivity of the interferometers in a narrow band around the emission frequency can be enhanced using a *signal recycling* technique [46, 47].

3.7 Stochastic background

A single interferometer would not be enough to detect the stochastic background (SB) of relic GW. Large SB intensity (SNR $\gg 1$) is not compatible with previous observations (such as COBE's), while a SNR ~ 1 would not be distinguishable from detector excess noise. The outputs of at least two detectors should be cross correlated. The two detectors should be far apart in order to decorrelate local noise and close enough to maintain correlation for GW in the VIRGO/LIGO range. A distance of some tens of km is suitable to fulfil these conditions [34, 37].

If a second VIRGO were built at 50 km distance with the same orientation as the first interferometer, assuming 1 year of observation time and SNR=1.65 (90% confidence level), the minimum detectable $\Omega_{\mathrm{gw}}^{\mathrm{min}}(f)$ would be given by [37]:

$$h_0\Omega_{\mathrm{gw}}^{\mathrm{min}}(f) \sim 3\cdot 10^{-7}\left(\frac{f}{100\mathrm{Hz}}\right)^3\left(\frac{\tilde{h}_n}{10^{-22}\mathrm{Hz}^{-1/2}}\right)^2 \tag{3.6}$$

where $\tilde{h}_n$ is the equivalent strain noise spectral density, which can be read directly on the plot of fig. 3.3.

If, as predicted from the standard inflationary models, the SB energy spectrum is constant ($\Omega_{\mathrm{gw}}(f) = \mathrm{const.}$) the minimum detectable level can be expressed as a function of the SNR and of the observation time as:

$$h_0\Omega_{\mathrm{gw}}^{\mathrm{min}} \simeq 2\cdot 10^{-7}\left(\frac{\mathrm{SNR}}{1.65}\right)^2\left(\frac{1\mathrm{yr}}{T}\right)^{1/2} \tag{3.7}$$

[1]Due to the noise incoherence in time, its Fourier transform only grows like $\sqrt{T}$ while the Fourier transform of a periodic signal grows linearly with the observation time. For this reason the SNR for a periodic source is expected to grow like $\sqrt{T}$.

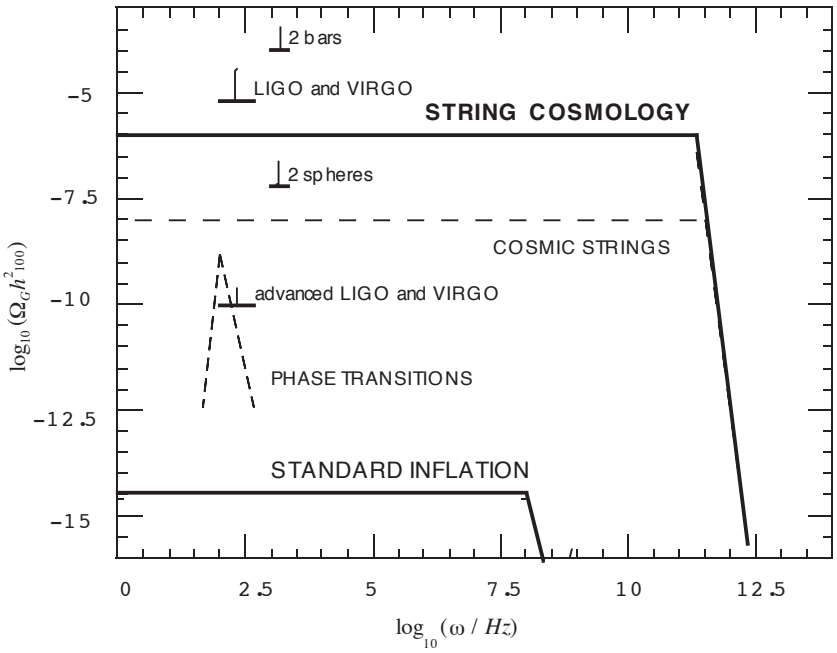

Figure 3.7: The stochastic background spectra expected from standard inflation and string models compared with the actual GW detectors (from [49]).

comparing the (3.7) with the (1.41) one sees immediately that VIRGO like interferometers are orders of magnitude less sensitive than what required to detect the cosmological stochastic background originated during the inflationary phase. The situation is not hopeless when the string cosmology models (see section 1.8) are considered. In fig. 3.7 the sensitivity of GW detectors[2] is compared with the stochastic background intensity expected from string models and standard inflation[3].

[2]The sensitivity refers to a couple of equal detectors in the same place.
[3]The figure is from [49]. We thank M.Gasperini for allowing to use it.

Chapter 4

VIRGO suspension: the super-attenuator

The mirror suspension system of an interferometric GW detector has to be a multiple task device: it must provide a steep low pass filtering for ground vibrations, with a cut-off frequency as low as possible, and it must be suitable for the control of the mirror position on a very large dynamic range. Moreover, the suspension internal noise must be kept as low as possible. Summarising, the requirements for a reliable suspension are:

- **isolation from external disturbances:** VIRGO aims to reach a target spectral sensitivity
$$\tilde{h}(10 \text{ Hz}) \sim 10^{-21}/\sqrt{\text{Hz}}$$
that means that the test masses have to be isolated down to a level of
$$\tilde{x}(10 \text{ Hz}) \sim 3 \cdot 10^{-18} \text{ m}/\sqrt{\text{Hz}}$$
corresponding to a mechanical attenuation factor of 10^{-11} (220 dB) at 10 Hz (assuming $\xi = 0.3$ in (2.16));

- **capability to control the mirror position:** the requirements on the mirror positions in order to lock the interferometer are very strict ($\delta x_{\text{rms}} \sim 10^{-12}$ m) and the mirror position must be controlled down to DC without injecting noise in the detection band. This result cannot be achieved by acting only on the mirror: control forces are to be exerted on various *control points* along the suspension, which has to be suitable for the purpose;

- **low level of internal disturbances:** the pendulum mode thermal noise dominates above 4 Hz. The possibility of lowering the thermal noise intensity depends on the use of high Q material rather than steel for the wires, and on the cooling of the suspension: none of these solution is ready to date for being adopted in first

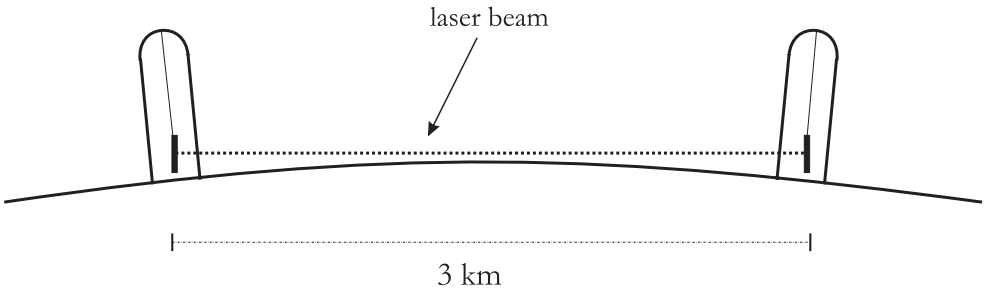

Figure 4.1: The direction of the gravity over the 3 km distance arm length changes by an angle $\alpha_{\rm grav} = 3 \cdot 10^{-4}$: a vertical displacement δy of one mirror will turn into a minimal differential displacement $\delta L = \alpha_{\rm grav} \cdot \delta y$ in the beam direction.

generation interferometers. Another source of internal non gaussian noise is the creep in the stressed mechanical parts of the suspension. The creep intensity can be reduced by choosing proper steels and applying suitable thermal treatments.

4.1 VIRGO superattenuator

A well designed and reliable vibrations isolator must be effective in all six degrees of freedom, because, in a real mechanical system, all angular and translation degrees of freedom are unavoidably coupled. For example, unattenuated vertical vibrations would turn into motion of the mirror in the beam direction at least because the suspensions of the input and end mirrors of a FP cavity at 3 km distance are not parallel, but form an angle $\alpha_{\rm grav} = 3 \cdot 10^{-4}$ due to the Earth curvature (fig. 4.1). The angle $\alpha_{\rm grav}$ is the minimal coupling factor between the beam direction and the vertical. Actually, a larger vertical-horizontal coupling factor ($\alpha_{\rm mech} \sim 0.01$, taken as a conservative estimate) is expected to originate from mechanical couplings between filters. This restriction and the requirement of having a system with low resonant frequencies, impose to design an isolator far more complicated than a chain of masses and simple springs. The suspension can be divided into 3 parts: the pre-isolator stage, the chain of passive filters, the mirror control system.

In the horizontal plane[1] the SA is essentially a multistage pendulum composed by a cascade of stages (fig. 4.2), hereafter called *filters*. Each filter is connected to the preceding and to the following ones by steel wires. The whole chain, from the suspension point to the mirror, is about 10 m high, the frequency of the main normal mode of the chain is $f = (1/2\pi)\sqrt{g/L} \sim 0.16$ Hz. A lower frequency mode is introduced by means of a

[1]In the following we refer to a xyz frame, where $\hat{x}$ is the axis parallel to the laser beam, $\hat{y}$ is the horizontal axis perpendicular to $\hat{x}$ and $\hat{z}$ is the vertical axis.

pre-isolator stage, as will be discussed in chapter 5.

To attenuate angular motions, filters are designed with high moments of inertia and are connected to the suspending wires as close as possible to the filter centre of mass. This geometry introduces short lever arms for restoring torques. The design allows angular mode frequencies of about 1 Hz or less.

The vertical attenuation is obtained providing each filter with a ring of high tensile strength steel springs, working in cantilever configuration with vertical action. The following stage is suspended from these springs so that, also in the vertical direction, the system acts as a chain of coupled oscillators. The lowest vertical resonance frequency achieved in this way is 1.4 Hz. A magnetic antispring system (see section 4.2) is used to "soften" the springs, and allows to lower the vertical resonance frequency to 0.4 Hz.

In the following, the SA mechanics design is described.

4.2 Passive attenuation: filters

Four fully passive *standard filters* are suspended from the top table. Each of them (see fig. 4.2) is designed to reduce the transmission of mechanical vibrations by two orders of magnitude in six degrees of freedom. The main body of the filter is a rigid steel cylinder, weighting about 100 Kg, 70 cm in diameter and 18.5 cm high, suspended to the upper stage by a steel piano wire, about 1.3 m long and with diameters ranging from 1.85 to 4 mm (depending on the load) . The wire is connected as close as possible to the filter centre of mass in order to minimise the coupling between the tilt and the horizontal motion. The filter supports the load of the lower stages through a converging set of cantilever triangular blade springs (see fig. 4.2 (b)).

The blades are pre-bent in order to return to be straight under load [69]. The number of blades decreases from the uppermost filter (12) to the lowest one (4) to match the supported load (each blade, designed to support about 50 Kg, is finely tuned to its specific load). The base of each triangular blade is clamped to the outer circumference of the bottom of the filter body. Thanks to the triangular shape the stress distribution is uniform along the blade, allowing to minimise the maximum internal stress, which is kept below 2/3 of the elastic limit of the material. Thorough experimental studies have been performed to select the best steel and thermal treatment for the blades, in order to reduce as much as possible the microcreep, which can be harmful even if the materials are stressed below the elastic limit [70].

The tip of each blade is attached to a central column which is constrained by a set of centering wires to move only in the vertical direction through the central hole of the filter body. The central column supports a *crossbar*, extending across the top surface of the filter body. The *moving part* of the filter (grey in fig. 4.2 (a)), composed by the crossbar and the column (attached to the tips of the blades), acts as the moving end of a vertical spring suspending the lower load through a wire. This wire is also attached as close as

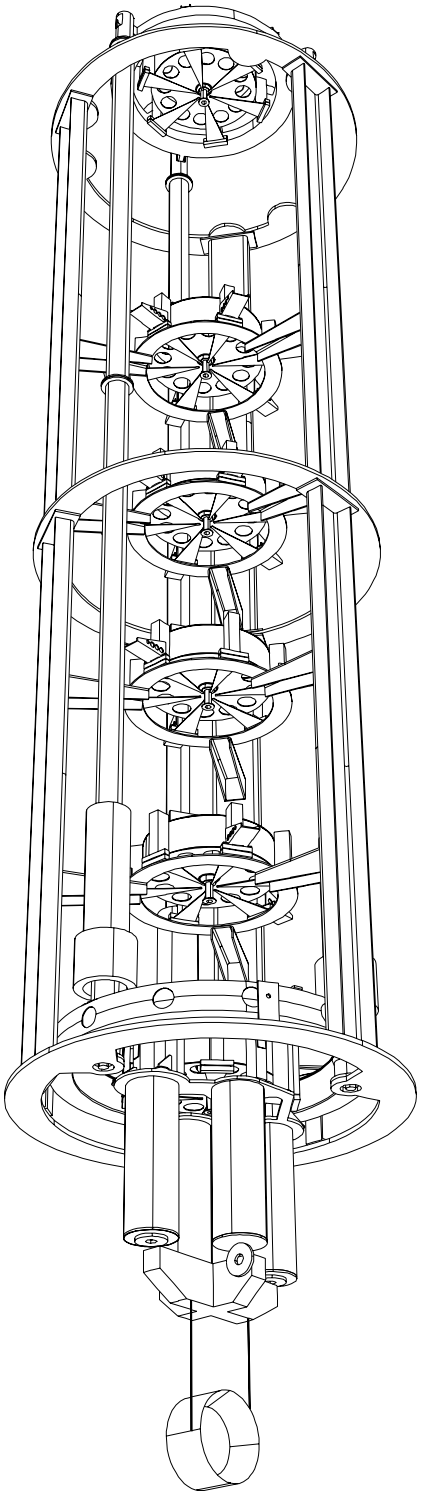

Figure 4.2: The superattenuator with the 6 m inverted pendulum pre-attenuator stage (see chapter 5). From the top to the bottom one can see the filter 0, 4 standard filters the steering filter (with its "legs"), the marionetta and the mirror.

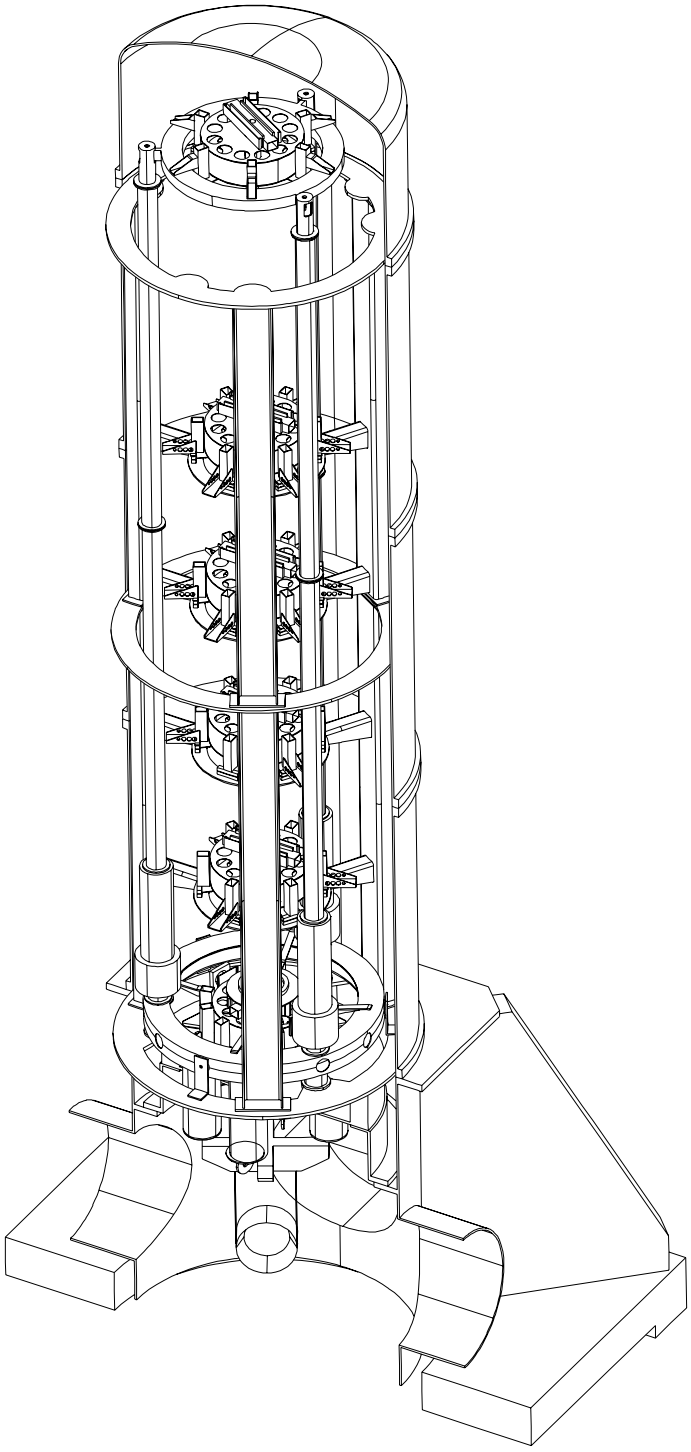

Figure 4.3: View of the SA inside its vacuum chamber.

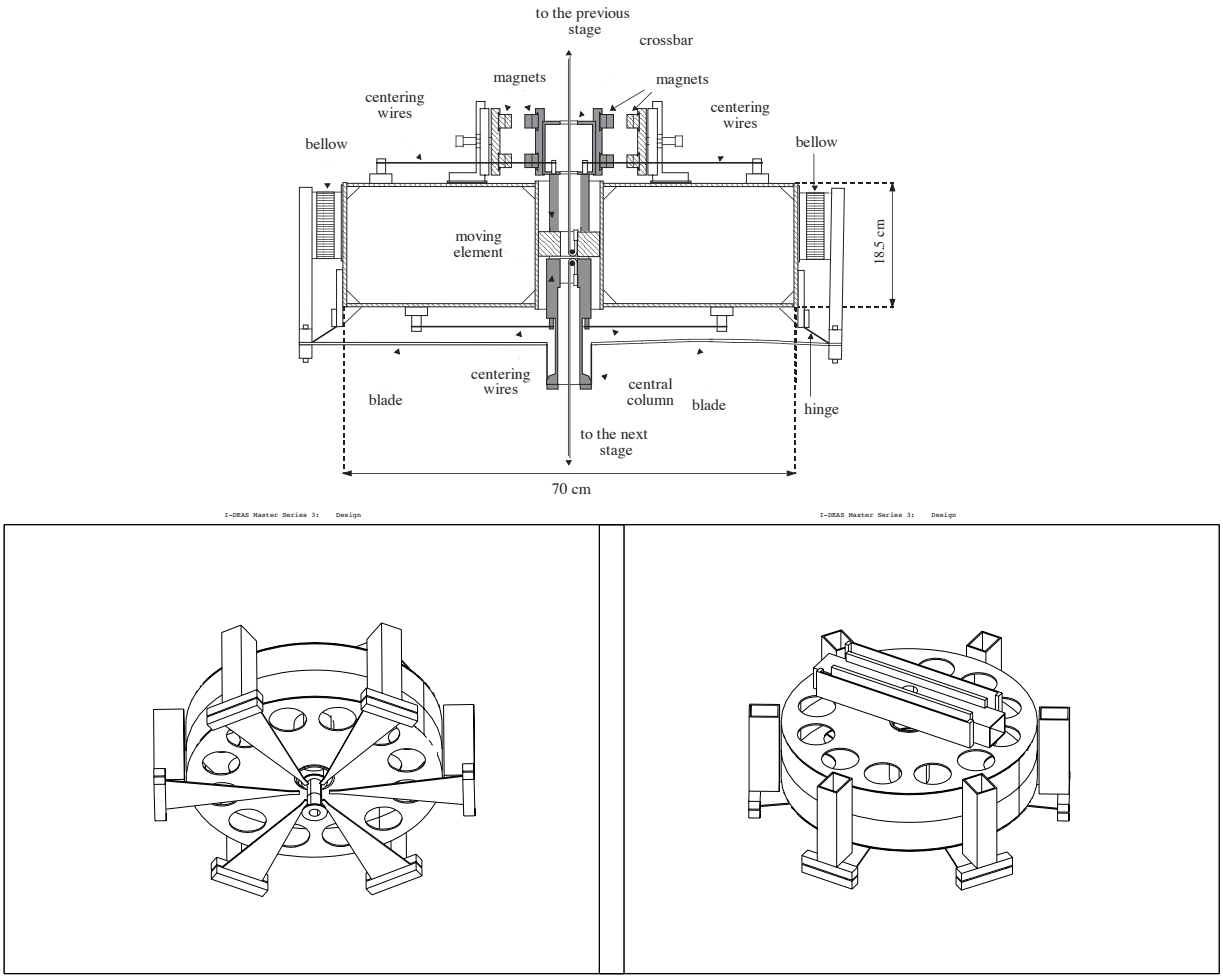

Figure 4.4: Standard filter: a) side view: the elements in grey can move with respect to the filter main body. In the actual design the bellows shown in the figure have been replaced by screws; b) bottom view; c) top view.

possible to the filter centre of mass. The minimum distance of the two points, of the upper and the lower wires allowed by the filter design is 10 mm. The resulting rocking frequency is below 1 Hz.

Once loaded, a filter has a *mechanical* vertical resonance frequency of 1.4 Hz, depending on the stiffness k_s of the blade springs and on the supported load. A magnetic antispring system has been designed to reduce that frequency to 0.4 Hz [75]. The crossbar supports two back-to-back arrays of magnets (fig. 4.2 (c)). Two similar arrays are fixed on the filter body facing the moving ones in a repulsive configuration. When the four magnetic arrays are exactly vertically aligned, the repulsive forces are purely horizontal and add up vectorially to zero. When the moving magnets (fixed on the crossbar) are vertically displaced by a small amount δy, a vertical *antispring* like force appears (fig. 4.5):

$$F_{\mathrm{as}} = k_{\mathrm{as}} \cdot \delta y$$

where k_{as} can be tuned to the desired value by changing the distance between the magnetic arrays. A vertical *antispring* of stiffness k_{as} effectively acts in parallel with the blade spring. The overall stiffness is thus reduced:

$$k = k_s - k_{\mathrm{as}}$$

that is, the vertical spring is softened (without altering its loaded working point) and the vertical frequency lowered. The antispring stiffness depends on the number of magnets and on the separation between them, which can be tuned to reach the desired strength and frequency. Moreover, a thermal dependence

$$\frac{1}{k_{\mathrm{as}}}\frac{\partial k_{\mathrm{as}}}{\partial T} = 0.004\ ^{\circ}\mathrm{C}^{-1} \tag{4.1}$$

has been measured [76], causing a variation of the vertical resonance frequency of the single filter of

$$\frac{\partial f_0}{\partial T} = 15 \pm 2\ \frac{\mathrm{mHz}}{^{\circ}\mathrm{C}} \tag{4.2}$$

at the working frequency of 0.4 Hz. Moreover, the relative vertical position of the tip of the blades and the body of the filter changes of about 300 μm/°C. Therefore, to keep the system under reasonable stability conditions a thermostabilisation of 0.2 °C is required [78, 79].

To tune the vertical position of the moving part of the filter with respect to the main body, the inclination of some of the blades can be manually changed by setting screws. This manual system allows the tuning of the filter working point (the suspended load vertical position) with a precision of 0.1 mm. A remote control fine tuning system of the vertical position (with the precision of less than 1 μm and a range of 1 mm) is obtained by a "soft" cantilever blade (acting in parallel with the main suspension blades), whose inclination can be changed by a motor. The soft spring pulls on the crossbar by means of

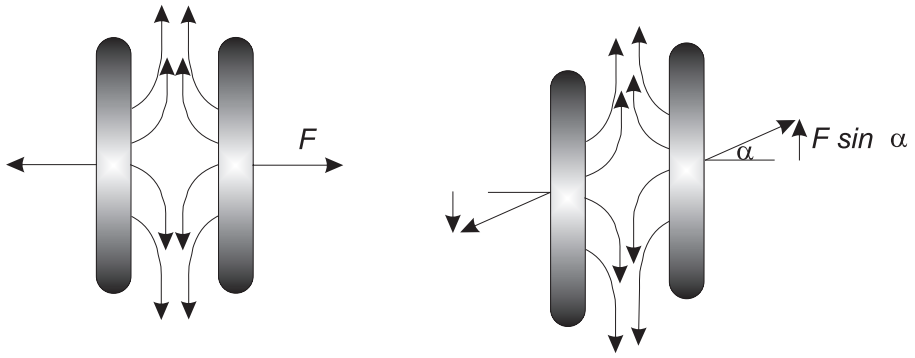

Figure 4.5: Magnetic antispring: working principle.

a wire, like a *fishing rod*, from which the name of this device. A LVDT sensor[2] measures the vertical displacement between the crossbar and the filter body: it provides diagnostics for the filter performance and the feedback signal for the fishing rod. The motor will be always switched off during the data taking: the filters will be operated as *fully passive attenuators*.

4.2.1 Filter attenuation performance

The major limitations to the filter attenuation performance come from the normal modes of its internal parts, mainly the crossbar (around 50 Hz) and the blades (above 100 Hz), and from the moment of inertia of the blades itself. In fig. 4.6 a vertical transfer function of one of the filter of the prototype SA chain is shown.

The overall effect of the resonances on the SA performance is visible in the calculated SA transfer function shown in fig. 4.9.

4.3 The controllable parts of the SA

A chain of 6 filters would fulfil the requirements on the passive attenuation of the seismic noise. In this section we describe the parts of the SA specifically designed for the control of the mirror position: the inverted pendulum top stage, the steering filter, the *marionetta*, the reference mass. In section 8.2 the role of each of these parts in the control of the superattenuator is described.

[2] An LVDT (Linear Variable Differential Transformer) is a displacement-to voltage transducer made of two coaxial coils. The *primary* coil is fed by a sinusoidal voltage and induces in the *secondary coil* a voltage with the same frequency whose amplitude is proportional to the coils relative displacement. The typical sensitivity of the LVDT used on the SA is about 10^{-9} m/$\sqrt{\text{Hz}}$.

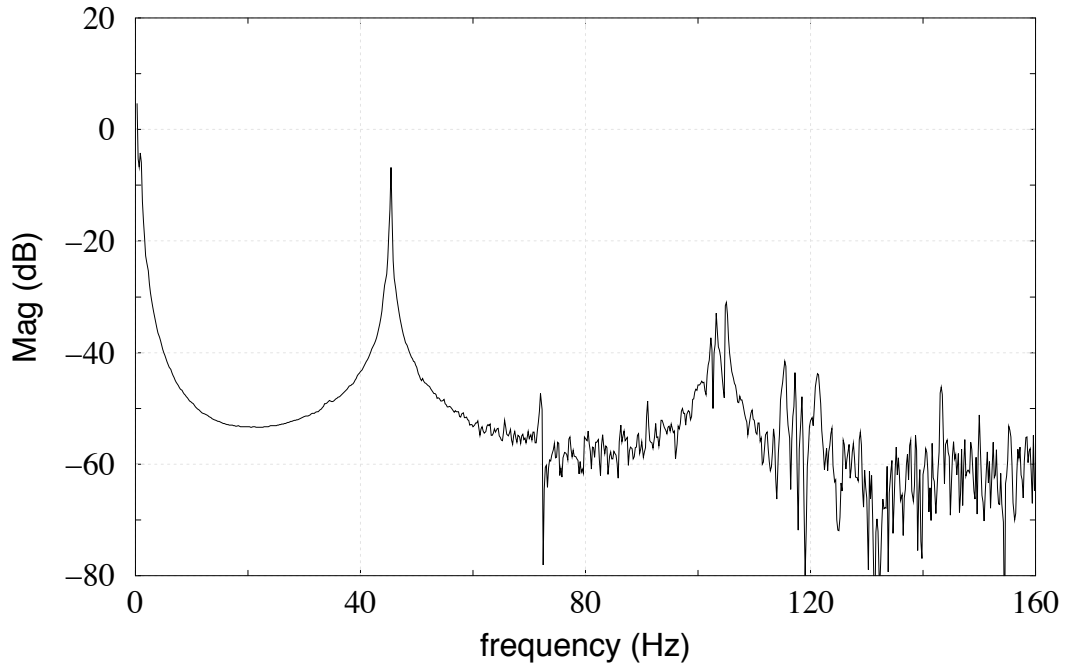

Figure 4.6: Vertical transfer function of a filter: the attenuation is larger than 40 dB between 5 and 42 Hz, with a maximum of 53 dB. The attenuation performance above 40 Hz is limited by the resonance modes of the crossbar (45 Hz) and the blades (above 100 Hz).

4.3.1 Top stage

The top stage is composed of two main parts: a 6 m high, three legged Inverted Pendulum (IP) supporting a modified filter, called *filter 0*.

The IP fulfils three main functions:

- to provide the SA with a suspension point positioning system;
- to introduce a very low frequency (30 mHz) horizontal filtering stage, reducing the SA resonant modes excitation levels and improving the overall SA attenuation performance;
- to provide a soft suspension stage at the top of the chain to allow active mode damping and seismic noise depression by means of inertial sensors and electromagnetic actuators.

The IP is the main subject of this thesis and will be described in details in the next chapter. The *filter 0* is a modified filter, designed to fulfil two main tasks:

- to provide in the vertical direction all the functions fulfilled in the horizontal plane by the IP;
- to support all the sensors and the actuators necessary for the active control of the SA.

The main differences between the filter 0 and a standard filter are:

- the presence of a hoist capable of changing the vertical position of the whole chain of ± 35 mm;
- the presence of a coil-magnet actuator acting between the main body and the cross-bar, designed for the active control of the SA vertical position;
- larger magnet arrays are used as antisprings, allowing to operate the filter at lower vertical frequency;
- a larger structure supporting two angular, three horizontal accelerometer and horizontal actuators for the SA active control.

4.3.2 Steering filter (filter 7)

The last filter of the chain is commonly called the *filter 7* [3] (see fig. 4.7). It is basically and functionally a standard filter but it is additionally provided with devices to fulfill additional functions:

- to exert forces and torques on the *marionetta*, to maintain it and the mirror in the required position. Four columns about 1 m long extend from the bottom of the filter in a parallelogram configuration. These columns support driving coils, facing small magnets fixed on the marionetta arms: forces and torques are obtained driving the coils with proper currents;
- to allow its own levelling: filter 7 must work horizontally to minimise the vertical-horizontal coupling factor close to the mirror. A balancing system, consisting of a remotely positionable mass which acts as a counterweight, is placed on the top of the filter body. The position of the mass is adjusted in the x, y directions by means of stepping motors;
- to allow its own precision remote control angular positioning against the mirror chamber roof. A *separating roof* lays between the filter 7 and the marionetta to maintain the differential vacuum existing between the tower and the pipe. The separating roof is provided with 4 pots housing the filter 7 legs. The right angular

[3] Actually this is the 5th filter of the chain. The name "filter 7" comes from the former SA design with 7 filters.

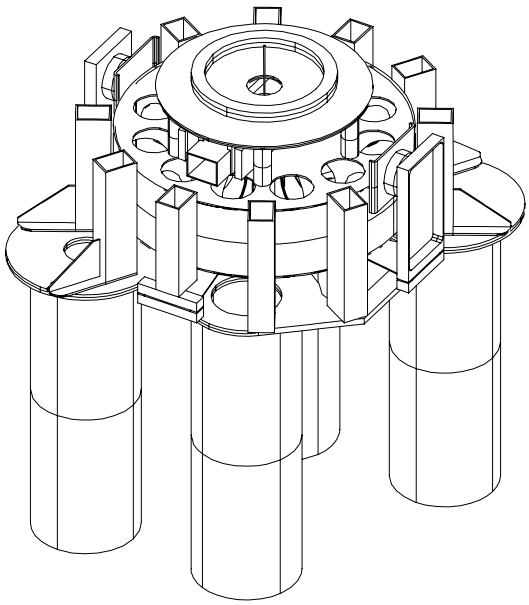

Figure 4.7: View of filter 7, with the balancing mass over the crossbar and the "legs".

positioning of the legs in the pots is allowed by means of ceramic ball bearings and controlled by a motorised set screw which rotate the filter 7 with respect to its suspension wire;

- to allow the pre-alignment of the marionetta with respect of the beam direction, by means of a second set of ceramic ball bearings and motorised set screws.

All the motors will be switched off during data taking: filter 7 will work passively, except for the continuous electromagnetic control of the marionetta.

4.3.3 Marionetta

The *marionetta* is the final stage supporting the mirror. It has been designed to steer and align the optical components for the interferometer locking. It is essentially an horizontal cross structure provided with two steel wire loops holding the mirror (see fig. 4.8), and two more which hold the *reference mass*. The marionetta arms are tipped with magnets, through which forces can be applied from filter 7. These forces allow fine control of the mirror on the three relevant degrees of freedom: the mirror rotations around its horizontal and vertical axes and the translation along the beam direction.

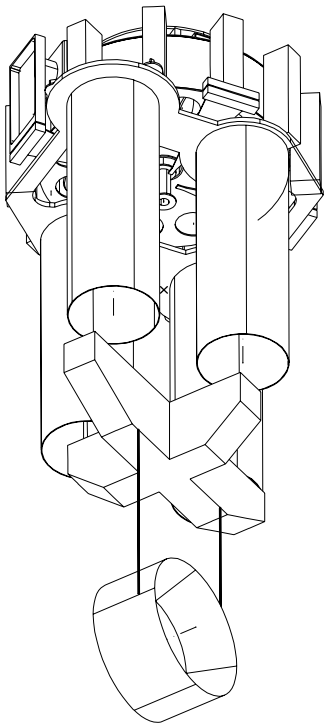

Figure 4.8: View of the marionetta-mirror system suspended from the filter 7. The mirror is surrounded by the reference mass. The coils (not shown in the figure) are supported by the "legs" of filter 7.

4.3.4 Reference mass-mirror

The mirror is the main optical component of the interferometer. The mirrors must be controlled along the beam direction with an accuracy of 10^{-18} m/$\sqrt{\text{Hz}}$ at 10 Hz, without generating vibrations or reinjecting seismic noise. Small AC corrections may be applied directly on the mirror from a *reference mass* (which surrounds the mirror as shown in fig. 4.8) which is itself suspended to the SA, and, like the mirror, is seismic noise free. The mirror is provided with four small permanent magnets in a parallelogram configuration. Four coils are mounted on the reference mass facing the four mirror magnets. The reference mass may be made of dielectric material in order to avoid Foucault current dissipation, that would increase the thermal noise on the mirror[4].

[4]In principle the reference mass is not necessary to control the interferometer: the filter 7-marionetta system has the required dynamics to achieve and maintain the locking, with the drawback of a larger excitation of the wire violin modes. The tests on the central interferometer will allow to decide whether it is possible to eliminate the reference mass from the system, thus achieving a simplification of the design.

4.4 Towers

The entire SA is contained into a tall vacuum chamber commonly called *tower*, thermostabilised to 0.2 °C and with a vacuum of 10^{-6} mbar. This vacuum level is 3 order of magnitude higher than the one required in the pipe. In the SA tower that level cannot be achieved, mainly because of the outgassing of the cables. Thus, a *separating roof* is placed between the filter 7 and the marionetta to maintain the differential vacuum. Two section of tube in the centre of the separating roof, 2 cm in diameter, allows the wire connecting the filter 7 and the marionetta to pass through.

Inside the tower a steel safety structure surround the SA. The structure supports safety shelves able to prevent the fall of filters in case of a wire breakdown. Moreover, the structure provides an external reference frame for the displacement sensors and the actuators of the SA top stage.

4.5 Sensors and actuators

Many adjustments are necessary to properly tune up all the SA degrees of freedom and to set the SA in the correct operation status. Thus, a set of sensors and actuators capable to monitor and control all the relevant internal d.o.f. has been designed. Moreover, the locking of the interferometer is performed by continuous actuation on three different points along the superattenuator (see section 8.2). More sensors and actuators are then foreseen, playing a direct role in the locking strategy.

We give here a schematic description of the SA read-out/adjustment system (a more detailed one concerning the sensors and actuators used for the SA active control will be the subject of chapter 6):

STATIC ADJUSTEMENTS These are the actuators used to set the SA in the correct working position. They are all motor driven and are to be switched off during data taking:

- **vertical position adjustment**:
  1. hoist on the filter 0: allows to lift the whole chain by ±35 mm. The error signal is provided by a CCD camera monitoring the mirror position;
  2. fishing rods on all filters: allows to adjust the vertical working point position of each filter in a range of a few mm and with an accuracy of less than 1 μm. The error signal is provided by the LVDT mounted on each filter;
- **horizontal position adjustment**: motor driven springs on filter 0 allow to horizontally translate and to rotate the filter 0 and then, to position the mirror (see chapters 6,8);
- **filter 7-marionetta relative position adjustment**:

1. filter 7 levelling: two motors allow to translate a plate rolling over spheres in order to balance the filter and maintain it horizontal;
2. rotations: two motors steer two ball bearing supports which allow the filter 7 to rotate with respect to its suspending wire and to the marionetta.

DYNAMIC ADJUSTMENTS: these include all the sensors and actuators used for the active controls of the suspension:

- **sensors and actuators for damping and slow positioning**: the damping of the SA resonances and the low frequency mirror positioning is performed acting on the top stage. The top stage is provided with:
  1. 3 horizontal LVDT position sensors, set in triangular configuration on the filter 0 ring;
  2. 3 horizontal accelerometers, set in triangular configuration on the filter 0 ring;
  3. 2 angular accelerometers, set on the filter 0 top ring, used as well for the horizontal active control;
  4. 1 vertical accelerometer, set on the filter 0 crossbar;
  5. 3 horizontal coil-magnet actuators, acting on the top stage from the external frame;
  6. 1 vertical coil-magnet actuator, acting between the filter 0 main body and its crossbar.
- **sensors and actuators for tilt active control**:
  1. 2 angular accelerometer on the inverted pendulum base ring, used as sensor of seismic tilt noise;
  2. 3 PZTs inside the IP feet, used as actuators to actively keep the IP base horizontal.
- **actuators for locking the interferometer**:
  1. 4 coil-magnet actuators on the filter 7-marionetta, moving the mirror in x, θ_y, θ_z;
  2. 4 coil-magnet actuators on the mirror-reference mass, moving the mirror in x, θ_y, θ_z.

4.6 Long and short towers

The input bench, the end mirror of the mode cleaner and the detection bench will be suspended from a short version of the SA composed by a 2 m high inverted pendulum, the filter 0, the steering filter and a modified marionetta. The residual motion of these components generates only common mode effects with respect to the two arms and does

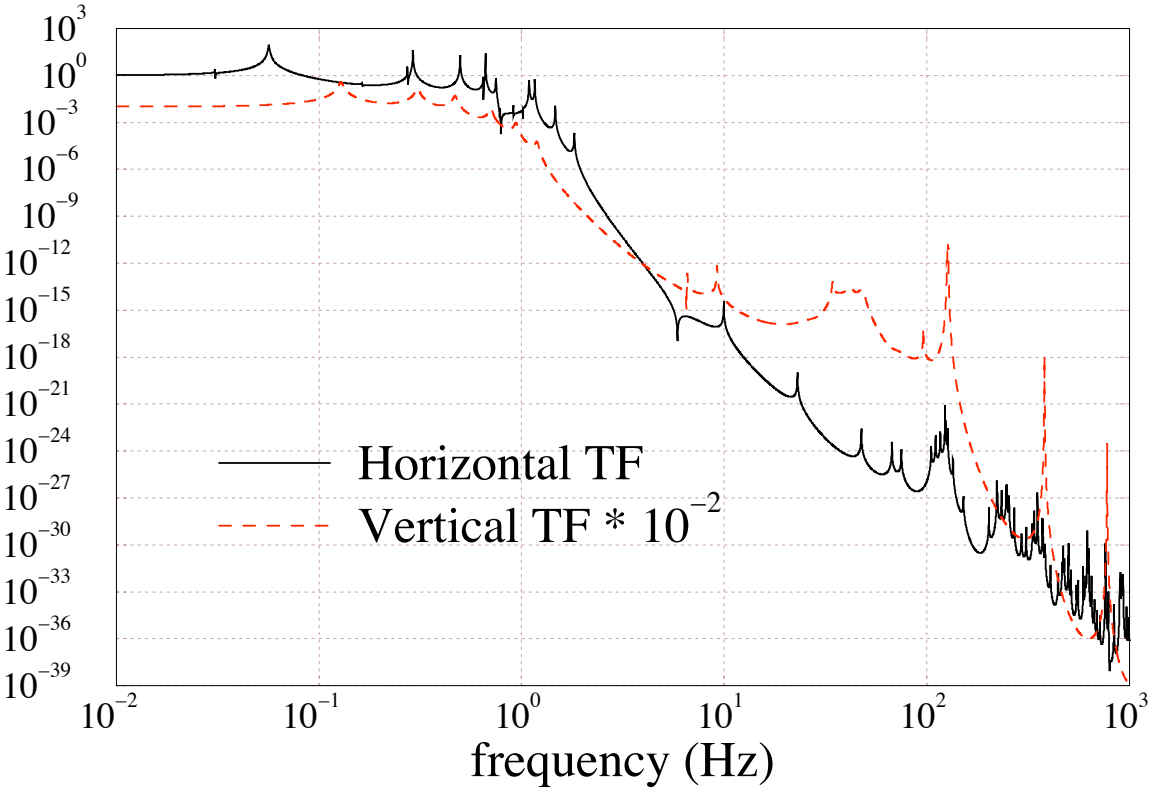

Figure 4.9: Simulated SA transfer function. A vertical-horizontal coupling factor $\alpha_{\text{mech}} = 0.01$ has been assumed.

not affect the interferometer output. Therefore, the attenuation requirements are less strict.

4.7 Superattenuator expected performance

To conclude this chapter we show the expected performance of the SA as a result of a 6 d.o.f. simulation code: in fig. 4.9 the calculated SA transfer function is shown. In the simulation a vertical-horizontal coupling $\alpha_{\text{mech}} = 0.01$ is assumed, while the coupling of the beam directions with the others degrees are considered negligible. Above 10 Hz the attenuation performance is degraded by the blades resonances and moment of inertia: a *plateau* is found rather than a f^{-2N} behaviour. The SA fulfils completely its specifications. The plateau is in a range where the residual seismic noise is largely dominated by thermal noise, as shown in fig. 3.4. The seismic noise starts to be dominating at $f < f_{\text{min}} = 2$ Hz.

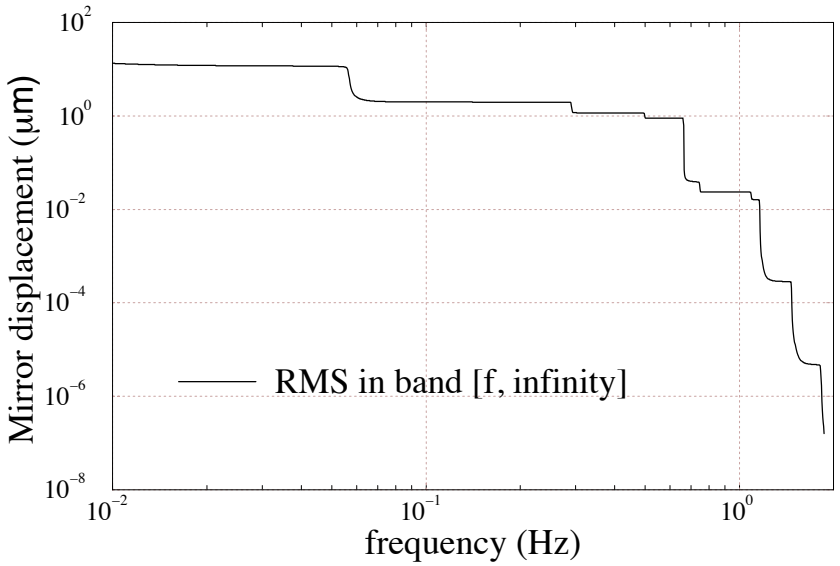

Figure 4.10: Integrated rms motion of the mirror as expected from the calculated SA transfer function of fig. 4.9.

We consider this as the *low frequency threshold* of the VIRGO detection band.

The seismic noise is attenuated by a huge factor above 10 Hz, but it is amplified at the resonances. This causes large resonant motions of the mirror. Fig. 4.10 shows that a root mean square motion of the mirror of tens of μm is expected at about 40 mHz[5]. Such a large seismic excited motion is not tolerable by the locking system and must be passively depressed (by means of the pre-isolator stage) and actively damped.

Non linear effects have been considered in the simulation [84]: fig. 4.11 shows that the effect of up-conversion associated to the quartic term of the antisprings potential is dominated by the linear behavior of the system.

A first measurement of the vertical transfer function of the SA has been done on the prototype chain now in construction at Pisa INFN laboratories [85, 86]. The measurement is shown in fig. 4.12 and has been performed without the filter 7 (only 5 out of 6 stages of vertical attenuation were present). An attenuation larger than 200 dB (10^{10}) has been achieved in the range 10-30 Hz.

[5]The exact value of this frequency depends on the inverted pendulum resonant frequency, as will be explained in the next chapters.

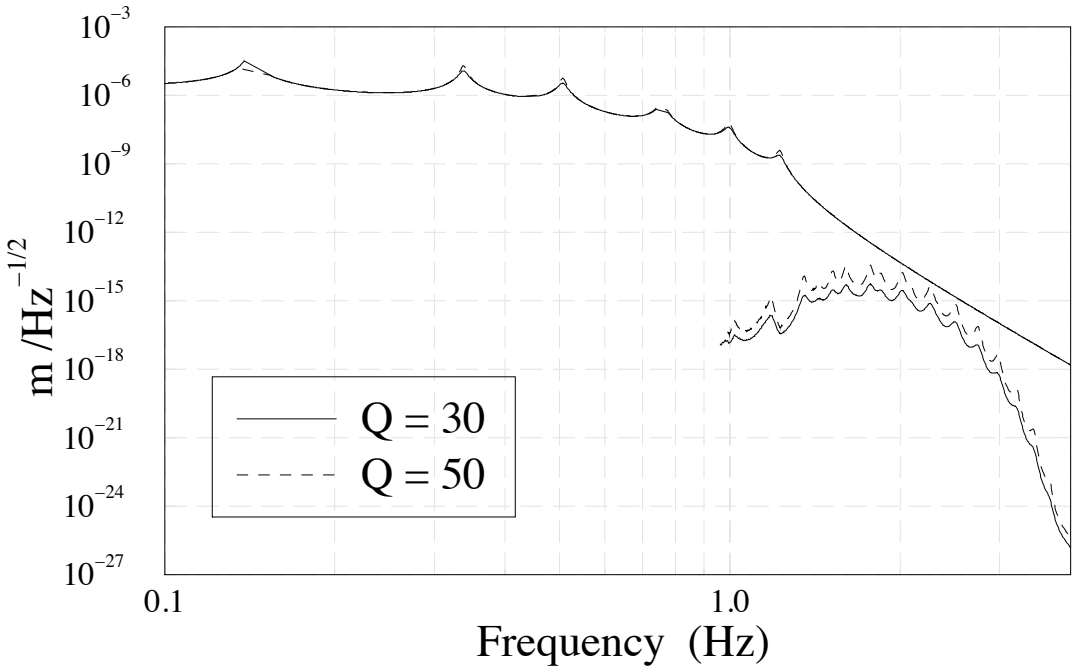

Figure 4.11: Effect of the antisprings nonlinearities on the SA vertical performance for two different values of the Q of the vertical resonance.

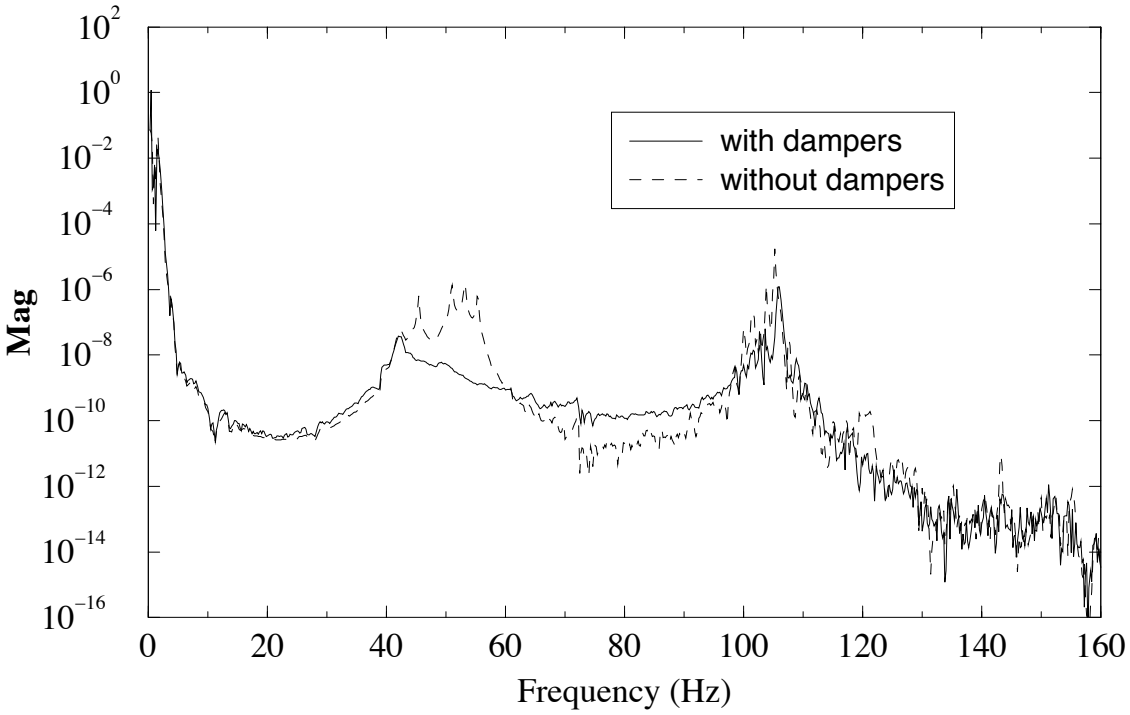

Figure 4.12: The vertical transfer function measured on the prototype SA chain without filter 7 (between filter 0 and filter 4). A maximum vertical-horizontal coupling factor of 0.01 is expected.

Chapter 5

The Inverted Pendulum Top Stage

5.1 The role of the superattenuator top stage

The performance of a multistage vibration isolator such as the SA depends on the frequencies of its normal modes. The physical length of the suspension limits the lowest resonant frequency achievable ($f_0 \sim \sqrt{g/l}$). The seismic motion of the suspension point is amplified at the resonant frequencies, leading to large resonant oscillations of the mirror. The suppression of these resonant motions requires active damping.

Various mechanical devices which mimic the behaviour of very long pendula, have been designed and tested with the purpose of using them as vibration isolators (see references [92]-[103])[1]

Many advantages are obtained when a standard multistage isolator is cascaded to an ultra-low frequency (ULF)[2] *pre-isolator* stage: the pre-isolation action can provide a large reduction of the intensity of the seismic noise driving the excitation of the chain normal modes. This turns into a smaller residual motion of the mirror and an easier locking of the interferometer. The very softness of an ULF stage makes it the ideal platform to apply the active resonance damping mentioned above. On the other hand, the ultra-low resonant frequency of the pre-isolator, being achieved by a small restoring force, makes possible to move the test mass over the long period range using gentle coil-magnet actuators with low power consumption.

The superattenuator chain will be suspended from a top stage which is itself a x, y, z, θ_z oscillator with a much lower resonant frequency (about 30 mHz) for the horizontal translation modes. The top stage is designed to act in both horizontal and vertical directions as a pre-isolator.

[1] An inverted pendulum pre-isolator had already been proposed for VIRGO in 1991 [92] and L.Holloway started working on a prototype at Urbana University. The results are unpublished.

[2] When speaking of vibration isolators the expression ULF refers to the frequencies from a few mHz to a few tens of mHz.

The top stage is composed by three rigid columns (legs) connected to ground through a flexible joint, supporting a top table. A modified filter (hereafter called *filter 0*) is placed on the top table and acts as a vertical preisolator. The 3-leg system is an *inverted pendulum* (IP). The two parts act in sequence: the IP attenuates the x, y, ϕ d.o.f., the filter 0 acts in z. The horizontal component of top stage for VIRGO SA is shown in fig. 5.1.

The design of the top stage presents several important aspects:

- it acts as a pre-isolator, introducing a resonant frequency f_0 at 30 mHz in the SA transfer function: as shown in (2.15), the coupling with seismic noise above the lowest resonant frequency f_0 is proportional to f_0^2. Reducing f_0 results into a reduction of the seismic excitation of the SA chain resonances: a 40 dB attenuation is expected at 300 mHz, close to the lowest chain resonances (see fig. 4.9);

- the inverted pendulum requires very low forces to be moved: at frequencies $f \ll f_0$ the force required to translate the load M of an amount x is:

$$F \approx M\omega_0^2 x \tag{5.1}$$

  Thus, only 0.4 N are required to translate 1 ton by 1 cm. Soft and "silent" electromagnetic actuators can be used to control the suspension point and the mirror position in the range DC-100 mHz;

- the inertial damping of the SA resonances will be performed acting only on the top table;

- the predicted performance of the top stage allowed to design a SA with only 5 filters instead of 7 (former design).

5.1.1 Inverted pendulum: basic principles

To understand the basic dynamics of an inverted pendulum let us think of a simple ideal model: a load of mass M is supported by a massless rigid vertical rod of length l (see fig. 5.2), connected to ground by means of an elastic joint of angular stiffness κ. Let θ be the angle between the rod and the vertical. The equation of motion is:

$$I\ddot{\theta} = -\kappa\theta + Mgl\sin\theta \tag{5.2}$$

where I is the moment of inertia of the system with respect to the suspension point O, $N_{\rm el} = -\kappa\theta$ is the elastic torque and $N_{\rm grav} = Mgl\sin\theta$ is the gravity torque. In the small angle approximation the (5.2) is written:

$$I\ddot{\theta} = -\kappa_{\rm eff}\theta \tag{5.3}$$

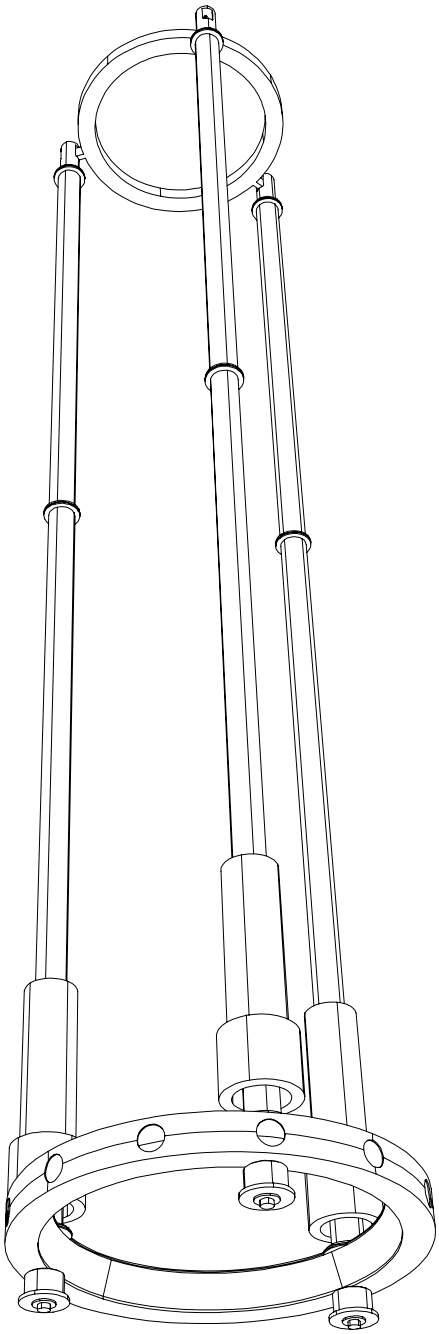

Figure 5.1: View of the VIRGO pre-isolator stage.

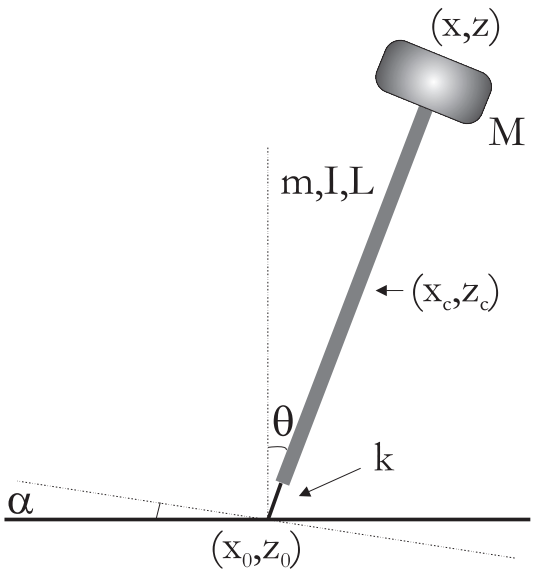

Figure 5.2: Schematic model of the inverted pendulum. When the rod mass and moment of inertia are negligible ($m, I \approx 0$) and $\alpha = 0$ the physics of the system is simply described by (5.2).

where:

$$\kappa_{\text{eff}} = \kappa - Mgl \tag{5.4}$$

is the *effective spring constant*: the gravity acts as an antispring, reducing the overall stiffness. The physics of the system is well described when looking at the potential energy:

$$U_{\text{pot}} = \frac{1}{2}\kappa\theta^2 + Mgl(\cos\theta - 1) \simeq \frac{1}{2}\kappa_{\text{eff}}\theta^2 + Mgl\frac{\theta^4}{4!} + O(\theta^6) \tag{5.5}$$

In the small angle approximation and for $\kappa > 0$ the quadratic term of the potential dominates and the system is a simple oscillator. By reducing the value of κ the potential "flattens" around $\theta = 0$ and this corresponds to small restoring force and small resonant frequency. When $\kappa_{\text{eff}} \approx 0$ the quartic term dominates at small angles (see fig. 5.3). When the gravity starts dominating ($\kappa_{\text{eff}} \lesssim 0$) $\theta = 0$ is no more a point of stable equilibrium: $U(\theta)$ has two minima at

$$\theta = \pm\sqrt{12\frac{-\kappa_{\text{eff}}}{Mgl}} \tag{5.6}$$

When $\kappa_{\text{eff}} \ll 0$ the potential is always negative and the system is unstable.

In the following, rather than using the angle θ we will refer to the IP linear displacement x measured at its top ($x = l\theta$) and to the linear stiffness $k = \kappa/l^2$. The equation of motion

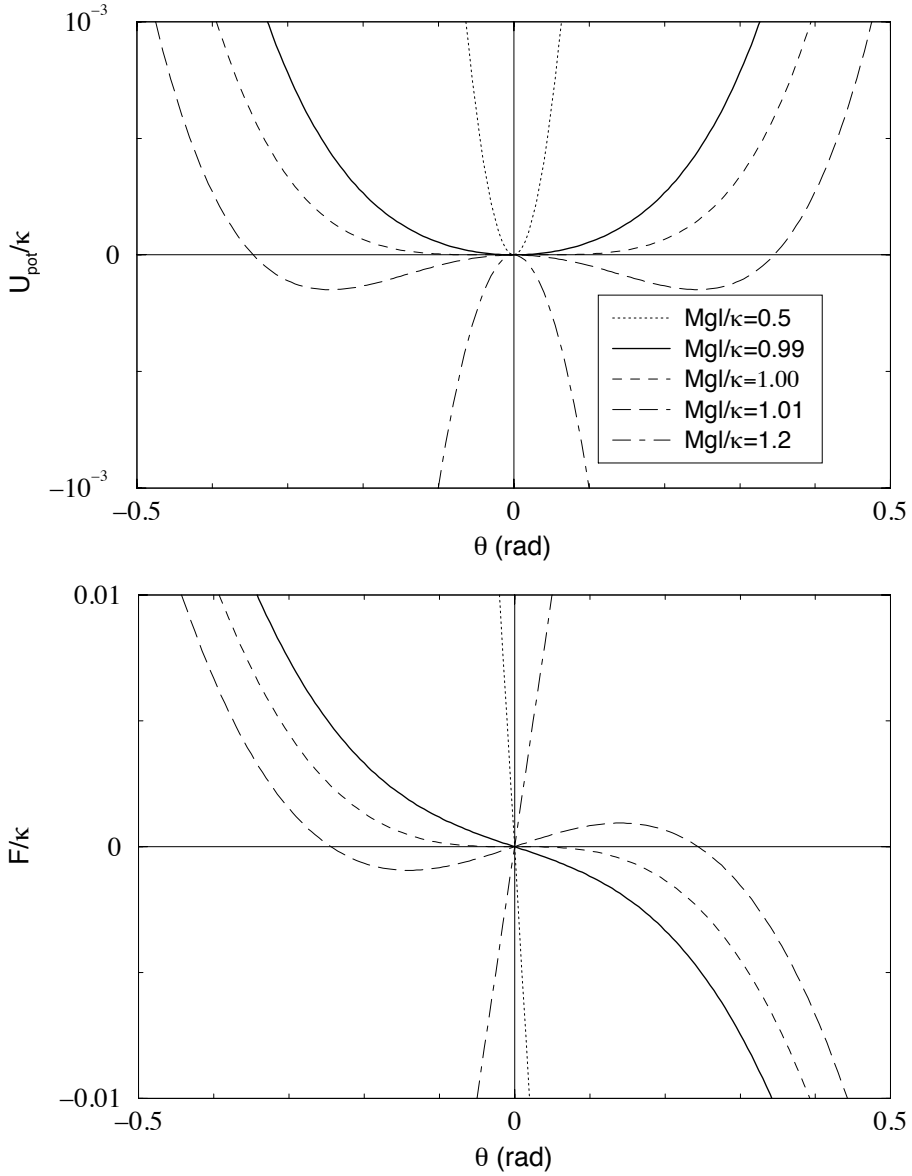

Figure 5.3: The reduced potential energy $U_{\rm pot}/\kappa$ is plotted for different values of the *gravity-elastic ratio* $R_{\rm ge} = Mgl/\kappa$: for $R \ll 1$ the system is far from instability, but the force dependence on θ is steep (high resonant frequency); for $R \lesssim 1$ the IP is still stable and a low resonance frequency is achieved; for $R = 1$ the restoring force around $\theta = 0$ is null; For $R \gtrsim 1$ the system becomes bi-stable; for $R \gg 1$ there is not any equilibrium position and the IP collapses.

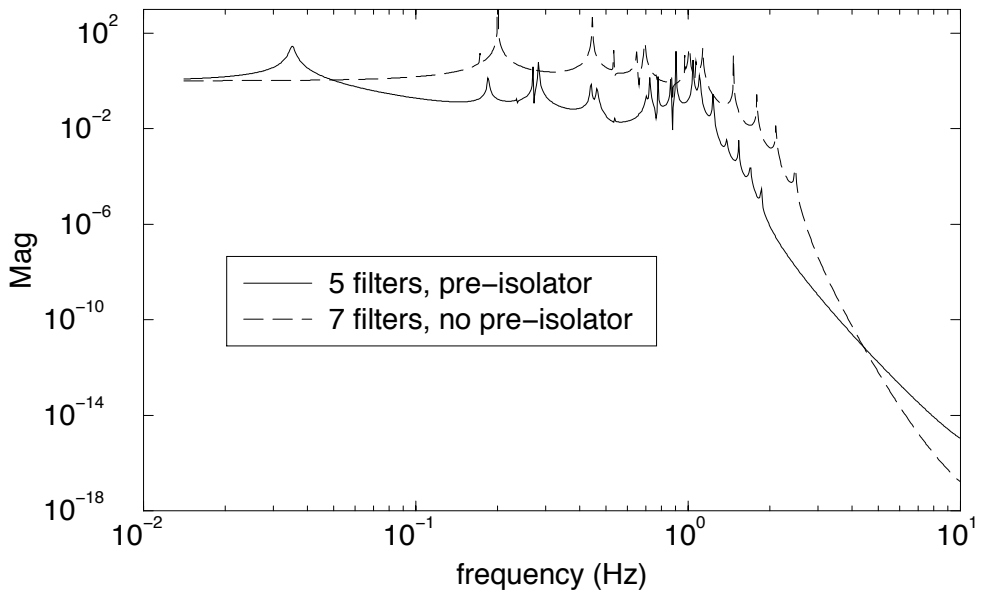

Figure 5.4: Calculated transfer function for a SA with 7 filters and no pre-isolator (former design) and the new SA with 5 filters and the pre-isolator stage (IP and filter 0).

for the variable x and for small displacements is written:

$$M\ddot{x} = -(k - \frac{Mg}{l})x + O(x^3) = \tilde{k}x + O(x^3) \tag{5.7}$$

When $\tilde{k} > 0$, the system is an oscillator resonating at frequency:

$$f_0 = \frac{1}{2\pi}\sqrt{\frac{k}{M} - \frac{g}{l}} \tag{5.8}$$

In principle, by properly tuning the spring stiffness and the suspended load one can obtain an arbitrarily small resonant frequency. Actually, in real mechanical systems, the frequency cannot be made arbitrarily small and still preserve the stability of the inverted pendulum[3]. The target frequency of 30 mHz seems to be an achievable compromise between the attenuation performance and the necessity of safe stability margin. fig. 5.4 shows the effect of the inverted pendulum on the attenuation performance of the SA: it introduces a double pole in the transfer function at 30 mHz, thus providing $1/f^2$ pre-attenuation starting at its resonance frequency. The lower the IP frequency the stronger is the pre-isolation effect[4]. With $f_0 = 30$ mHz, the passive pre-isolation factor at the frequency of the first mode of the chain ($f \sim 0.2$ Hz) is about 10.

[3]Without an adequate safety margin events such as random tilts and thermal drifts, can drive the system to instability.

[4]Naively one could think to design a longer superattenuator chain without the IP pre-isolator. It's

5.2 Theory of inverted pendulum

To understand the details of IP motion (see fig. 5.2) we write down the lagrangian $\mathcal{L}$ of the IP, including the effect of the leg mass and moment of inertia. We also consider the effect of the seismic tilt of the ground: let $\alpha(t)$ be the angle of the soil with respect to the horizontal axis as a function of the time. Let us name m the leg mass and J its moment of inertia with respect to its centre of mass (c.o.m.) C. Let (x, z) be the coordinates of the suspended mass (top of IP), (x_c, z_c) the coordinates of the leg c.o.m., x_0 the horizontal coordinate of the suspension point, α the soil tilt with respect to $\hat{x}$ axis, θ the leg angular displacement with respect to $\hat{z}$ axis. Let k be the linear stiffness of the elastic joint (defined to provide a restoring force $F_{\rm el} = -k \cdot \delta x$ when the top is displaced by an amount δx). We neglect the vertical seismic motion, which is completely transmitted to the top up to very high frequencies and then attenuated by the filter 0.

The lagrangian is:

$$\mathcal{L} = \frac{1}{2}M\dot{x}^2 + \frac{1}{2}m\dot{x_c}^2 + \frac{1}{2}J\dot{\theta}^2 - Mgz - mgz_c - \frac{1}{2}kl^2\left(\theta - \alpha(t)\right)^2 \tag{5.9}$$

For a uniform leg and for small oscillations we can write:

$$\begin{aligned} x_c &= \frac{1}{2}(x + x_0) \\ z_c &\simeq \frac{l}{2}(1 - \frac{1}{2}\theta^2) \\ z &\simeq l(1 - \frac{1}{2}\theta^2) \\ \theta &\simeq \frac{x - x_0}{l} \end{aligned}$$

Eq. (5.9) then becomes:

$$\begin{aligned} \mathcal{L} &= \frac{1}{2}M\dot{x}^2 + \frac{1}{8}m(\dot{x} + \dot{x}_0)^2 + \frac{1}{2}\frac{J}{L^2}(\dot{x} - \dot{x}_0)^2 + \\ &+ \frac{1}{2}\frac{g}{l}\left[M + \frac{m}{2}\right](x - x_0)^2 - \frac{1}{2}k\left(x - x_0 - l\alpha\right)^2 \end{aligned} \tag{5.10}$$

5.2.1 Equation of horizontal motion

The equation of motion derives from

$$\frac{\mathrm{d}}{\mathrm{d}t}\frac{\partial \mathcal{L}}{\partial \dot{x}} - \frac{\partial \mathcal{L}}{\partial x} = 0 \tag{5.11}$$

straightforward to calculate the length of such a chain to reach a first mode frequency $f_0 \approx 30$ mHz:

$$l = \frac{g}{(2\pi f_0)^2} \approx 276\ m.$$

.

that is:

$$\left[M+\frac{m}{4}+\frac{J}{l^2}\right]\ddot{x}+\left[\frac{m}{4}-\frac{J}{l^2}\right]\ddot{x}_0-\frac{g}{l}\left[M+\frac{m}{2}\right](x-x_0)+k(x-x_0-l\alpha)=0 \tag{5.12}$$

The (5.12) is immediately solved in the frequency domain:

$$\boxed{x(\omega)=\frac{1}{[\omega_0^2-\omega^2]}\left\{[\omega_0^2+\beta\omega^2]x_0(\omega)+y\alpha\right\}} \tag{5.13}$$

where:

$$\omega_0^2 = \frac{k-(M+\frac{m}{2})\frac{g}{l}}{M+\frac{m}{4}+\frac{J}{l^2}} \tag{5.14}$$

$$\beta = \frac{\frac{m}{4}-\frac{J}{l^2}}{M+\frac{m}{4}+\frac{J}{l^2}} \tag{5.15}$$

$$y = \frac{kl}{M+\frac{m}{4}+\frac{J}{l^2}} \tag{5.16}$$

Approximating the leg to a uniform beam (below its own resonant frequency) one has:

$$J=\frac{1}{12}ml^2 \tag{5.17}$$

and the previous equations simplify:

$$\omega_0^2 = \frac{k-(M+\frac{m}{2})\frac{g}{l}}{M+\frac{m}{3}}=\frac{k-A}{D} \tag{5.18}$$

$$\beta = \frac{\frac{m}{6}}{M+\frac{m}{3}}=\frac{C}{D} \tag{5.19}$$

$$y = \frac{kl}{M+\frac{m}{3}}=\frac{kl}{D} \tag{5.20}$$

To plot the transfer function (5.13) one has to eliminate the singularity at $\omega=\omega_0$, keeping into account the dissipation in the system. The main source of dissipation is the internal friction, which can be described [89, 80] replacing the stiffness k with the complex stiffness:

$$k \to k(1+i\phi(\omega)) \tag{5.21}$$

The factor ϕ is assumed to be constant over a wide range of frequencies ($\phi(\omega)=\phi$, see [5] and references therein, [100]) and its value depends on the material. Then in (5.13) the (5.18) and the (5.20) must be replaced by the new expressions:

$$\begin{cases} \omega_0 \to \omega_0+i(\phi k/D) \\ y \to y(1+i\phi) \end{cases} \tag{5.22}$$

The effect of tilt will be studied in section 5.4. For the time being the term $y\alpha$ in eq. (5.13) will be considered negligible.

5.3 The centre of percussion effect

Equation (5.13) is, in some way, surprising: at frequencies $f \gg f_0/\sqrt{\beta}$, the spectral motion of the top is:

$$x(\omega) \approx -\beta x_0(\omega). \tag{5.23}$$

There is a critical frequency $f_c = f_0/\sqrt{\beta}$ above which the transfer function $x(\omega)/x_0(\omega)$ flattens and the IP does not behave as an attenuator anymore. Including the effects of dissipation and neglecting the effect of tilt the (5.13) is written:

$$\frac{x(\omega)}{x_0(\omega)} = \frac{\omega_0^2 + \beta\omega^2 + i(k\phi/D)}{\omega_0^2 - \omega^2 + i(k\phi/D)} \tag{5.24}$$

In fig. 5.5 the transfer function (5.24) is calculated using the actual values of the parameters foreseen for the IP final design[5] and plotted for 3 different values of β. The presence of the $\beta\omega^2$ term in the (5.13) is associated to the *center of percussion* effect: when the base of the leg is shaken by translation seism at "high" frequencies ($\omega \gg \omega_0/\sqrt{\beta}$) the leg rotates around a "center of percussion" which remains still. Therefore, the leg top countershakes[6] of an amount depending on β (as shown in eq. (5.23).

From (5.23) it appears that, for the correct operation of the superattenuator stage, it is necessary to make $\beta = 0$ or small enough to push the critical frequency beyond all the other superattenuator resonances ($f_c \geq 5$ Hz). This is equivalent to setting the percussion point at $s = l$, that is to make P to coincide with the suspension point of the load or with the hinge point of the elastic joint. To make $\beta = 0$ there are three ways:

- to have massless legs ($m = 0 \Rightarrow \beta = 0$): unfeasible, but it is still useful to design legs as light as possible;
- to suspend the top table at the level of the percussion point: this would require an heavy leg segment sticking above the top table;
- to provide the legs with a *counterweight* below the elastic joint to move the percussion point at the height of the hinging point of the flexible joint.

5.3.1 The solution of the problem

The technical solution adopted is to have light aluminum legs and fit them with a counterweight below the elastic joint. The position of the percussion point along the leg depends

[5] $k = 740$ N/m, $M = 1260/3 = 420$ Kg (load per leg), $m = 30$ Kg, $l = 6$ m, $\phi \approx 10^{-3}$

[6] The center of percussion effect is well known to the baseball and cricket players: the batsman who does not hit the ball in the "sweet spot" of the bat hurts his wrist!

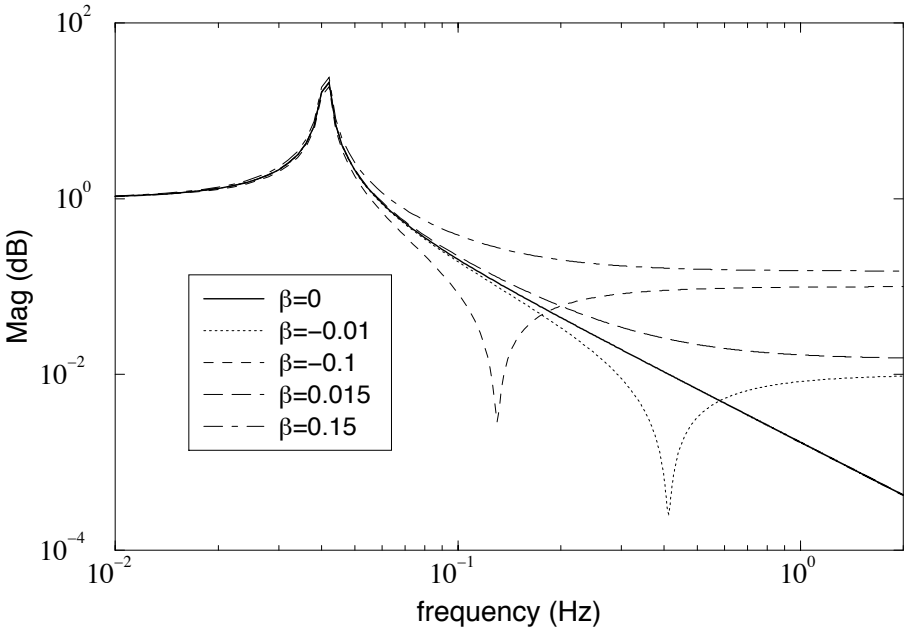

Figure 5.5: Inverted pendulum transfer function (5.24) calculated for different values of β: when $\beta = 0$ the transfer function is that of an ideal pendulum (no c.o.p. effect). When $\beta > 0$ the c.o.p. effect turns into a flattening of the transfer function. When $\beta < 0$ a dip is present, above which the transfer function flattens.

on the mass and the position of the counterweight, which both can be used to make P coincide with the desired position.

The new IP is shown in fig. 5.6: the counterweight is fixed below the IP flex point by means of a bell shaped structure. For the sake of simplicity we define the parameters in the following way:

- *masses*: let m_1 be the load mass, m_2 be the leg mass, m_3 be the bell mass and m_4 be the counterweight mass;

- *lengths*: let l_1 be the leg length, $l_2 = l_1/2$ be the distance of the leg c.o.m. from the suspension point. Analogously l_4 and $l_3 = l_4/2$ are defined (in the case of fig. 5.6 l_3 and l_4 are negative quantities);

- *momenta of inertia*: $J_1 = J_4 = 0$ (the load and the counterweight are considered as point masses), $J_{2/3} = m_{2/3} l_{1/4}^2/12$ (the leg and the beam are considered as thin rods).

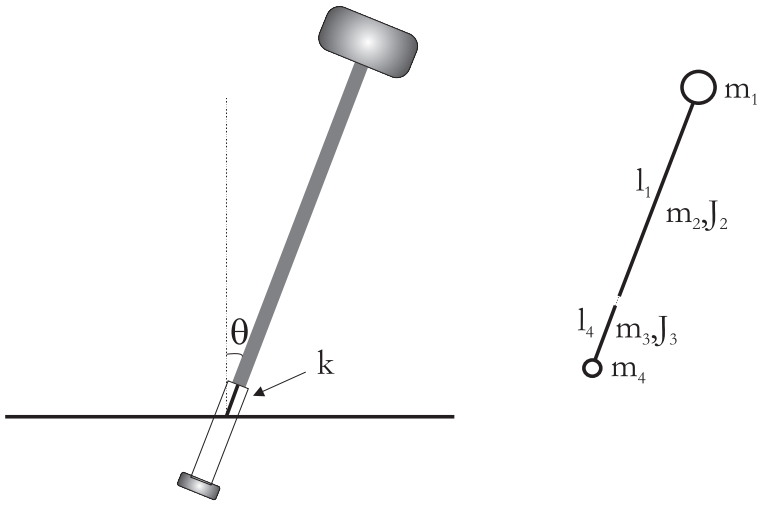

Figure 5.6: Schematic model of the inverted pendulum provided with a counterweight. Beside, the notation used in the calculation is shown.

It is useful to temporarily go back in θ units. The lagrangian is then written:

$$\mathcal{L} = \frac{1}{2}\sum_{i=1}^{4}\left[m_i\dot{x}_i^2 + J_i\dot{\theta}^2\right] - g\sum_i m_i z_i - \frac{1}{2}kl_1^2(\theta-\alpha)^2 \tag{5.25}$$

The coordinates are

$$x_i = x_0 + l_1\theta \tag{5.26}$$

$$z_i = l_i\left(1-\frac{1}{2}\theta^2\right) \tag{5.27}$$

The (5.25) can be written as a function of the variable θ:

$$\mathcal{L}(\theta,\dot{\theta}) = \frac{1}{2}\sum_i\left[m_i(\dot{x}_0^2 + l_i\dot{\theta})^2 + J_i\dot{\theta}^2\right] - g\sum_i m_i l_i\left(1-\frac{1}{2}\theta^2\right) - \frac{1}{2}kl_1^2(\theta-\alpha)^2 \tag{5.28}$$

The θ equation of motion is written:

$$\sum_i\left[m_i l_i(\ddot{x}_0 + l_i\ddot{\theta}) + J_i\ddot{\theta}\right] - g\sum_i m_i l_i\theta + kl_1^2(\theta-\alpha) \tag{5.29}$$

Solving (5.29) and remembering that

$$x_1(\omega) = x_0(\omega) + l_1\theta(\omega) \tag{5.30}$$

one finds the linear transfer function:

$$\boxed{x(\omega) = \frac{1}{[\Omega_0^2 - \omega^2]}\{[\Omega_0^2 + B\omega^2]x_0(\omega) + Y\alpha\}} \tag{5.31}$$

where:

$$\Omega_0^2 = \frac{kl_1^2 - g\sum_i m_i l_i}{I} \tag{5.32}$$

$$B = \frac{\sum_i [m_i l_i (l_1 - l_i) - J_i]}{I} \tag{5.33}$$

$$Y = \frac{kl_1^3}{I} \tag{5.34}$$

$$I = \sum_i \left[m_i l_i^2 + J_i\right] \tag{5.35}$$

The value of B can be tuned by changing the counterweight mass m_4 and its distance from the suspension point l_4. Equation (5.33) is useful to understand the physics and to estimate the value of the counterweight mass. For a precise calculation one should keep into account the details of the system, such as the legs non homogeneity and the distribution of the suspended mass. This was done with a finite element analysis which lead to the values of table 5.1.

5.4 The effect of tilt seismic motion

Let us now take into consideration the seismic tilt $\alpha(t)$. If $B = 0$ eq. (5.31) reduces to:

$$x(\omega) = \frac{1}{\Omega_0^2 - \omega^2}\left[\Omega_0^2 x_0(\omega) + Y\alpha(\omega)\right] \tag{5.36}$$

The seismic tilt is coupled with the horizontal motion of the IP top. To understand whether the effect of tilt can limit the performance of the pre-isolator stage, the two terms in square bracket have to be compared. The tilt dominates at frequencies where:

$$\alpha(\omega) > \frac{\Omega_0^2}{Y} x_0(\omega) \tag{5.37}$$

$\alpha(\omega)$ and $x_0(\omega)$ are measurable spectra (see fig. 2.5.1,5.9) correlated by the wave propagation speed in the soil. We can make some predictions about the behaviour of the tilt seism by using a simple model. Let P and Q be two points of the ground on the $\hat{x}$ axis, at distance δ (see fig. 5.7). A seismic wave, vertically polarised, propagates along the $\hat{x}$ axis

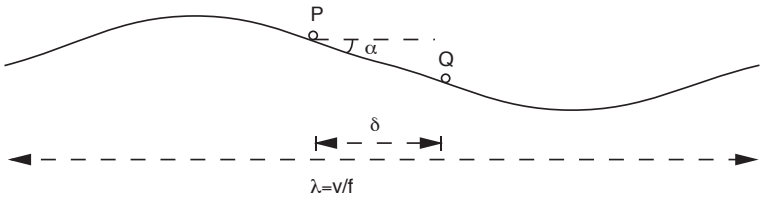

Figure 5.7: Tilt of the soil due to a monochromatic seismic wave of frequency f propagating with velocity v.

with speed v and frequency f (and wavelength $\lambda = v/f$). The surface vertical deformation of the ground due to the wave may be described by the profile:

$$y(x,t) = y_0 \sin\left(2\pi\frac{x}{\lambda} - \omega t\right) \tag{5.38}$$

At $t = t_0$ the tilt angle between P and Q is:

$$\alpha(t_0) \approx \frac{y(x_P,t_0) - y(x_Q,t_0)}{\delta} \overset{\delta \ll \lambda}{\longrightarrow} \frac{\partial y}{\partial x}(x,t_0) = -\frac{2\pi}{\lambda} y_0 \cos\left(2\pi\frac{x}{\lambda} - \omega t\right) \tag{5.39}$$

The spectral amplitude relationship between tilt and horizontal displacement is then:

$$\alpha(\omega) \approx \frac{2\pi}{\lambda} y_0(\omega) = \frac{\omega}{v} y_0(\omega) \tag{5.40}$$

The (5.40) is true when $\delta \ll \lambda$ that is at frequencies $f \ll v/\delta$. We are interested in the case where P and Q are two legs of the IP ($\delta \sim 1$ m). The value of v depends on the nature of the ground composition [81]: in hard rock $v \sim 3000$ m/s, while in sand $v \sim 500$ m/s. The laboratory is built on a sandy ground and we assume $v \sim 500$ m/s. With these values of v an δ the (5.40) holds true at frequencies $f \ll 500$ Hz, well beyond our range of interest.

Eq. (5.40) shows that the tilt seism is connected to the vertical seism $y_0(\omega)$. It has been measured that $x_0(\omega) \sim y_0(\omega)$ (the seismic noise is roughly isotropic). Then (5.37) reduces to:

$$f > f_t = \frac{1}{2\pi}\frac{\Omega_0^2}{Y} v \tag{5.41}$$

where we have defined a critical frequency f_t above which the tilt dominates the horizontal seism. At frequencies $f \gg f_t$:

$$x(\omega) \approx \frac{Y}{[\Omega_0^2 - \omega^2]}\alpha(\omega) \approx \frac{Y}{v}\frac{x_0(\omega)}{\omega} \tag{5.42}$$

that is, the IP ceases to attenuate with the usual $1/f^2$ law and its performance is reduced (see fig. 5.8). The effect is negligible if f_t is far beyond the SA resonances. In the case of VIRGO SA a value $f_t \sim 1$ Hz is expected (f_t depends on all the characteristics of IP mechanics and on the speed of seismic waves). Several uncertainties affect this prediction:

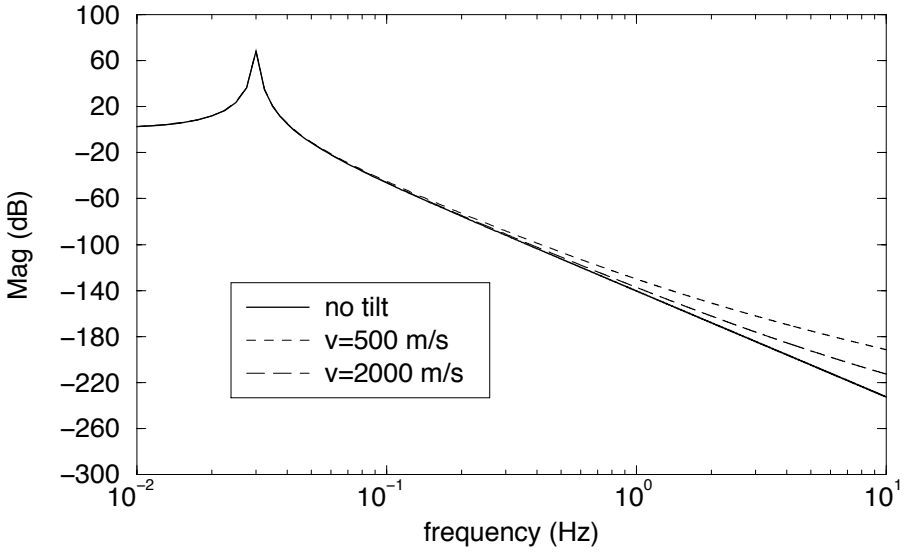

Figure 5.8: Effect of tilt on the IP performance: the transfer function magnitude (5.36) has been calculated for different values of the seismic waves speed in the ground.

- the model is too simple: the tilt is associated to horizontal waves propagating in one direction only. In a realistic model one should keep into account the contribution of the waves coming from every direction and adding incoherently. One expects these incoherent contribution to average and the resulting tilt to be less intense than that predicted from the simple one dimensional model;
- the velocity of the seismic waves is strongly dependent on the nature of the ground [81];
- the horizontal and the vertical seismic spectral densities have been assumed equal: actually we have measured intensities that can be different up to a factor 5.

If the effect of the tilt was relevant, it could be reduced by actively controlling the IP base: a rigid platform was introduced in the IP design as a base for the legs. The tilt of the platform would be sensed by angular accelerometer and, if necessary corrected by means of PZT actuators.

5.4.1 Estimate of the seismic waves speed

A custom made rotational accelerometer has been designed and realised to be used on the SA [54]. Such instrument has been used to perform a direct measurement of the tilt seismic noise. The result is shown in fig. 5.9.

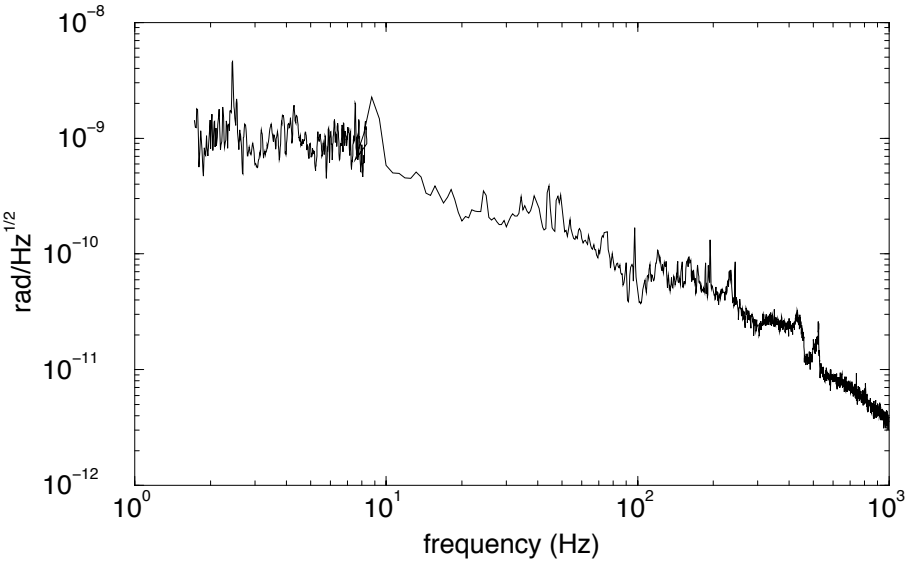

Figure 5.9: Tilt seism spectrum measured with an angular accelerometer.

From the measured spectrum it is possible to give an estimate of the *local* speed of seismic waves by using equations (2.16) and (5.40). The vertical seism is assumed to be equal to the horizontal one. Eq. (5.40) can be written as

$$\alpha_{\rm th}(\omega) \approx \frac{\omega}{v} x_0(\omega) = \frac{2\pi f}{v} \cdot \xi \cdot \frac{10^{-6}}{f^2} = \frac{2\pi\xi \cdot 10^{-6}}{v} \frac{1}{f} \tag{5.43}$$

where the factor ξ parametrizes the seismic activity intensity. From a fit of the data in fig. 5.9 one finds the experimental result:

$$\alpha_{\rm exp}(f) \sim \frac{4.6 \cdot 10^{-9}}{f} \ \ {\rm rad}/\sqrt{\rm Hz}$$

Thus, imposing

$$\alpha_{\rm th} = \alpha_{\rm exp}$$

one obtains

$$v \sim 1400 \cdot \xi \ {\rm m/s}$$

A mean value $\xi \sim 0.3 - 0.4$ has been measured in our laboratory [7]. The local speed of the seismic waves is then $v \sim 500$ m/s, as assumed earlier.

[7] To give a correct estimate of v one should have measured the vertical seism simultaneously to the tilt seism, in order to have the exact value of ξ. Unfortunately, at the moment when the measurement was performed the vertical accelerometers were not available. A complete measurement of seism (angular, vertical, horizontal) will soon be performed on the site where the detector is being built.

5.5 The IP quality factor

The main dissipation mechanism in the IP dynamics (at least during the operation under vacuum) is expected to be the structural damping. Long period pendulums have been used to study anelasticity [90] and, particularly, an inverted pendulum was studied by Saulson *et al.* to test the anelastic effects of its spring [91].

Let us consider an unidimensional oscillator composed of a mass m and a spring of stiffness k and loss factor ϕ with equation of motion:

$$m\ddot{x} + k(1 + i\phi)(x - x_0) = 0 \tag{5.44}$$

The transfer function is:

$$TF = \frac{x(\omega)}{x_0(\omega)} = \frac{{\Omega_0}^2(1 + i\phi)}{-\omega^2 + {\Omega_0}^2 + i\phi{\Omega_0}^2} \tag{5.45}$$

with ${\Omega_0}^2 = k/m$. The Q is immediately measured as the ratio of the transfer function magnitude at the resonance and that at $\omega = 0$:

$$Q = \left|\frac{TF(\Omega_0)}{TF(0)}\right| \simeq \frac{1}{\phi} \tag{5.46}$$

in the approximation $\phi \ll 1$. Therefore, Q does not depend on the resonant frequency as far as $\phi(\omega) = \text{const.}$.

In the case of the IP the antrispring action of the gravity has to be included in the calculation. The total "spring constant" can be written:

$$\tilde{k} = k_{\text{el}} - k_{\text{grav}} = k(1 + i\phi) - mg/l \tag{5.47}$$

where k_{el} and k_{grav} are the contributions of the spring (with its dissipation) and the gravitational antispring (non dissipative). The (5.47) can be rearranged in the form:

$$\tilde{k} = k_{\text{eff}}(1 + i\phi_{\text{eff}}) \tag{5.48}$$

where

$$k_{\text{eff}} = k - mg/l \tag{5.49}$$

$$\phi_{\text{eff}} = \phi\frac{k}{k_{\text{eff}}} \tag{5.50}$$

The (5.48) allows to calculate the Q as in the case of the simple oscillator. The IP quality factor is:

$$Q_{\text{IP}} \simeq \frac{1}{\phi_{\text{eff}}} = \frac{1}{\phi}\frac{k_{\text{eff}}}{k} \tag{5.51}$$

It is convenient to write the (5.51) in a different form. Remembering that (for an ideal IP with massless leg):

$$\omega_0^2 = \frac{k}{m} - \frac{g}{l} = \frac{k_{\text{eff}}}{m} \tag{5.52}$$

one finds:

$$Q_{\text{IP}} \simeq \frac{1}{\phi} \cdot \frac{\omega_0^2}{\omega_0^2 + g/l} \approx \begin{cases} \phi^{-1} & \text{for } \omega_0 \gg \sqrt{g/l} \\ \phi^{-1}\omega_0^2 l/g & \text{for } \omega_0 \ll \sqrt{g/l} \end{cases} \tag{5.53}$$

The value of the Q of the IP is not independent on the resonant frequency[8].

More information on the dissipation can be find out from the IP force-to-displacement transfer function: it has been shown by Saulson et al. [91] that the phase can provide a direct measurement of the loss factor if the dissipation is structural.

Let us consider the IP equation of motion when both structural and viscous damping mechanisms are present:

$$m\ddot{x} + [k(1 + i\phi) - mg/l]\,(x - x_0) + b\dot{x} = F_{\text{ext}} \tag{5.54}$$

where we assume that the excitation force F_{ext} acting on the IP top is large enough that $x - x_0 \simeq x$. The force-to-displacement transfer function is then:

$$TF = \frac{x}{F_{\text{ext}}} = \frac{1/m}{-\omega^2 + \omega_0^2 + i[\phi(\omega_0^2 + g/l) + \gamma\omega]} \tag{5.55}$$

where $\gamma = b/m$.

The transfer function phase is:

$$\text{phase} = \arctan\left[\frac{\Im(TF)}{\Re(TF)}\right] = \arctan\left[-\frac{\phi(\omega_0^2 + g/l) + \gamma\omega}{-\omega^2 + \omega_0^2}\right] \tag{5.56}$$

Let us consider the two cases where one dissipation mechanism dominates:

- **viscous damping:** in this case $\phi = 0$ and the phase is:

$$\text{phase} = \arctan\left[-\frac{\gamma\omega}{-\omega^2 + \omega_0^2}\right] \overset{\omega \ll \omega_0}{\longrightarrow} 0 \tag{5.57}$$

[8] In the case of a more realistic IP, as that described by the eq. (5.31), one has to modify (5.53) by substituting:

$$g/l \to (g \sum_i m_i l_i)/I$$

The error made by using (5.53) to predict the Q is about 1.6% for $f_0 = 30$ mHz and becomes smaller as the frequency increases.

- **structural damping:** in this case $\gamma = 0$ and the phase is:

$$\text{phase} = \arctan\left[-\frac{\phi(\omega_0^2 + g/l)}{-\omega^2 + \omega_0^2}\right] \overset{\omega \ll \omega_0}{\longrightarrow} -\phi\left(1 + \frac{g/l}{\omega_0^2}\right) \approx -\phi\frac{g/l}{\omega_0^2} \tag{5.58}$$

  At low frequencies the transfer function phase tends to a negative value proportional to ϕ: the phase measures ϕ amplified by the frequency compression factor.

Fig. 5.10 shows the expected phase behavior for an IP like that described in this thesis for viscous and structural damping.

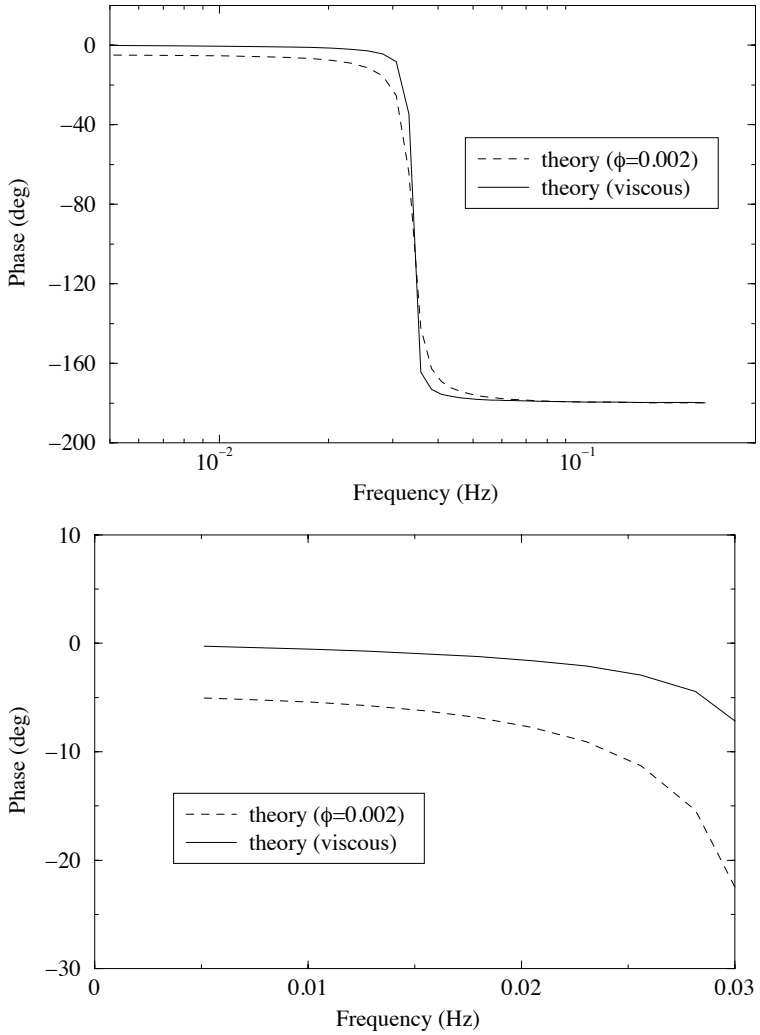

Figure 5.10: The phase of the force-to-displacement transfer function (5.55) calculated in the case of viscous and structural damping. The second plot is a zoom view of the first (low frequency part).

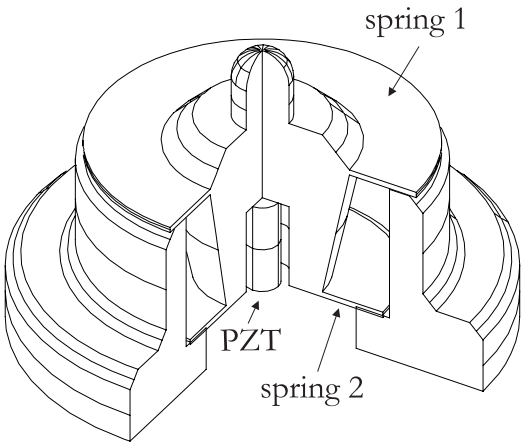

Figure 5.11: Foot supporting the base ring. The piezoelectric actuator (in the centre) and the twin cup springs providing the vertical elasticity are visible.

5.6 Design of the pre-isolator stage

A simple minded inverted pendulum cannot be used as a SA chain top stage because its rigid arm would occupy the central axis from where the SA chain is supposed to hang. The problem is simply solved by using three inverted pendulum legs linked together by a rigid ring over which the filter 0 lays and hooking the SA chain from its centre. Moreover, a three legged IP has 3 d.o.f. (x, y, θ_z) and acts as a pre-isolator also for the rotations around the vertical axis.

In this section the mechanics of the pre-isolator is described starting from the bottom. This description refers to the design of the IP prototype tested by the author in the framework of this thesis. After the tests some changes have been made to the design. The final design parameters are given as well.

5.6.1 Base

The IP base has been designed in order to allow the implementation of an active control system for the seismic tilt noise. Three elastic feet (fig. 5.11) will support the whole structure. Each foot will be provided with a coaxial piezoelectric actuator mounted within its base. Most of the load is supported by twin cup springs that guarantee high rigidity in all d.o.f. but the vertical direction, along which the cup springs allow for the piezo stroke

of about 30 μm.

A rigid steel ring (first mode of vibration 150 Hz) will lay between the feet and the legs (fig. 5.12). Two angular accelerometers will be placed over the ring and used as sensors of tilt. The accelerometer signals, properly recombined, will be used to drive the piezo actuators in the feet in order to keep the ring dynamically horizontal.

To allow for the legs counterweight below the flexible joint, the ring is provided with three stiff steel columns 80 cm high. The flexible joints are fixed on top of these columns (see fig. 5.12).

5.6.2 Legs

The flexible joints are the elastic elements which provide the restoring force in the horizontal IP motion. In the prototype they were steel rods of diameter $d = 27$ mm (machined with a precision of 0.01 mm) and length $l = 216$ mm. The theoretical joint stiffness is [66, 68]:

$$k = \frac{\pi}{64}\frac{Ed^4}{l^3}\frac{1}{[(L/l)^2 - L/l + 1/3]} \tag{5.59}$$

where L is the total length of the leg and E is the Young modulus of the material. The joints will be made of *maraging* steel, that has been proved to be a low hysteresis material [70]. The (5.59) does not keep into account the additional elasticity associated to the flexibility of the leg and of the other elements of the system. Thus, a precise estimate of the stiffness can be done only by means of a complete finite elements analysis. The final design flexible joints will be stiffer: $d_f = 31$ mm, $l_f = 236$ mm, to compensate for the longer legs and the increased total SA mass. If the actual stiffness were lower than predicted the system would fall into instability. For safety the stiffness is increased and some ballast is added on the SA to reduce the resonance frequency.

Each leg is essentially a light hollow cylinder made of aluminium with an inner diameter of 125 mm and an outer diameter of 130 mm. The total length of the leg, from the bottom of the flexible joint to the suspension point of the SA will be $L_f = 5918$ mm (the prototype was 700 mm shorter). The leg is composed by three sections flanged together and reinforced with titanium inserts. The total leg mass is 26 Kg. The frequency of the first flexural mode of the legs has been measured to be about 10 Hz (chapter 7): the legs may be considered rigid up to this frequency.

To tune the percussion point, the rigid leg structure extends below the joint through a bell shaped aluminium structure (weighting 9 Kg), supporting at its bottom edge two heavy steel rings (counterweight) at distance of about 0.9 m from the joint. One of the rings is threaded and can be moved in the vertical direction in order to allow the center of percussion tuning. The total mass of each counterweight is 17 Kg.

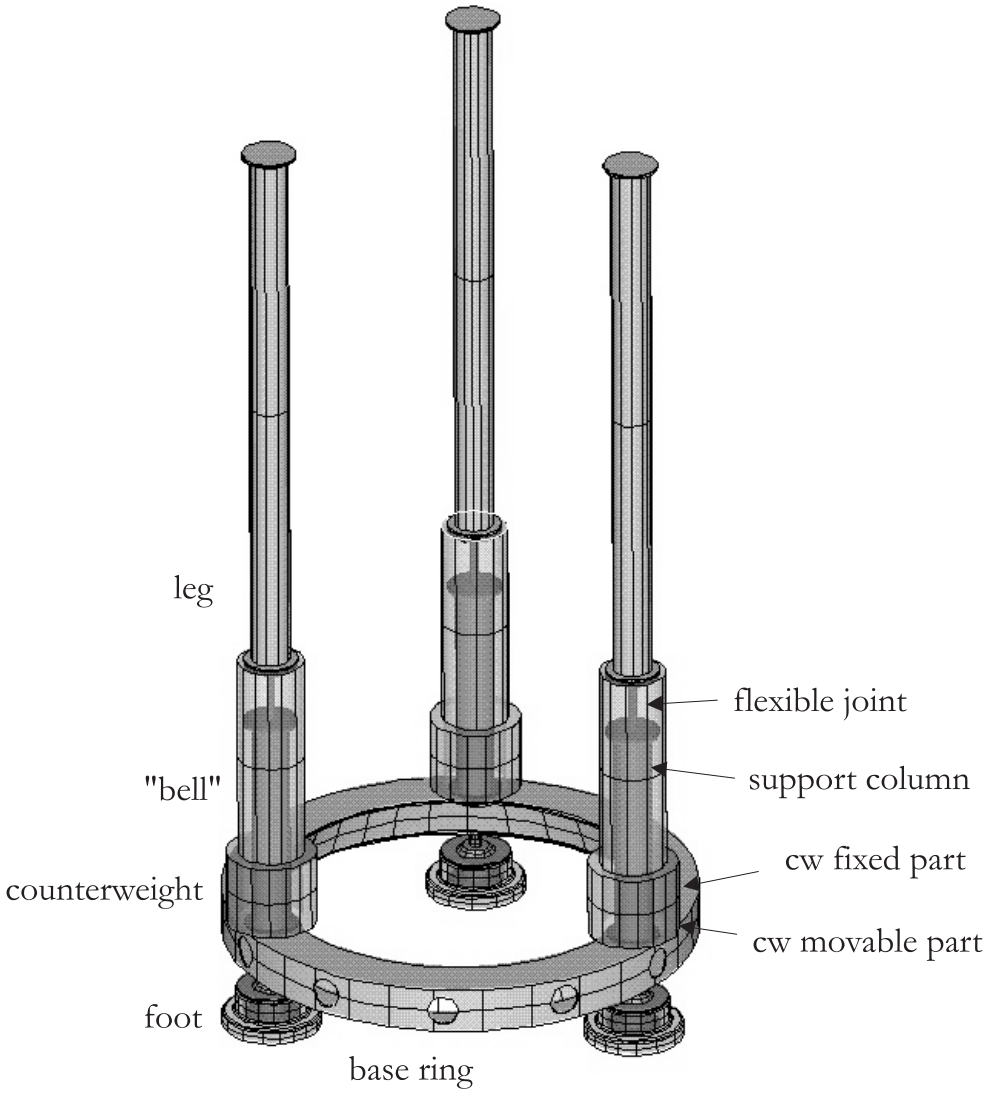

Figure 5.12: View of the bottom part of the inverted pendulum. From the top to the bottom one can see part of the legs, the light bell shaped structure, the counterweight, the ring, the feet. In transparency the support columns and the flexible joints are visible.

	FINAL	PROTOTYPE
CHAIN LENGTH (mm)	8663	
CHAIN WEIGHT (kg)	1260	
IP LENGTH (mm)	5918	5218
IP LEG WEIGHT (kg)	30	25
COUNTERWEIGHT (kg)	17+0.2÷6 @650 mm	17 @900 mm
"BELL" (kg)	9	9
JOINT DIAMETER (mm)	31	27
JOINT LENGTH (mm)	236	216
"JOINT STIFFNESS" (N/m)	740	580
JOINT STRESS (N/mm^2)	36	120

Table 5.1: Mechanical parameters for the IP prototype and for the final design. The counterweight mass in the final design can be increased or decreased by some kilos. The "joint stiffness" refers to forces applied at the leg top, has been calculated with a finite elements analysis and therefore includes the elasticity of all the other mechanical elements.

5.6.3 Top table

A top table is suspended on top of the three legs. Each leg is tipped with a stiff loop. The legs are linked to the top table through very soft joints, made of steel wire, 3 mm in diameter and 25 mm long, which hang from the loops and suspend one third the weight of the top table and the SA chain. In this way the system is soft with respect to rotations and the rotation mode frequency is minimised. The top table, from the IP point of view, is a rigid steel structure. On it there is room for 3 linear and two angular accelerometers, necessary for the active control of the SA.

In table 5.1 the final design IP parameters are listed.

5.7 Maximum stress evaluation

The IP has to be allowed to move of ± 20 mm in the horizontal plane without overstressing the flexible joints beyond their elastic limit. The joints are made of maraging steel, which has a yield point of about 1600 N/mm^2, more than twice that of a common steel [74]. In this section we give an estimate of the joints maximum stress.

Three different load conditions acts over the flexible joints: compression, bending moment for offset load, bending moment for imposed displacement.

Compression: due to the mass of the chain ($M/3$ over each leg) and the leg (m, including

the "bell" and the counterweight). The compressive stress on each joint is:

$$\sigma_c = \frac{(M/3+m)g}{\pi(d/2)^2} = 6 \quad \mathrm{N/mm^2} \tag{5.60}$$

where the final design parameters of table 5.1 have been used in the calculation.

Bending moment for offset load: when the top table moves of an amount Δ in the horizontal plane a bending moment on the joint arise due to the fact that the load is displaced with respect to the equilibrium position. The moment is simply $M_{\mathrm{ol}} = (M/3+m)g\Delta$. Let $\bar{J} = \pi d^4/64$ the joint cross section moment of inertia. The resulting stress is

$$\sigma_{\mathrm{ol}} = \frac{M_{\mathrm{ol}} d}{2\bar{J}} = \frac{32\Delta(M/3+m)g}{\pi d^3} = 48 \quad \mathrm{N/mm^2} \tag{5.61}$$

for $\Delta = \Delta_{\max} = 20$ mm.

Bending moment for imposed displacement: even if the leg was totally discharged by the load, a bending moment at the joint clamp occurs due to the imposed displacement of 20 mm over 6 m. The moment is given by:

$$M_{\mathrm{id}} = \frac{E\bar{J}\delta}{lL} \tag{5.62}$$

and the resulting stress is

$$\sigma_{\mathrm{id}} = \frac{E\Delta d}{2lL} = 38 \quad \mathrm{N/mm^2} \tag{5.63}$$

for $E = 2 \cdot 10^{11}$ Pa and $\Delta = \Delta_{\max} = 20$ mm.

From the numbers above one can conclude that the flexible joints work well below their elastic limit, and the IP can safely work out of the equilibrium position.

5.8 Effect of temperature on the IP

The IP prototype tests were performed in open air and not in thermostabilized environment. In this section we give a theoretical estimate of the effect of the temperature on the IP. We perform the calculation for the IP final design, using the parameter of the table 5.1. In this calculation, for the sake of simplicity, we assume that the resonant frequency has the dependence (5.8) on the stiffness k and the leg length l. Then the frequency derivative with respect to the temperature may be written:

$$\begin{aligned} \frac{\mathrm{d}f_0}{\mathrm{d}T} &= \left[\frac{\partial f_0}{\partial k}\frac{\mathrm{d}k}{\mathrm{d}T} + \frac{\partial f_0}{\partial l}\frac{\mathrm{d}l}{\mathrm{d}T}\right] = \\ &= \frac{1}{8\pi^2 f_0}\left[\frac{k}{M}\left(\frac{1}{k}\frac{\mathrm{d}k}{\mathrm{d}T}\right) - \frac{g}{l}\left(\frac{1}{l}\frac{\mathrm{d}l}{\mathrm{d}T}\right)\right] \end{aligned} \tag{5.64}$$

The thermal dilatation coefficient for aluminium is [83]:

$$\alpha = \frac{1}{l}\frac{\mathrm{d}l}{\mathrm{d}T} = 2.4 \cdot 10^{-5}\,^{\circ}\mathrm{K}^{-1} \tag{5.65}$$

Thus, a leg length variation of about 140 μm/°K is expected. For the stiffness, using eq. (5.59), one finds:

$$\begin{aligned} \frac{\mathrm{d}k}{\mathrm{d}T} &= \frac{\partial k}{\partial E}\frac{\mathrm{d}E}{\mathrm{d}T} + \frac{\partial k}{\partial l}\frac{\mathrm{d}l}{\mathrm{d}T} + \frac{\partial k}{\partial d}\frac{\mathrm{d}d}{\mathrm{d}T} = \\ &= \frac{k}{E}\frac{\mathrm{d}E}{\mathrm{d}T} + \frac{\partial k}{\partial l}\frac{\mathrm{d}l}{\mathrm{d}T} + \frac{4k}{d}\frac{\mathrm{d}d}{\mathrm{d}T} \end{aligned} \tag{5.66}$$

Using the value (5.65) one can easily verify that the first term in (5.66) is dominant: the joint stiffness variation with temperature depends mostly on the Young modulus variation. For the steel used [83]:

$$\frac{1}{k}\frac{\mathrm{d}k}{\mathrm{d}T} \approx \frac{1}{E}\frac{\mathrm{d}E}{\mathrm{d}T} = 10^{-3}\ \,^{\circ}\mathrm{K}^{-1} \tag{5.67}$$

The expected frequency variation around the working point of 30 mHz is then:

$$\frac{\mathrm{d}f_0}{\mathrm{d}T} \approx 0.7\ \mathrm{mHz}/^{\circ}\mathrm{K} \tag{5.68}$$

During the tests a maximum variation of 2 mHz in the resonant frequency has been observed during the day. The observed variation is consistent with the estimated one, consider that a temperature variation of a few degrees has been recorded in the laboratory. The frequency variation will be negligible in VIRGO, where the towers will be thermostabilised within 0.1 °C.

In fig. 5.13 the relative frequency variation with the temperature is plotted versus the translation resonant frequency f_0. The plot shows that the effect of the temperature becomes much larger when the IP is operated at a resonant frequency below 20 mHz. If the towers will be thermostabilised within 0.1 °C, a relative frequency variation of about 1% will be achievable at $f_0 = 15$ mHz.

5.9 Pre-isolators for other interferometers

Other groups involved in GW research have designed and tested long-period vibration isolation platforms to be cascaded in front of the mirror suspension system.

ACIGA group has proposed [94] a two-dimensional horizontal pre-isolator design based on the *Scott-Russell linkage*. The dynamics of the system simulates that of a long-radius conical pendulum. The main advantage of this design is that the restoring force is mainly gravitational. This allows to be less sensitive to thermal drifts and to minimise the internal dissipation: a $Q \sim 500$ has been measured at 30 mHz [95]. The pre-isolator has been

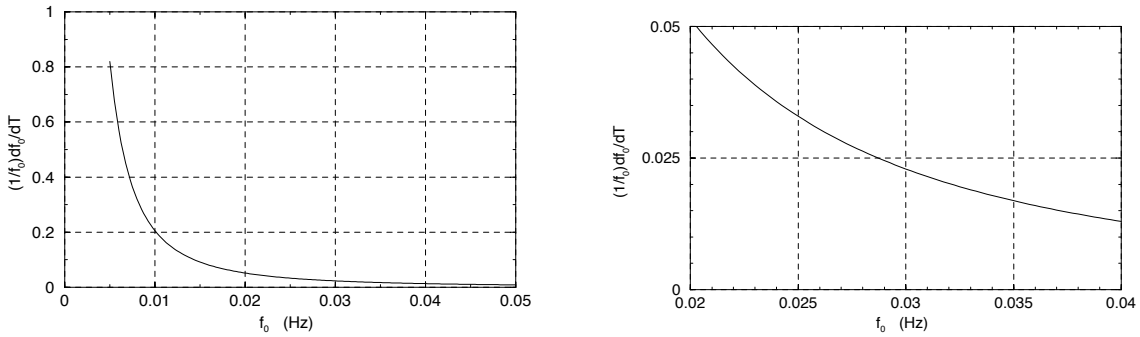

Figure 5.13: Relative variation $(1/f_0)\mathrm{d}f_0/\mathrm{d}T$ as a function of the resonant frequency f_0. The second plot is a zoom view around 30 mHz.

operated even at lower resonant frequencies and an attenuation of more than 90 dB at 2 Hz has been attained. Moreover, it is quite compact and fits within less than two meters of vertical space. On the other hand, it shows two main disadvantages: the design is quite complicated and it works as an isolator (and as an actuation platform) only for translations (therefore, it would not be possible to control the mirror rotations at low frequencies).

The TAMA group has developed a one-dimensional horizontal pre-isolator based on the *X-pendulum* design [96, 97]. Cascading two X-pendulums should provide attenuation for both translation d.o.f.. Its big advantage is the compactness (about 20 cm in vertical) and, for this reason, it is considered a good solution for the small TAMA vacuum chambers. The main problem with it is that parasitic resonances spoil its attenuation performance. A prototype suspension which makes use of couples of cascaded X-pendulums has been built and tested. It has been operated at a resonant frequency of 0.14 Hz, but it shows resonances at 2,5,10 Hz [98].

Chapter 6

Experimental setup

6.1 Introduction

In this chapter we describe the setup used to perform the tests on the IP. Fig. 6.1 shows the IP prototype used for the tests, with a table on the top instead of the filter 0. In fig. 6.2 a scheme of the experimental apparatus is shown. It can be divided into four logical blocks:

- **mechanical system:** a full scale inverted pendulum surrounded by the outer safety structure (not shown in fig. 6.1, visible in fig. 4.2, 4.3)S;
- **sensors:** 3 displacement sensors and 3 accelerometers used to monitor the top table motion, 1 accelerometer used to monitor the base motion;
- **actuators:** 3 coil-magnet and 3 mechanical actuators used for the top table positioning and active control; a pneumatic shaker has used to excite the IP for the transfer function measurement;
- **electronics**: the electronics includes the sensors read-out, the actuators drivers, the ADC-DSP-DAC boards.

The configuration of the sensors and the actuators on the top table is shown in fig. 6.3. All are placed on the vertices of equilateral triangles, with the sensing axes tangent to the top table. One additional accelerometer has been clamped in the very centre of the top table when measuring the horizontal transfer function in order not to be sensitive to the table rotation around the vertical axis (θ_z).

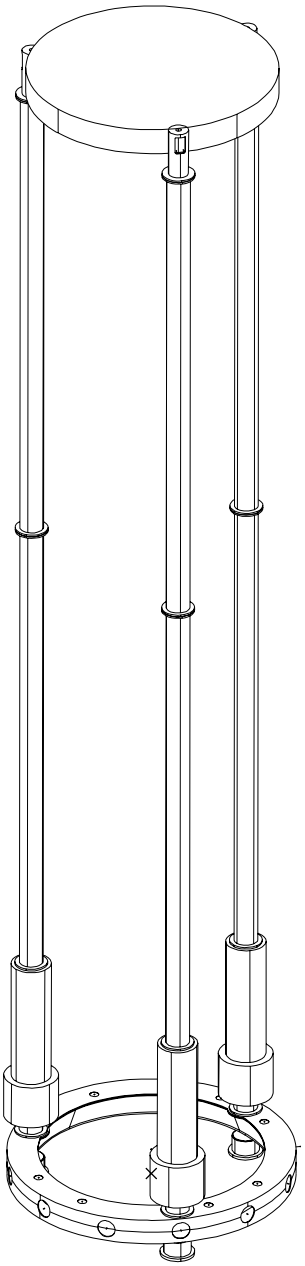

Figure 6.1: The IP prototype, with the dummy top table instead of the filter 0. The outer frame is not shown in this picture.

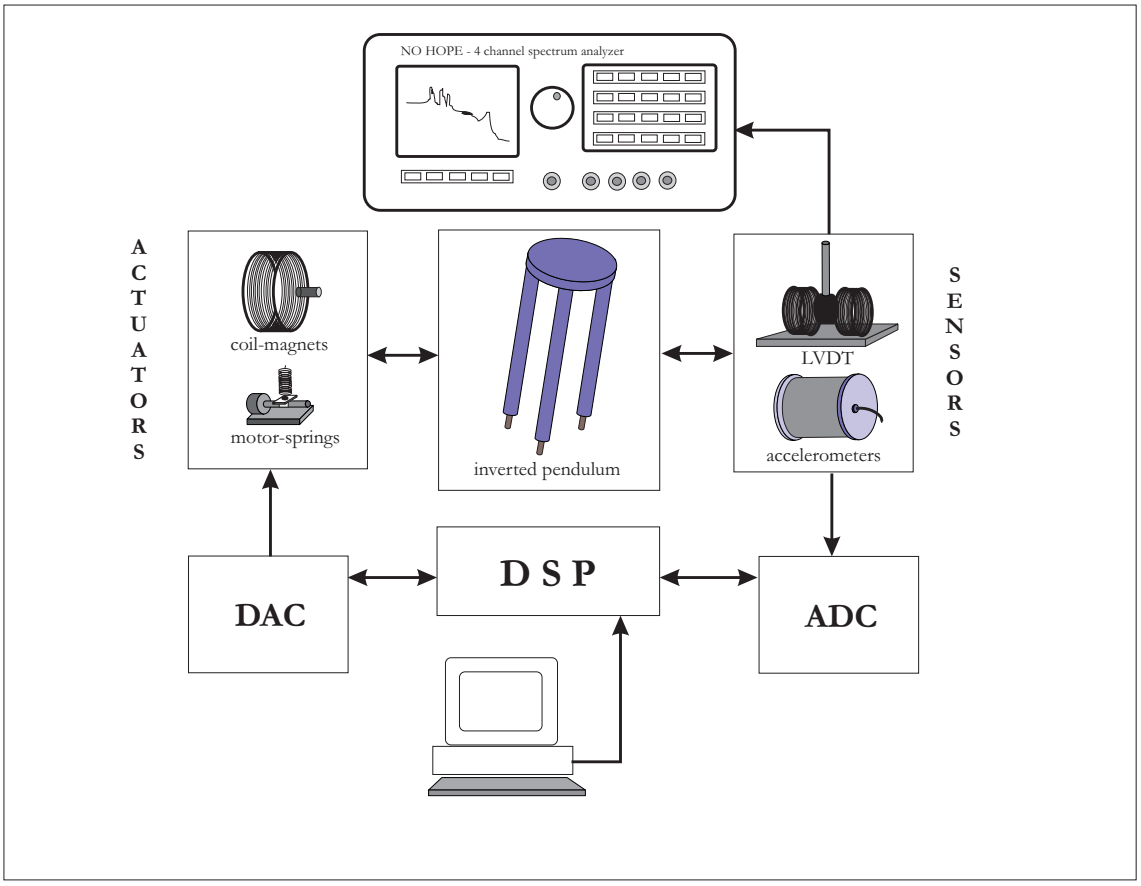

Figure 6.2: Logic scheme of the experimental setup: the mechanical system (IP) is monitored by displacement and acceleration sensors and acted upon by mechanical and electromagnetic actuator. A 4 channel spectrum analyzer is used to monitor the experiment. The sensor signals pass through an ADC, are processed by a DSP in order to build the desired feedback signals, and fed to the actuators through a DAC. Both the DSP and the spectrum analyser are used to provide the excitation signals in the transfer function measurement (white noise, couloured noise, sinusoidal signals, chirps).

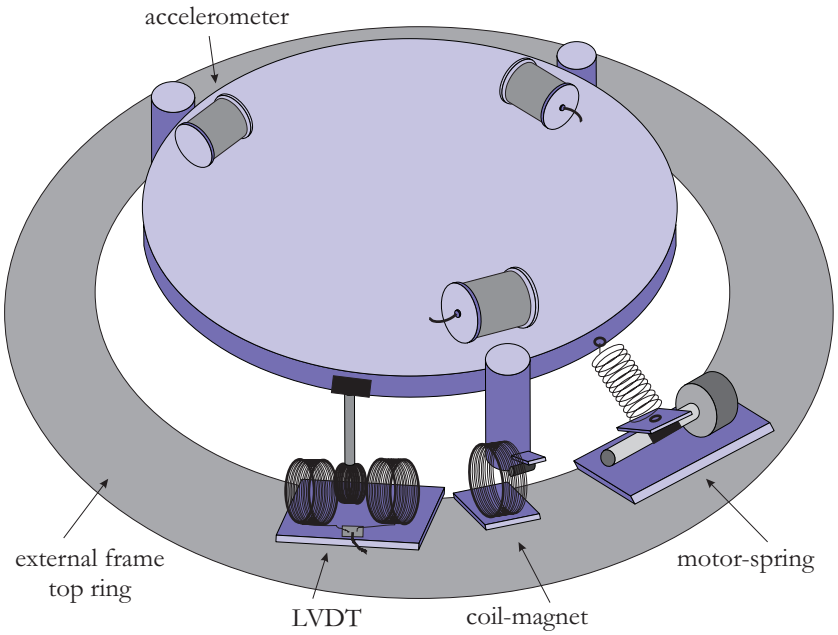

Figure 6.3: View of the top table: the 3 accelerometers are visible, whereas only 1 LVDT, 1 motor-spring and 1 coil-magnet actuators are shown. The others are placed near the accelerometers following the same triangular configuration.

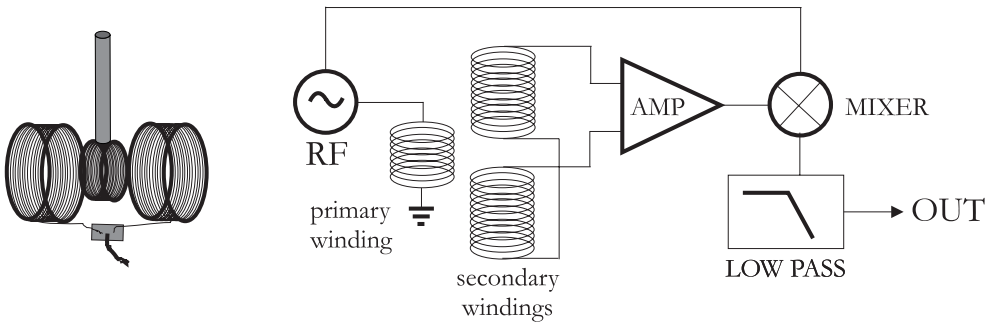

Figure 6.4: The LVDT sensor used on the IP with a scheme of the read-out electronics.

6.2 The IP prototype

The tested IP prototype was 5918 mm high (70 mm shorter than the final design one). Instead of the filter 0 it supported a round iron disk about 280 kg heavy. The additional load necessary to set the IP at the operation condition (translation frequency of 30 mHz) was placed on the top table in form of lead blocks. The IP feet are mounted on the base of a steel safety frame (sketched in fig. 6.1) which corresponds to the inner structure of the VIRGO vacuum tower. The upper ring of the frame is used as a support for the LVDT secondary winding (sec. 6.2.1), the coils and the motor driven slides (sec. 6.2.2).

6.2.1 Sensors

Two kinds of sensor have been used: *displacement* sensors and *acceleration* sensors. Both kinds of sensor are necessary for the active control of the IP (see chapter 8):

position sensors: the displacement sensors used are LVDT: *Linear Variable Differential Transformer*. A LVDT (fig. 6.4) is composed by a *primary* and a *secondary* windings. The primary winding (the central coil in fig. 6.4) is fed with a 20 kHz modulation signal. The secondary winding is composed by two coils, symmetric with respect to the primary and wound in opposite way. When the primary winding is displaced of an amount δx a signal at the modulation frequency and amplitude proportional to δx is induced on the secondary winding. The output signal is demodulated by a mixer, whose output is a DC signal of amplitude proportional to δx. The LVDT used have been designed to be linear over a range of 2 cm within 10%. The calibration curve of one of the LVDT is shown in fig. 6.5.

In the case of the IP the primary winding is rigidly connected to the top stage, while the secondary winding is clamped on the external safety frame: the LVDT measures

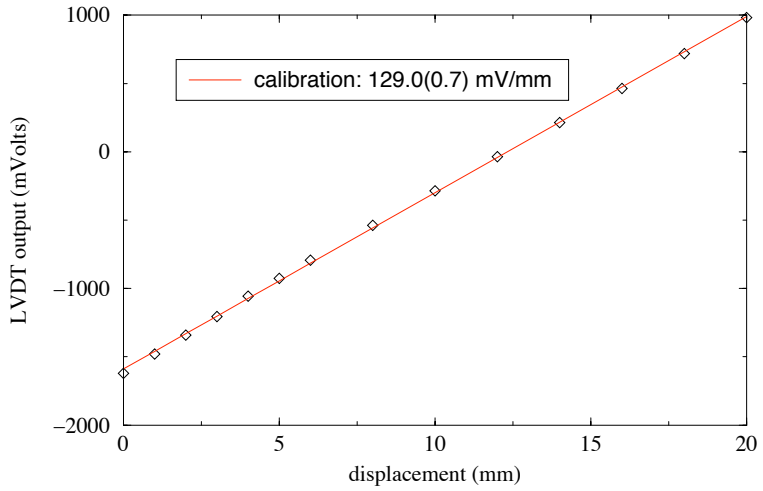

Figure 6.5: The LVDT calibration curve: the linearity range is larger than 2 cm. The sensitivity is 129.0 ± 0.7 mV/mm.

the *relative displacement* of the IP with respect to a reference frame which is not seismic noise free.

Accelerometers: custom made accelerometers are used, based on a LVDT sensor which monitors the motion of an *inertial mass* (a mass suspended by means of a spring). A feedback control keeps the mass on the LVDT null signal position (close to the mass equilibrium position). The feedback signal is proportional to the acceleration in the range 0-400 Hz. The accelerometer spectral sensitivity is better than 10^{-9} m/$\sqrt{\text{Hz}}$ in the range 0-2 Hz.

The accelerometers are of remarkable importance in the active damping of the SA resonances: the use of *inertial* sensors allows to widen the loop bandwidth without reinjecting noise into the system (see section 8.5). The actual accelerometer response can be described as

$$V_{\text{out}} = \sigma \left[g \sin\theta + \ddot{x} \right] \tag{6.1}$$

where θ is the tilt angle and σ is the calibration parameter[1].

[1]The calibration σ is slightly different for the three accelerometers used:

$$\begin{cases} \sigma_1 = 54.8 \pm 0.1 \ \frac{\text{Volt}}{\text{m/s}^2} \\ \sigma_2 = 59.1 \pm 0.1 \ \frac{\text{Volt}}{\text{m/s}^2} \\ \sigma_3 = 53.9 \pm 0.1 \ \frac{\text{Volt}}{\text{m/s}^2} \end{cases}$$

In the following, the conversion between the accelerometers spectra measured in Volt/$\sqrt{\text{Hz}}$ and the corresponding acceleration spectra (measured in $(m/s^2)/\sqrt{\text{Hz}}$) have been done using the proper value of σ for each sensor.

6.2.2 Actuators

Two sets of actuators are used: 3 electromagnetic coil-magnets pairs and 3 mechanical motor driven springs.

Motor-spring actuators The system is shown in fig. 6.6 a): the two ends of a spring are connected to the top table and to a movable slide. The slide can be moved in a range of ± 4 cm by means of a stepping motor, rigidly clamped to the external frame top ring. The stiffness of the actuator in the horizontal direction adds to the overall IP stiffness and makes the resonant frequency to increase: the IP has to be loaded with additional mass to return to the operational frequency. The final design of the actuator is slightly different: in the configuration of fig. 6.6 a torque is exerted on the slide due to the vertical component of the elastic force, thus increasing the friction between the slide and the endless screw transmitting the motion. Therefore, a different solution has been adopted (fig. 6.6 b): a 50 cm long plate, clamped on the slide, supports two horizontal springs connected to the IP leg. In this configurations the elastic force is completely horizontal. Moreover, the slide range will be ± 10 cm. A larger range allows to exert the same forces using springs with lower stiffness.

Coil-magnet actuators: Cylindrical magnets (2.5 cm long and 1 cm in diameter, with a magnetic field of 1 Tesla) were clamped on the IP legs, facing coils clamped on the frame top ring as shown in fig. 6.7 a). The actuators used had not been designed for the IP and had a limited linear range[2] (a few mm, see fig. 6.8 (a)). The final design of the actuator is very different (fig. 6.7 b): a pair of coils is used instead of one for linearity sake. The magnet is a cube with a 4 cm on the side, connected to the filter 0 by means of a rigid beam. This geometry ensures that the field gradient is constant (for constant current) in a large volume (± 2 cm along the axis, $\pm$ 2 cm radially, see fig. 6.8 (b)) [116].

The idea is to use the mechanical actuators for the positioning of the IP in the correct operation point and for the very low frequency ($f < 1$ mHz) control of the suspension. This could not be done with the coil-magnet pairs for two reasons: first, if the operation point would not coincide with the "zero" of the actuator, permanent currents would be needed in the coil to keep the position, thus increasing the power dissipation into the thermostabilised tower; second, and more important, the system would not be stable in case of electrical black out.

[2]By *linear range* we mean the range where the force per unit current α exerted does not depend on the magnet position with respect to the coil.

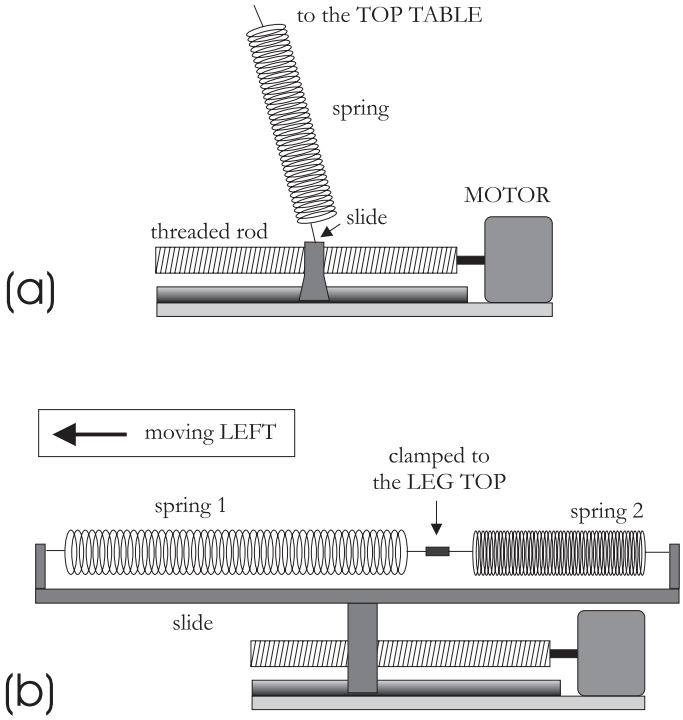

Figure 6.6: a) The mechanical actuator used for the test of the IP prototype. b) The final design of the motor-spring actuator.

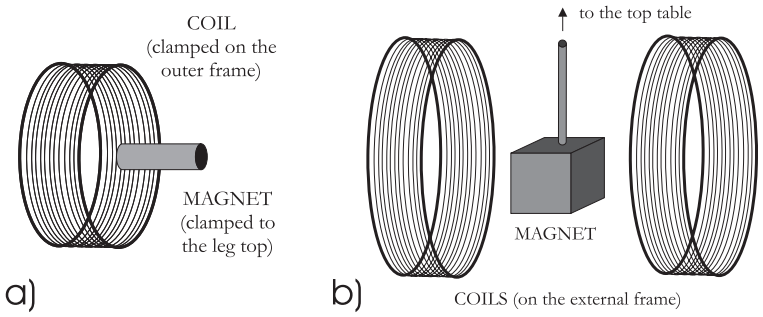

Figure 6.7: a) The coil-magnet actuator used in the prototype test. b) The final design of the coil-magnet actuator.

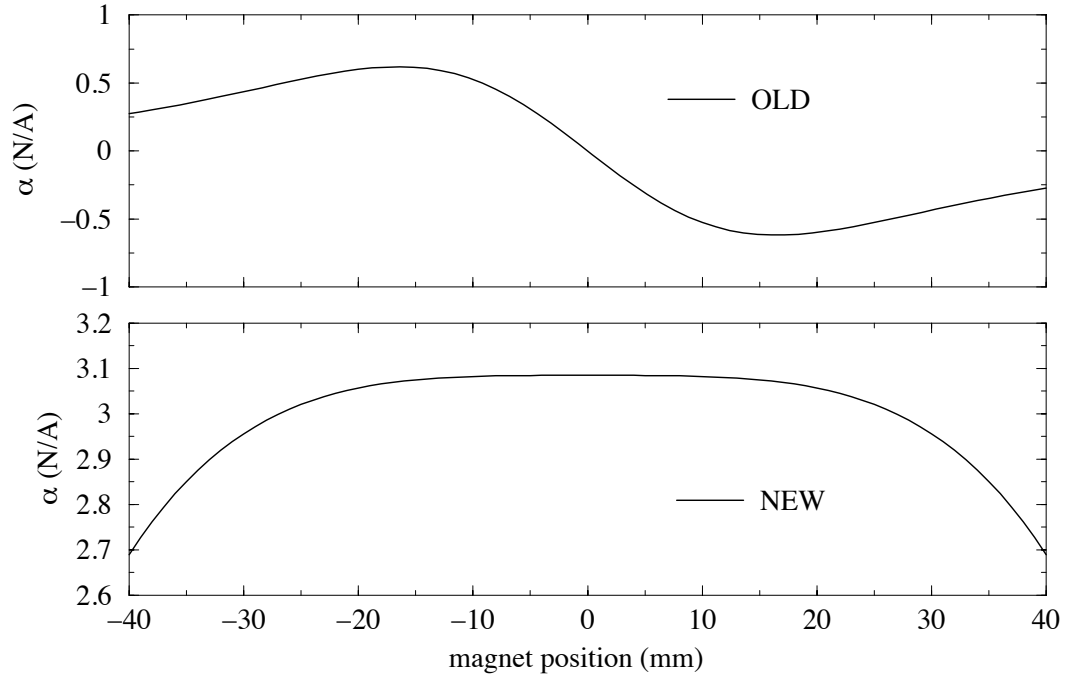

Figure 6.8: Response of the old and new coil-magnet actuators: the force per unit current α is plotted as a function of the magnet position with respect to the coil x. The function $\alpha(x)$ is odd for the old actuator and even for the new one (due to the action of the coil pair). The old actuator response is approximately constant only around the working point $x = R/2$, within a few mm (R is the coil radius), whereas the new one presents a much larger flat response range (some cm).

6.3 Digital Signal Processing

A custom made DSP board, based on a Motorola DSP96002 Digital Signal Processor, has been developed at INFN Pisa laboratory in the past years and has been used to implement the SA active control system. There are several advantages in using a digital system instead of an analog one for feedback controls:

- the DSP is controlled by the user through a general purpose computer. The feedback filter is described by a set of numerical data and some of the filter parameters (such as the gain) can even be changed without stopping the feedback loop;
- high precision (about 1%) is sometimes required on the zero/pole frequency introduced, which cannot be achieved using analogue components.

In the next chapters it is described in detail how the DSP is used in the test. Here we describe the general set-up.

6.3.1 Hardware

The usual set-up is represented in fig. 6.2: the analogue outputs of the 3 sensors are sampled at 20 kHz by 3 ADC. The digital signals obtained are sent to the DSP board through a dedicated bus. The DSP filters and combines the signals, producing 3 output signals to drive the 3 actuators, via 3 DAC.

- the ADC is a 16 bit (14.5 effective bit due to the ADC noise) board with 4 input channels and a dynamics of 5 volts. The resolution is then $5/2^{14.5}$ V=$2.15 \cdot 10^{-4}$ V, the sampling frequency is 160 kHz;
- the DAC is a 20 bit board (18.2 effective bit) with a dynamic of 5 V, a resolution of $1.66 \cdot 10^{-5}$ V and a sampling frequency of 500 kHz.
- the DSP is able to perform a sum and a multiplication in one clock cycle. The clock frequency is 16 MHz: the implementation of a pole/zero filter of the type $(s + s_z)/(s + s_p)$ requires 250 ns.

6.3.2 Software

The DSP is programmed using its own assembler language, but a user friendly software has been realised by VIRGO Pisa electronic group [113]. The software allows to implement filters directly via computer (see fig. 6.9), by means of a list of simple instructions containing all information and parameters such as:

- the sampling frequency;

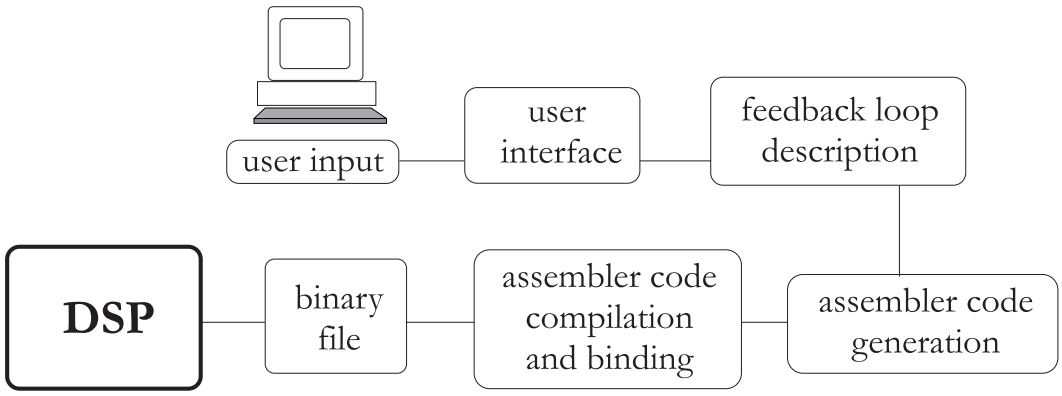

Figure 6.9: Logic scheme of the DSP control.

- the ADC channels addresses where the input signal has to be sampled;
- the variables to be used;
- the operation to perform on the variables (amplification, linear combinations);
- the poles and zeroes defining the filters to be implemented;
- the addresses of the DAC channels for the output signals.

As an example we show how to implement the system of fig. 6.10. The process can be logically split into 3 parts:

1. 4 ADC channels are read: the signals are filtered and the last 2 are summed. 3 new signals `in1,in2,in3` are obtained. This is done by the first 4 lines of the program shown in fig. 6.11. The lines contain the information on the filter used. for instance, editing `lowpass.flt` one can implement poles and zeroes of the filter. Fig. 6.12 shows an example: a low pass filter with 3 poles at 1 kHz has been used;
2. the 3 signals are recombined by a matrix (line `MAT` in fig. 6.11): `c1,c2,c3` are obtained;
3. the new signals are filtered and sent to 3 DAC channels.

6.4 Excitation system

An excitation system has been designed and built in order to measure the system performance [99]. The excitation system (shaker) is shown in figure 6.13. The high pressure air

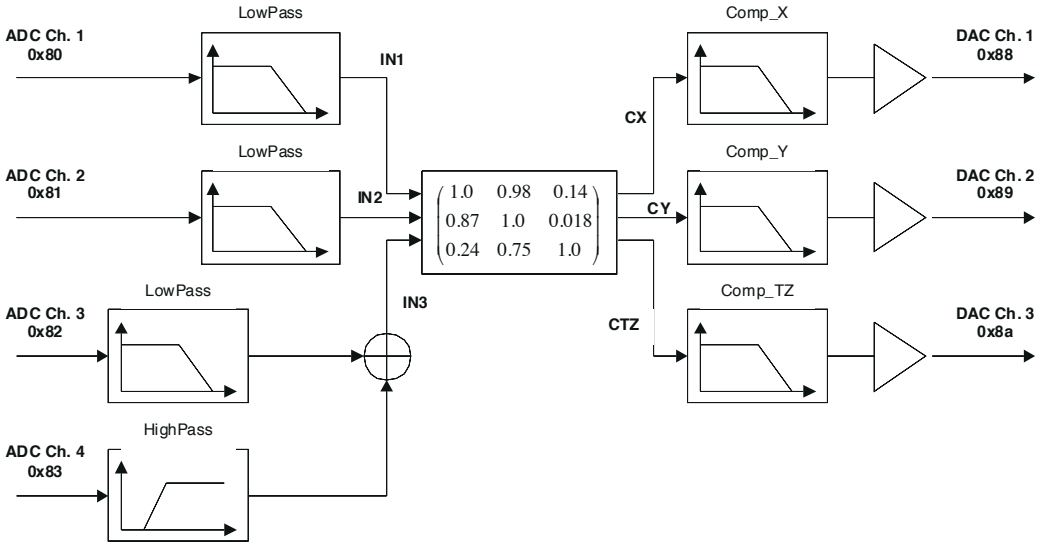

Figure 6.10: Scheme of the operations implemented with the filter of fig. 6.11.

is first regulated to a constant value and supplied via a computer controlled proportional valve to one chamber of the double action piston. A second proportional valve is also fitted to allow this chamber of the piston to be exhausted to the room. This allows a variable pressure from 0 to about 7.5 bar to be applied to this "pushing" side of the piston. The other chamber of the piston is fed with a stabilised bias pressure of approximately 4 bar by a second regulator. This gives the required "pull" action for low applied pressures and"push" action for high applied pressures. In order to obtain the best possible response speeds from the system (i.e. for shaking at $f > 10$ Hz), the variable pressure end of the piston was arranged to have the minimum possible volume. The motion of the push rod is limited by a (piston mounted) plate and (casing mounted) rods and nuts, to stay within a few millimetres of this end limit. The movement of the piston is sensed by a resistive readout and controlled via DSP.

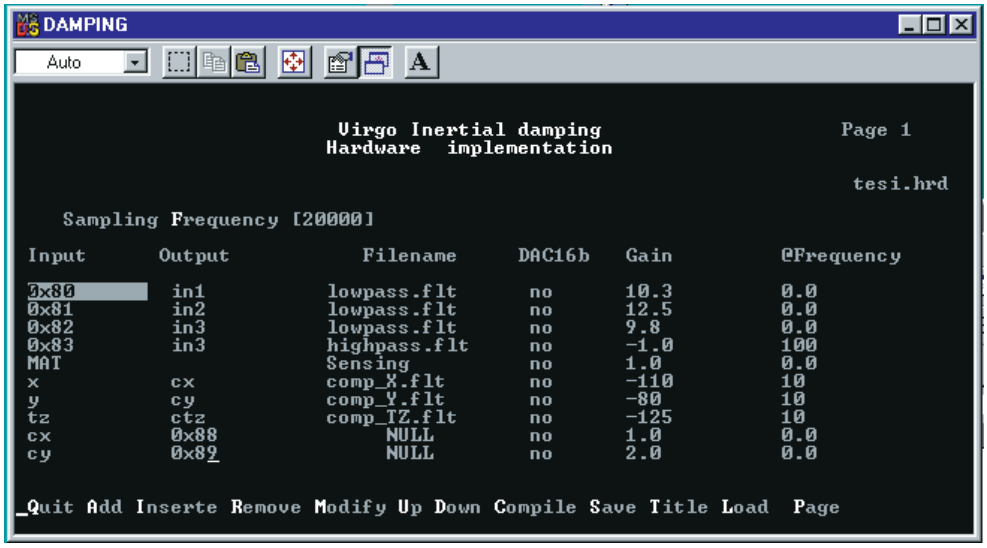

Figure 6.11: User interface of the DSP software: the program used to implement the system of fig. 6.10 is shown.

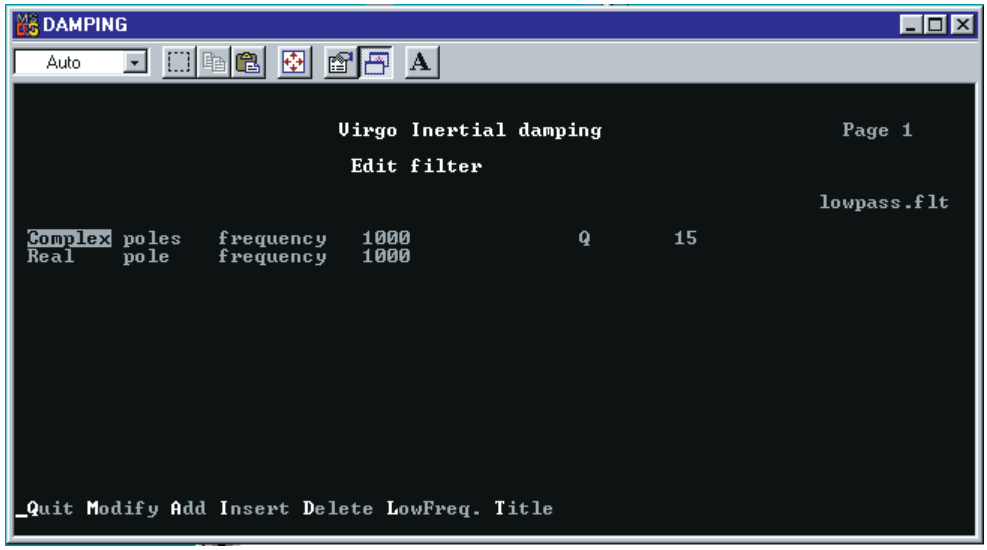

Figure 6.12: Example of implementation of a 3 poles low pass filter.

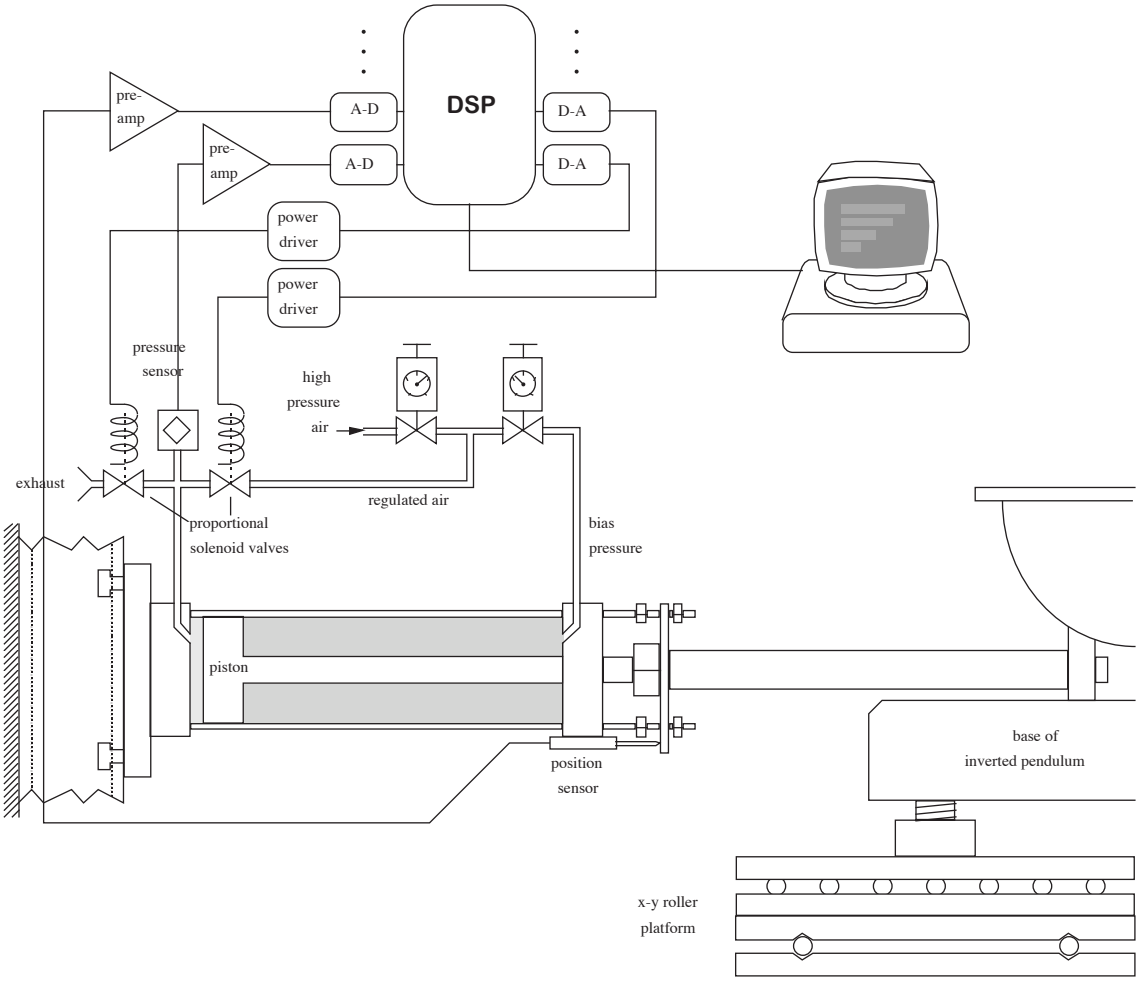

Figure 6.13: The shaker used to excite the IP.

Chapter 7

Tests of the Inverted Pendulum as a Preisolator

7.1 IP characterisation

In chapter 5 we have described what should be the characteristics of a reliable pre-isolator for the mirror suspension. In this chapter we present the tests performed to validate the IP and their results. All the tests of this chapter are aimed to verify the *passive* IP performance, whereas the subject of the next chapter is the problem of the IP active control.

The main purpose of this group of tests was the measurement of the mechanical transfer function in various working conditions, to learn about the passive attenuation performance, the effect of the centre of percussion, the effect of spurious resonances (such as the legs normal modes).

7.2 Load curve

As a test of the mathematical model developed in chapter 5 we have measured the dependence of the horizontal resonant frequency of the pendulum as a function of the load, to verify equation (5.18). The minimum value for the load was $M_0 = 296$ kg (the mass of the top table plus the 3 accelerometers). Lead blocks were added on the top table to increase the load. A typical spectrum of the accelerometer output is shown in fig. 7.1: the highest frequency peak corresponds to the rotational mode of the IP (easily identifiable because the signals of the 3 accelerometers have the same phase). The first peak correspond to the degenerate IP translation modes[1].

[1]The two translation peaks are to be degenerate because of the IP cylindrical symmetry. Actually, increasing the frequency resolution, a splitting of the peak shows up, because the springs used for the IP

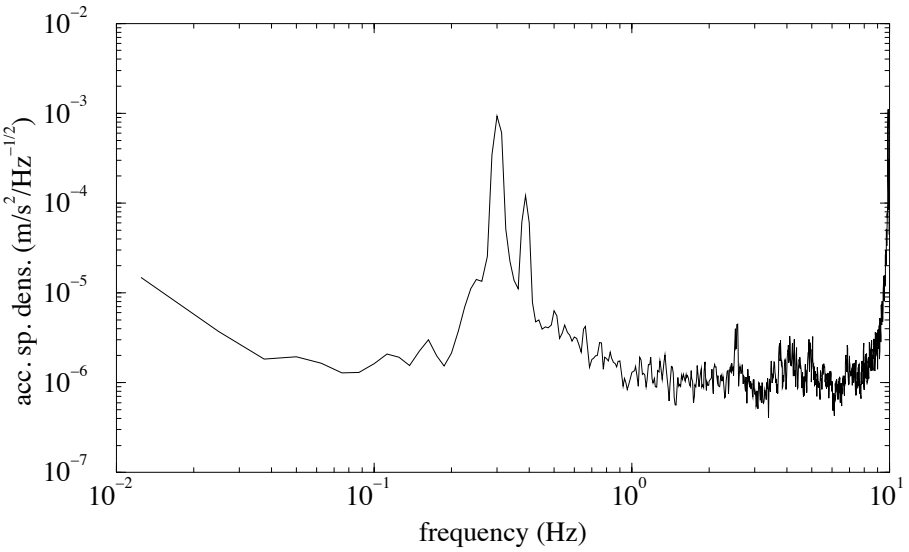

Figure 7.1: Spectrum measured by an accelerometer on the top of the inverted pendulum.

Fig. 7.2 shows the result of the measurement. The experimental points are fit by the function

$$f_0 = \frac{1}{2\pi}\sqrt{\frac{k - (M + \frac{m}{2})\frac{g}{l}}{M + \frac{m}{3}}} \tag{7.1}$$

where m is the leg mass and M is the load per leg, with $k = 566 \pm 10$ N/m. The theoretical stiffness calculated using eq. (5.59) was $k_{\text{th}} = 855 \pm 10$ N/m. The discrepancy can be explained by considering that the joint is not the only elastic elements of the leg. The flexural elasticity of the 6 m leg itself and of the support column should have been considered in the calculations, but had been neglected in (5.59). A finite elements analysis including these effects has been performed predicting an effective stiffness $k_{\text{f.e.a.}} = 570$ N/m.

This test calibrated the calculation tools. Following its results better joint calculations were possible. As an added safety, it has been decided to design the final IP with joints stiffer than necessary and to distribute a ballast of about 100 kilograms on the filters to compensate for the excess stiffness. The chosen frequency is finely tuned by removing a fraction of the ballast.

---

positioning may break the symmetry.

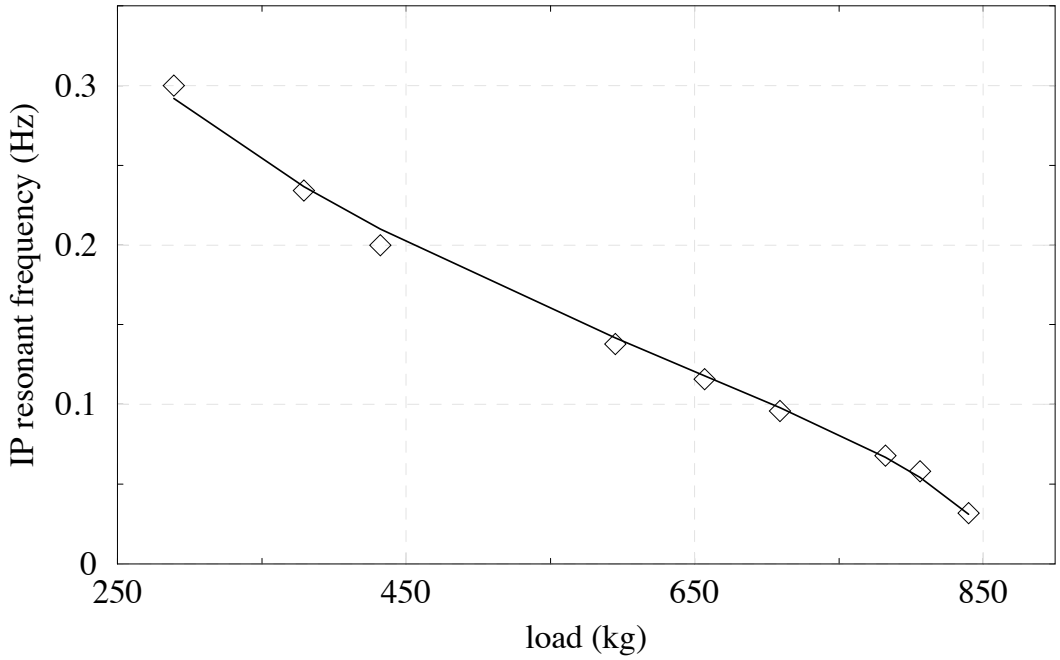

Figure 7.2: Frequency of the translation mode with respect to the load on top (dummy filter plus added load). The experimental data are compatible with a stiffness $k = 566 \pm 10$ N/m.

7.3 Seismic excited transfer function

To measure the IP transfer function, the system has been provided with two accelerometers: the first (A0) has been clamped on the base ring platform, the second (A1) in the very centre of the top table (to minimize its sensitivity to the twist mode of the IP). The two accelerometers had the same orientation. The measured transfer function is shown in fig. 7.3. From these measurements it is evident that the IP is behaving as an efficient vibration filter, but it is hard to prove whether the attenuation is in agreement with the predicted $1/f^2$ performance or not. Moreover, for lack of sufficient ground excitation, it is not possible to make a meaningful measurement above 1 Hz, where one expects to observe the effect of the centre of percussion. This is not surprising: very little force is needed to move the IP and air currents, moved by shutting doors or human activity, affect the measurement. It is than necessary to design a more effective system to excite the IP base with sufficient energy to dominate the environmental noise. A comment should be done about the effect of seismic tilt on the IP performance (see section 5.4): above a critical frequency (depending on the speed of the seismic waves) the contribution of the seismic induced tilt should dominate over that of the purely horizontal seismic noise. In this range the IP transfer function is expected to take a $1/f$ rather than a $1/f^2$ behaviour. Assuming

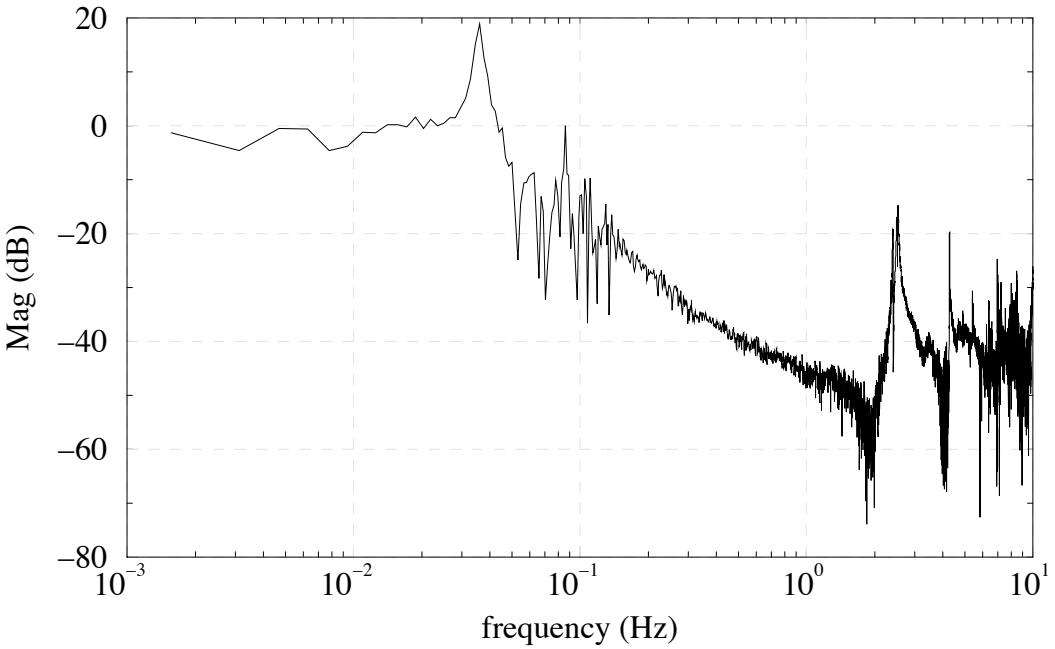

Figure 7.3: Seismic excited transfer function, measured as the ratio of the accelerometer spectra. The straight line represents the $1/f^2$ behaviour expected in absence of tilt.

a wave speed of 500 m/s one expects a change of slope in the transfer function at about 1 Hz (see eqs. (5.41),(5.42)). In fig. 7.3 a change of slope at about 0.3 Hz can be observed, but the effect can be explained also by the resonant structures visible at frequencies above 1 Hz. Even if the "excess noise" above 0.3 Hz were the effect of tilt, the isolation performance would be only slightly affected: only 10 dB of attenuation are lost at 1 Hz. Even without active tilt control, the IP would be capable to fulfil its pre-isolation function.

7.4 Inverted pendulum transfer function

7.4.1 Measurement strategy

The inverted pendulum transfer function has been finally measured exciting the system by means of the shaker described in section 6.4. Particular care has been devoted at choosing the right excitation signal to feed the shaker. White noise spectrum would not have been satisfactory: an uniformly distributed excitation energy of amplitude, adequate in the resonance region, would have been too low in the high attenuation region.

The best choice turned out to be a "coloured" swept sine excitation. In swept sine

mode the transfer function is measured by steps: at each step, a sinusoidal excitation is provided to the shaker with fixed frequency and proper amplitude.

The experimental set-up is sketched in fig. 6.2. Originally, both the IP base and its safety frame were shaken as a whole. It was soon realised that a peak due to acoustic coupling, corresponding to the resonant frequency of the frame, was dominating the measurements at 3 Hz. The safety frame was then disconnected from the base and lifted a few mm with the help of the crane. In this configuration the frame was not excited and the peak disappeared. It is interesting to compare the measurements performed with and without the frame (fig. 7.5). The wide peak at 3 Hz is overlapped to the dip: it is impossible to study the effect of the centre of percussion when the frame is connected.

7.4.2 Results

The measured transfer function is shown in fig. 7.4. Some comments are needed:

- the IP is resonant at 33 ± 2 mHz and has a quality factor $Q = 33 \pm 2$ (see section 7.7);
- an attenuation of 65 dB is achieved at 1 Hz;
- the resonances at about 9 and 15 Hz are associated to the main modes of vibration of the leg-counterweight systems. These resonances limit the attenuation performance of the IP. To avoid this problem larger diameter legs and/or materials more rigid than aluminium should be used. Nevertheless, as explained in the next section, from the point of view of the overall SA performance those resonances are practically harmless. The IP is designed to act as a filter in the region of the chain resonances (0.2 to 2 Hz), in order to reduce the mirror residual rms displacement.

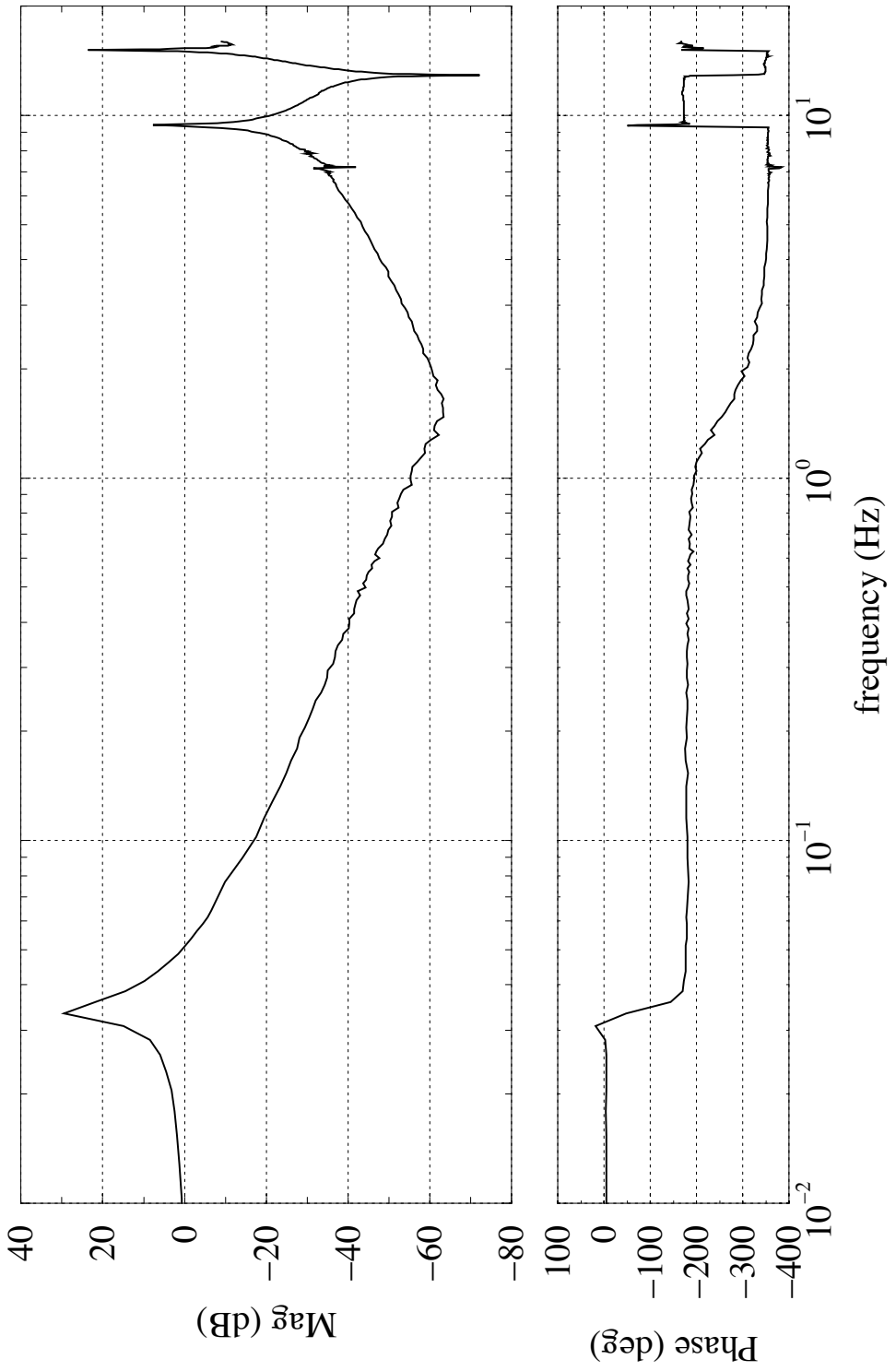

Figure 7.4: Inverted pendulum transfer function.

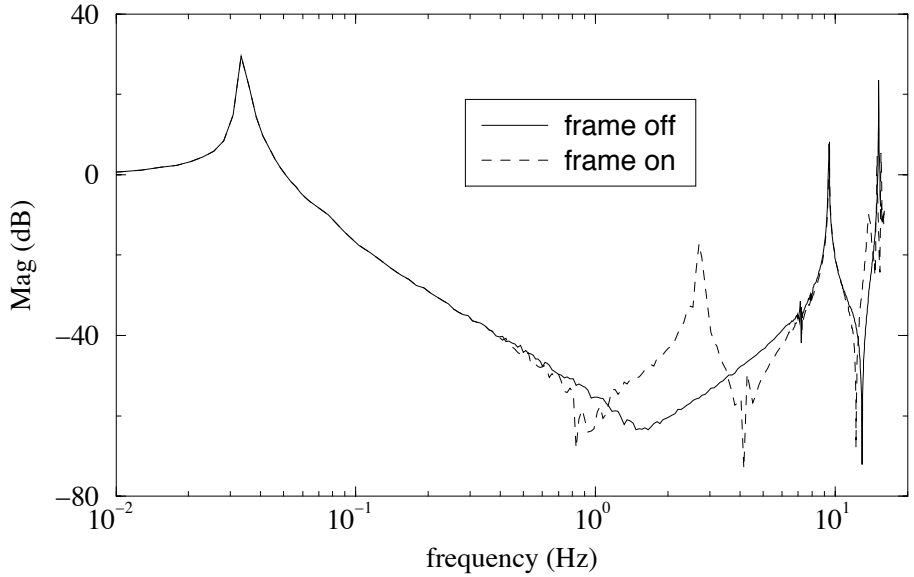

Figure 7.5: Inverted pendulum transfer functions measured with the frame connected and disconnected.

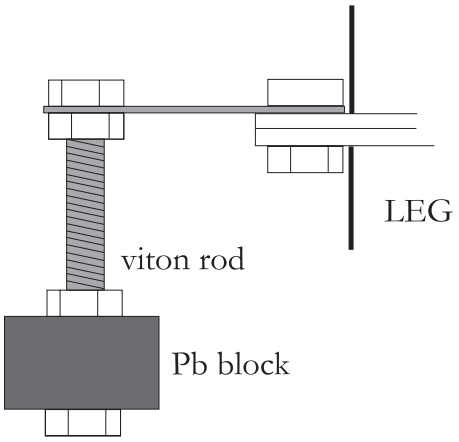

Figure 7.6: The passive damper for the leg.

7.4.3 Effect of the leg resonance

The IP acts as a filter from 30 mHz up to a few Hz. The performance at higher frequency is limited by the 9 Hz high Q leg first mode of oscillation. The experience achieved on the blade springs has been exploited to design a passive damper for the legs, to minimise the effect of the leg resonance. The damper is sketched in fig. 7.6. It is composed of a viton rod clamped to the leg mid length holding a 0.3 Kg lead block. The viton rod length can be adjusted in order to match the damper and the legs resonant frequencies. The result of the damping test is shown in fig. 7.7. A gain of 24 dB has been achieved on the peak amplitude.

The effect of the finite rigidity of the legs has been included in the simulation of the SA performance. In fig. 3.4 the residual seismic noise is compared with the thermal noise level: even without damping the peak of the legs resonance is a factor $\sim 10^3$ below the thermal noise level at 10 Hz.

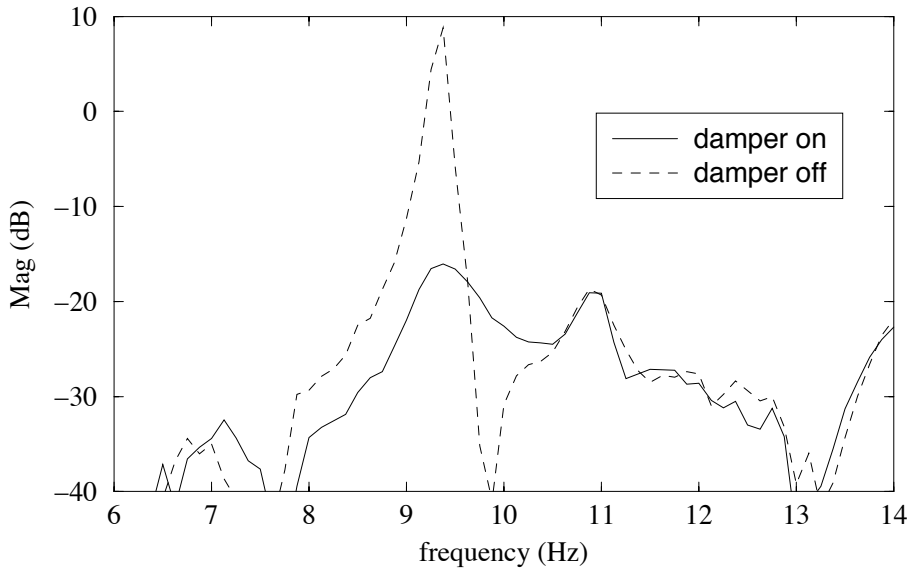

Figure 7.7: Effect of the passive damper on the leg resonance.

7.5 Centre of percussion tuning

More measurements of the transfer function with different centre of percussion tuning are shown in fig. 7.8,7.9. They have been obtained by moving the sliding part of the counterweight or by adding load to it. The curves (a) and (b) have been obtained with the movable part of the counterweight all the way up and down respectively (lowered by 3 cm): there is not notable difference. A larger effect has been measured when some lead blocks were added. The added loads were 2.7 kilos per leg (curve (c)) and 5.7 kilos per leg (curve (d)). When the movable part of the counterweight (5 kilos) and the added load are removed one obtains the curve (e). From the test it comes out that:

- the dip is moved from 1 to 5 Hz with a counterweight change of 10.7 kilos per leg, the low frequency part of the transfer function (below 0.5 Hz) remains unchanged;
- adjusting the counterweight position by a few cm has little effect: the tuning mechanism was under dimensioned;
- changing the counterweight mass is a more effective to tune of the centre of percussion position.

Despite what was expected from the mathematical model of chapter 5 the role played by the centre of percussion tuning in the actual IP prototype is of secondary importance beacause the IP attenuation is limited mostly by the legs resonance. In principle one wants to tune the counterweight in order to push the frequency of the dip at infinity. In practice, because of the presence of the legs resonance pushing the dip at high frequency worsen the isolation performance (see fig. 7.10). The best is obtained keeping the dip in the 1-5 Hz range to guarantees a $1/f^2$ behaviour below 1 Hz. Therefore, the expensive position tuning mechanism was replaced with a counterweight of variable mass.

An important and positive observation should be made about the results of fig. 7.8: ten days passed between the first and the fifth measurements without changes of the common low frequency part. We consider this reproducibility as an evidence of the stability of the system.

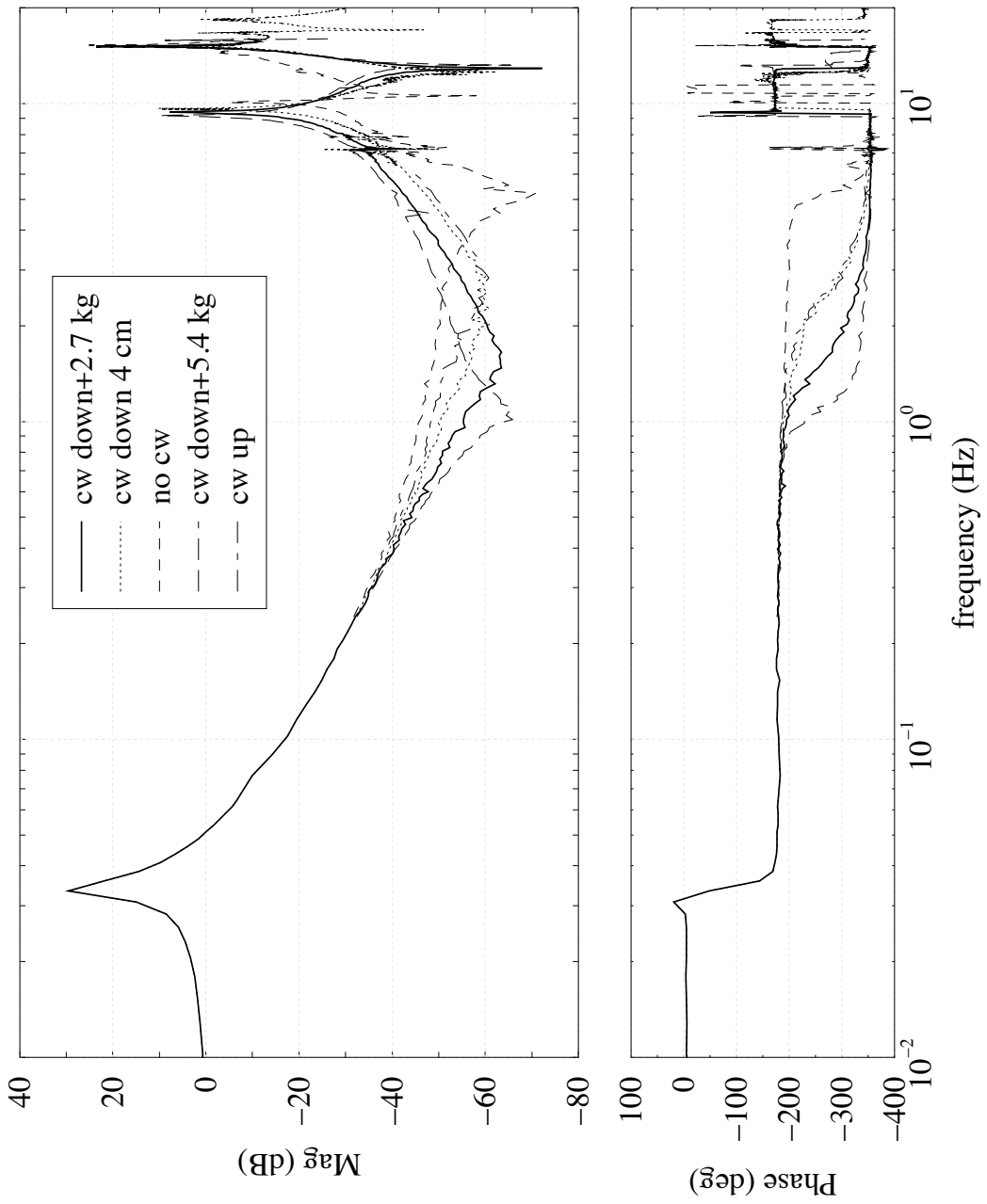

Figure 7.8: IP transfer function for different counterweight configurations.

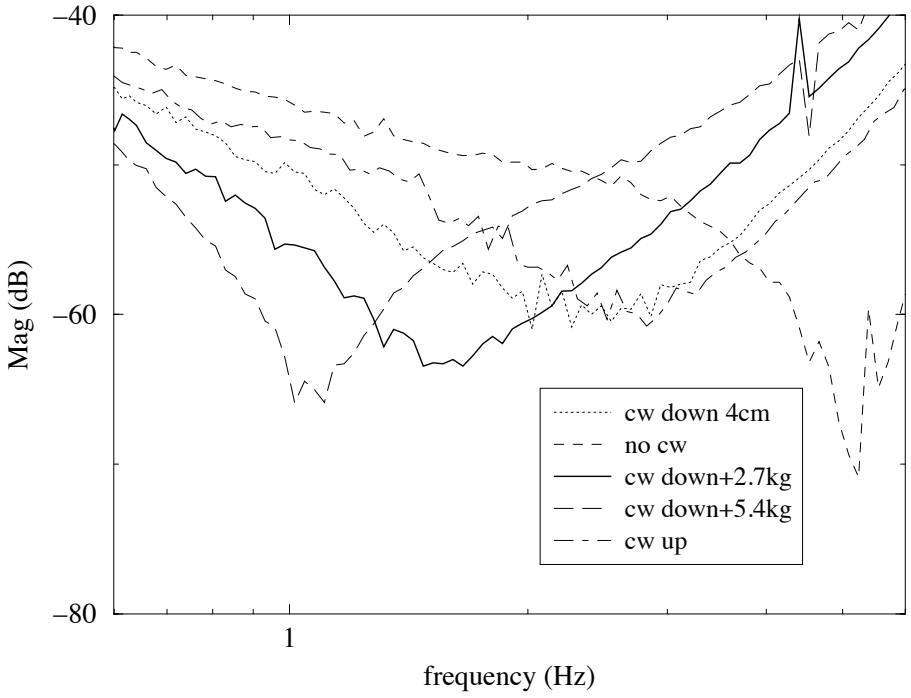

Figure 7.9: Effect of the centre of percussion tuning on the IP transfer function (zoom).

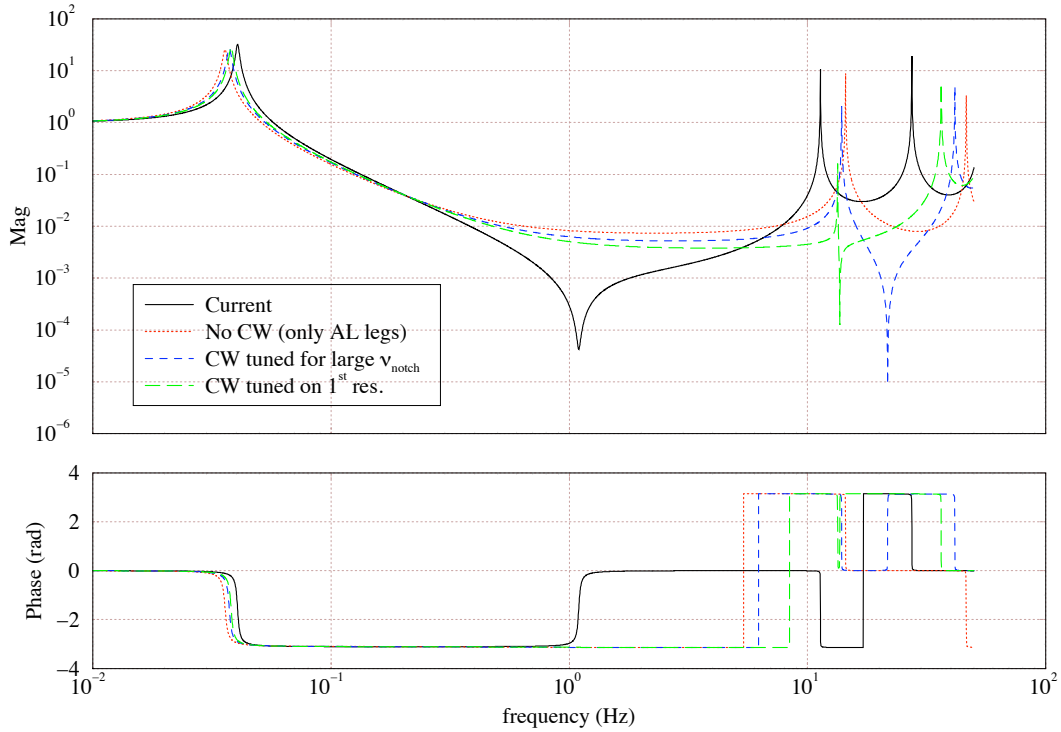

Figure 7.10: Simulated IP transfer function: pushing the c.o.p. notch at high frequency or at the frequency of the leg resonance worsen the attenuation performance in the range of interest.

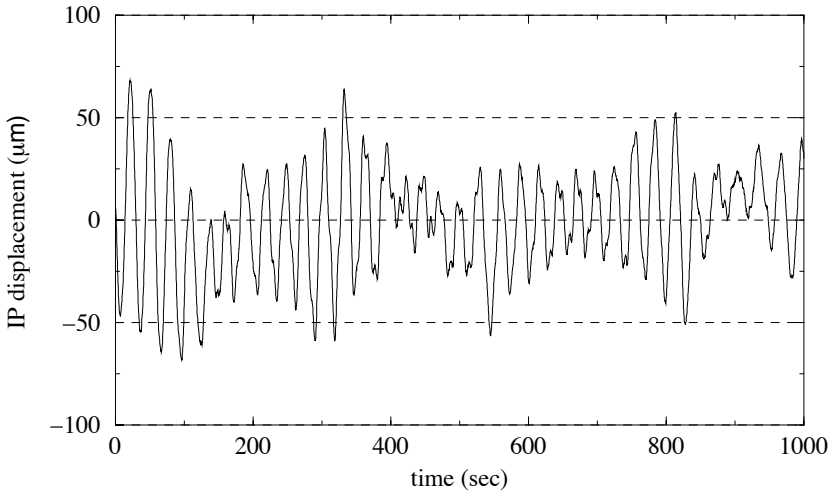

Figure 7.11: Ip motion as recorded by one of the LVDT, in a usual working day. The main oscillation has a period of 30 s. and is due an IP translation mode. The "evelope" is due to the beating of the two translation modes. Its period (about 500 s.) is compatible with a 2 mHz mode splitting.

7.6 Estimate of the rms residual noise

Fig. 7.11 shows a time record of 1000 seconds of the IP displacement measured by one of the LVDT. The rms oscillation amplitude is less than 26 μm: the measurement is compatible with the predictions. It is possible to make an estimation of the seismically excited rms resonant motion of the IP. The seismic noise at 30 mHz (measured at S.Piero INFN laboratories on a Sunday to avoid human activity noise) is

$$x_0(f_0) \sim 7 \cdot 10^{-6} \ \mathrm{m}/\sqrt{\mathrm{Hz}} \tag{7.2}$$

The intensity of seismic noise in a workday is usually larger by a factor 2-3.

It is better to estimate the rms motion by multiplying the measured transfer function times the measured ground seismic noise. In fig. 7.12 the seismic noise measured on the IP base is compared with the spectral noise expected on its top from the transfer function of fig. 7.4. Then, from the spectral residual noise we calculated the integrated rms noise:

$$x_{\mathrm{rms}}(f) = \sqrt{\int_f^\infty \tilde{x}^2(\nu) d\nu} \tag{7.3}$$

The previous equation express the rms noise as a function of the frequency where the integration starts. The function $x_{\mathrm{rms}}(f)$ is plotted in fig. 7.13. From the plot one can see that the expected undamped rms at while the rms at 10 mHz is 24 μm.

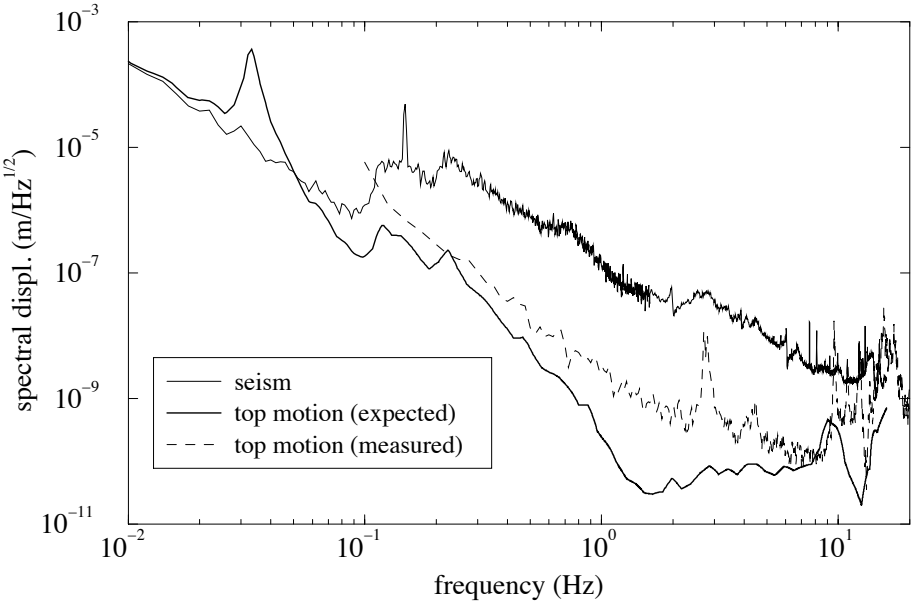

Figure 7.12: A spectrum of seismic noise measured on the IP base compared with the *expected* spectrum of the residual seism the top table, obtained multiplying the base spectrum times the IP transfer function and with the one measured on a workday: the excess noise is mainly acoustic.

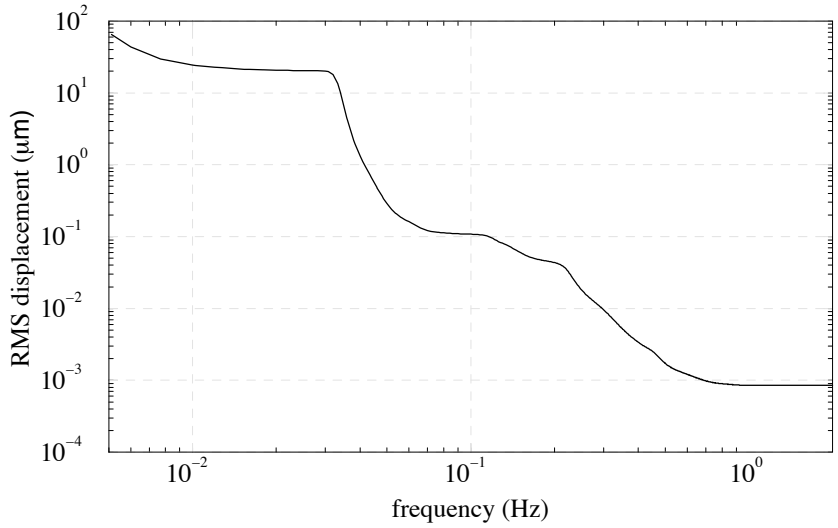

Figure 7.13: Integrated rms from the effective top table spectrum.

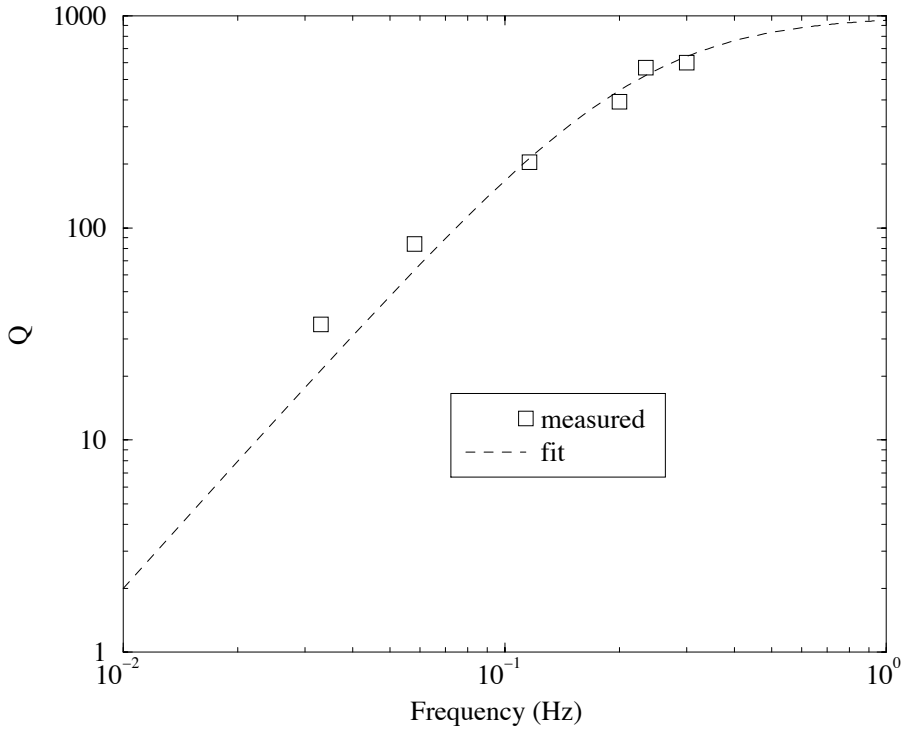

Figure 7.14: The Q of the IP as a function of the resonant frequency, fit by the function (5.53) with a value $\phi = 0.001$.

7.7 Some considerations on the IP Q and ϕ

In section 5.5 we have shown that the Q of the IP depends on that resonant frequency according to eq. (5.53), which predicts $Q \propto \omega_0^2$ at low frequency. The measurements of Q for different resonant frequencies can be used to find out an estimate of the dissipation factor ϕ. In fig. 7.14 the measured quality factors are compared with the theoretical expectations in case of structural damping (see eq. (5.53))[2]. The IP leg elasticity is in non negligible fraction contributed by the aluminium leg itself. The measured ϕ is then in part contributed by the internal dissipation in the aluminum and so, it represents an upper limit on the loss factor associated to the Maraging steel used for the flexible joints.

Some more information about the ϕ can be found out from the IP force-to-displacement transfer function phase, as discussed in section 5.5. This can be done using the new coil-magnet actuators, able to move the IP top of more than ± 1 cm, on the final IP now mounted in the Pisa laboratories.

[2]The correction factor to take into account the non zero mass of the IP legs has been included.

Chapter 8

Inverted Pendulum Control

8.1 Introduction

In the previous chapters we have described how the VIRGO suspensions are expected to be effective in depressing the seismic noise above a few Hz, where the mirror can be considered as a free mass. Up to now only the *passive* operation of the SA has been considered.

From the SA transfer function (fig. 4.9) it comes out that

- below 30 mHz the SA tracks the ground motion which is completely transmitted to the mirror. The source of the largest displacement noise in this range is expected to be the tidal deformation of the Earth crust (some hundreds of μm over a 3 km distance);
- in the SA resonance region ($0.03 < f < 2$ Hz) the ground motion is amplified due to the high Q resonances. The suspended mirrors will oscillate with an amplitude of a few tens of microns and the oscillation will have two main spectral components: 30 mHz (IP resonant frequency) and 200 mHz (first SA mode resonant frequency).

Both the tidal drift and the residual resonant motions of the mirrors are at least 8 orders of magnitude beyond the maximum rms displacement tolerable by the locking. It is the job of the IP and filter 0 active controls to eliminate or compensate these residual movements. The idea of using active vibration suppression on mirror suspension systems has been tested in several ways (see [104, 105, 106, 107, 108, 109, 60, 63, 64, 65]). In the last years, the JILA group has developed a six d.o.f. active vibration isolation system which can be suitable for applications in gravitational waves experiments [110, 111].

In this chapter an outline of the suspension control logic is given, stressing the role of the inverted pendulum as a positioning device. Experimental results of the active control of the IP prototype are presented. The work presented here is preliminary. More

theoretical studies and experimental tests will be necessary to implement the complete IP control with the SA chain suspended.

8.2 The control of the suspension

The IP top stage makes the VIRGO superattenuator suitable for the control of the mirror position. The *suspension control* aims to achieve the requirements on the rms and the spectral displacement of every optical components necessary to lock the interferometer.

The SA is provided with actuators capable of modifying the mirror position at three levels: the top stage-external frame, the steering filter-marionetta, the mirror-reference mass. The mirror control will be realised by acting hierarchically on the three points. The necessity of splitting the feedback action comes from the limited dynamic range of every physical actuator. The filter 7-marionetta actuation system as a dynamic range[1] of $10^7\ \sqrt{\text{Hz}}$. It can be shown that with this dynamic range the maximum mirror displacement which can be induced from the marionetta without introducing noise in the detection band is about 10 μm. Therefore, larger motions have to be compensated for elsewhere.

In fig. 8.1 a scheme of the hierarchical suspension control strategy is shown. The actuation points are:

- **inverted pendulum:** the largest motions to be compensated or damped are in the low frequency range, where very low forces are required to move the entire chain (and the mirror) by acting on the IP. The allowed motion is ± 1 cm in the band 0-0.1 Hz. The motor-spring actuators are used for the compensation of ultra slow drifts ($f \ll 1$ mHz), the coil-magnets are used elsewhere;
- **marionetta:** the feedback action of the steering filter upon the marionetta can control residual motions up to ± 10 μmin the band 0.1-1 Hz without introducing noise into the system;
- **mirror:** control forces can be exerted directly on the mirror from the seismic isolated reference mass at frequencies above 1 Hz, thus bypassing the wires and reducing the excitation of the violin modes.

The SA top stage has a fundamental role in the VIRGO locking strategy. Two kinds of controls are performed acting on the inverted pendulum to stabilise the mirror position within the effective marionetta dynamic range:

[1] Here the dynamic range $\tilde{d}$ is defined as:

$$\tilde{d} = \frac{F_{\max}}{F_n(f)}\ \sqrt{\text{Hz}}$$

where $F_{\max}$ is the maximum force that the actuator can exert, and $F_n(f)$ is the force spectral density noise in $\text{N}/\sqrt{\text{Hz}}$ induced by the electronic noise. This definition is very useful to characterise an actuator over a wide band.

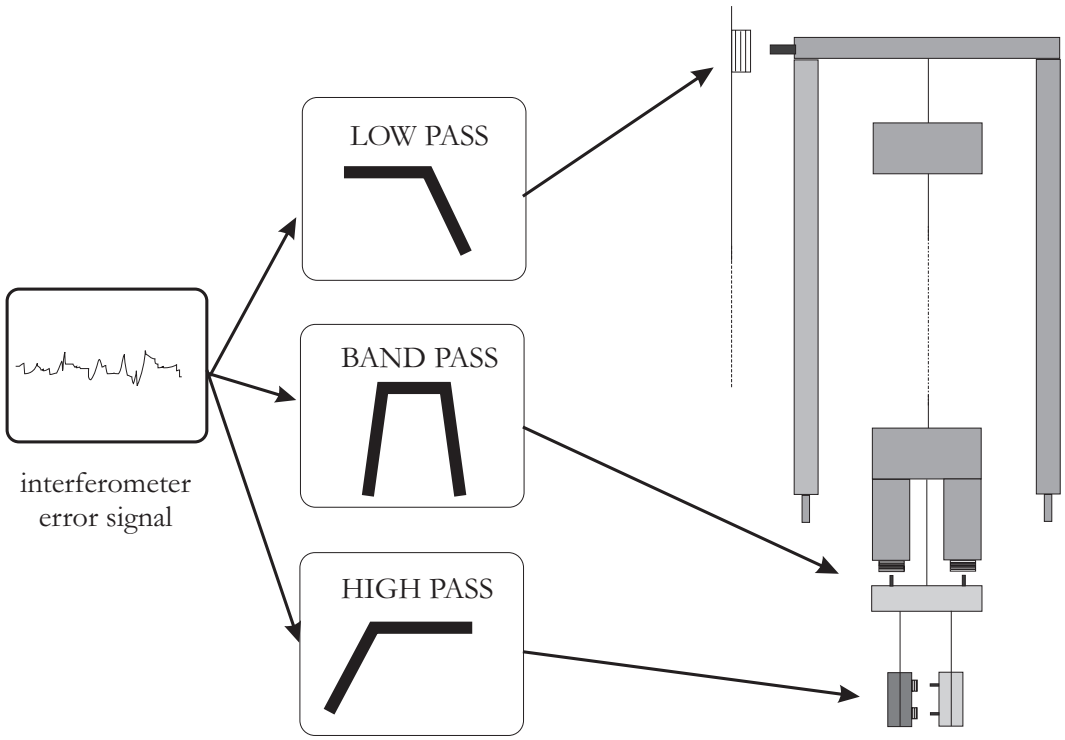

Figure 8.1: Hierarchical active control of the suspension: the error signal provided by the photodiodes is divided in 3 bands. The low frequency motions (DC-100 mHz, with a maximum amplitude ~ 10 mm) are compensated by acting on the IP, the range 0.1-1 Hz (with a maximum amplitude ~ 10 μm) is controlled by the steering filter-marionetta actuation system, while above 1 Hz forces are exerted directly on the mirror from the reference mass.

position control: it concerns the compensation of the very low frequency drifts and makes use of the low frequency part of the interferometer output as error signal. Before the locking acquisition, the preliminary positioning of the mirror will be controlled by local displacement sensors (LVDT on the IP top and CCD cameras monitoring the mirror).

The mechanical actuators (motorised springs) set the SA suspension point at the desired operation position and control it at frequencies well below 1 mHz to relieve the DC load from the electromagnetic actuators (coil-magnet pairs). The coil-magnet actuators working at nulled DC currents have the advantage that, in case of a sudden feedback failure, the SA suspension point position remains stationary and the power consumption (and heat dissipation) is minimised.

inertial damping: the residual motions of the test masses associated to the SA resonances are too large with respect to the marionetta dynamic range: to lock the interferometer, and to maintain it locked, an active damping of the IP and of the main SA normal modes is required. This control is defined *inertial damping* because accelerometers are used as sensors.

8.3 Inverted pendulum control

The IP is a 3 degree of freedom mechanical system: 3 independent sensors are required to fully determine its position and 3 independent actuators to move the IP in the required settings. The sensors and the actuators are mounted on the top stage in triangular configuration. Each sensor is, in principle, sensitive to movements in all the 3 IP normal modes (which will be defined x, y, θ, although they do not correspond necessarily to pure translations and rotations). In the same way, each actuator will generate movements of the IP involving a mix of the 3 modes. The basic idea of the IP controls, which applies both to the inertial damping and the position control, is to *diagonalise* the sensing and control actions: the aim is to pass from the sensors/actuators space, to a space where each normal mode is independently sensed and acted upon. Mathematically, this means to realize a coordinate transformation such that the equations of motions get the form:

$$\ddot{x}_i + \omega_i^2 x_i = q_i \tag{8.1}$$

where the x_i (for $i = 1, 2, 3$) is a normal mode coordinate, $\omega_i/2\pi$ is the resonant frequency of the i-th mode and q_i is the generalized force corresponding to the coordinate x_i [88]. Experimentally this means to find 3 linear combinations of the sensor outputs, defined *virtual sensors*, each sensitive to a single normal mode and, correspondingly, 3 linear combinations of the excitation coil currents (*virtual actuators*) which excite each mode separately. In control theory terminology, this means to break down a *multiple in-multiple out* (MIMO) system into many *single in-single out* (SISO) systems. The control of a SISO

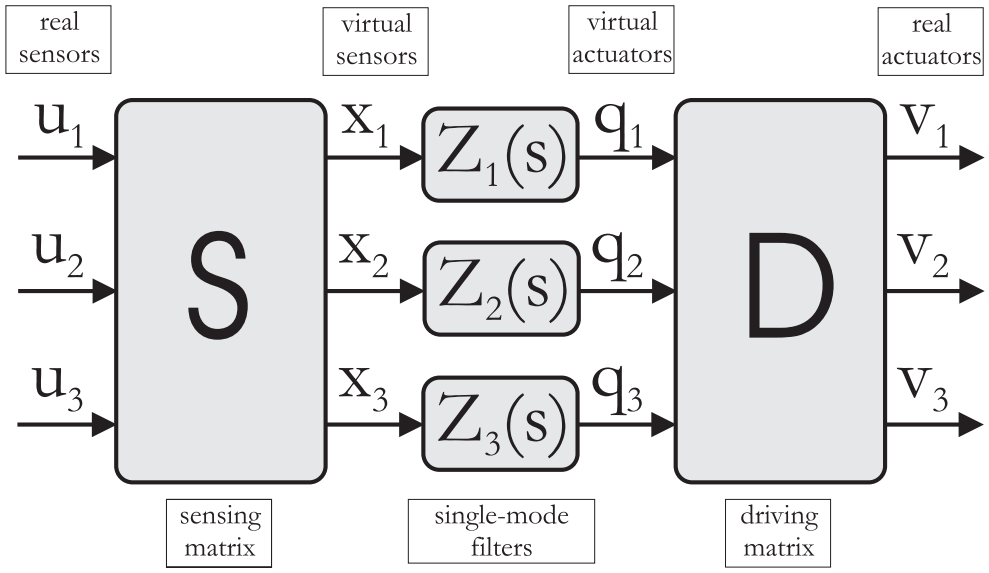

Figure 8.2: Decomposition of a 3-mode system into 3 non interacting 1-mode systems.

system is much easier: every mode is controlled by an independet feedback loop, simplifying greatly the loop design and the stability requirements. In this chapter we describe an approach to the problem which follows strictly what was done experimentally. A more general approach would require the system description in the state space representation [114] and an effort is being done in this direction [115].

8.3.1 Virtual sensors and actuators

Exciting the j-th actuator with the signal $v_j(s)$ and measuring the output signal $u_i(s)$ from the i-th sensor one obtains the 3×3 transfer function matrix $\mathbf{H} = \{h_{ij}\}$:

$$h_{ij}(s) = \frac{u_i(s)}{v_j(s)} \tag{8.2}$$

Let $\mathbf{u} = (u_1, u_2, u_3)$ be a vector made by the three physical sensor outputs and $\mathbf{v} = (v_1, v_2, v_3)$ the vector of the voltages on the three physical feedback drivers (excitation signals). Then the equation:

$$\mathbf{u} = \mathbf{H}\mathbf{v} \tag{8.3}$$

holds true by definition. Each transfer function h_{ij} is the superposition of the three normal modes[2] and can be approximated in the form:

$$h_{ij}(s) = \sum_{k=1}^{3} a_k \frac{\omega_k^2(1+i\phi_k)}{s^2+\omega_k^2+i\phi_k\omega_k^2} = \sum_k a_k P_k(s) \tag{8.4}$$

where $\omega_k/2\pi$ and ϕ_k are the resonant frequency and the loss factor of the k-th mode (the quality factor of each mode is $Q_k = 1/\phi_k$. Mathematically the task is to define a new basis and transform the (8.3) into an equation with the same form:

$$\mathbf{x} = \tilde{\mathbf{H}}\mathbf{q} \tag{8.5}$$

where $\tilde{\mathbf{H}}$ is a diagonal matrix and its elements have the form

$$\tilde{h}_{kl}(s) = \frac{x_l(s)}{q_k(s)} = \delta_{kl} \cdot b_k \left[\frac{\omega_k^2(1+i\phi_k)}{s^2+\omega_k^2+i\phi_k\omega_k^2}\right] = \delta_{kl} \cdot b_k P_k(s) \tag{8.6}$$

where δ_{kl} is the Kronecker symbol ($\delta_{kk} = 1$, $\delta_{kl} = 0$ for $k \neq l$). Each diagonal element of the transfer function matrix corresponds to a *normal mode* of the IP. We define $\mathbf{x}$ the normal modes vector and $\mathbf{q}$ the generalised force vector acting purely on that mode.

Each component x_k is naturally associated to a *virtual displacement sensor* (the desired linear combination of physical sensors sensitive to a single mode and *blind* to the others). In the same way, the component q_k of the generalised force vector can be associated to a *virtual actuator* (the linear combination of the 3 currents feeding the coils which excites just one mode). The system is well described by fig. 8.2. To experimentally determine the transformation from the real to the virtual sensors and actuators one must measure the $\mathbf{S}$ (*sensing*) and $\mathbf{D}$ (*driving*) matrices defined by the relations:

$$\mathbf{v} = \mathbf{Dq} \tag{8.7}$$

$$\mathbf{x} = \mathbf{Su} \tag{8.8}$$

such that:

$$\boxed{\mathbf{x} = [\mathbf{SHD}]\mathbf{q} = \tilde{\mathbf{H}}\mathbf{q}} \tag{8.9}$$

where $\tilde{\mathbf{H}}$ is a diagonal matrix.

[2] In a rigouorous approch it is not correct to reduce to the normal mode representation a dissipative system, because usually it is not possible to diagonalise simultaneously the kinetic energy, potential energy and dissipation matrices [88]. Nevertheless, in a phenomenological approach (see for instance [89]) the system can be described in terms of normal modes including "by hand" a dissipative term for each mode.

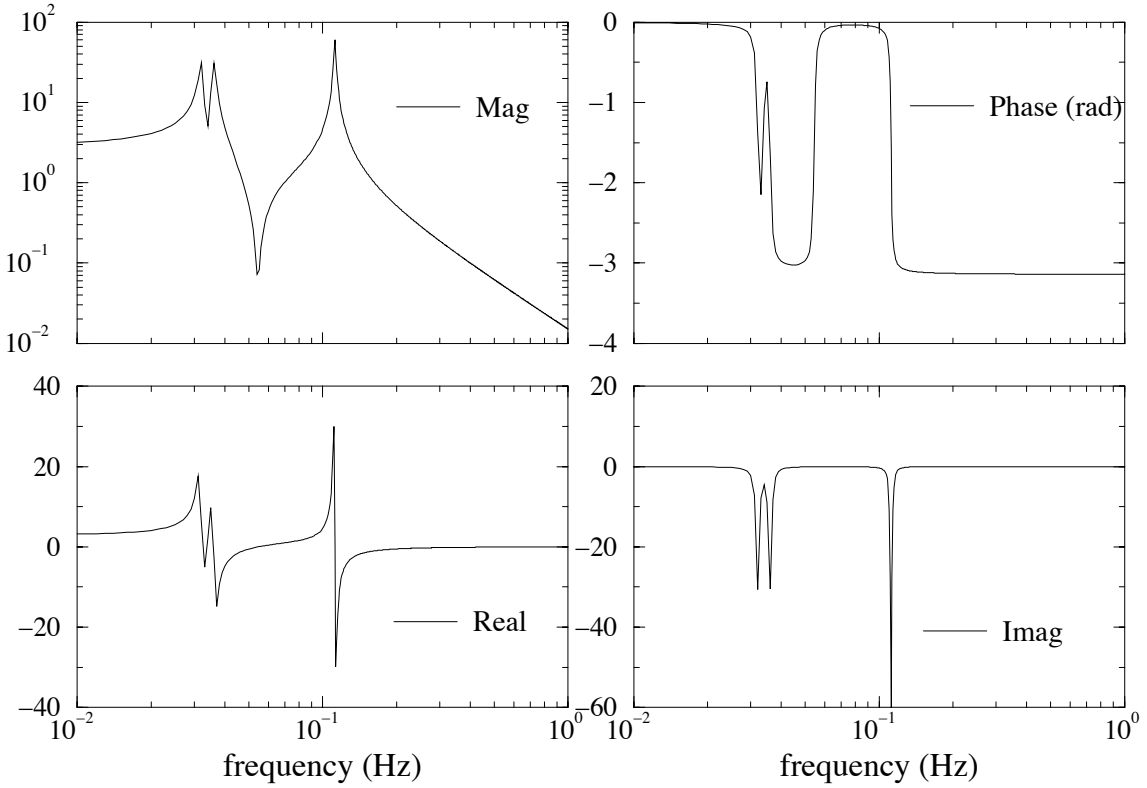

Figure 8.3: Simulation of the transfer function $h_{ij}(f)$: magnitude, phase, real part and imaginary part are shown.

8.3.2 Measurement of the sensing and driving matrices

The matrix $\mathbf{S^{-1}}$ is measured in the following way: one of the coils (for instance the coil 1) is excited with white noise and the 3 transfer functions $h_{i1}(s)$ are measured. Each $h_{i1}(s)$ shows 3 peaks (see fig. 8.3 (a) as an example). At the peaks the real part of the transfer function is zero, while the value of the imaginary part of the $h_{i1}(s)$ (magnitude and sign) carries the information on how each sensor responds to each mode (and determines $\mathbf{S^{-1}}$)[3]. In fig. 8.3 (c) and (d) the real and imaginary parts of $h_{i1}(s)$ are shown.

The detailed determination of $\mathbf{S}$ goes as follows: from (8.9) one gets

$$\mathbf{H} = \mathbf{S^{-1}}\tilde{\mathbf{H}}\mathbf{D^{-1}} \tag{8.10}$$

thence, using (8.6) and defining the matrices elements with the symbols $\mathbf{S^{-1}} = \{\sigma_{ij}\}$ and

[3]Actually, this statement is true if $Q_i \gg 1$ and if the resonant frequencies are not too close.

$\mathbf{D^{-1}} = \{\Delta_{ij}\}$ one gets:

$$\begin{aligned} h_{i1}(s) &= \sum_{k=1}^{3} \sigma_{ik}\tilde{h}_{kl}(s)\Delta_{l1} = \\ &= \sum_{k=1}^{3} b_k P_k(s)\sigma_{ik}\Delta_{k1} \end{aligned} \tag{8.11}$$

The imaginary part of the transfer function is:

$$\Im[h_{i1}(s)] = \sum_{k=1}^{3}[b_k\sigma_{ik}\Delta_{k1}]\Im[P_k(i\omega)] \tag{8.12}$$

with

$$\Im[P_k(i\omega)] = -\frac{\phi_k\omega_k^2\omega^2}{(\omega_k^2-\omega^2)^2+\phi_k^2\omega_k^4} \tag{8.13}$$

When measuring the value of the $\Im[h_{i1}(s)]$ at the resonant frequency $s = i\omega_k$ the k-th term in (8.12) dominates over the other two non resonant terms. Then the peak values of measured $\Im[h_{i1}(s)]$ can be written[4]:

$$\begin{aligned} \Im[h_{i1}(j\omega_1)] &\approx -Q_1 b_1\sigma_{i1}\Delta_{11} \\ \Im[h_{i1}(j\omega_2)] &\approx -Q_2 b_2\sigma_{i2}\Delta_{21} \\ \Im[h_{i1}(j\omega_3)] &\approx -Q_3 b_3\sigma_{i3}\Delta_{31} \end{aligned} \tag{8.14}$$

In this way 9 numbers are measured which form the matrix:

$$\begin{aligned} \mathbf{M} &= \begin{bmatrix} \Im[h_{11}(i\omega_1)] & \cdots & \Im[h_{11}(i\omega_3)] \\ \vdots & & \vdots \\ \Im[h_{31}(i\omega_1)] & \cdots & \Im[h_{31}(i\omega_3)] \end{bmatrix} = \\ &= \begin{bmatrix} -Q_1 b_1\sigma_{11}\Delta_{11} & \cdots & -Q_3 b_3\sigma_{13}\Delta_{31} \\ \vdots & & \vdots \\ -Q_1 b_1\sigma_{31}\Delta_{11} & \cdots & -Q_3 b_3\sigma_{33}\Delta_{31} \end{bmatrix} \end{aligned} \tag{8.15}$$

The matrix $\mathbf{M}$ is immediately rewritten in terms of the columns of $\mathbf{S^{-1}}$:

$$\mathbf{M} = \left[\alpha_1\sigma^{(1)}, \alpha_2\sigma^{(2)}, \alpha_3\sigma^{(3)}\right] \tag{8.16}$$

with $\alpha_k = -Q_k b_k \Delta_{k1}$.

[4]This approximation is the main source of error in the sensing matrix determination. Its validity is discussed in section 8.4.4.

The matrix $\mathbf{M}$ is physically equivalent to $\mathbf{S^{-1}}$: the response of the three sensors to the k-th mode is:

$$\mathbf{u} = \sigma^{(1)} x_k \tag{8.17}$$

If $\mathbf{M}$ is used instead of $\mathbf{S^{-1}}$ one gets:

$$\mathbf{u'} = \alpha_k \sigma^{(1)} x_k \tag{8.18}$$

that is, the response of each sensor to the k-th mode is amplified by a gain factor α_k. Then, the only effect of using $\mathbf{M}$ instead of $\mathbf{S^{-1}}$ is a scaling of the sensors response to the different modes[5]: $\mathbf{M}$ is physically equivalent to $\mathbf{S^{-1}}$. Therefore, the sensing matrix $\mathbf{S}$ is obtained simply inverting $\mathbf{M}$.

Once the sensing matrix is obtained, to determine $\mathbf{D}$ we started from the relation

$$\mathbf{x} = \mathbf{SHv} = \mathbf{N}(s)\mathbf{v} \tag{8.22}$$

where $\mathbf{N}(s) = \mathbf{SH}(s) = \{n_{ij}\}$. The matrix element $n_{ij}(s)$ is the transfer function between the j-th *physical* actuator and the i-th *virtual* sensor. $\mathbf{N}(s)$ is a frequency dependent matrix. On the other hand the aim is to measure the frequency independent $\mathbf{D}$. One easy way to achieve the result is to measure n_{ij} at a given frequency. Namely, one can excite the k-th actuator with a sinusoidal signal at frequency ν_k and measure the 9 numbers:

$$\begin{aligned} \frac{x_i(s_1)}{v_1} &= n_{i1}(s_1) \\ \frac{x_i(s_2)}{v_2} &= n_{i2}(s_2) \qquad \text{for } i = 1,2,3 \\ \frac{x_i(s_3)}{v_3} &= n_{i3}(s_3) \end{aligned} \tag{8.23}$$

where $s_k = i \cdot 2\pi\nu_k$ The measured numbers are complex and may be written in the form

$$n_{ij} = |n_{ij}(\nu_j)|\, e^{i\phi_{ij}(\nu_j)} \tag{8.24}$$

[5]The problem may by considered from a different point of view. The two matrices satisfy the equation:

$$\mathbf{S^{-1}} = \mathbf{\Lambda M} \tag{8.19}$$

where

$$\mathbf{\Lambda} = \mathrm{diag}\{\alpha_1^{-1}, \alpha_2^{-1}, \alpha_3^{-1}\} \tag{8.20}$$

is the gain matrix. The following relation between the vectors $\mathbf{u}$ and $\mathbf{u'}$ holds:

$$\mathbf{u'} = \mathbf{\Lambda u} \tag{8.21}$$

Equation (8.21) says that the effect of using $\mathbf{M}$ instead of $\mathbf{S^{-1}}$ is that of changing the modulus of the basis vectors but not their directions.

If the excitation frequencies are small ($\nu_k \ll \omega_1/2\pi$), one can show that the imaginary parts of the matrix elements are negligible, and it is

$$\phi_{ij}(\nu_j) \approx \begin{cases} 0 \\ \pi \end{cases} \tag{8.25}$$

It comes out that the phase term $e^{i\phi_{ij}(\nu_j)}$ simply determines the sign of the matrix element. Comparing the (8.24) with the relation

$$\mathbf{N} = \mathbf{SH} = \tilde{\mathbf{H}}\mathbf{D^{-1}} \tag{8.26}$$

one finds out that $\mathbf{N}$ is physically equivalent to $\mathbf{D^{-1}}$. The effect of multiplying $\mathbf{D^{-1}}$ times the diagonal matrix $\tilde{\mathbf{H}}$ is just a scaling of the matrix lines. Each line of $\mathbf{D^{-1}}$ describes the combination the currents to the 3 coils that excite a single mode. Line scaling just changes the amplitude of the mode excitation without changing the ratios of the coil currents. The driving matrix $\mathbf{D}$ can be simply found inverting $\mathbf{N}$. The main steps of the diagonalisation procedure are schematically represented in fig. 8.4.

8.4 Test of the IP as a positioning stage

In this section the strategy adopted for the IP positioning is described. The main points are:

- the position sensors diagonalisation;
- the mechanical actuators diagonalisation;
- the feedback filter design.

8.4.1 Position sensors diagonalisation (1^{st} step)

As explained in section 8.3.2, to measure $\mathbf{S^{-1}}$ we excited the IP by means of the coil 1 and measured the value of $\Im[h_{1i}]$ at the resonances f_x, f_y, f_θ. In fig. 8.5 transfer functions h_{11}, $\Im[h_{11}]$, $\Re[h_{11}]$ are shown as an example. The resonant frequencies are:

$$\begin{cases} f_x = 32 \text{ mHz} \\ f_y = 36 \text{ mHz} \\ f_\theta = 112 \text{ mHz} \end{cases}$$

To observe the splitting of the x and y modes a resolution of at least 1 mHz is required and at least 1000 seconds per each measurement were needed. In fact, the measurement times are even longer when averages are required or when a "catastrophic event", such as a door violently shut, affects the measurement.

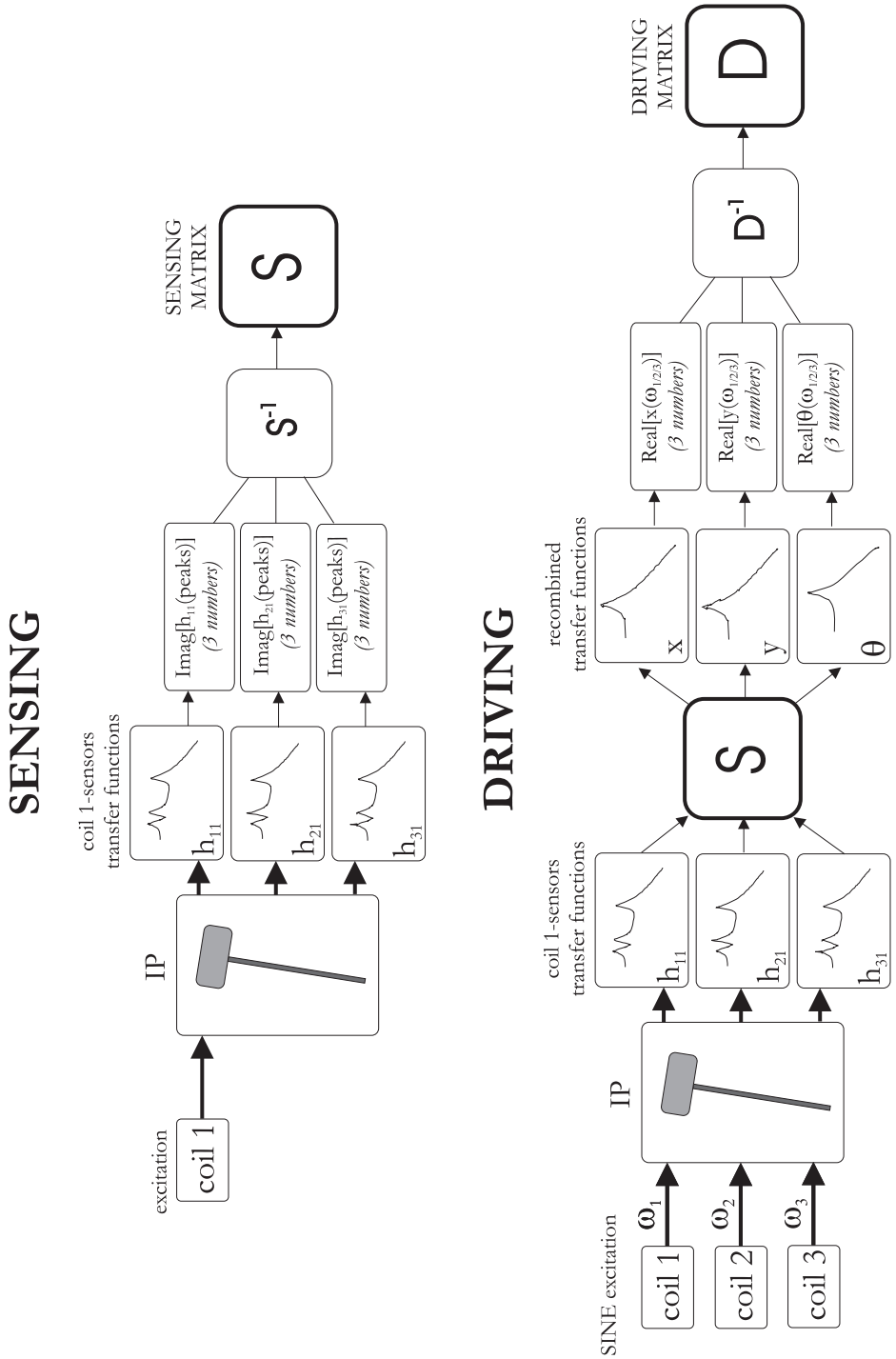

Figure 8.4: Logical scheme explaining the steps followed to measure the sensing and driving matrices.

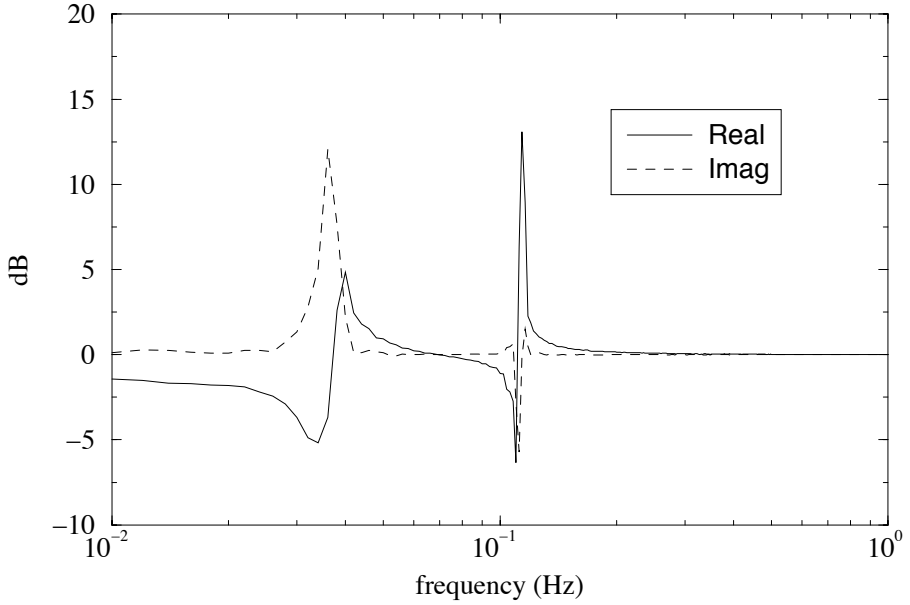

Figure 8.5: Real and imaginary parts of the measured transfer function $h_{11}(f)$: the real part is null at the resonance.

The measured $\mathbf{M}$ is:

$$\begin{bmatrix} \Im[h_{11}(i\omega_x)] & \cdots & \Im[h_{11}(i\omega_\theta)] \\ \vdots & & \vdots \\ \Im[h_{13}(i\omega_x)] & \cdots & \Im[h_{13}(i\omega_\theta)] \end{bmatrix} = \begin{bmatrix} -8.51 & -28.8 & -4.55 \\ 72.3 & 11.2 & -3.74 \\ -33.6 & 21.1 & -5.03 \end{bmatrix}$$

The equivalent sensing matrix $\mathbf{S}$ is obtained by inverting of $\mathbf{M}$ and scaling the lines of the matrix obtained:

$$\mathbf{S} = \begin{bmatrix} -0.09 & 1 & -0.66 \\ -1 & 0.22 & 0.74 \\ -0.96 & -0.58 & -1 \end{bmatrix} \tag{8.27}$$

An important observation should be done on the structure of the sensing matrix: the elements of the third line are all negative: this is the case when the sensor signals are all in phase and it corresponds to a rotation of the IP: the third line of $\mathbf{S}$ contains the information about the θ normal mode, while the first two lines correspond to the two translation modes.

8.4.2 Actuators diagonalisation (1st step)

To measure $\tilde{\mathbf{D}}$ we follow the procedure described in section 8.3.2. The coils were excited with sinusoidal signals of the same amplitude at frequencies $\nu_1 = 12$, $\nu_2 = 16$, $\nu_3 = 20$ mHz respectively and observed the 3 *virtual* sensors: the k-th peak amplitude carries the information of each single mode response to the k-th coil. Thus, we measured the numbers described by (8.24) and obtained:

$$\mathbf{N} = \begin{bmatrix} 253 & 176 & 163 \\ 127 & 230 & 164 \\ 203 & 151 & 291 \end{bmatrix} \tag{8.28}$$

The driving matrix $\mathbf{D}$ is obtained inverting $\mathbf{N}$ and scaling the columns by the arbitrary gain. The result is:

$$\mathbf{D} = \begin{bmatrix} -0.54 & -1 & -1 \\ 1 & 0.07 & -0.62 \\ -0.31 & 0.90 & -0.93 \end{bmatrix} \tag{8.29}$$

The elements of the third columns are all negative: the three actuators acts in phase and excite the θ mode.

To check if the diagonalisation is effective we excited with white noise each individual virtual actuators and monitored the virtual sensors response. The result is shown in fig. 8.6.

8.4.3 Diagonalisation results (1st step)

Fig. 8.6 shows clearly that the diagonalisation is not "perfect". Several sources of error affect the determination of the sensing and driving matrices and are discussed in the next session. Here we want to evaluate numerically how good the diagonalisation is. It is evident that the diagonalisation fails at high frequency where the signal-to-noise ratio is too low, but this is not important for the position control we want to implement. The residual coupling can be evaluated directly at the resonant peaks or at the DC level.

Evaluation of coupling at the resonant peaks: when the k-th mode is excited the resonant peak at frequency $\omega_k/2\pi$ is visible also in the non excited modes due to non perfect decoupling. The effect is particularly evident in the third plot of fig. 8.6 (θ excited). The ratio the peak height in the excited mode with respect to the same peak in the other modes is a measurement of the coupling. We define the coupling matrix $\mathbf{C} = \{c_{ij}\}$ where, for instance:

$$c_{13} = c_{x\theta} = \frac{\text{height of the } \theta \text{ peak in the non excited mode } x}{\text{height of the peak of the excited mode } \theta}$$

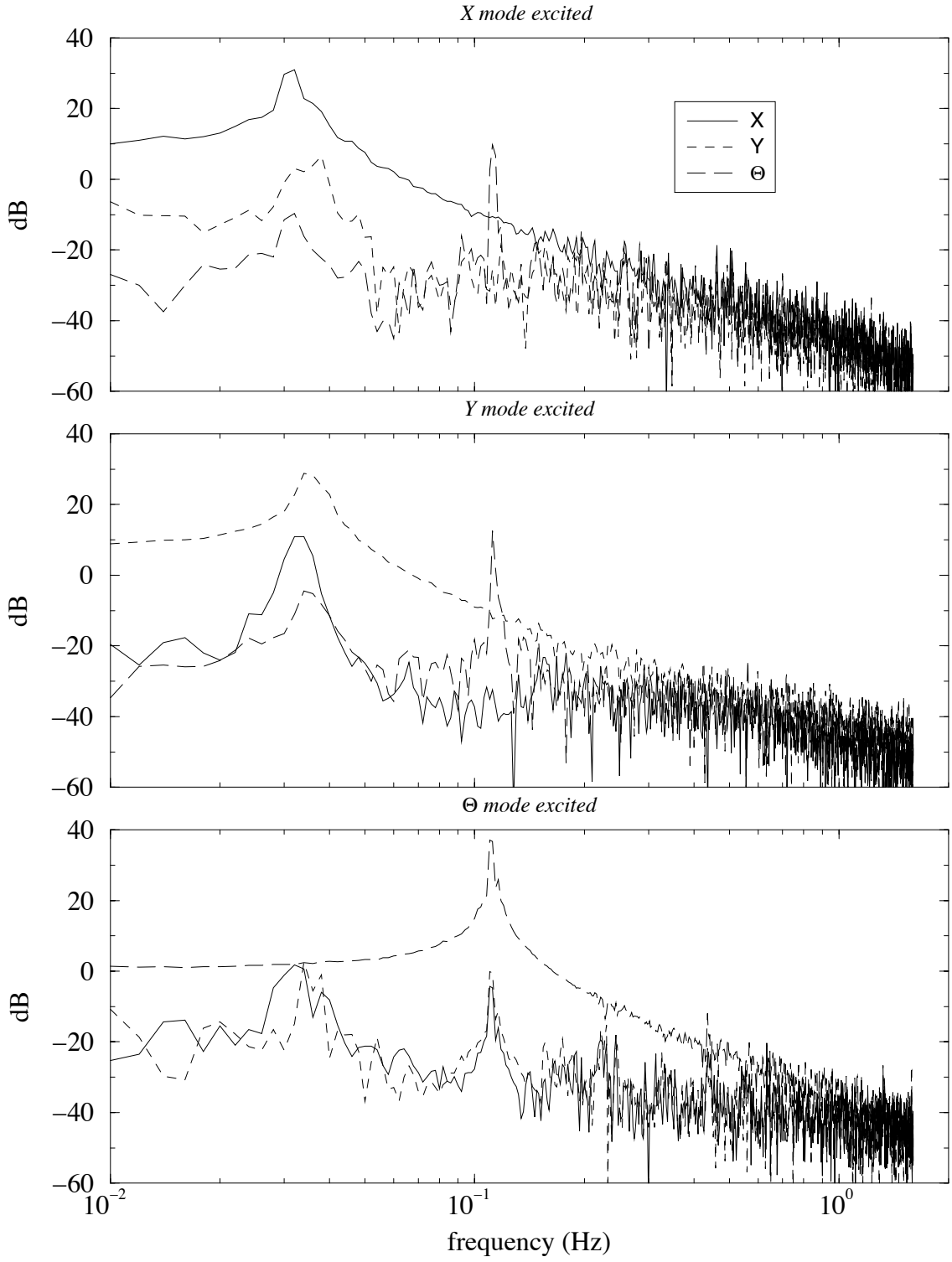

Figure 8.6: Transfer functions of the diagonalised system with x mode excited, y mode excited, θ mode excited respectively.

This definition is not suitable for the diagonal elements, but it is straightforward to define $c_{kk} = 1$. The matrix elements have been measured from the data:

$$\mathbf{C} = \begin{bmatrix} 1 & 7.1 \cdot 10^{-2} & 8.4 \cdot 10^{-3} \\ 3.9 \cdot 10^{-2} & 1 & 1.5 \cdot 10^{-2} \\ 9.4 \cdot 10^{-3} & 2.1 \cdot 10^{-2} & 1 \end{bmatrix} \tag{8.30}$$

The matrix $\mathbf{C}$ is expected to be symmetric. The asymmetry allows to estimate the error on the matrix elements, and we can summarize the coupling factors:

$$c_{xy} = c_{yx} = (5.5 \pm 1.5) \cdot 10^{-2} \tag{8.31}$$
$$c_{x\theta} = c_{\theta x} = (8.9 \pm 0.5) \cdot 10^{-3} \tag{8.32}$$
$$c_{y\theta} = c_{\theta y} = (1.8 \pm 0.3) \cdot 10^{-2} \tag{8.33}$$

Evaluation of coupling at DC: the values of the measured transfer functions of fig. 8.6 at DC (well below the resonant frequencies) are a measurement of the matrix $\tilde{\mathbf{H}}$ in that range. The DC levels have been measured by averaging the points below 20 mHz. The result is:

$$\tilde{\mathbf{H}}_{\mathbf{DC}} = \begin{bmatrix} 3.4 \pm 0.4 & 0.15 \pm 0.15 & 0.25 \pm 0.15 \\ 0.3 \pm 0.2 & 2.9 \pm 0.2 & 0.15 \pm 0.15 \\ 0.04 \pm 0.02 & 0.06 \pm 0.02 & 1.16 \pm 0.04 \end{bmatrix} \tag{8.34}$$

The columns of the matrix $\tilde{\mathbf{H}}_{\mathbf{DC}}$ can be normalized so that the DC level of the excited mode is 1 (this is equivalent to rescaling each plot of fig. 8.6, without changing the modes ratio) and one gets:

$$\tilde{\mathbf{H}}_{\mathbf{DC}} = \begin{bmatrix} 1 & 5 \cdot 10^{-2} & 2 \cdot 10^{-1} \\ 9 \cdot 10^{-2} & 1 & 10^{-1} \\ 10^{-2} & 2 \cdot 10^{-2} & 1 \end{bmatrix} \tag{8.35}$$

Maximum DC couplings of 10% are measured.

8.4.4 Errors

The coupling matrices $\mathbf{C}$ and $\tilde{\mathbf{H}}_{\mathbf{DC}}$ obtained above present both diagonal dominance but with different values of the couplings. This seems to indicate that the hypothesys of frequency independent diagonalisation may be wrong. This is the case when the system is non linear: the coil-magnet actuators used have response that can be considered linear only in a limited range (a few mm). Moreover, the SNR in the DC region for the non excited modes is low and, consequently, the measurement of the couplings with the second method is less reliable.

The residual couplings between the modes is associated to several effects of different nature:

the approximations used: the approximation of eq. (8.15) (where the contribution of the non-resonant terms has been neglected) introduces an error of about 2% on the elements of the columns 1 and 2 of the matrix $\mathbf{S^{-1}}$. As a demonstration, let us compare the resonant term $\Im[P_k(i2\pi f_k)]$ with the non resonant ones $\Im[P_l(i2\pi f_k)]$ ($l \neq k$). Using eq. (8.13) one can calculate the ratio:

$$\frac{\Im[P_l(i2\pi f_k)]}{\Im[P_k(i2\pi f_k)]} = \left(\frac{f_l}{f_k}\right)^2 \frac{1}{Q_k^2\left(1-\frac{f_l^2}{f_k^2}\right)^2+1} \tag{8.36}$$

Using the measured frequencies and quality factor one gets:

$$\frac{\Im[P_y(i2\pi f_x)]}{\Im[P_x(i2\pi f_x)]} \approx 0.02 \qquad \frac{\Im[P_\theta(i2\pi f_x)]}{\Im[P_x(i2\pi f_x)]} \approx 10^{-4} \tag{8.37}$$

The calculations for the other P_k lead to similar results which can be summarized in this way: in the matrix $\mathbf{S^{-1}}$ the columns 1 and 2 (associated to the translation modes) are coupled to a level of about 2%, while the coupling with the θ mode is negligible. The error on the sensing matrix propagates also to the driving matrix $\mathbf{D}$ (see eq. (8.26)). The coupling associated to this effect can be reduced by iterating the diagonalisation procedure;

non linear effects: a relevant contribution to the residual coupling comes from the limited linear range of the coil magnet actuators: for a correct operation, the magnet should move around a point at distance $R/2$ from the center of the coil of radius R (see fig. 6.8). This is not guaranteed by the setup geometry. It may happen one or more coils to work in non linear regime, where a slight change in the IP equilibrium position leads to a substantial change in the actuator response. The size of the effect can be estimated from fig. 6.8 (a): suppose that one of the magnet is at distance 20 mm from the coil center (instead of 17 mm, proper working point). In this point the actuator response changes of $\delta\alpha \approx 1.5 \cdot 10^{-2}$ N/A $\cdot$ mm which corresponds to a relative variation

$$\frac{\delta\alpha}{\alpha} \approx 2.5\ \%/\text{mm}$$

The effect is even larger ($\approx$10%/mm) if the magnet distance from the coil is less than $R/2$. Such an error on a single coil affects the corresponding column of the matrix $\mathbf{D}$ coupling the 3 modes. We can say that the driving matrix is *unstable* with respect to small changes ($\sim$ 1 mm) of the IP operation position. This problem will be solved by using the new coil-magnet actuators described in chapter 6 (see fig. 6.8 (b)).

variation of the system parameters with the time: in section 5.8 we have shown that the IP resonant frequencies are expected to change with the temperature. A maximum variation of 2 mHz during the day has been observed. This effect may change the coupling of the two transation modes.

8.4.5 Improving the sensors and actuators diagonalisation

It is possible to improve the result, either by simply reiterating the diagonalisation process or using a different method. Eventually the matrix accuracy will be limited by external perturbations and non linear effects, and large improvements can be obtained only by improving the setup. Still, the exercise is useful.

The system of virtual sensors and actuators is still described by eq. (8.9), where $\tilde{\mathbf{H}}$ is only close to be diagonal. The aim is to find two correction matrices $\tilde{\mathbf{S}}$ and $\tilde{\mathbf{D}}$ such that

$$\bar{\mathbf{H}} = \tilde{\mathbf{S}}\tilde{\mathbf{H}}\tilde{\mathbf{D}} \tag{8.38}$$

is a "truly" diagonal matrix (or better, with a larger diagonal dominance with respect to $\tilde{\mathbf{H}}$.

The basic idea of this method is to algebraically diagonalise $\tilde{\mathbf{D}}$ at two given non resonant frequencies, assuming that the sensing and the driving matrices do not depend on frequency and, consequently, the diagonalisation is the same over the whole range of interest. The two frequencies are chosen one well above and one well below the normal mode frequencies, because in these conditions ("far from the peaks") the imaginary parts of the transfer functions are negligible.

We measured the matrix $\tilde{\mathbf{H}}(\mathbf{s})$ at f_a =14 mHz (below the normal mode frequencies) and at f_b =320 mHz (above the normal mode frequencies) and defined:

$$\begin{aligned}
\mathbf{M_1} = \tilde{\mathbf{H}}(i2\pi f_a) &= \begin{bmatrix} 2553 & 64 & 39 \\ -5 & 2006 & 25 \\ -22 & 39 & 783 \end{bmatrix} \\
\mathbf{M_2} = \tilde{\mathbf{H}}(i2\pi f_b) &= \begin{bmatrix} -157 & -9 & 24 \\ -12 & -199 & 44 \\ -11 & -26 & -852 \end{bmatrix}
\end{aligned} \tag{8.39}$$

$\mathbf{M_1}$ and $\mathbf{M_2}$, because of the choice of f_a and f_b, are real matrices. An observation should be done: $\mathbf{M_1}$ and $\mathbf{M_2}$ show diagonal dominance, but some of their off diagonal elements are not negligible. Then we calculated the matrix

$$\mathbf{L} = \begin{bmatrix} 0.99 & -0.08 & 0.03 \\ 0.13 & -0.99 & 0.06 \\ 0.01 & 0.01 & -1.00 \end{bmatrix} \tag{8.40}$$

which diagonalises the matrix $\mathbf{M_1 M_2^{-1}}$. Numerically

$$\mathbf{L^{-1} M_1 M_2^{-1} L} = \mathrm{diag}\{-16.3, -10.0, -0.92\} \tag{8.41}$$

where the three diagonal elements are the eigenvalues of $\mathbf{M_1 M_2^{-1}}$ and the columns of $\mathbf{L}$ are the corresponding eigenvectors.

We show in the following that the matrices

$$\begin{cases} \tilde{\mathbf{S}} = \mathbf{L^{-1}} \\ \tilde{\mathbf{D}} = \mathbf{M_2^{-1}L} \end{cases} \tag{8.42}$$

diagonalise $\tilde{\mathbf{H}}$ at $f = f_a$ and $f = f_b$. Using (8.38), (8.41) and (8.42):

$$\begin{array}{rcl} \bar{\mathbf{H}}(i2\pi f_a) & = & \mathbf{L^{-1}}\tilde{\mathbf{H}}(i2\pi f_a)\mathbf{M_2^{-1}L} = \mathbf{L^{-1}M_1M_2^{-1}L} = \text{diagonal} \\ \bar{\mathbf{H}}(i2\pi f_b) & = & \mathbf{L^{-1}}\tilde{\mathbf{H}}(i2\pi f_b)\mathbf{M_2^{-1}L} = \mathbf{L^{-1}M_2M_2^{-1}L} = \mathbf{I} \end{array} \tag{8.43}$$

where $\mathbf{I}$ is the identical matrix.

The matrices $\tilde{\mathbf{S}}$ and $\tilde{\mathbf{D}}$ allow to transform the coordinates $(\mathbf{x}, \mathbf{q})$ obtained with the 1^{st} step diagonalisation into the new coordinates $(\bar{\mathbf{x}}, \bar{\mathbf{q}})$, for which

$$\bar{\mathbf{x}} = \bar{\mathbf{H}}\bar{\mathbf{q}} \tag{8.44}$$

To write $(\bar{\mathbf{x}}, \bar{\mathbf{q}})$ in terms of $(\mathbf{u}, \mathbf{v})$, the original real sensors and actuators coordinates, one can rewrite (8.38) as a function of the actuator-to-sensor transfer function matrix $\mathbf{H}$:

$$\bar{\mathbf{H}} = \tilde{\mathbf{S}}\tilde{\mathbf{H}}\tilde{\mathbf{D}} = \mathbf{L^{-1}}\left[\mathbf{SHD}\right]\mathbf{M_2^{-1}L} = \bar{\mathbf{S}}\mathbf{H}\bar{\mathbf{D}} \tag{8.45}$$

where

$$\begin{cases} \bar{\mathbf{S}} = \mathbf{L^{-1}S} \\ \bar{\mathbf{D}} = \mathbf{DM_2^{-1}L} \end{cases} \tag{8.46}$$

It can be shown that the following relations between the old and the new coordinates hold:

$$\mathbf{v} = \bar{\mathbf{D}}\bar{\mathbf{q}} \tag{8.47}$$

$$\bar{\mathbf{x}} = \bar{\mathbf{S}}\mathbf{u} \tag{8.48}$$

The previous relations have the same form of the equations (8.7) and (8.8) which defined the new sensing and driving matrices. Numerically:

$$\begin{aligned} \bar{\mathbf{S}} = \mathbf{L^{-1}S} &= \begin{bmatrix} 0.04 & 1 & 0.93 \\ -1 & -0.30 & 0.56 \\ 0.77 & -0.54 & 1 \end{bmatrix} \\ \bar{\mathbf{D}} = \mathbf{DM_2^{-1}L} &= \begin{bmatrix} -0.37 & -1 & -0.99 \\ 1 & 0.12 & -0.67 \\ -0.45 & 0.92 & -1 \end{bmatrix} \end{aligned} \tag{8.49}$$

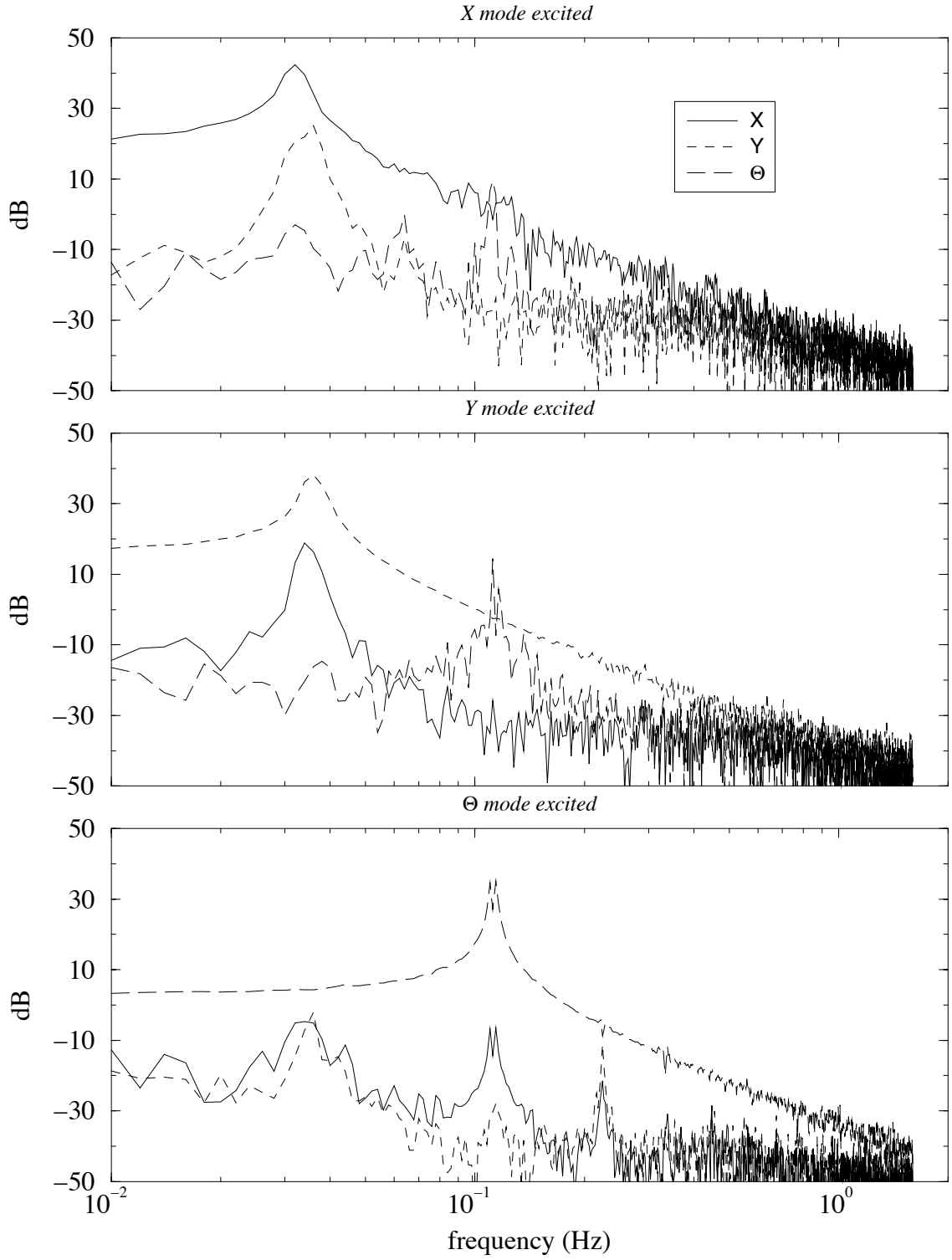

Figure 8.7: Transfer functions of the diagonalised system (second step): a) x mode excited, b) y mode excited, θ mode excited.

8.4.6 Diagonalisation results (2^{st} step)

The result of the 2^{st} step diagonalisation is shown in fig. 8.7 and must be compared with that of fig. 8.6. As in section 8.4.3 we calculate the couplings factors at the resonant peaks:

$$c_{xy} = c_{yx} = (8.1 \pm 0.1) \cdot 10^{-2} \quad (8.50)$$
$$c_{x\theta} = c_{\theta x} = (7.0 \pm 1.5) \cdot 10^{-3} \quad (8.51)$$
$$c_{y\theta} = c_{\theta y} = (1.3 \pm 0.5) \cdot 10^{-3} \quad (8.52)$$

and the transfer function matrix at DC:

$$\tilde{\mathbf{H}}^{(\mathbf{2})}_{\mathbf{DC}} = \begin{bmatrix} 11.0 \pm 0.5 & 0.5 \pm 0.4 & 0.35 \pm 0.3 \\ 0.4 \pm 0.2 & 7.4 \pm 0.3 & 0.20 \pm 0.15 \\ 0.3 \pm 0.2 & 0.11 \pm 0.05 & 1.47 \pm 0.03 \end{bmatrix} \quad (8.53)$$

which, rescaling the columns becomes:

$$\tilde{\mathbf{H}}_{\mathbf{DC}} = \begin{bmatrix} 1 & 7 \cdot 10^{-2} & 2 \cdot 10^{-1} \\ 4 \cdot 10^{-2} & 1 & 10^{-1} \\ 3 \cdot 10^{-2} & 10^{-2} & 1 \end{bmatrix} \quad (8.54)$$

The more significant improvement with respect to the 1^{st} step result is that the $y - \theta$ peak coupling factor has been reduced of more than one order of magnitude. Again, the maximum coupling factor is about 10%, due mostly to the non linear behavior of the actuators.

8.4.7 Diagonalisation of the mechanical actuators

The sensing matrix obtained before was used also to determine the driving matrix of the mechanical actuators. The driving matrix for the motors was measured at the same way as that for the coil-magnet actuators at the first step and lead to the result:

$$\mathbf{D}_{\mathbf{mot}} = \begin{bmatrix} 0.43 & 0.78 & -1 \\ -1 & 0.41 & -0.70 \\ 0.11 & -1 & -0.82 \end{bmatrix} \quad (8.55)$$

8.4.8 Position control

Within the limits of the diagonalisation accuracy the system can be considered uncoupled into 3 independent oscillators, each provided with its own virtual sensor and actuator, on which to close a feedback loop. In this section we describe how the low frequency position control is implemented. When the feedback loops are closed each virtual oscillator can be

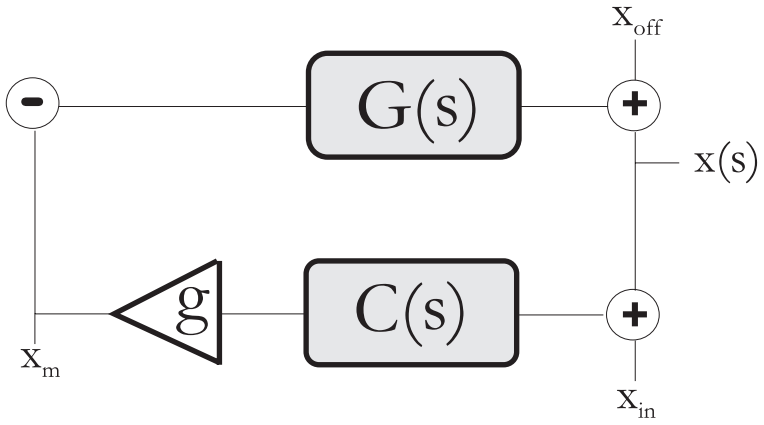

Figure 8.8: Logic scheme of the loop.

described by the logic scheme of fig. 8.8, where $G(s)$ has the form of the pendulum functions $P_k(s)$ defined in (8.4), $C(s)$ is the motor transfer function and g is an adjustable gain. Moreover, $x_{\rm off}$ is any input to be compensated for (such as an initial offset with respect to the working position), x_m is the top table displacement induced by the motor, while x_{in} is a *control signal* for the IP. The motor displacement is proportional to the integral of the input signal. Thus, the actuator transfer function is that of a pure integrator[6]:

$$C(s) = \frac{\alpha}{s} \tag{8.56}$$

where α is a constant with the dimension of a frequency. The system equations in the Laplace domain are:

$$x(s) = x_{\rm off}(s) - G(s)x_m(s) \tag{8.57}$$

$$x_m(s) = g\frac{\alpha}{s}[x_{\rm in}(s) + x(s)] \tag{8.58}$$

Then:

$$x(s) = \frac{x_{\rm off}(s) - gG(s)x_{\rm in}(s)\alpha/s}{1 + gG(s)\alpha/s} \tag{8.59}$$

This control system will be operated only in ultra-low frequency (from DC to a fraction of mHz). In that band $G(s) \simeq 1$ and the (8.59) reduces to

$$x(s) = \frac{x_{\rm off}(s) - gx_{\rm in}(s)\alpha/s}{1 + g\alpha/s} \tag{8.60}$$

In the following we analyze the (8.60) in some relevant cases:

[6]We are assuming that the spring connecting the motor to the top table can be considered *rigid*, that is, the transfer function between the motor displacement and the induced table displacement is equal to unity in the frequency range where the system works.

1. The simplest problem to be solved using the motors is the correction of an offset. In (8.60) we assume $x_{\text{in}}(s) = 0$. An offset of amplitude x_0 can be modeled as a step function:

$$x_{\text{off}}(t) = \begin{cases} 0 & \text{if} \quad t < 0 \\ x_0 & \text{if} \quad t \geq 0 \end{cases} \tag{8.61}$$

Then

$$x_{\text{off}}(s) = \frac{x_0}{s} \tag{8.62}$$

and

$$x(s) = \frac{x_0}{s + g\alpha} \tag{8.63}$$

Inverse transforming the (8.63) one finds the time evolution of the pendulum position when the loop is closed:

$$x(t) = \mathcal{L}^{-1}[x(s)] = x_0 e^{-g\alpha t} \tag{8.64}$$

Thus g defines the time constant of the process ($\tau = 1/g\alpha$) and the loop bandwidth. In fact, the unity gain is obtained solving

$$|gG(s)C(s)| \simeq \left|\frac{g\alpha}{s}\right| = 1 \tag{8.65}$$

whose solution is the unity gain frequency:

$$f_{\text{u.g.}} = \frac{g\alpha}{2\pi} \tag{8.66}$$

2. A slightly different situation occurs when one wants to move the IP of the amount X_0 with respect to the i-th virtual sensor. Then, in this case, there is no initial offset ($x_{\text{off}} = 0$) while the input has to be

$$x_{in}(t) = \begin{cases} 0 & \text{if} \quad t < 0 \\ -X_0 & \text{if} \quad t \geq 0 \end{cases} \tag{8.67}$$

Then

$$x(s) = X_0 \frac{g\alpha}{s(g\alpha - s)} = X_0 \left[\frac{1}{s} + \frac{1}{g\alpha - s}\right] \tag{8.68}$$

Inverse transforming the last equation:

$$x(t) = X_0 \left[1 - e^{-g\alpha t}\right] \tag{8.69}$$

Then, the IP approaches the position in a time that, as in the previous example, depends on the loop gain g. This demonstrates that x_{in} can be used as a *control signal* for the IP.

3. The third case we want to discuss is more general and it is definitely the most interesting. We assume that $x_{\rm in}(s)$ is the ultra-low frequency part of the interferometer error signal and we aim to force the IP to follow it. From eq. (8.60)

$$x(s) = -\frac{g\alpha/s}{1+g\alpha/s}x_{\rm in}(s) \tag{8.70}$$

In the high gain-low frequency limit the previous equation becomes

$$x(s) = -x_{\rm in}(s) \tag{8.71}$$

Then the IP is forced to follow the error signal, whatever its spectrum is.

8.4.9 Test results

In fig. 8.9 the results of the work are shown. In the initial situation the IP is wobbling[7] around a certain equilibrium position which does not correspond with the zero of the three virtual sensors. At $t = 0$ the three loops are turned on, the motors start running and the IP approaches the zero in about 400 seconds. The length of this time depends on the loop gain and the time constant. At $t = 450$ sec. the IP is moved of an amount 0.65 along the $\hat{y}$ axis with no disturbance of the other d.o.f.. In fig. 8.10 displacement along the 3 modes are shown, when a lower time constant (higher gain) is used. The new positions are reached in just few tens of seconds at the cost of "disturbing" the other modes: this drawback may be avoided with a further improvement of the driving matrix.

[7]The wobblying is due the resonances still undamped.

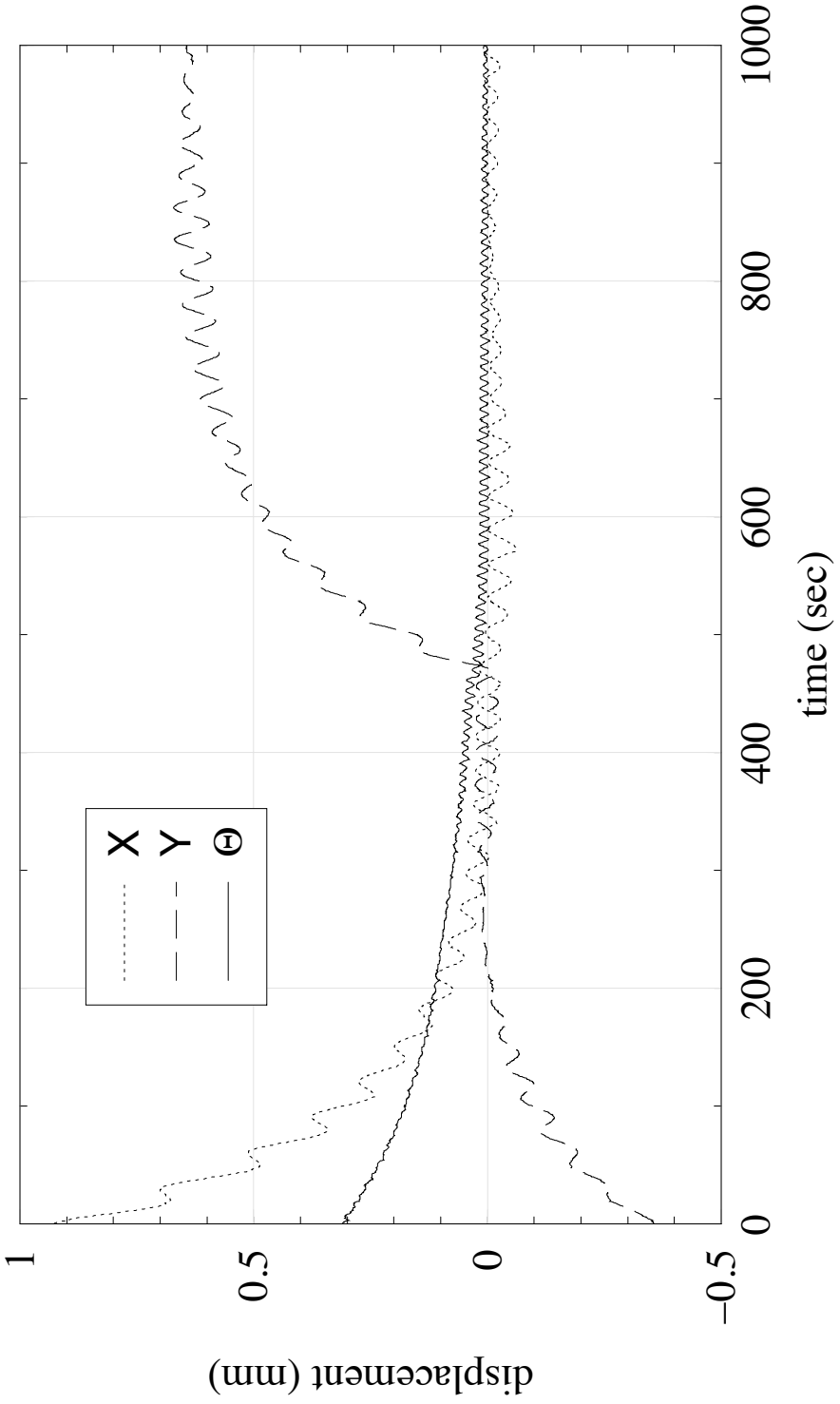

Figure 8.9: Control of the IP position: at $t = 0$, when the feedback is turned on, the IP is displaced by 0.9 mm in the $\hat{x}$ direction, -0.35 mm in $\hat{y}$ direction and rotated by 0.3 mm ($\theta \approx 0.35$ mrad) around the $\hat{z}$ axis. The IP is moved in the *zero* position in 400 sec (the time depends on the feedback gain). At $t \approx 450$ sec a displacement of 0.65 mm along $\hat{y}$ direction is imposed. The IP reaches the new position in 250 sec.

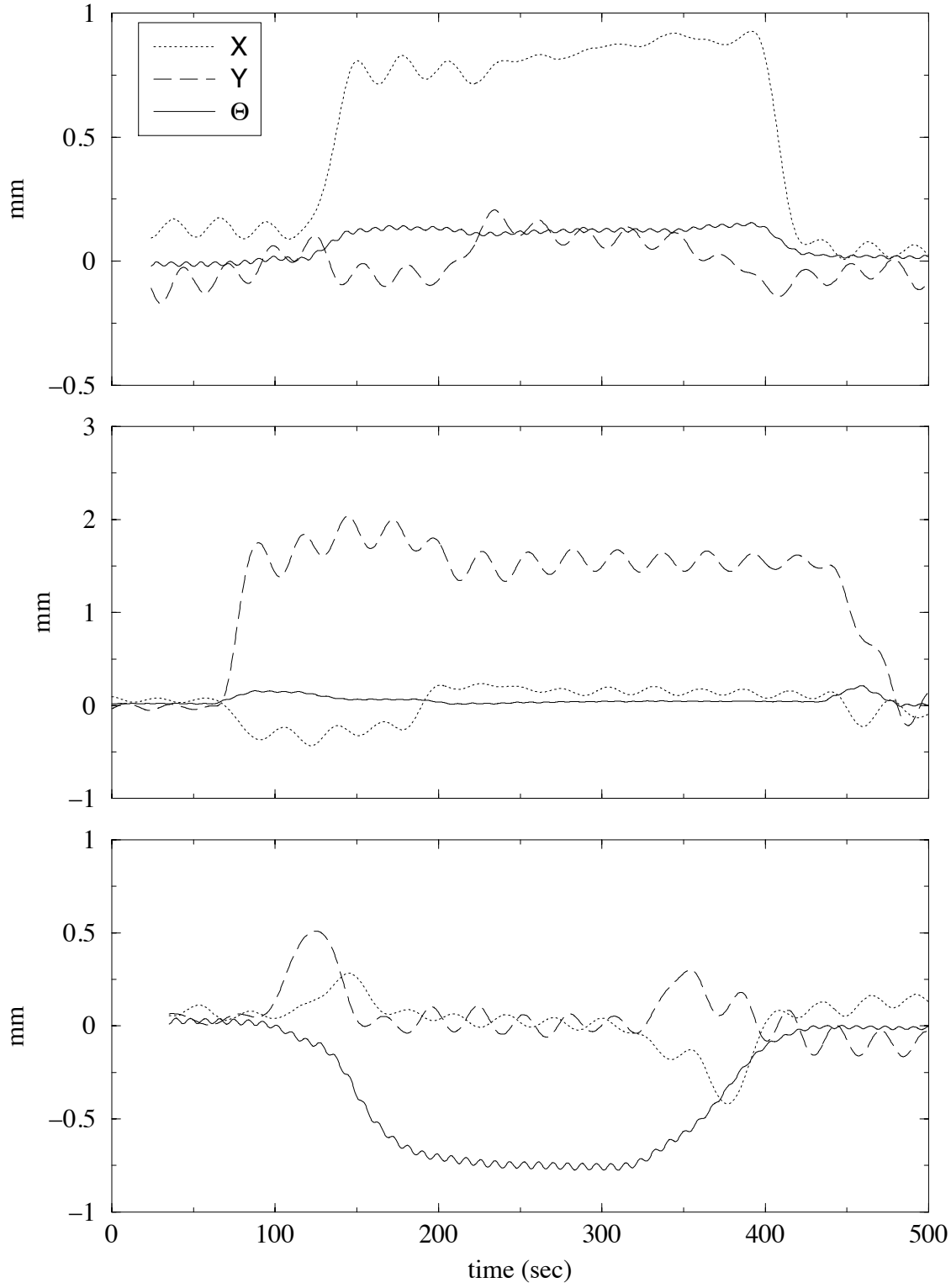

Figure 8.10: Control of the IP position (higher gain).

8.5 Inertial damping

Even if the IP is controlled at very low frequency this is not sufficient to meet the requirements on the residual motion imposed by the marionetta dynamic range: a damping of the SA resonances is needed. In this section we present some preliminary tests of inertial damping of the IP resonances. The damping strategy is based on the same idea described above: the system is diagonalised and controlled with 3 different feedback loops, each acting on a virtual one-dimensional oscillator, using accelerometers instead of displacement sensors. The reason for this can be explained with a simple model. Let $F_{\rm exc}$ and $F_{\rm fb}$ be the excitation force and the feedback force respectively. The equation of motion for each SISO system (virtual actuators-virtual sensors) can be written in the form:

$$F_{\rm exc} + F_{\rm fb} - k(x - x_0) = m\ddot{x} \tag{8.72}$$

which Laplace transforming and including a dissipation term Γ becomes:

$$\frac{F_{\rm exc}(s) + F_{\rm fb}(s)}{m} + \omega_0^2 x_0(s) = \left(s^2 + \omega_0^2 + i\Gamma\right) x(s) \tag{8.73}$$

Let $G(s)$ be the mechanical IP transfer function:

$$G(s) = \frac{x(s)}{x_0(s)} = \frac{\omega_0^2}{s^2 + \omega_0^2 + i\Gamma} \tag{8.74}$$

Then, the (8.73) can be written in a simpler form:

$$x(s) = G(s)\left[\Phi_{\rm exc} + \Phi_{\rm fb} + x_0(s)\right] \tag{8.75}$$

where the forces have been re-defined in order to have the same dimension of x:

$$\Phi_{\rm exc} = \frac{F_{\rm exc}(s)}{m\omega_0^2} \quad ; \quad \Phi_{\rm fb} = \frac{F_{\rm fb}(s)}{m\omega_0^2} \tag{8.76}$$

Use of displacement sensors When displacement sensors the system can be described by the logic scheme of fig. 8.11 (a). In this case the feedback force is:

$$\Phi_{\rm fb} = C(s)(x - x_0) \tag{8.77}$$

where $C(s)$ is a proper feedback filter. If the system is excited only by the seism ($F_{\rm exc} = 0$) the closed loop transfer function is immediately obtained by the (8.75):

$$G_{\rm c.l.}(s) = \frac{G(s)\left[1 + C(s)\right]}{1 + G(s)C(s)} \tag{8.78}$$

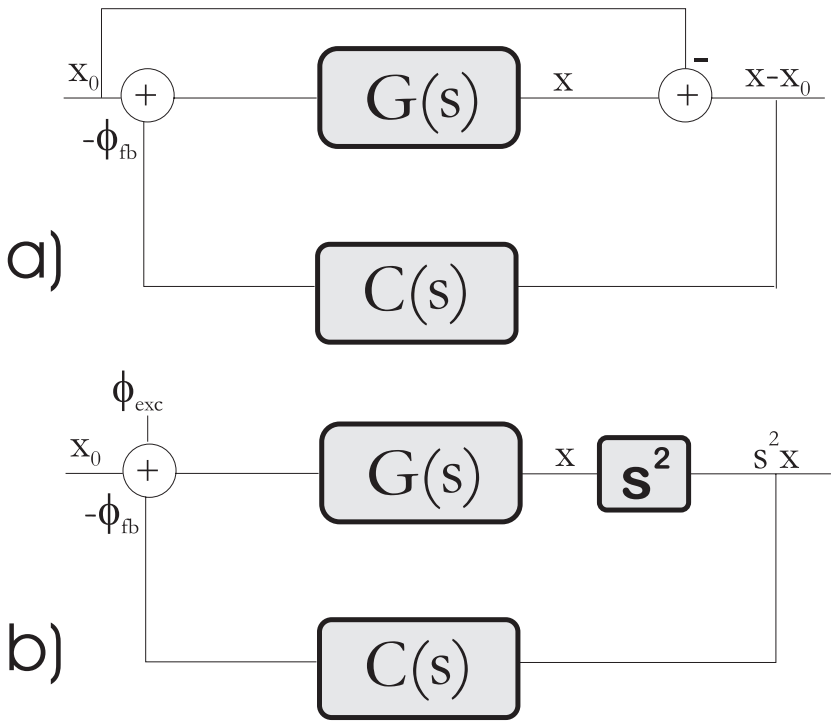

Figure 8.11: Loop scheme when: a) a position sensor is used; b) an inertial sensor is used.

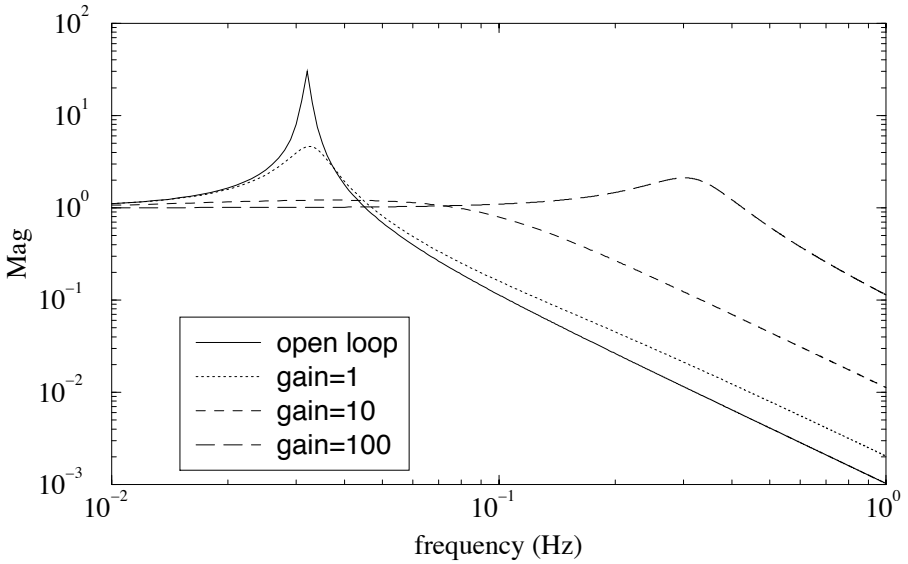

Figure 8.12: Effect of the feedback when a displacement sensor is used. The closed loop transfer function (8.78) is calculated using the filter (8.79) and for $C_0 = 0, 1, 10, 100$.

A damping is achieved if a filter of the form

$$C(s) = C_0(s + \omega_z) \tag{8.79}$$

where $\omega_0/2\pi$ is the frequency of the normal mode to be damped, $\omega_z \ll \omega_0$ and C_0 is a gain factor. With $\omega_z = 0$ a pure viscous feedback force is obtained ($F_{\rm fb} \propto \dot{x}$), but $\omega_z > 0$ is necessary in order not to cut the DC component of the LVDT output. In fig. 8.12 a simulation of the effect of the feedback is shown. When $C_0 = 1$ a damping of the peak is evident. As the gain increases and the loop bandwidth becomes larger, the transfer function tends to a constant value. The reason for this is simple: an infinitely effective feedback would make the displacement sensor output null, that is would make $x = x_0$. This is good in the resonance region (it damps the peak), and bad in the high frequency region, where it "freezes" the pendulum with respect to the external reference frame, thus short circuiting the attenuation action of the pendulum.

Use of inertial sensors when an accelerometer is used the system is described by fig. 8.11 (b). The feedback force is:

$$\Phi_{\rm fb} = C(s)s^2x(s) \tag{8.80}$$

and the closed loop transfer function is written:

$$\frac{x(s)}{x_0(s)} = \frac{G(s)}{1 + s^2 G(s) C(s)} \tag{8.81}$$

A proper form of the filter in this case is:

$$C(s) = C_0 \cdot \frac{s + \omega_0}{(s + \omega_1)(s + \omega_2)} \tag{8.82}$$

where $\omega_1 \ll \omega_0 \ll \omega_2$. Fig. 8.14 shows a simulation of the effect of the feedback on the IP transfer function (8.81) while in fig. 8.13 the open loop gain function $s^2 G(s) C(s)$ is plotted.

In principle, the gain is limited only by the accelerometer noise level. In fact, stricter limits exist (see section 8.5.4) but, nonetheless, using accelerometers allows to implement wideband feedback controls while position sensors are good only for pure viscous damping (and, even in this case, there is re-injection of noise above the resonant frequency).

In the following tests we measure the transfer functions between the virtual actuators and the virtual accelerometers. To compare the model with the experiment one has to calculate the function $s^2 x(s)/\Phi_{\text{exc}}$. If the coil excitation is large enough to dominate the seismic one ($\Phi_{\text{exc}} \gg x_0$) from the (8.75) one gets the force-to-acceleration transfer function:

$$\frac{s^2 x(s)}{\Phi_{\text{exc}}} = \frac{s^2 G(s)}{1 + s^2 G(s) C(s)} \tag{8.83}$$

The (8.83) is plotted in fig. 8.14.

8.5.1 Diagonalisation of acceleration sensors

The normal modes to be damped have frequencies 32, 36 and 112 mHz. The procedure to diagonalise the set of accelerometers was the same used for the LVDT. In fig. 8.15 the non-diagonalised IP transfer function is shown. We remark that it is obtained as:

$$\frac{\text{output of the } i\text{-th accel.}}{\text{force of the } j\text{-th coil}} \propto \frac{s^2 u_i(s)}{v_j(s)} = s^2 h_{ij}(s) \tag{8.84}$$

where $u_i(s), v_j(s), h_{ij}(s)$ have been defined in 8.3.1.

The results of the diagonalisation procedure (fig. 8.16) show that the sensing and driving matrices are affected by non negligible errors. For instance, the first graph (x mode excited) shows that x and θ are coupled at about 10%: the θ transfer function below 70 mHz reproduces exactly the x transfer function, 20 dB lower. In this case an

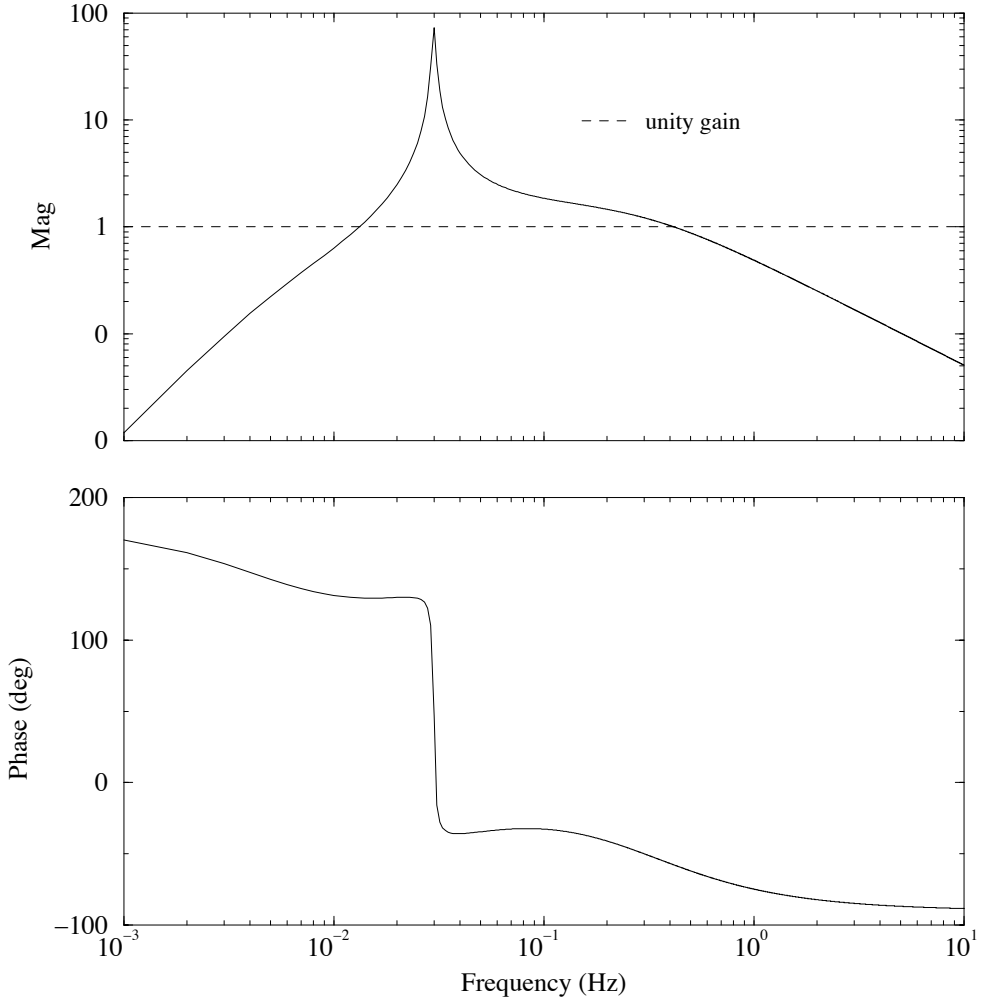

Figure 8.13: Open loop gain function (magnitude and phase).

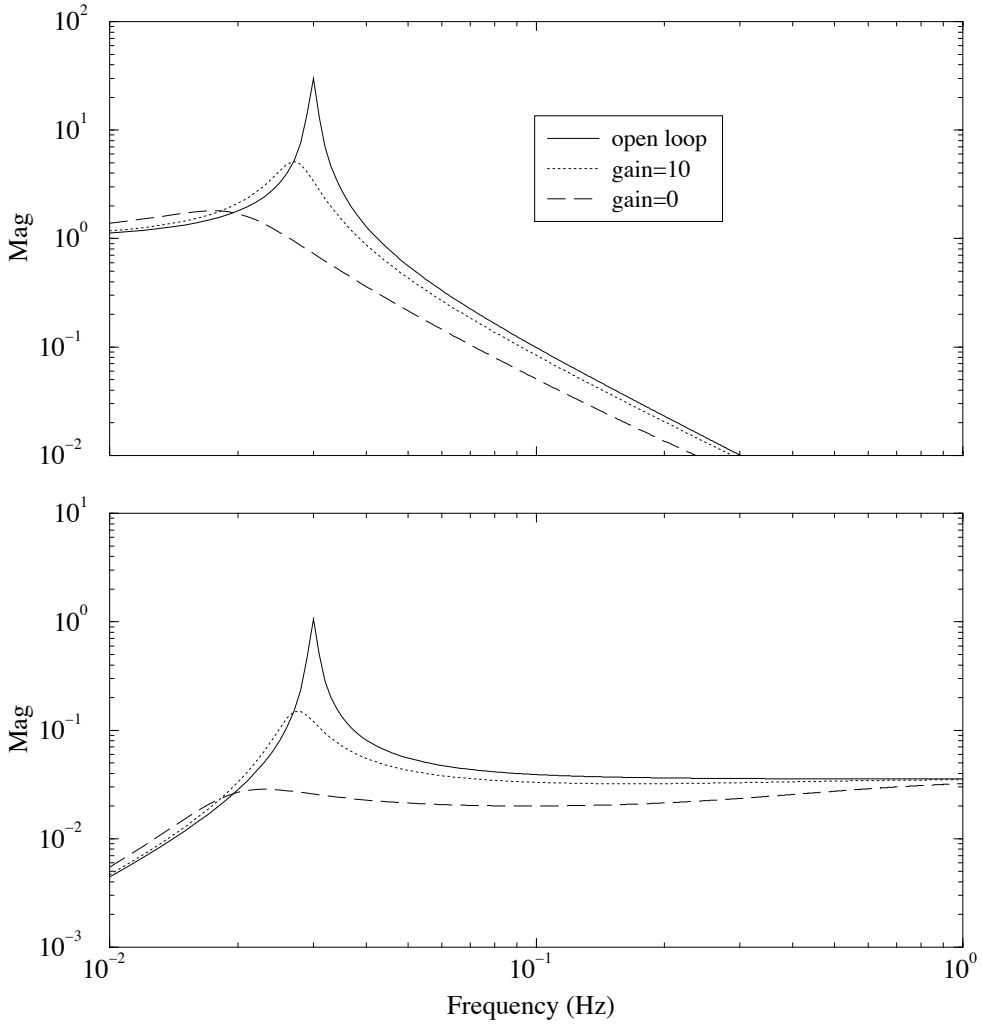

Figure 8.14: Effect of the inertial damping on a SISO. The first plot shows the IP closed loop transfer function (8.81) calculated using the filter (8.82). In the second plot the force-to-acceleration transfer function (8.83) is shown.

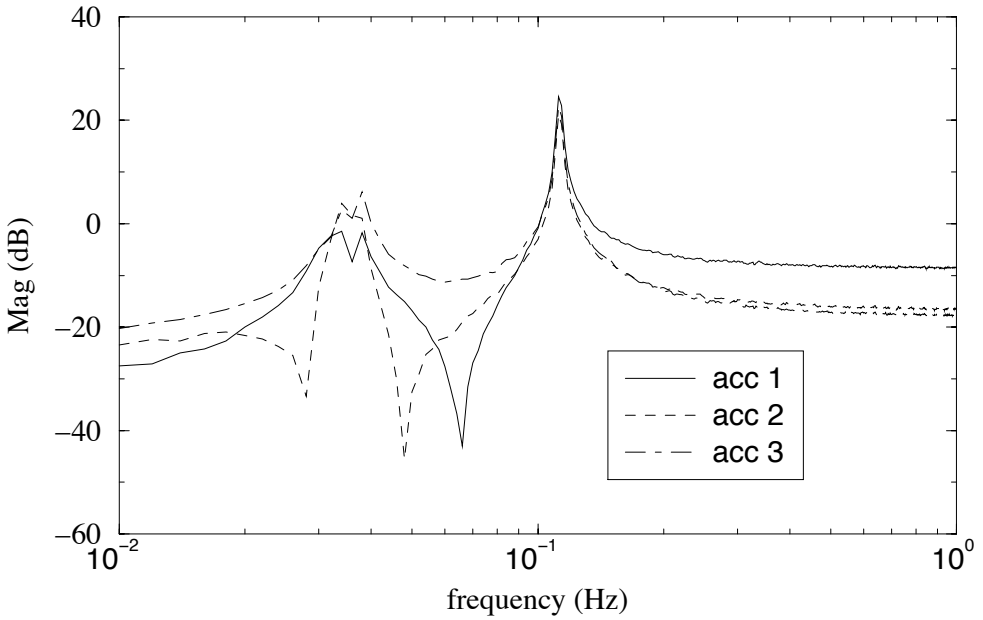

Figure 8.15: IP force-to-acceleration transfer function (real actuator-to-real accelerometer). At this stage the IP is a MIMO system and 3 resonance peaks are present in the transfer function.

iteration of the procedure was certainly required but was not done for lack of time[8]. The results presented in the following have to be considered preliminary. They have been a good test of the method, and a very good practice looking forward to performing the inertial damping of the complete SA.

8.5.2 DSP instructions

The DSP filter used is shown in the table 8.1.

With the lines 1-3 the DSP read the ADC channels `0x81-0x83` (the accelerometers outputs) and define them with the labels `a1,a2,a3`. With the line 4 the sensing matrix (`ACCsensing`) recombines the real sensors and the virtual sensors outputs `ax,ay,ath` are obtained. The lines 5-10 send both the real and virtual sensors outputs to 3 DAC channels. Each signal can be turned off/on by switching the `GAIN` to 0/1 and can be monitored on the spectrum analyser. In the lines 11-13 each virtual sensor is *filtered* to create the corresponding feedback force driving the virtual actuator.

With line 14 the virtual actuators signals `fx,fy,fth` are transformed into three cur-

[8]The setup was needed for the assembly of a complete superattenuator chain suspended from the IP.

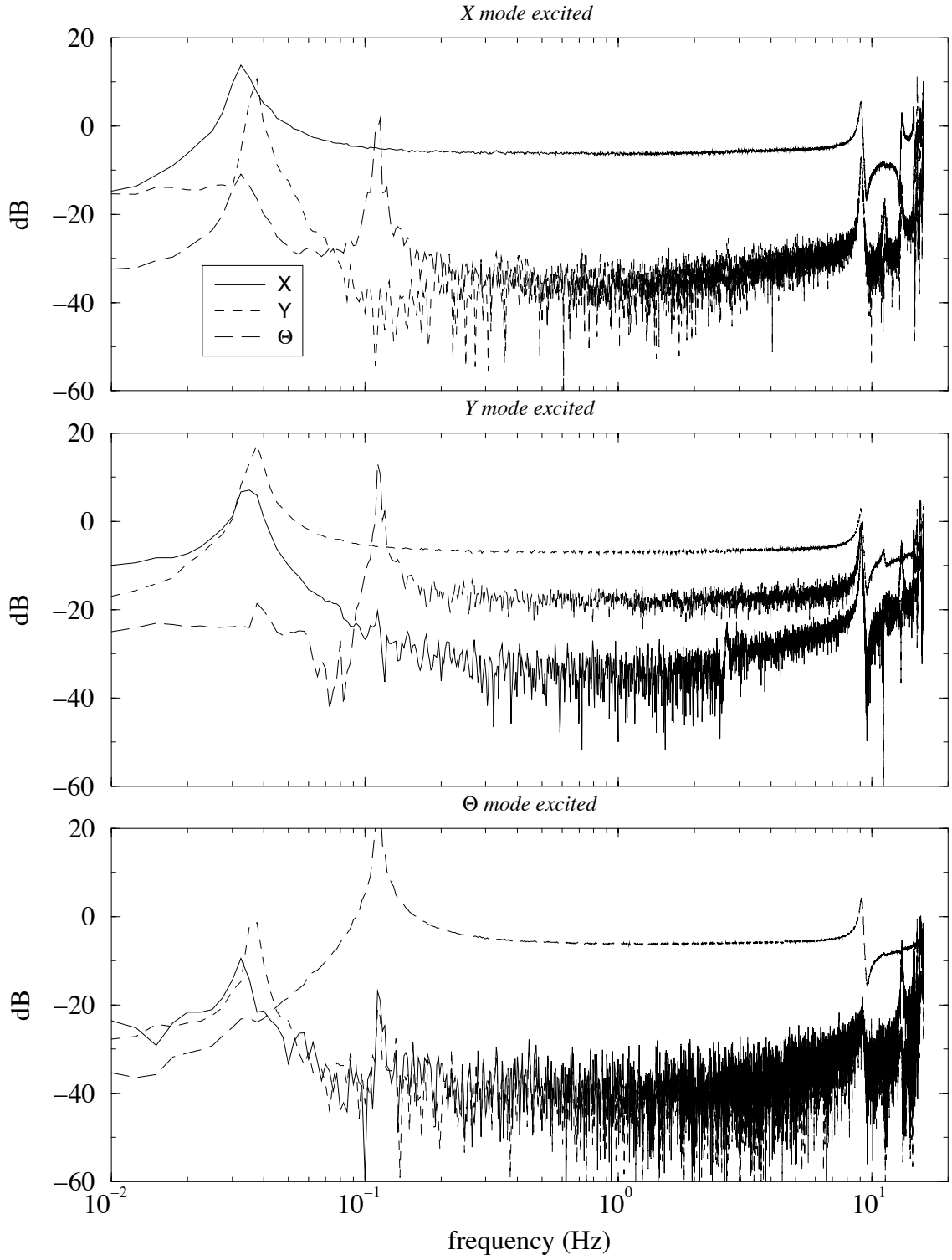

Figure 8.16: Diagonalised transfer functions (virtual actuators-to-virtual accelerometers).

line	INPUT	OUTPUT	FILTER	GAIN	@FREQUENCY
1	0x81	a1	NULL	1.0	0.0
2	0x82	a2	NULL	1.0	0.0
3	0x83	a3	NULL	1.0	0.0
4	MAT		ACCsensing	1.0	0.0
5	a1	0x81	NULL	0	0.0
6	a2	0x82	NULL	0	0.0
7	a3	0x83	NULL	0	0.0
8	ax	0x81	NULL	1.0	0.0
9	ay	0x82	NULL	1.0	0.0
10	ath	0x83	NULL	1.0	0.0
11	ax	fx	dampX.flt	1.0	0.0
12	ay	fy	dampY.flt	1.0	0.0
13	ath	fth	dampTH.flt	1.0	0.0
14	MAT		ACCdriving	1.0	0.0
15	f1	0x85	NULL	1.0	0.0
16	f2	0x86	NULL	1.0	0.0
17	f3	0x87	NULL	1.0	0.0

Table 8.1: The DSP program used to perform the IP inertial damping.

rents `f1,f2,f3` driving the coils by the driving matrix:

$$\begin{pmatrix} f_1 \\ f_2 \\ f_3 \end{pmatrix} = \mathbf{D} \cdot \begin{pmatrix} f_x \\ f_y \\ f_\theta \end{pmatrix} \tag{8.85}$$

Finally, the currents so obtained are sent to the DAC channels (`0x85,0x86,0x87` connected to the coil drivers.

8.5.3 Damping results

Once the system is diagonal one can implement three uncoupled feedback loop to damp the three modes.

The result of the inertial damping for the three modes is shown in fig. 8.17. The gain at the peak is about 20 dB for the translation modes and almost 50 dB for the rotation mode. To understand the meaning of these numbers one should measure the residual rms motion of the top table.

In fig. 8.18,8.19 the *open loop* and *closed loop* spectra measured by one of the accelerometers and the rms residual motion calculated from these spectra are shown.

Some comments are needed:

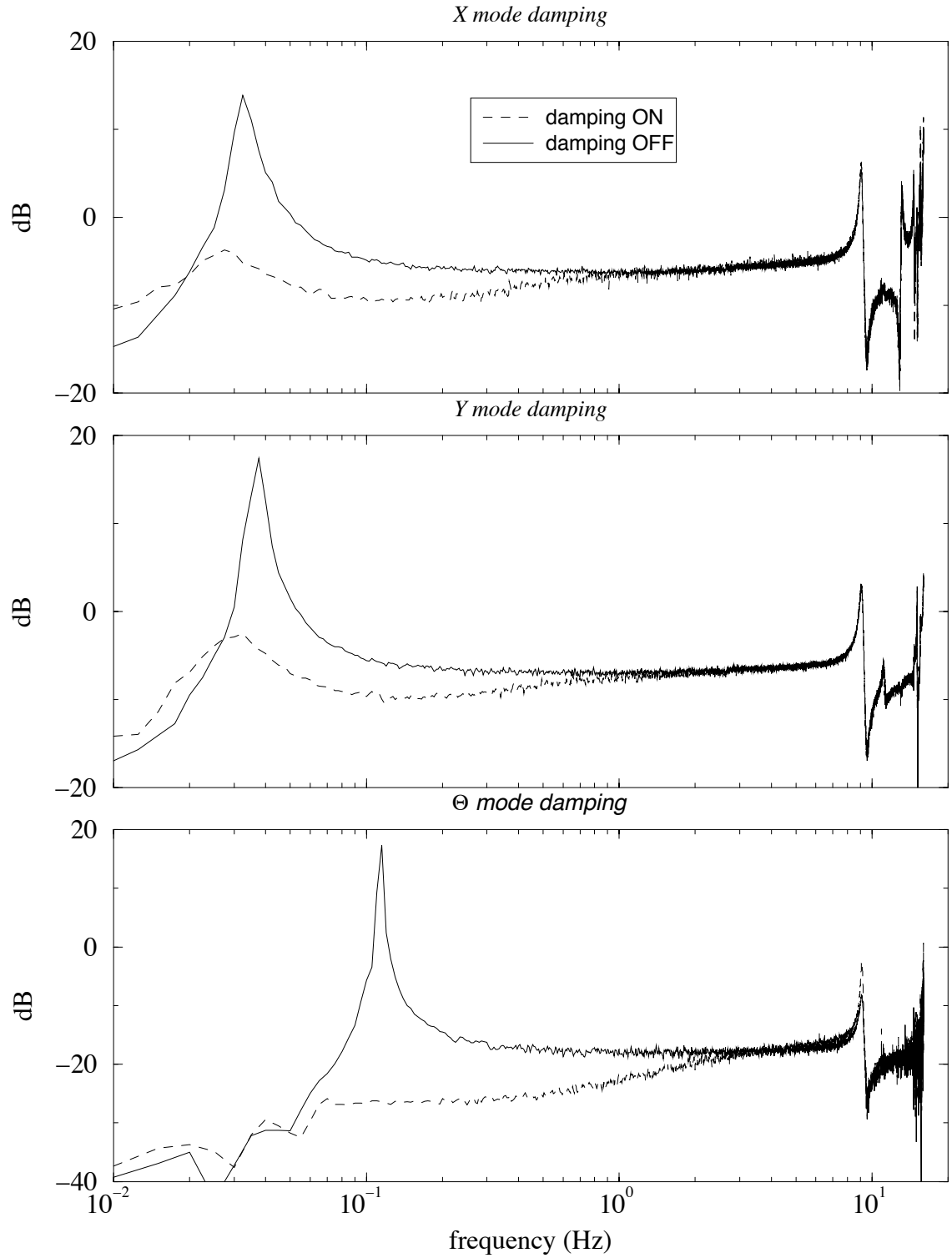

Figure 8.17: Effect of the inertial damping on the three modes. These figure must be compared with fig. 8.14 (b).

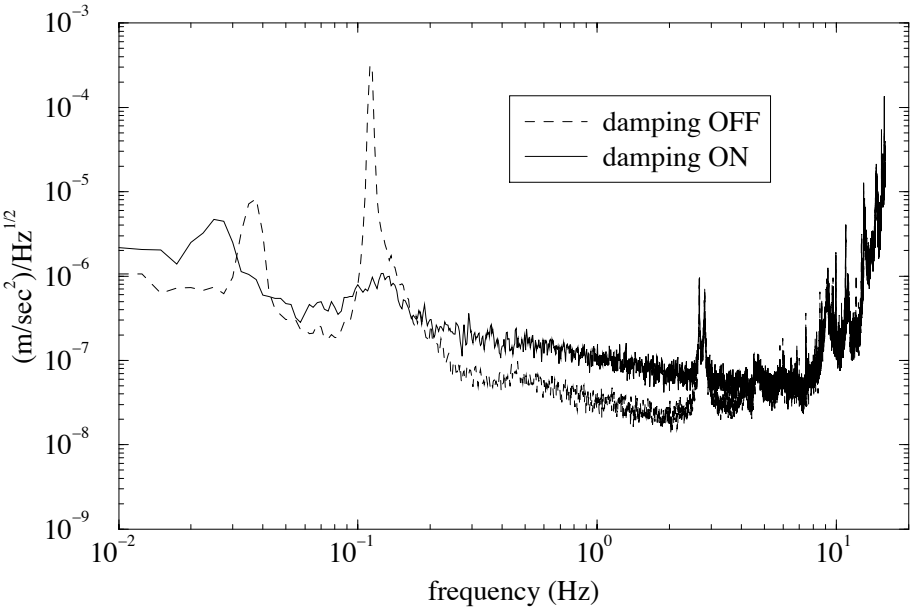

Figure 8.18: The acceleration noise spectral density measured by an accelerometer on the top table with damping on and off.

- the noise measured by an accelerometer on the edge of the top table is larger than that measured by a sensor on the very centre of the table, not sensitive to the rotation mode. Therefore, the second figure shows the motion of an outer point of the table, larger than the motion actually trasmitted to the mirror through the SA chain;

- the rms motion at 100 mHz is reduced from more than 30 to 0.3 μm. The 1 μmresidual motion target is achieved at 30 mHz, whereas the marionetta has to control the mirror above 50-100 mHz;

- the implementation of the inertial damping with the SA chain suspended will be more difficult: the many SA resonances in the range 0.2-2 Hz will mess up the transfer functions, introducing phase rotations which, if not compensated, could lead to instability or, at least, impose narrower bandwidth of the feedback loops;

- the noise introduced below 30 mHz and above 100 mHz is due to a bad mode diagonalisation.

In fig. 8.20 the effect of damping on the output of the virtual sensor θ is shown, for different values of the feedback gain.

8.5.4 Noise introduced at low frequency

Some explanations are necessary for the noise introduced below the resonant frequency (fig. 8.17, 8.19). This effect is connected to a non perfect parallelism of the legs. The simple 2-dimensional model of fig. 8.21 can help: if the legs are convergent (or divergent within an angle α, the top table does not stay horizontal during the IP motion but moves along a curve. With some algebra (see [112]) one can show that when the IP is displaced of an amount x with respect to the equilibrium position, the top table is tilted of an angle β:

$$\beta \simeq \frac{\alpha x}{a} \tag{8.86}$$

where a is the table radius. The angle α is positive or negative for converging or diverging legs respectively. The output of an accelerometer on the top table would be (see eq.(6.1)):

$$V \propto \ddot{x} + g\beta \tag{8.87}$$

which, using (8.86) and passing in the Fourier space becomes:

$$\tilde{V}(\omega) \propto \left(-\omega^2 + \frac{g\alpha}{a}\right) x \tag{8.88}$$

At frequencies $f \ll f_n = \sqrt{g\alpha/a}/2\pi$ the accelerometer measures the angle rather than the acceleration. In the real case the top table moves along a curved surface and two tilt angles β_x, β_y define its position. In this situation the three accelerometers are not independent and the diagonalisation is impossible in this range of frequencies. The order of magnitude of the critical frequency f_n can be estimated: an accurate mounting of the legs may ensure $\alpha \leq 1$ mrad, $a = 0.8$ m. Therefore $f_n \sim 20$ mHz, as expected from the measured trasfer functions of fig. 8.17.

A possible solution of the problem is to use of two angular accelerometers on the top table to measure independently the tilt and subtract the effect from the linear accelerometers outputs. The problem with this solution is that the angular accelerometers response is not reliable at such low frequencies. A second possible solution is the use of the LVDT signals. We show in the following that at frequencies lower than the IP resonant frequency the LVDTs provide a good correction signal. The transfer function of a 1-dimensional ideal IP can be written (neglecting the losses) simply:

$$\frac{x(\omega)}{x_0(\omega)} = \frac{\omega_0^2}{\omega_0^2 - \omega^2}$$

which is ~ 1 for $\omega \ll \omega_0$. The output of an LVDT measuring the IP top position x with respect to the ground x_0 is then:

$$x(\omega) - x_0(\omega) = \left[\frac{\omega_0^2}{\omega_0^2 - \omega^2} - 1\right] x_0 = \frac{\omega^2}{\omega_0^2 - \omega^2} \cdot x_0 \tag{8.89}$$

Then, for $\omega \ll \omega_0$:

$$x(\omega) - x_0(\omega) \simeq \omega^2 x_0(\omega) \simeq \omega^2 x(\omega) \tag{8.90}$$

The last equation shows that the position sensors effectively replace the accelerometers in the range of frequency where the accelerometers fail. This work has shown the feasibility of the different ingredients that still need to be combined and harmonised to get a working controlled mirror suspension. The complete control strategy will be tested on the complete superattenuator chain.

8.6 The next future

In the next months the techniques described in this thesis will be used on the new prototype superattenuator. Fig. 8.22 shows a spectrum measured on the IP top stage by one of the accelerometers. The first 3 resonances correspond to the translation and rotation modes of the IP and to the first pendula mode of the suspended chain respectively. The peaks at higher frequencies correspond to the superior SA chain modes.

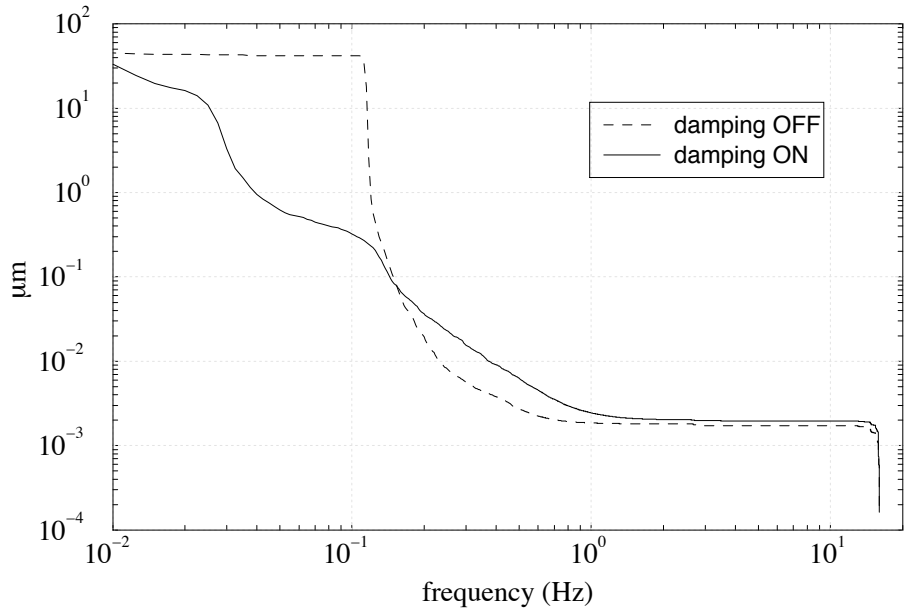

Figure 8.19: The rms dislacement calculated from the spectra of fig. 8.18 is shown.

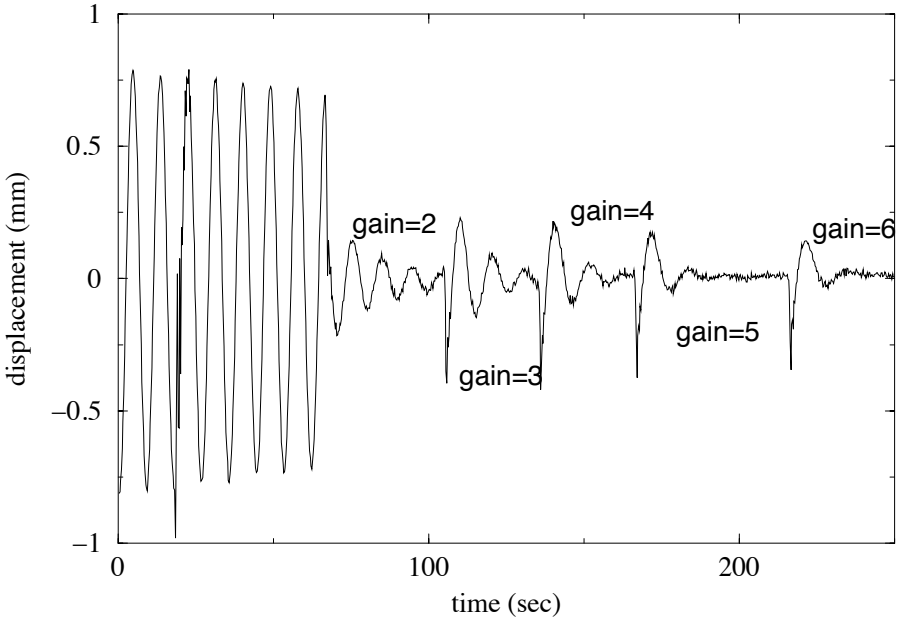

Figure 8.20: Effect of the inertial damping on the θ mode time signal for different values of the feedback gain.

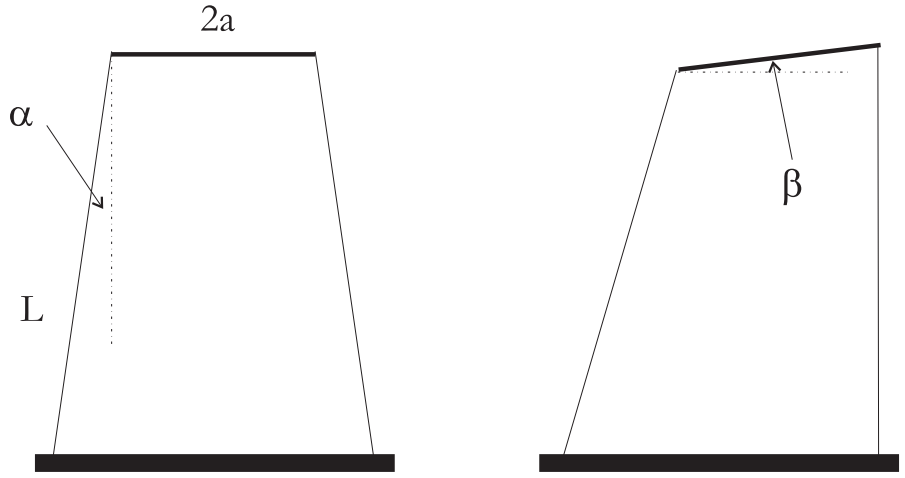

Figure 8.21: The effect of non parallel legs on the motion of the IP top table: the table moves along a curved surface as the IP is displaced from its equilibrium postition.

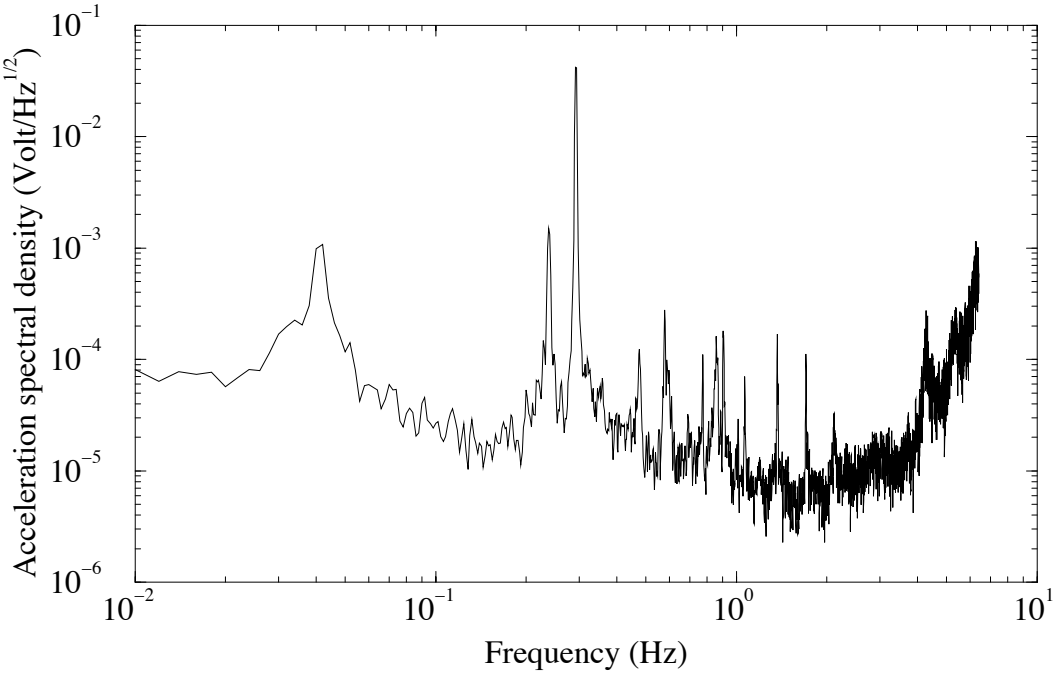

Figure 8.22: Acceleration spectral density measured on the top stage of the prototype SA chain, showing all the modes of the system (see for comparaison fig. 7.1).

Conclusions

Summary of results

We summarize here the main results of this work:

- an Inverted Pendulum top stage for the VIRGO superattenuator, suitable as horizontal pre-isolator and as a platform for active controls, has been conceived, designed and built;
- the tests proved that the Inverted Pendulum is an effective and stable horizontal pre-isolator. An attenuation of 65 dB at 1 Hz has been achieved;
- the tests proved that the Inverted Pendulum is an effective positioning device for the entire SA chain and that, consequently, it can be used as the low frequency actuation point in the VIRGO locking strategy;
- the damping of the Inverted Pendulum resonances has been performed using inertial sensors and digital signal processing.

The Inverted Pendulum has been accepted as suitable for the use in VIRGO. The production of 5 out of the 9 IP necessary for VIRGO has been completed. The mounting of the first complete SA chain on the Cascina site will start by the end of 1998.

Bibliography

[1] A.Einstein, *Ann. der Phys.*, **49**, 769 (1916).

[2] C.W.Misner, K.S.Thorne, J.Wheeler, *Gravitation*, San Francisco (1973).

[3] S.Weinberg, *Gravitation and Cosmology*, New York (1972).

[4] K.S.Thorne, in *300 Years of Gravitation*, S.Hawking and W.Israel eds., Cambridge Univ. Press (1987).

[5] P.R.Saulson, *Fundamentals of Interferometric Gravitational Wave Detectors*, World Scientific (1994).

[6] A.Abramovici, *et al.*, *Science*, **256**, 325 (1992).

[7] C.Bradaschia, *et al.*, *Nucl. Instrum. Meth. A*, **289**, 518 (1992).

[8] J.Hough, K.Danzmann, *et al.*, *GEO600 Proposal*, unpublished (1994).

[9] K.Kuroda, *et al.*, in *Proceedings of the 1st International Conference on GW: Sources and Detectors*, eds. F.Fidecaro, I.Ciufolini, World Scientific, Singapore (1997).

[10] D.McClelland, D.G.Blair, R.J.Sandeman, *AIGO: A Southern Hemisphere Second Generation Gravitational Wave Observatory*, in *Proceedings of the 7th Marcel Grossmann Meeting on General Relativity*, Part B, (Stanford Univ. July 1994), Eds: R.T. Jantzen, G.M. Keiser, Series ed. R. Ruffini, World Scientific Pub.Co, 1415-1417 (1996).

[11] J.H.Taylor, J.M.Weisberg, *Ap. J.*, **253**, 908-920 (1982).

[12] J.H.Taylor, J.M.Weisberg, *Ap. J.*, **345**, 434-450 (1989).

[13] J.H.Taylor, A.Wolszcan, T.Damour, J.M.Weisberg, *Nature*, **355**, 132-136 (1992).

[14] J.H.Taylor, *Rev. Mod. Phys.*, **66**, 3, 711-719 (1994).

[15] R.A.Hulse, *Rev. Mod. Phys.*, **66**, 3, 699-710 (1994).

[16] T.Damour, J.H.Taylor, *Ap. J.*, **366**, 501-511 (1991).

[17] T.Damour, G.Esposito-Farèse, gr-qc/9803031 (1998).

[18] T.Damour, gr-qc/9711061 (1997), to appear in the *Proc. of the Princeton 250th Anniversary Conf. on Critical Problems in Physics*, Princeton Univ. Press.

[19] D.G.Blair, *Sources of gravitational waves*, in *The Detection of Gravitational Waves*, ed. D.G.Blair, Cambridge University Press (1991).

[20] S.Bonazzola, J.A.Marck, *Astrophysical Sources of Gravitational Radiation*, Annu. Rev. Nucl. Part. Sci., **45**, 655-717 (1994).

[21] K.S.Thorne, *Gravitational waves from compact bodies*, in *Proc. of IAU Symposium 165, Compact Stars in Binaries*, also gr-qc/9506084 (1995).

[22] K.S.Thorne, *Probing black holes and relativistic stars with gravitational waves*, gr-qc/9706079 (1997).

[23] É.É.Flanagan, *Astrophysical sources of gravitational radiation and prospects for their detection*, gr-qc/9804024 (1998).

[24] L.Blanchet, *Class.Quant. Grav.*, **15**, 113 (1998).

[25] C.Cutler, É.É.Flanagan, *Phys. Rev. D*, **49**, 2658-2697 (1994).

[26] L.Blanchet, T.Damour, B.R.Iyer, C.M.Will, A.G.Wiseman, *Phys. Rev. Lett.*, **74**, 3515 (1995).

[27] B.Paczyński, *Ap. J.*, **308**, L-43 (1986).

[28] M.Zimmermann, E.Szedenits, *Phys. Rev. D*, **20**, 351 (1979).

[29] E.Costa, *et al.*, *Nature*, **387**, 783 (1997).

[30] B.Paczyński, astro-ph/9712123 (1997).

[31] K.Iwamoto, *et al.*, astro-ph/9806382, Submitted to *Nature* (1998).

[32] A.Wolszczan, *Nature*, **350**, 688 (1991).

[33] B.F.Schutz, *Nature*, **323**, 310-311 (1986).

[34] É.É.Flanagan, *Phys. Rev. D*, **48**, 2389 (1993).

[35] L.P.Grishchuk, *Sov. Phys. JETP*, **40**, 409 (1975).

[36] B.Allen, *The stochastic gravity-wave background: sources and detection*, in *Proc. of the Les Houches School on Astrophysical Sources of Gravitational Waves*, eds. J.A.Marck and J.P.Lasota, Cambridge University Press (1996).

[37] M.Maggiore, *High-energy physics with gravitational waves experiments*, gr-qc/9803028 (1998).

[38] A.Abramovici, *et al.*, *Phys. Lett. A*, **218**, 157 (1996).

[39] D.C.Agnew, *Review of Geophysics*, **24**, 3, 579-624 (1986).

[40] P.R.Saulson, *Phys. Rev. D*, **30** (4), 732-736 (1984).

[41] G.Cagnoli, L.Gammaitoni, J.Kovalik, F.Marchesoni, M.Punturo, VIRGO Note PER-1390/054 (1996).

[42] H.B.Callen, T.A.Welton, *Phys. Rev.*, **83** (1), 34-40 (1951).

[43] B.F.Schutz, in *Gravitational Waves Data Analysis*, ed. B.F.Schutz, Reidel (1988).

[44] M.Beccaria, G.Cella, A.Ciampa, E.Cuoco, G.Curci, A.Viceré, VIRGO Note NTS 096/024 (1996).

[45] J.Y.Vinet, *et al.*, *Phys. Rev. D*, **56**, 6085 (1997).

[46] B.J.Meers, *Phys. Rev. D*, **38**, 2317-2326 (1988).

[47] K.A.Strain, B.J.Meers, *Phys. Rev. Lett.*, **66**, 1391-1394 (1991).

[48] E.Gourgoulhon, S.Bonazzola, in *Proceedings of the 1st International Conference on GW: Sources and Detectors*, eds. F.Fidecaro, I.Ciufolini, World Scientific, Singapore (1997).

[49] M.Gasperini, in *String theory in curved spacetimes*, 333, World Scientific, Singapore (1998).

[50] M.Gasperini, *Relic gravitons from the pre-Big Bang: what we know and what we don't know*, in *New developments in string gravity and physics at the Planck energy scale*, ed. N.Sanchez, World Scientific (1996). Also hep-th/9607146.

[51] A.Buonanno, M.Maggiore, C.Ungarelli, *Phys. Rev. D*, **55**, 3330-3336, (1997).

[52] R.Brustein, in *Proceedings of the 1st International Conference on GW: Sources and Detectors*, eds. F.Fidecaro, I.Ciufolini, World Scientific, Singapore (1997).

[53] R.Flaminio, H.Heitmann, *Phys. Lett.A*, **214**, 112-122 (1996).

[54] A.N.Luiten, M.Beccaria, M.Bernardini, E.Bougleux, S.Braccini, C.Bradaschia, E.Cuoco, R.De Salvo, R.Del Fabbro, A.Di Virgilio, I.Ferrante, F.Fidecaro, A.Gaddi, A.Gennai, A.Giazotto, L.Holloway, P.La Penna, G.Losurdo, S.Malik, S.Mancini, M.Mazzoni, H.B.Pan, F.Paoletti, A.Pasqualetti, D.Passuello, P.G.Pelfer, R.Poggiani, P.Popolizio, F.Raffaelli, R.Stanga, A.Vicerè, Z.Zhang, *Rev. Sci. Instrum.*, **68**, 1889 (1997).

[55] A.Giazotto, *Phys. Rep.*, **182**, 6, 365-425 (1989).

[56] R.Del Fabbro, A.Di Virgilio, A.Giazotto, H.Kautzky, V.Montelatici, D.Passuello, *Phys. Lett. A*, **124**, 253 (1987).

[57] R.Del Fabbro, A.Di Virgilio, A.Giazotto, H.Kautzky, V.Montelatici, D.Passuello, *Phys. Lett. A*, **132**, 237 (1988).

[58] R.Del Fabbro, A.Di Virgilio, A.Giazotto, H.Kautzky, V.Montelatici, D.Passuello, *Phys. Lett. A*, **133**, 471 (1988).

[59] R.Del Fabbro, A.Di Virgilio, A.Giazotto, H.Kautzky, V.Montelatici, D.Passuello, *Rev. Sci. Instrum.*, **59**, 292 (1988).

[60] C.Bradaschia, R.Del Fabbro, L.Di Fiore, A.Di Virgilio, A.Giazotto, H.Kautzky, V.Montelatici, D.Passuello, *Phys. Lett. A*, **137**, 329 (1989).

[61] J.Winterflood, PhD Thesis, University of Western Australia, in preparation.

[62] J.Giaime, P.Saha, D.shoemaker, L.Sievers, *Rev. Sci. Instrum.*, **67**, 208 (1996).

[63] G.Losurdo, *Tesi di Laurea*, Dipartimento di Fisica, Università degli Studi di Pisa (1993), unpublished.

[64] A.Gennai, *Tesi di Laurea*, Facoltà di Ingegneria, Università degli Studi di Pisa (1993), unpublished

[65] R.Flaminio, *Tesi di Dottorato*, Dipartimento di Fisica, Università degli Studi di Pisa (1994), unpublished.

[66] L.Landau, E.Lifchitz, *Théorie de l'Elasticité*, MIR (1967).

[67] A.Viceré, private communication (1996).

[68] R.De Salvo, A.Gaddi, G.Gennaro, L.Holloway, G.Losurdo, J. Winterflood, *A Proposal for a Pre-Isolator Stage for the VIRGO Superattenuator*, VIRGO Note NTS 096/034 (1996).

[69] S.Braccini, C.Bradaschia, R.Del Fabbro, A.Di Virgilio, I.Ferrante, F.Fidecaro, R.Flaminio, A.Gennai, A.Giassi, A.Giazotto, G.Gorini, G.Losurdo, F.Palla, A.Pasqualetti, D.Passuello, R.Poggiani, G.Torelli, Z.Zhang, *Rev. Sci. Instrum.*, **67** (8), 2899-2902 (1996).

[70] M.Beccaria, M.Bernardini, S.Braccini, C.Bradaschia, G.Cagnoli, C.Casciano, G.Cella, E.Cuoco, V.Dattilo, G.De Carolis, R.De Salvo, A.Di Virgilio, G.T.Feng, I.Ferrante, F.Fidecaro, F.Frasconi, A.Gaddi, L.Gammaitoni, A.Gennai, A.Giazotto, L.Holloway, J.Kovalik, P.La Penna, G.Losurdo, S.Malik, S.Mancini, F.Marchesoni,

J.Nicolas, F.Palla, H.B.Pan, F.Paoletti, A.Pasqualetti, D.Passuello, R.Poggiani, P.Popolizio, M.Punturo, F.Raffaelli, V.Rubino, R.Valentini, A.Vicerè, F.Waharte, Z.Zhang, *Nucl. Instrum. Meth. in Phys. Res. A*, 455-469 (1998).

[71] G.Cagnoli, J.Kovalik, L.Gammaitoni, F.Marchesoni, M.Punturo, S.Braccini, R.De Salvo, F.Fidecaro, G.Losurdo, *Phys. Lett. A*, **237**, 21-27 (1997).

[72] G.Cagnoli, Tesi di Dottorato, Università degli Studi di Perugia (1998).

[73] M.Bernardini, S.Braccini, C.Bradaschia, C.Casciano, G.Cella, A.Ciampa, E.Cuoco, G.Curci, V.Dattilo, R.De Salvo, A.Di Virgilio, G.Feng, I.Ferrante, F.Fidecaro, F.Frasconi, A.Gaddi, A.Gennai, A.Giazotto, P.La Penna, G.Losurdo, S.Mancini, M.Mazzoni, F.Palla, H.B.Pan, A.Pasqualetti, R.Passaquieti, D.Passuello, R.Poggiani, P.Popolizio, F.Raffaelli, S.Rapisarda, R.Stanga, A.Vicerè, J.Winterflood, Z.Zhang, *Class. Quantum Grav.*, **15**, 1-24 (1998).

[74] G.Feng, *et al.*, VIR-TRE-PIS-4600-129 (1997).

[75] M.Beccaria, M.Bernardini, E.Bougleux, S.Braccini, C.Bradaschia, C.Casciano, G.Cella, E.Cuoco, E.D'Ambrosio, G.De Carolis, R.Del Fabbro, R.De Salvo, A.Di Virgilio, I.Ferrante, F.Fidecaro, R.Flaminio, A.Gaddi, A.Gennai, G.Gennaro, A.Giazotto, L.Holloway, P.La Penna, G.Losurdo, S.Malik, S.Mancini, J.Nicolas, F.Palla, H.B.Pan, F.Paoletti, A.Pasqualetti, D.Passuello, R.Poggiani, P.Popolizio, F.Raffaelli, A.Vicerè, F.Waharte, Z.Zhang, *Nuc. Instrum. Meth. in Phys. Res. A*, **394**, 397-408 (1997).

[76] S.Braccini, *Tesi di Perfezionamento*, Scuola Normale Superiore di Pisa (1996).

[77] R.Valentini, private communication (1996).

[78] S.Braccini, C.Casciano, R.De Salvo, F.Fidecaro, VIRGO Note NTS 096/032 (1996).

[79] S.Braccini, C.Casciano, R.De Salvo, R.Del Fabbro, F.Fidecaro, VIRGO Note NTS 096/045 (1996).

[80] A.S.Nowick, B.S.Berry, *Anelastic Relaxation in Crystalline Solids*, Academic Press (1972).

[81] F.Press, *Handbook of physical constants*, revised ed., Memoir (1997).

[82] R.E.Smallman, *Modern Physical Metallurgy*, Butterworth, Oxford (1985).

[83] American Society of Metals, *Metals Handbook 10th edition*, vol.1, 793-800 (1990).

[84] A.Vicerè, Talk at the Conference *Around VIRGO*, Tirrenia (Pisa), 20-24 September 1998.

[85] P.Ruggi, Tesi di Laurea, Dipartimento di Fisica, Università di Pisa, in preparation.

[86] P.Ruggi, C.Casciano, *et al.*, *Superattenuator vertical transfer function*, VIRGO Note in preparation.

[87] C.Zener, *Elasticity and anelasticity of metals*, University of Chicago Press (1948).

[88] H.Goldstein, *Classical Mechanics*, Addison-Wesley, Reading (1980).

[89] P.R.Saulson, *Phys. Rev. D*, **42**, 2437-2445 (1990).

[90] T.J.Quinn, C.C.Speake, L.M.Brown, *Philos. Mag. A*, **65**, 261 (1992)

[91] P.R.Saulson, R.T.Stebbins, F.D.Dumont, S.E.Mock, *Rev. Sci. Instrum.*, **65** (1), 182-191 (1994).

[92] VIRGO Collaboration, *Final Conceptual Design*, unpublished (1992).

[93] M.Pinoli, D.G.Blair, L.Ju, *Meas. Sci. Technol.*, **4**, 995-999 (1993).

[94] J.Winterflood, D.G.Blair, *Phys. Lett. A*, **222**, 141 (1996).

[95] J.Winterflood, G.Losurdo, D.G.Blair, to be submitted to *Phys. Lett. A*.

[96] M.A.Barton, K.Kuroda, *Rev. Sci.Instrum.*, **65** (12), 3775-3779 (1994).

[97] M.A.Barton, N.Kanda, K.Kuroda, *Rev. Sci.Instrum.*, **67** (11), 3994- 3999 (1996).

[98] D.Tatsumi, M.A.Barton, T.Uchiyama, K.Kuroda, *A two-dimensional low frequency vibration attenuator using X-pendulums*, Submitted to *Rev. Sci. Instrum.* (August 1998).

[99] G.Losurdo, J.Winterflood, *Performance of the inverted pendulum as a pre-isolator for the VIRGO superattenuator*, VIRGO Note VIR-TRE-PIS-4600-142 (1998).

[100] R.De Salvo, *et al.*, *Filter 0 prototype performance as a vertical pre-isolator for the VIRGO superattenuator*, accepted for publication, *Nucl. Instrum Meth.* (1998).

[101] G.Losurdo, *et al.*, *An Inverted Pendulum Pre-Isolator Stage for the VIRGO Suspension System*, to be submitted to *Rev. Sci. Instrum.* (1998).

[102] L.Holloway, *Proc. of the 6th San Miniato Seminar on experimental apparatus for high energy physics and astrophysics*, *Nucl. Phys. B, Proc. Suppl.*, **54** (1997).

[103] J.Liu, Li Ju, D.G.Blair, *Phys. Lett. A*, **228**, 243 (1997).

[104] N.A.Robertson, R.W.P.Drever, I.Kerr, J.Hough, *J. Phys. E*, **15**, 1101 (1982).

[105] P.S.Linsay, D.H.Shoemaker, *Rev. Sci. Instrum.*, **53**, 1014 (1982).

[106] P.R.Saulson, *Rev. Sci. Instrum.*, **55**, 1315 (1984).

[107] A.Giazotto, D.Passuello, A.Stefanini, *Rev. Sci. Instrum.*, **57**, 1145 (1986).

[108] D.Shoemaker, R.Schilling, L.Schnupp, W.Winkler, K.Maischberger, A.Rüdiger, *Phys. Rev. D*, **38** 423 (1988).

[109] M.Stephens, P.Saulson, J.Kovalik, *Rev. Sci. Instrum.*, **62**, 924 (1991).

[110] R.Stebbins, *et al.*, *Proc. SPIE*, **2264**, 27 (1994).

[111] D.B.Newell, *Six Degree of Freedom Active Vibration Isolation at 1 Hz and Above*, PhD Thesis, University of Colorado (1994), unpublished.

[112] G.Losurdo, *et al.*, *Effect of non-parallelism of the Inverted Pendulum legs on the accelerometers response and consequences for the inertial damping*, VIRGO Note in preparation.

[113] A.Gennai, S.Mancini, F.Paoletti, D.Passuello, S.Rapisarda, R.Taddei, *Digital Signal Processor VME board (DSPV96) for the suspension electronics*, VIRGO Note in preparation.

[114] D.H.Owens, *Feedback and Multivariable Systems*, Peter Peregrinus Ltd. (1978).

[115] A.Gennai, T.Maiani, S.Mancini, D.Passuello, VIRGO Note VIR-NOT-PIS-1390-101 (1997).

[116] V.Dattilo, *Coil-magnet actuators for the SA top stage*, VIRGO Note, in preparation.

Acknowledgments

In the end, the moment of writing the last page of the thesis has come and the first person I think of is my friend Tito: this work is devoted to him.

Thanks to all the people of PISA VIRGO Group, and especially to those of the Superattenuator group for their support.

Thanks to Francesco Fidecaro and Riccardo De Salvo.

Thanks to Diego Passuello, Alberto Gennai, John Winterflood, Stefano Gaggero.

Thanks to Lee Holloway, Andrea Gaddi and Andrea Vicerè.

Finally, thanks to the "Gravity Waves people" of UWA with whom I had a beatiful time in Perth.